Voltage Imaging with a Near-Infrared Phosphine Oxide Rhodamine Voltage Reporter

By

Monica Alejandra Gonzalez

A dissertation submitted in partial satisfaction of requirements for the degree of

Doctor of Philosophy

in

Chemistry

in the

Graduate Division

of the

University of California, Berkeley

Committee in charge:

Professor Evan W. Miller

Professor Helen S. Bateup

Professor Michael A. Marletta

Fall 2020

Voltage Imaging with a Near-Infrared Phosphine Oxide Rhodamine Voltage Reporter

By Monica A. Gonzalez

Abstract

Light can be used to provide an optical readout of relative changes in membrane potential in a minimally invasive manner with high spatiotemporal resolution via the use of fluorescent voltage reporters. These reporters localize to cell membranes and are composed of three primary elements: a fluorophore, a molecular wire, and an electron rich aniline donor. The donor modulates the fluorescence of the reporter in response to changes in the membrane potential of a cell through a photo induced electron transfer (PeT) process.[1]The existing color palette of these reporters is limited to the visible range of light (< 700 nm). Near-infrared (NIR) fluorescent dyes are favorable since the use of NIR light avoids cellular autofluorescence, is less damaging than visible light, and can be used simultaneously with other tools in the visible spectrum such as calcium indicators and optogenetic actuators.[2] To take advantage of these properties, we synthesized and characterized four NIR voltage reporters using a phosphine oxide rhodamine fluorophore with a maximum absorbance at 704 nm and peak emission at 723 nm. These NIR phosphine oxide rhodamine voltage reporters, poRhoVRs, exhibit fractional changes in fluorescence ranging from 13-43% per 100 mV with good signal to noise ratios. We have successfully used poRhoVR to monitor spontaneous neuronal activity in cultured neurons as well as activity evoked through field stimulation or via optogenetic activation. We have also used poRhoVR in mouse retina in conjunction with GCaMP6f, to monitor pharmacologically induced changes in activity, while offering greater spatial resolution than possible with multi-electrode arrays. These poRhoVR dyes can easily be modified to be genetically targetable by appending chemical handles for proteins such as HaloTag.[3]

References

(1) Miller, E. W.; Lin, J. Y.; Frady, E. P.; Steinbach, P. A.; Kristan, W. B.; Tsien, R. Y. Optically Monitoring Voltage in Neurons by Photoinduced Electron Transfer through Molecular Wires. *Proc. Natl. Acad. Sci. U. S. A.* **2012**, *109* (6), 2114–2119. https://doi.org/10.1073/pnas.1120694109.

(2) Smith, A. M.; Mancini, M. C.; Nie, S. Bioimaging: Second Window for in Vivo Imaging. *Nat. Nanotechnol.* **2009**, *4* (11), 710–711. https://doi.org/10.1038/nnano.2009.326.

(3) Deal, P. E.; Liu, P.; Al-Abdullatif, S. H.; Muller, V. R.; Shamardani, K.; Adesnik, H.; Miller, E. W. Covalently Tethered Rhodamine Voltage Reporters for High Speed Functional Imaging in Brain Tissue. *J. Am. Chem. Soc.* **2020**, *142* (1), 614–622. https://doi.org/10.1021/jacs.9b12265.

Para mi familia y mi esposo.

Lo logramos.

Acknowledgements

Throughout my academic career I have been surrounded by amazing mentors, teachers, and professors. They each, in their own way contributed to the knowledge and skills that I have gained through the years. I am grateful to have had a chance to learn from every one of them.

I am especially grateful to my graduate advisor, Evan Miller, for allowing me the privilege of working in his lab. He always listened patiently as I explained difficulties I encountered in my experiments or as I described new ideas for future projects. He regularly set aside time to discuss my progress and his door was always open. Thank you, Evan, for providing me with the opportunity to share our research at various conferences and for your support through these years.

Aside from my graduate advisor, I also had the opportunity to work with two other amazing professors. Thank you, Chris Chang, for your guidance during my first summer and semester at Berkeley and for your continued support. Thank you, Dan Nomura, for such a fun rotation. Your love for research is infectious.

None of what I have accomplished would have been possible without my undergraduate research advisor, Dr. Dave Ball. The work you do is thankless. You have prepared me for all the stress and challenges of graduate school. You have inspired me to become a professor and prepare future generations of chemists for graduate school and beyond.

Not only have I benefited and learned from an array of brilliant professors, but I have also been fortunate to have talented lab mates and collaborators. Gloria and Pei, thank you for all you have taught me. Gloria, your fierce confidence is an inspiration to all the young Latinas in science. Pei, your lively personality brightened everyone's day and you were never scared of asking Evan the tough questions, like 'When are we going to Hawaii?' Thank you, Ali, for teaching me everything neuron related. Without you, I may have never discovered MATLAB's time-saving capabilities. Kevin, I am grateful for your willingness to persevere through countless rounds of retina imaging. Jun and Lakshmi, thank you for a wonderful collaboration. The both of you were always eager to brainstorm troubleshooting techniques together.

Jeremy and Julie, I am grateful to have had the opportunity to mentor the both of you. I wish you the best as you continue in your careers.

To my ChemBio cohort, Fred, Carl, Tyler, Sarah, and Ben, you added a brightness to my graduate school experience. Tyler, Carl, and Fred, thank you for taking my mind off graduate school with your endless, but entertaining discussions of politics. Sarah, I could always count on you to laugh at them alongside with me. Ben, you are the epitome of kindness. I am convinced a kinder human does not exist.

Cruz and Natalie, the both of you have grown up too fast. Baby brother, you have such a big heart. Despite being much younger than me, you never failed to offer me words of

encouragement. Natalie, your curiosity for the world around you is unparalleled. Watching you develop a passion for science has been an inspiration for me.

Stephanie, thank you for showing me around the City. Our weeknight hikes and dinners were some of my favorite moments in graduate school. Exploring the Bay with you gave me a reprieve from my never-ending list of experiments.

Mom and Dad, I know that you worried when you could not help me with my homework or college applications. I know it was frustrating to watch me struggle as I became the first in our family to attend college and graduate school, but you were both always by my side, cheering me on. I want you to know that your support and your belief in my potential has been my greatest motivator. You have sacrificed so much for my siblings and me. I am immensely grateful and proud to be your daughter. *Los quiero mucho.*

Jose, where do I begin? Twelve years ago, when we first met, I think it is safe to say that neither of us had an inkling of what the future had in store. You have been my constant partner throughout so many milestones in my career and in life. Nothing makes me happier than to be able to share this achievement with you. Thank you, for your love and encouragement.

As I transition into the next phase of my scientific career, the world has been utterly transformed by an ongoing global pandemic. For the last nine months I have been glued to my phone, checking the news for the latest updates in case numbers, stay-at-home orders, and testing availability. I have been consuming every bit of news related to COVID-19 so that I can keep my loved ones healthy. Through all this, I have gained a deeper, newfound appreciation for science. This pandemic has underscored the importance and impact of scientific research. Scientists have developed novel vaccines in less than a year to combat the pandemic, giving us all a reason to hope for normal again. These breakthroughs in COVID-19 research could not have been possible without scientists sharing their research with others across the globe. So, writing this thesis in the middle of a pandemic has taken on a new meaning. Communication in the scientific community can lead to great things and with this thesis I share with readers a small piece of the amazing work we do in the Miller Lab. Enjoy!

Table of Contents

Chapter 1

Optical Methods for Observing Neuron Activity

1.1 Neurons and Membrane Potential

Cells expend energy to maintain an uneven distribution of ions across their plasma membranes creating a potential difference across their membranes. Neurons communicate primarily through rapid changes in membrane potential called action potentials that occur on the order of milliseconds (**Figure 1.1.1**). Action potentials are rapid increases in membrane potential, depolarizations, followed by decreases in membrane potential as the cell returns to its resting membrane potential (**Figure 1.1.1**). Action potentials can vary in shape, width, and height.[1] The shapes of action potentials can depend on the type of neuron and also vary across a single neuron as it progresses through the cell.[1] The frequency and pattern of firing, bursting or non-bursting, encodes specific information that can be communicated to other neurons. The pattern of activity is also dependent on the type of neuron and can differ between neurons in a brain slice or dissociated culture.[1] Detection of action potentials has long been done using electrodes. In patch clamp electrophysiology, neurons are punctured with a glass pipette filled with salt solution that acts as an electrode. With this technique accurate measurements of changes in cellular membrane potential can be made for an individual cell. Multiple cells can be measured at a time with multi-electrode arrays. In these experiments, cells sit on top of an array of small electrodes that can detect the changes in extracellular potential. While multiple cells can be monitored, the signal detected by the electrodes is an average measurement of cells surrounding the electrodes. Also, the area in between electrodes cannot be accurately measured.

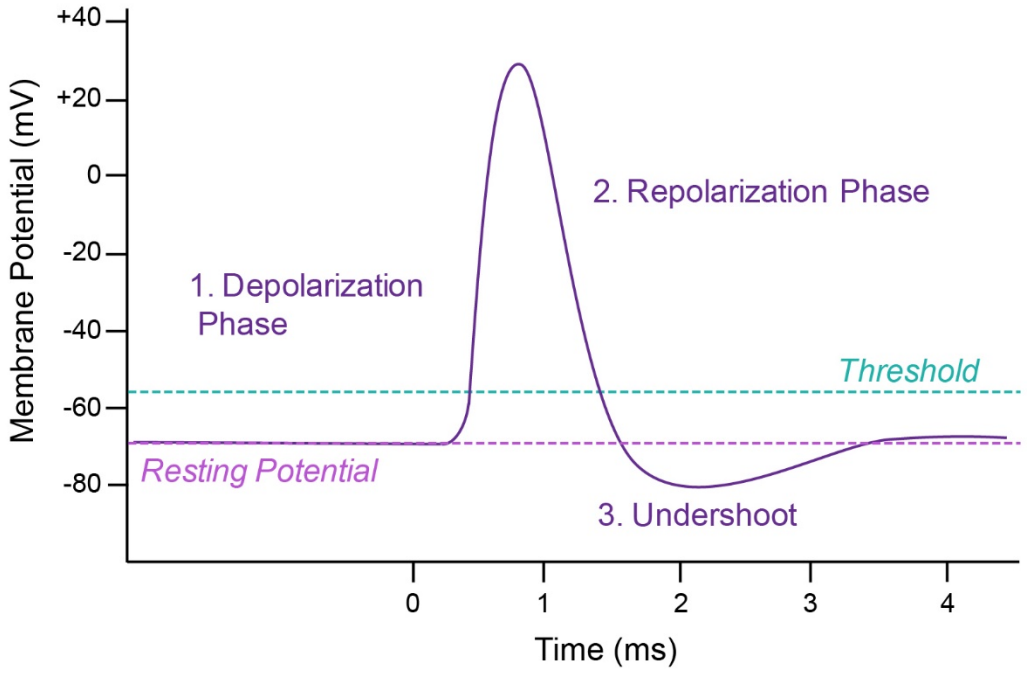

Figure 1.1.1 A generalized diagram of an action potential in a neuron. After reaching a threshold membrane potential the action potential begins and enters a **1. Depolarization Phase** in which the membrane potential becomes increasingly positive. This is followed by a **2. Repolarization Phase** as the neuron to return to its resting

potential. As the neuron begins to repolarize its membrane potential dips below resting potentially briefly and this is known as the **3. Undershoot**. Adapted from *Biological Science* (Figure 45-5), by S. Freeman, 2005, Pearson.

Fluorescence microscopy has revolutionized the life sciences. Advances in both synthetic and genetically encoded fluorophores make fluorescence microscopy routine in laboratories across the globe. Efforts to increase spatial resolution in the detection of neuron activity has led to the development of various fluorescence-based indicators. Small molecule indicators can typically be applied as aqueous solutions to numerous cells at a time, while genetically encoded indicators can be widely expressed in tissues in addition to cells. Early indicators focused on detecting the calcium transients associated with action potentials.[2–4] In neurons, calcium channels responsible for these transients become activated near the peak of an action potential and become fully activated during the falling phase of an action potential.[1] Despite the increased spatial resolution provided by calcium indicators, accurate detection of action potentials and their firing frequency can be difficult because calcium transients occur on the longer timescale than action potentials. New fluorescent probes have focused on directly detecting changes in membrane potential through genetically encoded voltage indicators and voltage sensitive dyes. These tools provide great spatial resolution while maintaining a high level of accuracy.

1.2 Advances in Fluorescence Microscopy

Progress in areas like super-resolution microscopy[5,6], light-sheet microscopy[7], and tissue clearing,[8–10] coupled with fluorescent dyes bring the high spatial and temporal resolution of optical microscopy to bear on samples ranging from single molecules to interacting cells. However, optical imaging in intact tissues and organisms remains challenging. Commonly used fluorophores, like fluorescein and rhodamine, possess excitation and emission profiles within the visible region of the spectrum and overlap extensively with endogenous chromophores, especially heme.[11,12] Although alternative imaging modalities like magnetic resonance imaging, positron emission tomography, and photoacoustic imaging afford excellent penetration into thick tissue, these modalities require specialized instrumentation, are half-life limited, require radioactive reagents, and/or cannot access the micrometer spatial and millisecond time resolution routinely afforded by optical microscopy.[13] In the context of neurobiology, an outstanding challenge is tracking neuronal voltage dynamics with sub-micron spatial resolution and sub-millisecond temporal resolution within intact tissues. Although two-photon (2P) microscopy provides access to structures in deeper tissue, traditional raster-scanning 2P microscopy cannot achieve the temporal resolution required to image large numbers of neurons simultaneously. For this reason, it is imperative to develop voltage indicators that absorb and emit at longer wavelengths of light so that they may be used in conjunction with faster imaging techniques.[14]

1.3 Efforts Towards Red-shifting Fluorophores

Fluorescent dyes and voltage indicators that possess near-infrared (NIR, 700 – 1000 nm)[15–19] excitation and emission profiles are of considerable interest because they can potentially bridge the gap between modalities with good tissue penetration but poor resolution and optical microscopy, with excellent spatial resolution, but poor tissue penetration. First, NIR photons scatter less than visible photons in thick tissue. Second, by avoiding overlap with endogenous chromophores like heme (<650 nm) and water (>900 nm),[11,12,20] fluorophores that operate in the so-called NIR window provide profound advantages for tissue and *in vivo* imaging. Finally, NIR fluorophores can be more readily deployed for multiplex imaging alongside existing fluorescent labels, indicators, and actuators that use visible wavelengths of light, on account of the larger spectral separation between the two.

Red-shifting fluorescent proteins (FPs) often relies on changes to the chromophore contained within the green fluorescent protein (GFP) or other similar FPs. Changes to the chromophore can be made through the introduction of unnatural amino acids.[21–23] A second approach involves mutations of the amino acids surrounding the chromophore in the binding pocket of the FP. By modulating the number of hydrogen bonding interactions between the chromophore and the protein, absorption and emission profiles can be altered.[24] Using bacterial phytochromes, FPs that absorb and emit beyond 700 nm have been developed.[25,26]

FPs often exhibit broad absorption and emission profiles, making them difficult to implement in multi-color imaging. NIR FPs also tend to have lower quantum yields and be less photostable than their synthetic NIR counter parts.[25–28] For this reason, synthetic small molecule fluorophores are a more attractive option, and they are also easier to modify than FPs.

Traditionally employed synthetic NIR dyes, such as porphyrins and phthalocyanins,[15] polyme-thines,[15] BODIPY derivatives,[29–31] and xanthenes with extended annulation[32–34] often have high molecular weights, high hydrophobicities, low water solubility, a propensity to aggregate, low quantum yields and chemical or photochemical instability, complicating their use in biological contexts. Several creative approaches have recently been employed to address these concerns.[19,33,35–37] In particular, xanthene-based dyes are attractive because the compact, fused 3-ring system promotes stability and decreases molecular weight. Annulation of xanthenes can push their absorbance into ranges >700 nm,[32] at the expense of decreased water solubility and quantum yield. More recent efforts have focused on replacing oxygen with carbon[38–40] or other heteroatoms such as Si[41–43] and P (**Figure 1.3.1**). Indeed, recent examples of phosphinate[44] and phosphine-oxide based xanthene dyes[28,45] demonstrate this unique scaffold can access absorption profiles at or above 700 nm while maintaining a compact, three-ring structure (**Figure 1.3.1**).

While numerous approaches to NIR-emitting fluorophores exist, there are relatively few examples of NIR-absorbing fluorescent reporters—fluorophores that sense and respond reversibly to changes in specific physiological phenomena, for example, metal ions, reactive

oxygen species, or transmembrane potential. The few examples of NIR-absorbing indicators tend to employ polymethine, rather than xanthene, scaffolds.[9,46–48]

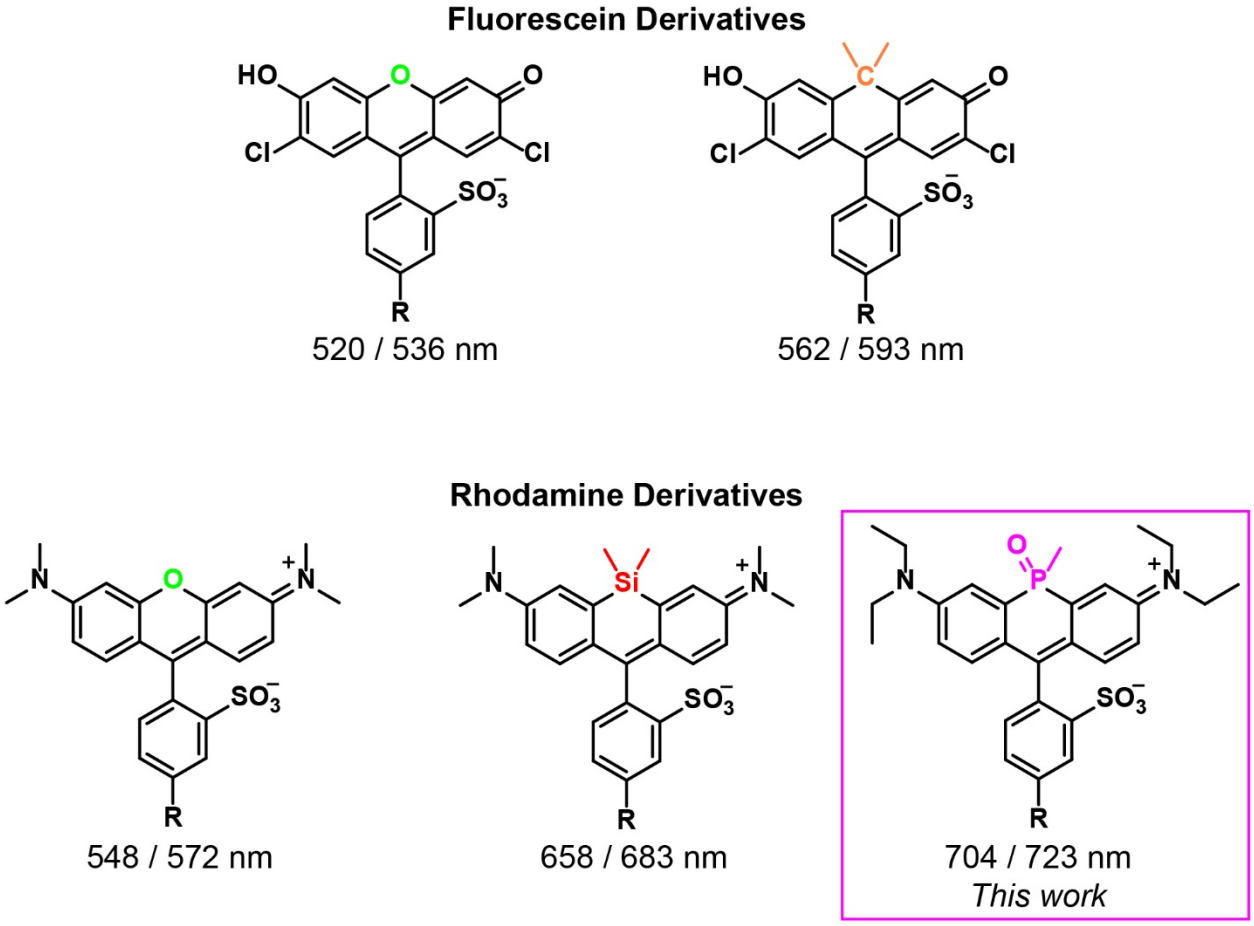

Figure 1.3.1 Structures of various xanthene-based fluorophores used in voltage reporters in the Miller Lab.[27,40,49,50] Below each structure are the maximum absorption and emission wavelengths. This thesis details the development of phosphine oxide rhodamine voltage reports (poRhoVRs).

Therefore, we were eager to adapt phosphorous-substituted xanthenes into a fluorescent voltage-sensing scaffold. Previous work in our lab suggests that xanthene dyes with a range of bridgehead (O,[51] C,[40] Si[27]) and terminal atoms (O[40,51], or substituted N[27,52]) can be employed as voltage-sensitive dyes via introduction of a lipophilic, conjugated molecular wire (**Figure 1.3.1**). We hypothesized that the installation of phenylenevinylene molecular wires into the context of a phosphorous-substituted xanthene dye would yield voltage-sensitive indicators with emission and excitation maxima above 700 nm (**Figure 1.3.1**). This would fill an important void: although there are several examples of chemically-synthesized[53–56] and genetically encoded[57–60] voltage indicators with emission maxima beyond 700 nm, to date, there are no examples of xanthene-based voltage-sensitive fluorophores with peak excitation above 700 nm.

1.4 Genetically Encoded Voltage Indicators

Genetically encoded voltage indicators (GEVIs) are protein-based sensors that localize to the cell membrane. They operate through a variety of mechanisms. In one technique, light activated microbial proton pumps, rhodopsins, have been engineered to make their fluorescence voltage sensitive.[61] This technique was used in the development of Arch[62] and QuasAr.[57] FRET-opsin GEVIs, such as Ace2N-mNeon attach a fluorescent protein to a rhodopsin and their FRET interactions are voltage sensitive.[63,64] In another technique, fluorescent proteins are coupled to a voltage sensing domain derived from phosphatases or voltage gated ion channels as is done in ArcLight[65] and FlaSh[66], respectively. In this system changes in the membrane potential of a cell cause conformational changes in the voltage sensing domain which in turn alter the emission of the fluorescent protein. In some cases the fluorescent reporter can be replaced by a fluorescent dye in a hybrid system as is done in Voltron.[67] VSFP butterfly adds a second fluorescent protein to the voltage sensing domain to create a FRET-based system for detecting membrane potential.[68] Archon[69] and QuasAr[57] both emit fluorescence at about 720 nm, making them some of the reddest GEVIs to date. Both however do not have peak absorption at or above 700 nm.

Because they are genetically encoded, GEVIs can be expressed in specific cells. They also do not require the introduction of exogenous dyes into a sample or reapplication. However, expression levels in tissues and cells can be variable leading to differences in sensitivity and brightness within a sample.[70] GEVIs are also not as bright or as fast as other voltage sensing dyes.[70] GEVIs also often suffer from broad excitation and emission profiles since most incorporate FPs.

1.5 Voltage Sensing Dyes

Small molecule voltage sensing dyes (VSDs) are synthetic dyes whose fluorescence and emission are dependent on the potential in the surrounding cell membrane.[71] These dyes can exist as lipophilic anions that migrate into the cell membrane as it depolarizes, becoming fluorescent in the nonpolar environment[71]. A similar approach is used in dyes that pair two fluorescent molecules together to make a FRET based sensor. In these dyes a lipophilic ion is redistributed within the cell membrane.[72] During hyperpolarization, the fluorescent lipophilic ion moves closer to the exterior of the membrane and participates in FRET with a dye anchored to the surface.[72] In a hybrid system, a genetically encoded fluorescent protein can be used as the stationary half of the FRET pair.[73] Dependence on the movement and accumulation of ions in the membrane leads to a slow response to changes in membrane potential.[71] Other faster dyes shift their emission and excitation with changes in cellular membrane potential.[74–76] A popular example of these electrochromic VSDs is di-4-ANEPPS.[76] Since these dyes require detection at multiple wavelengths, they are difficult to use in combination with other tools such as calcium indicators and optogenetic actuators. In

addition to complexities in detecting signal, these di-4-ANEPPS have displayed some phototoxic effects in cells.[77]

In the Miller lab we have developed various VSDs termed voltage reporters (VRs), that modulate their fluorescence through a photoinduced electron transfer (PeT) process. These VRs consist of three primary components, a molecular wire with an electron rich donor and a fluorophore (**Figure 1.5.1**).[49] At rest, the interior of the cell has a deficit in positive charge compared to the extracellular environment, making PeT a favorable process and results in diminished VR fluorescence (**Figure 1.5.1**). Upon depolarization, the ion channels open to allow the entry of cations into the cell, changing the balance of charges leading to a more positive intracellular environment. This makes PeT a less favorable process and VR fluorescence increases (**Figure 1.5.1**).

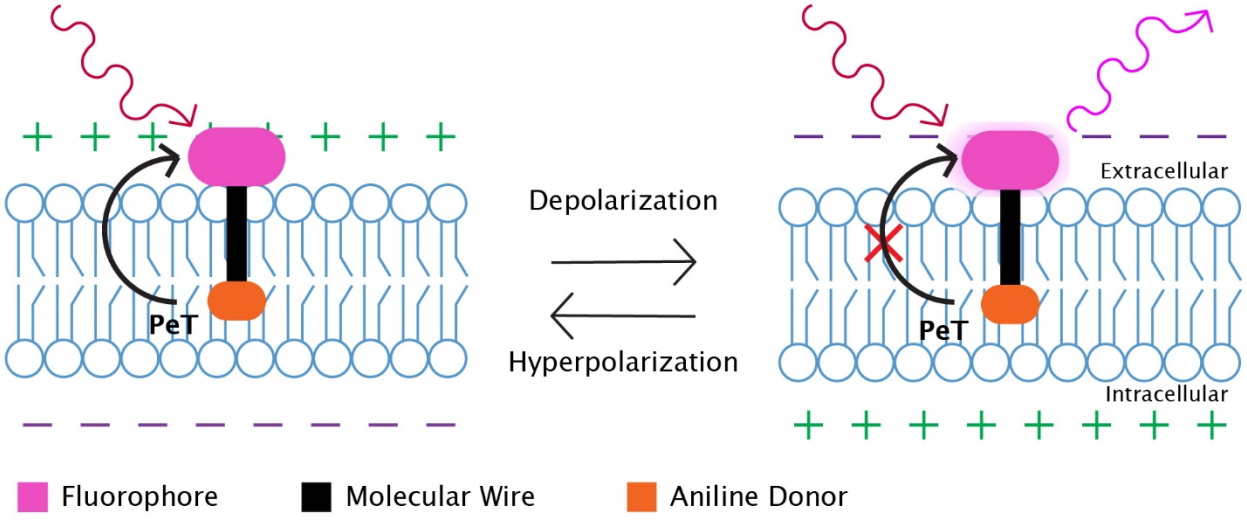

Figure 1.5.1 Voltage Reporters detect cellular membrane potential through a photoinduced electron transfer process (PeT).

The modular structure of VRs enables facile alteration. New molecular wires can be used to improve photostability[78] and voltage sensitivity can be fine-tuned by making substitutions on the electron rich aniline donor.[52] A wide range of fluorophores can be incorporated into the structure of VRs. The most prevalent fluorophores are xanthene-based dyes such as fluorescein[49,79], rhodol[80] and rhodamine[50,52]. By replacing the atom at the bridgehead position with other elements such as carbon[38,39,81], silicon[42,82] and phosphorous[45] VRs can be redshifted (**Figure 1.3.1**). Dyes with near-infrared emission and excitation are beneficial because red light is not absorbed or scattered by tissues as much higher energy light.[83] This allows red light to penetrate deeper into tissue. This thesis details the synthesis and characterization of phosphine oxide rhodamine voltage reporters (poRhoVRs). These dyes have excitation and emission maxima beyond 700 nm and are the reddest VRs to date.

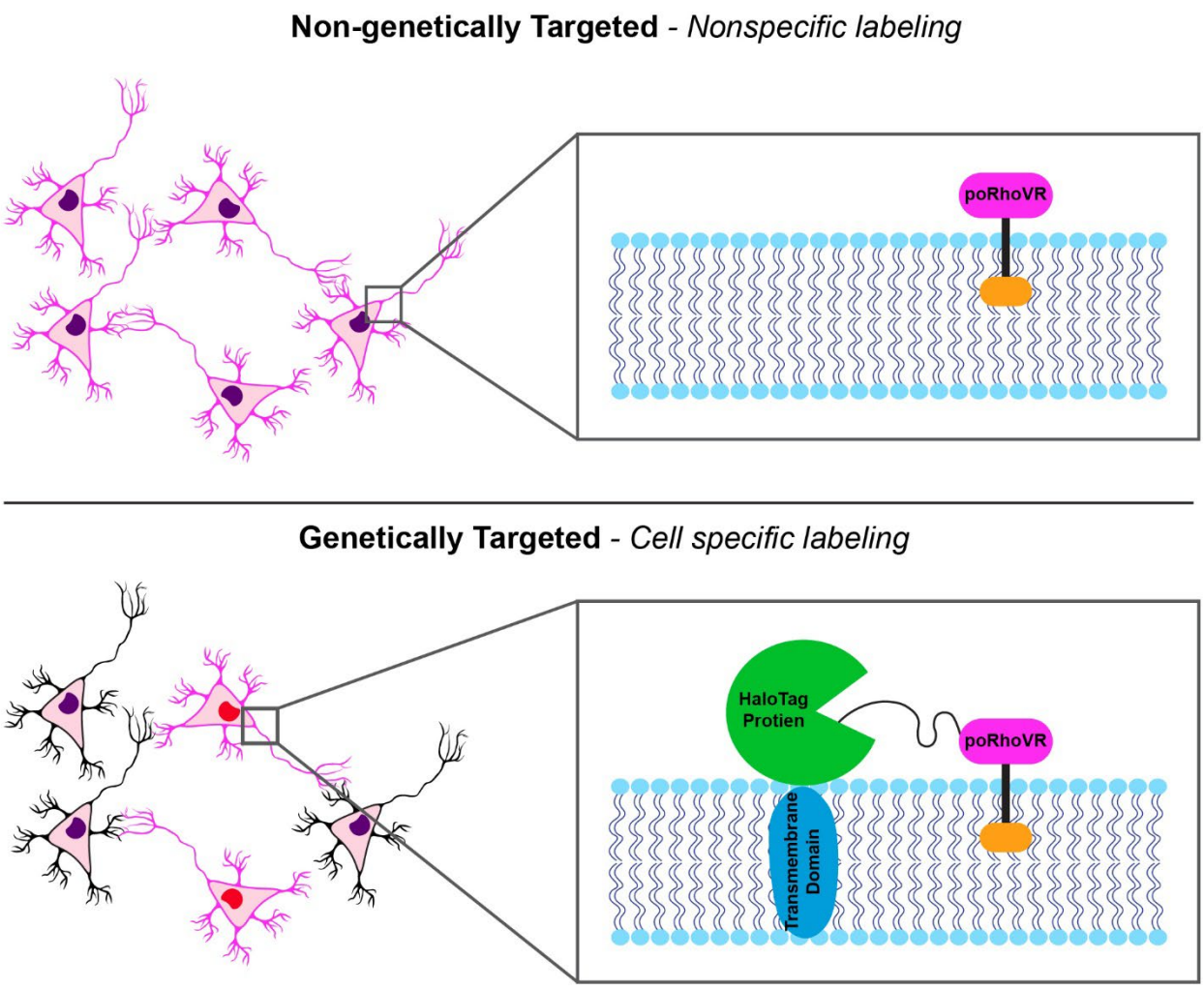

Figure 1.5.2 Potential future modifications to make poRhoVRs genetically targetable using HaloTag.

Compared to GEVIs, VRs lack cell specificity because they interact with all membranes indiscriminately. However, with the addition of photocaging groups[84], enzymatically cleavable groups[85] or protein reactive groups cell specificity can be attained. In the future these strategies can also be applied to poRhoVRs to generate NIR, cell-specific dyes greatly enhancing their properties (**Figure 1.5.2**).

1.6 Summary and Future Directions

Chapter 2 of this thesis explains the design and synthesis of poRhoVRs. In this work a total of 4 poRhoVRs were synthesized and all had absorption and emission profiles extending past 700 nm. **Chapter 3** details initial characterization of poRhoVR indicators in HEK cells and dissociated rat hippocampal neurons. In choosing the best performing poRhoVR, we took into consideration brightness, voltage sensitivity and signal to noise ratios measured in

recordings of cultured neurons. poRhoVR can be used alongside calcium indicators such as GCaMP and Oregon Green BAPTA as well as the optogenetic actuator ChannelRhodopsin-2. In **Chapter 4**, bath application of poRhoVR allowed us to make optical voltage recordings that correlated well with electrical recordings from multi-electrode arrays. **Appendix 5** details a MATLAB script that automated the drawing of regions of interest (ROIs) in optical recordings of the retina. This script detects the electrodes from the MEA and uses them to define the ROI positions. In **Appendix 1**, more detailed information about the optimization of the reduction of a poRhoVR intermediate can be found. **Appendix 2** delves into the effects of ryanodine and dantrolene on calcium transients associated with action potentials in cultured neurons. **Appendix 3** presents initial progress that has been made to synthesize voltage reporters with increased sensitivities by incorporating a second molecular wire. A new strategy for recording calcium fluctuations in neurons over time is described in **Appendix 4**. This new strategy uses a methionine proximity-activated imaging reporter (Met PAIR) to detect differences in calcium levels of neurons that have been treated with tetrodotoxin or placed in high potassium environments.

Despite numerous advances in microscopy, widefield microscopy is still routinely used and remains the most accessible. Illumination sources for widefield microscopes often rely on light emitting diodes (LEDs). As fluorophores move further into the NIR range, LEDs with peak emissions around 700 nm are needed. Currently many of the NIR LEDs centered around 700 nm have diminished power outputs compared to their blue-shifted counterparts. Incorporation of improved LEDs into widefield microscopes would allow researchers to fully take advantage of these new NIR sensors like poRhoVRs. Tunable lasers at 700 nm can already provide powerful excitation light and are used in many fast and deep imaging techniques such as lattice light sheet microscopy.[14] In combination with these imaging techniques, poRhoVRs have the potential to provide detailed and accurate recordings of voltage dynamics in tissue.

Many modifications can be made to poRhoVRs to increase their cell specificity. Covalent tags, such as HaloTag[86] and SpyTag[87], can be incorporated into poRhoVRs (**Figure 1.5.2**). These covalent tags can be appended as a reactive handle to the fluorophores and their corresponding proteins, HaloTag protein or SpyCatcher, can be expressed in specific cells (**Figure 1.5.2**). In this manner, cells expressing the necessary proteins can be selectively stained by VRs. Multiplex imaging with other genetically targeted VRs[86,87] will allow us to study the different firing patterns unique to different neuron types and to tease out the direction that signals travel in a tissue. Currently poRhoVRs label cells non-specifically but, a genetically targetable poRhoVR (**Figure 1.5.2**) has the potential to selectively label the retinal ganglion cell layer and isolate those signals from the rest of the tissue. A second VR with an orthogonal targeting group[86,87] can be added to label bipolar and amacrine cells in the retina. In this multiplex experiment we could compare activity from these two layers of cells. With poRhoVRs NIR absorption and emission multi-color imaging is a possibility.

1.7 References

(1) Bean, B. P. The Action Potential in Mammalian Central Neurons. *Nat. Rev. Neurosci.* **2007**, *8* (6), 451–465. https://doi.org/10.1038/nrn2148.

(2) Grynkiewicz, G.; Poenie, M.; Tsien, R. Y. A New Generation of Ca2+ Indicators with Greatly Improved Fluorescence Properties. *J. Biol. Chem.* **1985**, *260* (6), 3440–3450.

(3) Tsien, R. Y. THE GREEN FLUORESCENT PROTEIN. *Annu. Rev. Biochem.* **1998**. https://doi.org/10.1146/annurev.biochem.67.1.509.

(4) Miyawaki, A.; Llopis, J.; Heim, R.; Michael McCaffery, J.; Adams, J. A.; Ikura, M.; Tsien, R. Y. Fluorescent Indicators for Ca2+ Based on Green Fluorescent Proteins and Calmodulin. *Nature* **1997**, *388* (6645), 882–887. https://doi.org/10.1038/42264.

(5) Huang, B.; Babcock, H.; Zhuang, X. Breaking the Diffraction Barrier: Super-Resolution Imaging of Cells. *Cell* **2010**, *143* (7), 1047–1058. https://doi.org/10.1016/j.cell.2010.12.002.

(6) Sahl, S. J.; Hell, S. W.; Jakobs, S. Fluorescence Nanoscopy in Cell Biology. *Nat. Rev. Mol. Cell Biol.* **2017**, *18* (11), 685–701. https://doi.org/10.1038/nrm.2017.71.

(7) Power, R. M.; Huisken, J. A Guide to Light-Sheet Fluorescence Microscopy for Multiscale Imaging. *Nat. Methods* **2017**, *14* (4), 360–373. https://doi.org/10.1038/nmeth.4224.

(8) Richardson, D. S.; Lichtman, J. W. Clarifying Tissue Clearing. *Cell* **2015**, *162* (2), 246–257. https://doi.org/10.1016/j.cell.2015.06.067.

(9) Hirayama, T.; Van De Bittner, G. C.; Gray, L. W.; Lutsenko, S.; Chang, C. J. Near-Infrared Fluorescent Sensor for in Vivo Copper Imaging in a Murine Wilson Disease Model. *Proc. Natl. Acad. Sci.* **2012**, *109* (7), 2228–2233. https://doi.org/10.1073/pnas.1113729109.

(10) Chung, K.; Wallace, J.; Kim, S. Y.; Kalyanasundaram, S.; Andalman, A. S.; Davidson, T. J.; Mirzabekov, J. J.; Zalocusky, K. A.; Mattis, J.; Denisin, A. K.; Pak, S.; Bernstein, H.; Ramakrishnan, C.; Grosenick, L.; Gradinaru, V.; Deisseroth, K. Structural and Molecular Interrogation of Intact Biological Systems. *Nature* **2013**, *497* (7449), 332–337. https://doi.org/10.1038/nature12107.

(11) Weissleder, R. A Clearer Vision for in Vivo Imaging. *Nat. Biotechnol.* **2001**, *19*, 316–317.

(12) Friebel, M.; Helfmann, J.; Netz, U.; Meinke, M. Influence of Oxygen Saturation on the Optical Scattering Properties of Human Red Blood Cells in the Spectral Range 250 to 2000 Nm. *J. Biomed. Opt.* **2009**, *14* (3), 034001. https://doi.org/10.1117/1.3127200.

(13) Tsien, R. Y. Imagining Imaging's Future. *Nat. Rev. Mol. Cell Biol.* **2003**, *4* (SUPPL.),

16–21.

(14) Chen, B. C.; Legant, W. R.; Wang, K.; Shao, L.; Milkie, D. E.; Davidson, M. W.; Janetopoulos, C.; Wu, X. S.; Hammer, J. A.; Liu, Z.; English, B. P.; Mimori-Kiyosue, Y.; Romero, D. P.; Ritter, A. T.; Lippincott-Schwartz, J.; Fritz-Laylin, L.; Mullins, R. D.; Mitchell, D. M.; Bembenek, J. N.; Reymann, A. C.; Böhme, R.; Grill, S. W.; Wang, J. T.; Seydoux, G.; Tulu, U. S.; Kiehart, D. P.; Betzig, E. Lattice Light-Sheet Microscopy: Imaging Molecules to Embryos at High Spatiotemporal Resolution. *Science (80-.).* **2014**, *346* (6208). https://doi.org/10.1126/science.1257998.

(15) Fabian, J.; Nakazumi, H.; Matsuoka, M. Near-Infrared Absorbing Dyes. *Chem. Rev.* **1992**, *92* (6), 1197–1226. https://doi.org/10.1021/cr00014a003.

(16) Alfano, R. R.; Demos, S. G.; Gayen, S. K. Advances in Optical Imaging of Biomedical Media. *Ann. N. Y. Acad. Sci.* **1997**, *820* (112), 248–271. https://doi.org/10.1111/j.1749-6632.1997.tb46200.x.

(17) Tung, C. H.; Lin, Y.; Moon, W. K.; Weissleder, R. A Receptor-Targeted near-Infrared Fluorescence Probe for in Vivo Tumor Imaging. *ChemBioChem* **2002**, *3* (8), 784–786. https://doi.org/10.1002/1439-7633(20020802)3:8<784::AID-CBIC784>3.0.CO;2-X.

(18) Frangioni, J. V. In Vivo Near-Infrared Fluorescence Imaging. *Curr. Opin. Chem. Biol.* **2003**, *7* (5), 626–634. https://doi.org/10.1016/j.cbpa.2003.08.007.

(19) Cosco, E. D.; Caram, J. R.; Bruns, O. T.; Franke, D.; Day, R. A.; Farr, E. P.; Bawendi, M. G.; Sletten, E. M. Flavylium Polymethine Fluorophores for Near- and Shortwave Infrared Imaging. *Angew. Chemie - Int. Ed.* **2017**, *56* (42), 13126–13129. https://doi.org/10.1002/anie.201706974.

(20) Hilderbrand, S. A.; Weissleder, R. Near-Infrared Fluorescence: Application to in Vivo Molecular Imaging. *Curr. Opin. Chem. Biol.* **2010**, *14* (1), 71–79. https://doi.org/10.1016/j.cbpa.2009.09.029.

(21) Lee, D.; Hyun, J. H.; Jung, K.; Hannan, P.; Kwon, H. B. A Calcium- A Nd Light-Gated Switch to Induce Gene Expression in Activated Neurons. *Nat. Biotechnol.* **2017**, *35* (9), 858–863. https://doi.org/10.1038/nbt.3902.

(22) Wang, L.; Chen, X.; Guo, X.; Li, J.; Liu, Q.; Kang, F.; Wang, X.; Hu, C.; Liu, H.; Gong, W.; Zhuang, W.; Liu, X.; Wang, J. Significant Expansion and Red-Shifting of Fluorescent Protein Chromophore Determined through Computational Design and Genetic Code Expansion. *Biophys. Reports* **2018**, *4* (5), 273–285. https://doi.org/10.1007/s41048-018-0073-z.

(23) Zhang, S.; Ai, H. wang. A General Strategy to Red-Shift Green Fluorescent Protein-Based Biosensors. *Nat. Chem. Biol.* **2020**, *16* (12), 1434–1439. https://doi.org/10.1038/s41589-020-0641-7.

(24) Rodriguez, E. A.; Campbell, R. E.; Lin, J. Y.; Lin, M. Z.; Miyawaki, A.; Palmer, A. E.; Shu, X.; Zhang, J.; Tsien, R. Y. The Growing and Glowing Toolbox of Fluorescent and Photoactive Proteins. *Trends Biochem. Sci.* **2017**, *42* (2), 111–129. https://doi.org/10.1016/j.tibs.2016.09.010.

(25) Shcherbakova, D. M.; Verkhusha, V. V. Near-Infrared Fluorescent Proteins for Multicolor in Vivo Imaging. *Nat. Methods* **2013**, *10* (8), 751–754. https://doi.org/10.1038/nmeth.2521.

(26) Shcherbakova, D. M.; Cox Cammer, N.; Huisman, T. M.; Verkhusha, V. V.; Hodgson, L. Direct Multiplex Imaging and Optogenetics of Rho GTPases Enabled by Near-Infrared FRET Article. *Nat. Chem. Biol.* **2018**, *14* (6), 591–600. https://doi.org/10.1038/s41589-018-0044-1.

(27) Huang, Y. L.; Walker, A. S.; Miller, E. W. A Photostable Silicon Rhodamine Platform for Optical Voltage Sensing. *J. Am. Chem. Soc.* **2015**. https://doi.org/10.1021/jacs.5b06644.

(28) Grzybowski, M.; Taki, M.; Senda, K.; Sato, Y.; Ariyoshi, T.; Okada, Y.; Kawakami, R.; Imamura, T.; Yamaguchi, S. A Highly Photostable Near-Infrared Labeling Agent Based on a Phospha-Rhodamine for Long-Term and Deep Imaging. *Angew. Chemie Int. Ed.* **2018**, *57* (32), 10137–10141. https://doi.org/10.1002/anie.201804731.

(29) Kubo, Y.; Watanabe, K.; Nishiyabu, R.; Hata, R.; Murakami, A.; Shoda, T.; Ota, H. Near-Infrared Absorbing Boron-Dibenzopyrromethenes That Serve as Light-Harvesting Sensitizers for Polymeric Solar Cells. *Org. Lett.* **2011**, *13* (17), 4574–4577. https://doi.org/10.1021/ol201770g.

(30) Liu, P.; Gao, F.; Zhou, L.; Chen, Y.; Chen, Z. Tetrathienyl-Functionalized Red- and NIR-Absorbing BODIPY Dyes Appending Various Peripheral Substituents. *Org. Biomol. Chem.* **2017**, *15* (6), 1393–1399. https://doi.org/10.1039/c6ob02612e.

(31) Kubota, Y.; Kimura, K.; Jin, J.; Manseki, K.; Funabiki, K.; Matsui, M. Synthesis of Near-Infrared Absorbing and Fluorescing Thiophene-Fused BODIPY Dyes with Strong Electron-Donating Groups and Their Application in Dye-Sensitised Solar Cells. *New J. Chem.* **2019**, *43* (3), 1156–1165. https://doi.org/10.1039/c8nj04672g.

(32) Koide, Y.; Urano, Y.; Hanaoka, K.; Piao, W.; Kusakabe, M.; Saito, N.; Terai, T.; Okabe, T.; Nagano, T. Development of NIR Fluorescent Dyes Based on Si-Rhodamine for in Vivo Imaging. *J. Am. Chem. Soc.* **2012**, *134* (11), 5029–5031. https://doi.org/10.1021/ja210375e.

(33) Azuma, E.; Nakamura, N.; Kuramochi, K.; Sasamori, T.; Tokitoh, N.; Sagami, I.; Tsubaki, K. Exhaustive Syntheses of Naphthofluoresceins and Their Functions. *J. Org. Chem.* **2012**, *77* (7), 3492–3500. https://doi.org/10.1021/jo300177b.

(34) Lee, L. G.; Berry, G. M.; Chen, C. -H. Vita Blue: A New 633-nm Excitable Fluorescent Dye for Cell Analysis. *Cytometry* **1989**, *10* (2), 151–164. https://doi.org/10.1002/cyto.990100206.

(35) Yuan, L.; Lin, W.; Zhao, S.; Gao, W.; Chen, B.; He, L.; Zhu, S. A Unique Approach to Development of Near-Infrared Fluorescent Sensors for in Vivo Imaging. *J. Am. Chem. Soc.* **2012**, *134* (32), 13510–13523. https://doi.org/10.1021/ja305802v.

(36) Sibrian-Vazquez, M.; Escobedo, J. O.; Lowry, M.; Fronczek, F. R.; Strongin, R. M. Field Effects Induce Bathochromic Shifts in Xanthene Dyes. *J. Am. Chem. Soc.* **2012**, *134* (25), 10502–10508. https://doi.org/10.1021/ja302445w.

(37) Gorka, A. P.; Nani, R. R.; Schnermann, M. J. Harnessing Cyanine Reactivity for Optical Imaging and Drug Delivery. *Acc. Chem. Res.* **2018**, *51* (12), 3226–3235. https://doi.org/10.1021/acs.accounts.8b00384.

(38) Grimm, J. B.; Sung, A. J.; Legant, W. R.; Hulamm, P.; Matlosz, S. M.; Betzig, E.; Lavis, L. D. Carbofluoresceins and Carborhodamines as Scaffolds for High-Contrast Fluorogenic Probes. *ACS Chem. Biol.* **2013**, *8* (6), 1303–1310. https://doi.org/10.1021/cb4000822.

(39) Grimm, J. B.; Gruber, T. D.; Ortiz, G.; Brown, T. A.; Lavis, L. D. Virginia Orange: A Versatile, Red-Shifted Fluorescein Scaffold for Single- And Dual-Input Fluorogenic Probes. *Bioconjug. Chem.* **2016**, *27* (2), 474–480. https://doi.org/10.1021/acs.bioconjchem.5b00566.

(40) Ortiz, G.; Liu, P.; Naing, S. H. H.; Muller, V. R.; Miller, E. W. Synthesis of Sulfonated Carbofluoresceins for Voltage Imaging. *J. Am. Chem. Soc.* **2019**, *141* (16), 6631–6638. https://doi.org/10.1021/jacs.9b01261.

(41) Fu, M.; Xiao, Y.; Qian, X.; Zhao, D.; Xu, Y. A Design Concept of Long-Wavelength Fluorescent Analogs of Rhodamine Dyes: Replacement of Oxygen with Silicon Atom. *Chem. Commun.* **2008**, No. 15, 1780. https://doi.org/10.1039/b718544h.

(42) Koide, Y.; Urano, Y.; Hanaoka, K.; Terai, T.; Nagano, T. Evolution of Group 14 Rhodamines as Platforms for Near-Infrared Fluorescence Probes Utilizing Photoinduced Electron Transfer. *ACS Chem. Biol.* **2011**, *6* (6), 600–608. https://doi.org/10.1021/cb1002416.

(43) Pastierik, T.; Šebej, P.; Medalová, J.; Štacko, P.; Klán, P. Near-Infrared Fluorescent 9-Phenylethynylpyronin Analogues for Bioimaging. *J. Org. Chem.* **2014**, *79* (8), 3374–3382. https://doi.org/10.1021/jo500140y.

(44) Zhou, X.; Lai, R.; Beck, J. R.; Li, H.; Stains, C. I. Nebraska Red: A Phosphinate-Based near-Infrared Fluorophore Scaffold for Chemical Biology Applications. *Chem. Commun.* **2016**, *52* (83), 12290–12293. https://doi.org/10.1039/c6cc05717a.

(45) Chai, X.; Cui, X.; Wang, B.; Yang, F.; Cai, Y.; Wu, Q.; Wang, T. Near-Infrared Phosphorus-Substituted Rhodamine with Emission Wavelength above 700 Nm for Bioimaging. *Chem. - A Eur. J.* **2015**, *21* (47), 16754–16758. https://doi.org/10.1002/chem.201502921.

(46) Sasaki, E.; Kojima, H.; Nishimatsu, H.; Urano, Y.; Kikuchi, K.; Hirata, Y.; Nagano,

T. Highly Sensitive Near-Infrared Fluorescent Probes for Nitric Oxide and Their Application to Isolated Organs. *J. Am. Chem. Soc.* **2005**, *127* (11), 3684–3685. https://doi.org/10.1021/ja042967z.

(47) Zhang, Z.; Achilefu, S. Design, Synthesis and Evaluation of near-Infrared Fluorescent PH Indicators in a Physiologically Relevant Range. *Chem. Commun.* **2005**, No. 47, 5887–5889. https://doi.org/10.1039/b512315a.

(48) Kiyose, K.; Kojima, H.; Urano, Y.; Nagano, T. Development of a Ratiometric Fluorescent Zinc Ion Probe in Near-Infrared Region, Based on Tricarbocyanine Chromophore. *J. Am. Chem. Soc.* **2006**, *128* (20), 6548–6549. https://doi.org/10.1021/ja060399c.

(49) Miller, E. W.; Lin, J. Y.; Frady, E. P.; Steinbach, P. A.; Kristan, W. B.; Tsien, R. Y. Optically Monitoring Voltage in Neurons by Photoinduced Electron Transfer through Molecular Wires. *Proc. Natl. Acad. Sci. U. S. A.* **2012**, *109* (6), 2114–2119. https://doi.org/10.1073/pnas.1120694109.

(50) Kulkarni, R. U.; Vandenberghe, M.; Thunemann, M.; James, F.; Andreassen, O. A.; Djurovic, S.; Devor, A.; Miller, E. W. In Vivo Two-Photon Voltage Imaging with Sulfonated Rhodamine Dyes. *ACS Cent. Sci.* **2018**. https://doi.org/10.1021/acscentsci.8b00422.

(51) Kulkarni, R. U.; Yin, H.; Pourmandi, N.; James, F.; Adil, M. M.; Schaffer, D. V.; Wang, Y.; Miller, E. W. A Rationally Designed, General Strategy for Membrane Orientation of Photoinduced Electron Transfer-Based Voltage-Sensitive Dyes. *ACS Chem. Biol.* **2017**, *12* (2), 407–413. https://doi.org/10.1021/acschembio.6b00981.

(52) Deal, P. E.; Kulkarni, R. U.; Al-Abdullatif, S. H.; Miller, E. W. Isomerically Pure Tetramethylrhodamine Voltage Reporters. *J. Am. Chem. Soc.* **2016**, *138* (29), 9085–9088. https://doi.org/10.1021/jacs.6b05672.

(53) Shoham, D.; Glaser, D. E.; Arieli, A.; Kenet, T.; Wijnbergen, C.; Toledo, Y.; Hildesheim, R.; Grinvald, A. Imaging Cortical Dynamics at High Spatial and Temporal Resolution with Novel Blue Voltage-Sensitive Dyes. *Neuron* **1999**, *24* (4), 791–802. https://doi.org/10.1016/S0896-6273(00)81027-2.

(54) Zhang, F.; Wang, L. P.; Boyden, E. S.; Deisseroth, K. Channelrhodopsin-2 and Optical Control of Excitable Cells. *Nat. Methods* **2006**, *3* (10), 785–792. https://doi.org/10.1038/nmeth936.

(55) Yan, P.; Acker, C. D.; Zhou, W. L.; Lee, P.; Bollensdorff, C.; Negreane, A.; Lotti, J.; Sacconi, L.; Antic, S. D.; Kohl, P.; Mansvelder, H. D.; Pavone, F. S.; Loew, L. M. Palette of Fluorinated Voltage-Sensitive Hemicyanine Dyes. *Proc. Natl. Acad. Sci. U. S. A.* **2012**, *109* (50), 20443–20448. https://doi.org/10.1073/pnas.1214850109.

(56) Matiukas, A.; Mitrea, B. G.; Pertsov, A. M.; Wuskell, J. P.; Wei, M. De; Watras, J.; Millard, A. C.; Loew, L. M. New Near-Infrared Optical Probes of Cardiac Electrical Activity. *Am. J. Physiol. - Hear. Circ. Physiol.* **2006**, *290* (6), 2633–2643.

https://doi.org/10.1152/ajpheart.00884.2005.

(57) Hochbaum, D. R.; Zhao, Y.; Farhi, S. L.; Klapoetke, N.; Werley, C. A.; Kapoor, V.; Zou, P.; Kralj, J. M.; MacLaurin, D.; Smedemark-Margulies, N.; Saulnier, J. L.; Boulting, G. L.; Straub, C.; Cho, Y. K.; Melkonian, M.; Wong, G. K. S.; Harrison, D. J.; Murthy, V. N.; Sabatini, B. L.; Boyden, E. S.; Campbell, R. E.; Cohen, A. E. All-Optical Electrophysiology in Mammalian Neurons Using Engineered Microbial Rhodopsins. *Nat. Methods* **2014**, *11* (8), 825–833. https://doi.org/10.1038/NMETH.3000.

(58) Monakhov, M. V.; Matlashov, M. E.; Colavita, M.; Song, C.; Shcherbakova, D. M.; Antic, S. D.; Verkhusha, V. V.; Knöpfel, T. Screening and Cellular Characterization of Genetically Encoded Voltage Indicators Based on Near-Infrared Fluorescent Proteins. *ACS Chem. Neurosci.* **2020**. https://doi.org/10.1021/acschemneuro.0c00046.

(59) Kannan, M.; Vasan, G.; Huang, C.; Haziza, S.; Li, J. Z.; Inan, H.; Schnitzer, M. J. .; Pieribone, V. A. . Fast, Invivo Voltage Imaging Using a Red Fluorescent Indicator. *Nat. Methods* **2018**, *15* (12), 1108–1116. https://doi.org/10.1038/s41592-018-0188-7.

(60) Treger, J. S.; Priest, M. F.; Iezzi, R.; Bezanilla, F. Real-Time Imaging of Electrical Signals with an Infrared FDA-Approved Dye. *Biophys. J.* **2014**, *107* (6), L09-L12. https://doi.org/10.1016/j.bpj.2014.07.054.

(61) Hayashi, S.; Tajkhorshid, E.; Schulten, K. Molecular Dynamics Simulation of Bacteriorhodopsin's Photoisomerization Using Ab Initio Forces for the Excited Chromophore. *Biophys. J.* **2003**, *85* (3), 1440–1449. https://doi.org/10.1016/S0006-3495(03)74576-7.

(62) Kralj, J. M.; Douglass, A. D.; Hochbaum, D. R.; MacLaurin, D.; Cohen, A. E. Optical Recording of Action Potentials in Mammalian Neurons Using a Microbial Rhodopsin. *Nat. Methods* **2012**, *9* (1), 90–95. https://doi.org/10.1038/nmeth.1782.

(63) Gong, Y.; Wagner, M. J.; Li, J. Z.; Schnitzer, M. J. Imaging Neural Spiking in Brain Tissue Using FRET-Opsin Protein Voltage Sensors. *Nat. Commun.* **2014**, *5*. https://doi.org/10.1038/ncomms4674.

(64) Gong, Y.; Huang, C.; Li, J. Z.; Grewe, B. F.; Zhang, Y.; Eismann, S.; Schnitzer, M. J. High-Speed Recording of Neural Spikes in Awake Mice and Flies with a Fluorescent Voltage Sensor. *Science (80-.).* **2015**. https://doi.org/10.1126/science.aab0810.

(65) Jin, L.; Han, Z.; Platisa, J.; Wooltorton, J. R. A.; Cohen, L. B.; Pieribone, V. A. Single Action Potentials and Subthreshold Electrical Events Imaged in Neurons with a Fluorescent Protein Voltage Probe. *Neuron* **2012**, *75* (5), 779–785. https://doi.org/10.1016/j.neuron.2012.06.040.

(66) Siegel, M. S.; Isacoff, E. Y. A Genetically Encoded Optical Probe of Membrane Voltage. *Neuron* **1997**, *19* (4), 735–741. https://doi.org/10.1016/S0896-6273(00)80955-1.

(67) Abdelfattah, A. S.; Kawashima, T.; Singh, A.; Novak, O.; Liu, H.; Shuai, Y.; Huang, Y. C.; Campagnola, L.; Seeman, S. C.; Yu, J.; Zheng, J.; Grimm, J. B.; Patel, R.; Friedrich, J.; Mensh, B. D.; Paninski, L.; Macklin, J. J.; Murphy, G. J.; Podgorski, K.; Lin, B. J.; Chen, T. W.; Turner, G. C.; Liu, Z.; Koyama, M.; Svoboda, K.; Ahrens, M. B.; Lavis, L. D.; Schreiter, E. R. Bright and Photostable Chemigenetic Indicators for Extended in Vivo Voltage Imaging. *Science (80-.).* **2019**. https://doi.org/10.1126/science.aav6416.

(68) Akemann, W.; Mutoh, H.; Perron, A.; Park, Y. K.; Iwamoto, Y.; Knöpfel, T. Imaging Neural Circuit Dynamics with a Voltage-Sensitive Fluorescent Protein. *J. Neurophysiol.* **2012**, *108* (8), 2323–2337. https://doi.org/10.1152/jn.00452.2012.

(69) Piatkevich, K. D.; Jung, E. E.; Straub, C.; Linghu, C.; Park, D.; Suk, H. J.; Hochbaum, D. R.; Goodwin, D.; Pnevmatikakis, E.; Pak, N.; Kawashima, T.; Yang, C. T.; Rhoades, J. L.; Shemesh, O.; Asano, S.; Yoon, Y. G.; Freifeld, L.; Saulnier, J. L.; Riegler, C.; Engert, F.; Hughes, T.; Drobizhev, M.; Szabo, B.; Ahrens, M. B.; Flavell, S. W.; Sabatini, B. L.; Boyden, E. S. A Robotic Multidimensional Directed Evolution Approach Applied to Fluorescent Voltage Reporters Article. *Nat. Chem. Biol.* **2018**, *14* (4), 352–360. https://doi.org/10.1038/s41589-018-0004-9.

(70) Milena M. Milosevic, Jinyoung Jang, Eric J. McKimm, Mei Hong Zhu, S. D. A. In Vitro Testing of Voltage Indicators : Archon1, ArcLightD, ASAP1, ASAP2s, ASAP3b, BongwooriPos6, BeRST1, FLicR1 and Chi-VSFP-Butterfly. *eNeuro* **2020**, *7* (5). https://doi.org/10.1523/ENEURO.0060-20.2020.

(71) Miller, E. W. Small Molecule Fluorescent Voltage Indicators for Studying Membrane Potential. *Curr. Opin. Chem. Biol.* **2016**, *33*, 74–80. https://doi.org/10.1016/j.cbpa.2016.06.003.

(72) González, J. E.; Tsien, R. Y. Improved Indicators of Cell Membrane Potential That Use Fluorescence Resonance Energy Transfer. *Chem. Biol.* **1997**, *4* (4), 269–277. https://doi.org/10.1016/S1074-5521(97)90070-3.

(73) Chanda, B.; Blunck, R.; Faria, L. C.; Schweizer, F. E.; Mody, I.; Bezanilla, F. A Hybrid Approach to Measuring Electrical Activity in Genetically Specified Neurons. *Nat. Neurosci.* **2005**, *8* (11), 1619–1626. https://doi.org/10.1038/nn1558.

(74) Lebeuf, R.; Férézou, I.; Rossier, J.; Arseniyadis, S.; Cossy, J. Straightforward Synthesis of the Near-Infrared Fluorescent Voltagesensitive Dye RH1691 and Analogues Thereof. *Org. Lett.* **2009**, *11* (21), 4822–4825. https://doi.org/10.1021/ol901846g.

(75) Fromherz, P.; Hübener, G.; Kuhn, B.; Hinner, M. J. ANNINE-6plus, a Voltage-Sensitive Dye with Good Solubility, Strong Membrane Binding and High Sensitivity. *Eur. Biophys. J.* **2008**. https://doi.org/10.1007/s00249-007-0210-y.

(76) Fluhler, E.; Burnham, V. G.; Loew, L. M. Spectra, Membrane Binding, and Potentiometric Reponses of New Charge Shift Probes†. *Biochemistry* **1985**, *24* (21),

5749–5755. https://doi.org/10.1021/bi00342a010.

(77) Schaffer, P.; Ahammer, H.; Müller, W.; Koidl, B.; Windisch, H. Di-4-ANEPPS Causes Photodynamic Damage to Isolated Cardiomyocytes. *Pflügers Arch. Eur. J. Physiol.* **1994**, *426* (6), 548–551. https://doi.org/10.1007/BF00378533.

(78) Boggess, S. C.; Gandhi, S. S.; Siemons, B. A.; Huebsch, N.; Healy, K. E.; Miller, E. W. New Molecular Scaffolds for Fluorescent Voltage Indicators. *ACS Chem. Biol.* **2019**, *14* (3), 390–396. https://doi.org/10.1021/acschembio.8b00978.

(79) Woodford, C. R.; Frady, E. P.; Smith, R. S.; Morey, B.; Canzi, G.; Palida, S. F.; Araneda, R. C.; Kristan, W. B.; Kubiak, C. P.; Miller, E. W.; Tsien, R. Y. Improved PeT Molecules for Optically Sensing Voltage in Neurons. *J. Am. Chem. Soc.* **2015**, *137* (5), 1817–1824. https://doi.org/10.1021/ja510602z.

(80) Kulkarni, R. U.; Kramer, D. J.; Pourmandi, N.; Karbasi, K.; Bateup, H. S.; Miller, E. W. Voltage-Sensitive Rhodol with Enhanced Two-Photon Brightness. *Proc. Natl. Acad. Sci. U. S. A.* **2017**, *114* (11), 2813–2818. https://doi.org/10.1073/pnas.1610791114.

(81) Ortiz, G.; Liu, P.; Naing, S.; Muller, V.; Miller, E. Long-Wavelength Fluorophores for Voltage Sensing. **2019**, No. 2. https://doi.org/10.26434/chemrxiv.7663124.v2.

(82) Huang, Y.-L.; Walker, A. S.; Miller, E. W. A Photostable Silicon Rhodamine Platform for Optical Voltage Sensing. *J. Am. Chem. Soc.* **2015**, *137* (33), 10767–10776. https://doi.org/10.1021/jacs.5b06644.

(83) Smith, A. M.; Mancini, M. C.; Nie, S. Bioimaging: Second Window for in Vivo Imaging. *Nat. Nanotechnol.* **2009**, *4* (11), 710–711. https://doi.org/10.1038/nnano.2009.326.

(84) Grenier, V.; Walker, A. S.; Miller, E. W. A Small-Molecule Photoactivatable Optical Sensor of Transmembrane Potential. *J. Am. Chem. Soc.* **2015**, *137* (34), 10894–10897. https://doi.org/10.1021/jacs.5b05538.

(85) Liu, P.; Grenier, V.; Hong, W.; Muller, V. R.; Miller, E. W. Fluorogenic Targeting of Voltage-Sensitive Dyes to Neurons. *J. Am. Chem. Soc.* **2017**, *139* (48), 17334–17340. https://doi.org/10.1021/jacs.7b07047.

(86) Deal, P. E.; Liu, P.; Al-Abdullatif, S. H.; Muller, V. R.; Shamardani, K.; Adesnik, H.; Miller, E. W. Covalently Tethered Rhodamine Voltage Reporters for High Speed Functional Imaging in Brain Tissue. *J. Am. Chem. Soc.* **2020**, *142* (1), 614–622. https://doi.org/10.1021/jacs.9b12265.

(87) Grenier, V.; Daws, B. R.; Liu, P.; Miller, E. W. Spying on Neuronal Membrane Potential with Genetically Targetable Voltage Indicators. *J. Am. Chem. Soc.* **2019**, *141* (3), 1349–1358. https://doi.org/10.1021/jacs.8b11997.

Chapter 2

Design and Synthesis of a Phosphine Oxide Rhodamine Voltage Reporter

Portions of this work appeared as a preprint:

Gonzalez, M. A.; Walker, A. S.; Cao, K. J.; Lazzari-Dean, J. R.; Settineri, N.; Kong, E.-J.; Kramer, R. H.; Miller, E. W.; Voltage imaging with a NIR-absorbing phosphine oxide rhodamine voltage reporter. *ChemRxiv.* **2019**, Preprint: DOI: 10.26434/chemrxiv.10025789.v1.

Portions of this work were performed in collaboration with the following people:

Synthesis was done with the assistance of Julie Kong.

X-ray crystallography and analysis were performed by Nicholas Settineri.

2.0 Introduction

Voltage reporters (VRs) are composed of three primary components, **Figure 2.0.1**, a fluorophore, molecular wire, and electron rich aniline donor. A wide variety of VRs have been previously made in the Miller lab with BeRST1 being the reddest. The donor modulates the fluorescence of the reporter in response to changes in the membrane potential of a cell through a photo induced electron transfer (PeT) process.[4] None, however, have absorption and emission that approaches 700 nm. There is a myriad of benefits associated with fluorophores whose emission and absorption falls in the near-infrared (NIR) range.[6] Firstly, NIR light is lower in energy and therefore less damaging to tissue and cells when used for illumination. Secondly, NIR light is absorbed and scattered to a lesser extent than other higher energy wavelengths. Lastly, fluorophores with NIR emission avoid any added background fluorescence arising from cellular autofluorescence.

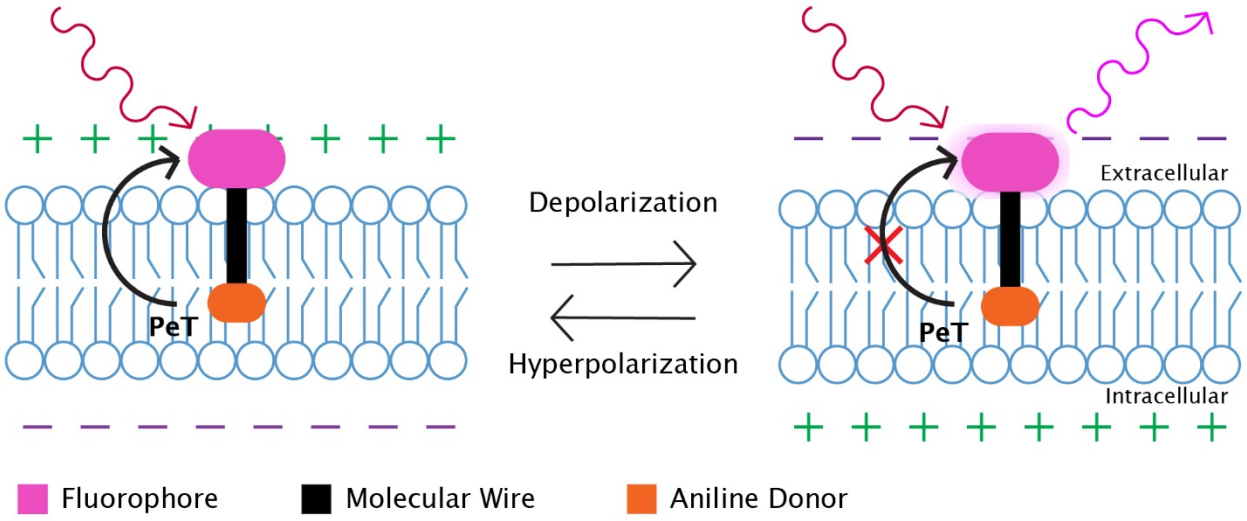

Figure 2.0.1 Voltage Reporters detect cellular membrane potential through a photoinduced electron transfer process (PeT).

Rhodamine fluorophores can be redshifted by replacing the oxygen at the bridgehead position with different elements such as phosphorous. This work has been previously reported by Chai and coworkers and we sought to take advantage of this novel phosphine oxide rhodamine and incorporate it into our VRs to create a VR whose photophysical properties would move further into the NIR range.[1] Modifications were made to the original phosphine oxide rhodamine to impart water solubility to the fluorophore as well as prevent the internalization of the dye and provide a chemical handle through which the molecular wire could be appended. This chapter details the synthesis of this new phosphine oxide rhodamine voltage reporter (poRhoVR) and describes optimizations for various reactions in the scheme.

2.1 General Synthetic Scheme

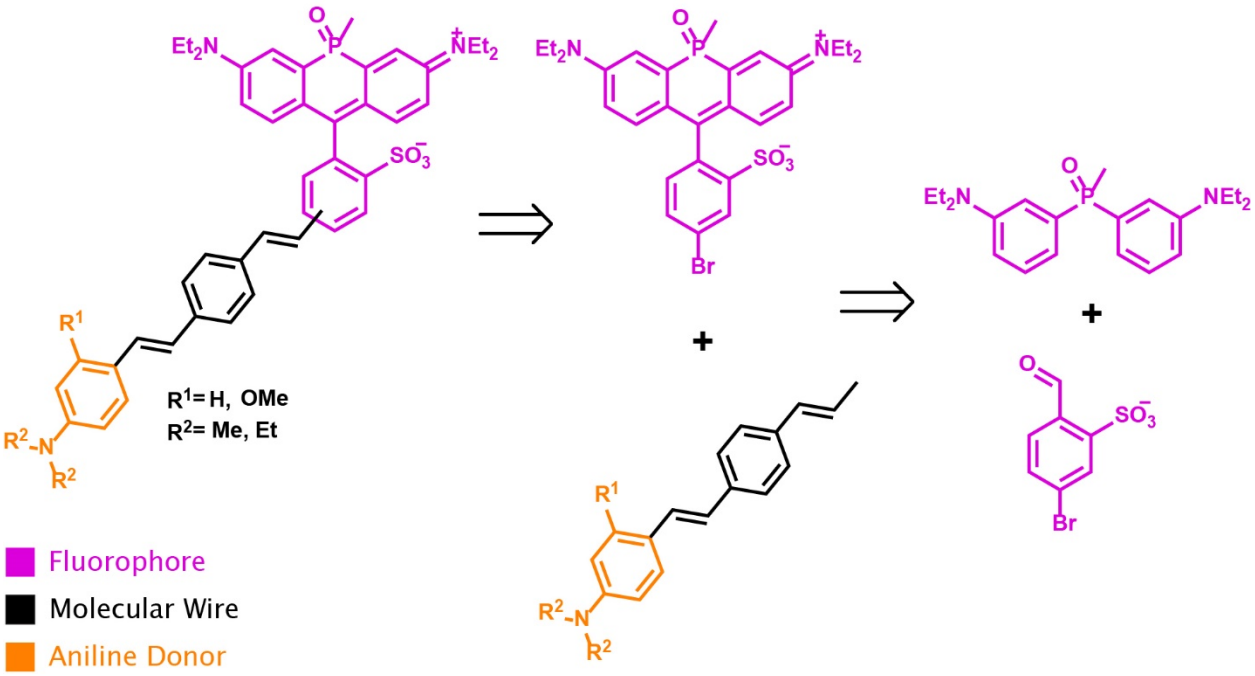

Figure 2.1.1. Retrosynthetic scheme for poRhoVR.

As shown in **Figure 2.1.1**, synthesis of poRhoVRs can be broken down into 2 key compounds: the fluorophore and the molecular wire containing the aniline donor. A phosphine oxide rhodamine fluorophore would make a significantly redshifted VR that emits past 700 nm. The fluorophore can be assembled from a phosphine oxide and a sulfonated bromobenzaldehyde. The sulfonate aides in water solubility and its negative charge prevents the dye from becoming internalized. **Scheme 2.1.1** shows the complete synthesis of 4 different poRhoVR dyes. Synthesis of **5** closely follows a previously reported synthesis with some optimization done in the synthesis of compounds **4** and **5**.[1] The fluorophores **8** and **9** were synthesized via a condensation with a sulfonated benzaldehyde. This reaction required optimization, but it was still the best method that avoided any potential deprotonation of the methyl substituent on the phosphorous atom by organolithiates commonly used in other rhodamine synthetic routes.

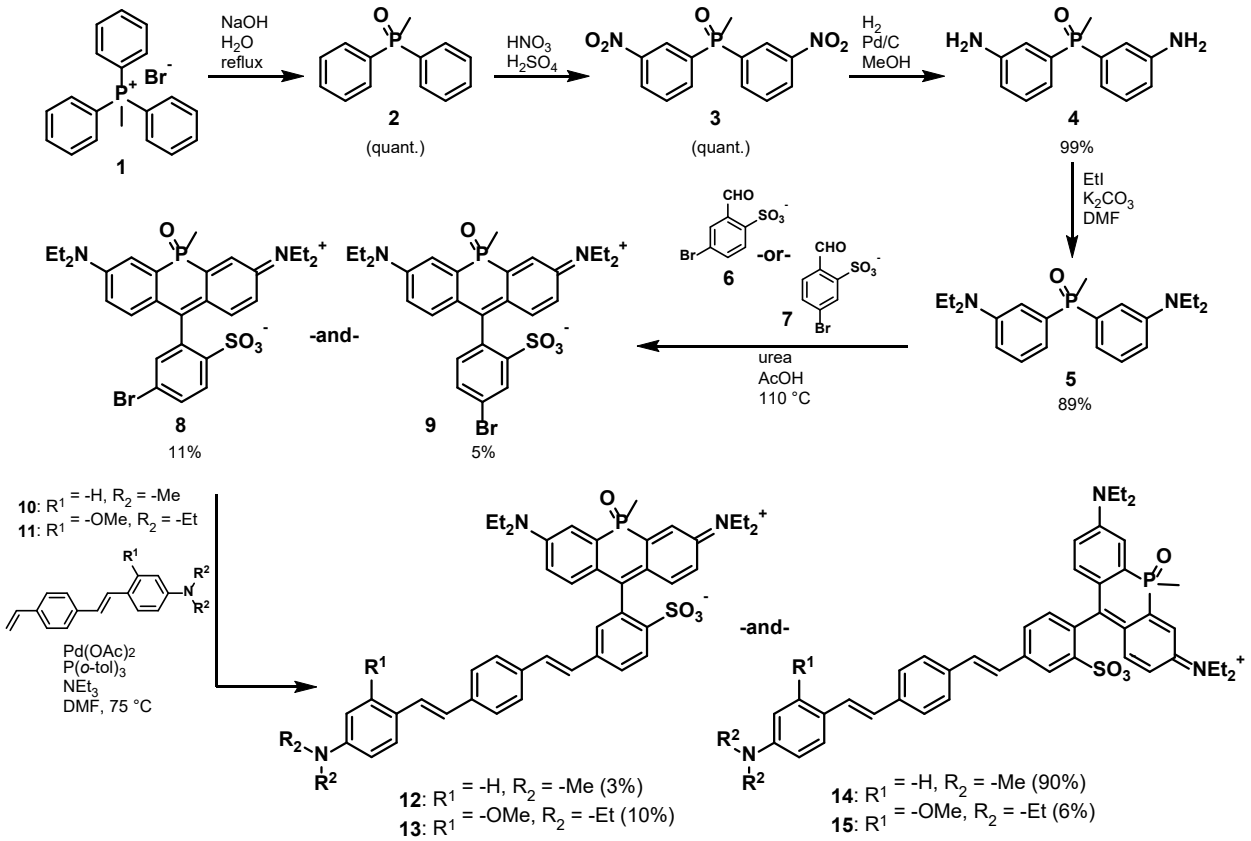

Scheme 2.1.1 Complete synthesis of poRhoVR dyes.

poRhoVRs were accessed in 6 steps from commercially available triphenylphosphonium salts (**Scheme 2.1.1**). Anilino phosphine oxide **4** was prepared in high yield over three previously reported steps.[1, 7] Efforts towards eliminating reduction impurities can be found in **Appendix 1**. Phosphine oxide **4** was alkylated through a slightly modified procedure using ethyl iodide and potassium carbonate in dimethyformamide (DMF) to produce phosphine oxide **5** in a modest yield (89%). The key sulfonated phosphorous rhodamine precursors with bromine substitution for installation of the phenylenevinylene molecular wire were prepared in one step by condensing bromosulfobenzaldehyes[4] **6** or **7** with phosphine oxide **5** in the presence of urea[1] and glacial acetic acid (**Scheme 2.1.1**). Other attempts at condensation with methane sulfonic acid or propionic acid or acetic acid without urea resulted in no reaction or were extremely low yielding. This is likely due to the electron-withdrawing properties of the phosphine oxide moiety which lowers the nucleophilicity of the aniline rings. Addition of urea to the reaction helped to further activate the aldehyde for electrophilic attack and overcome the weak nucleophilicity of phosphine oxide **5**.

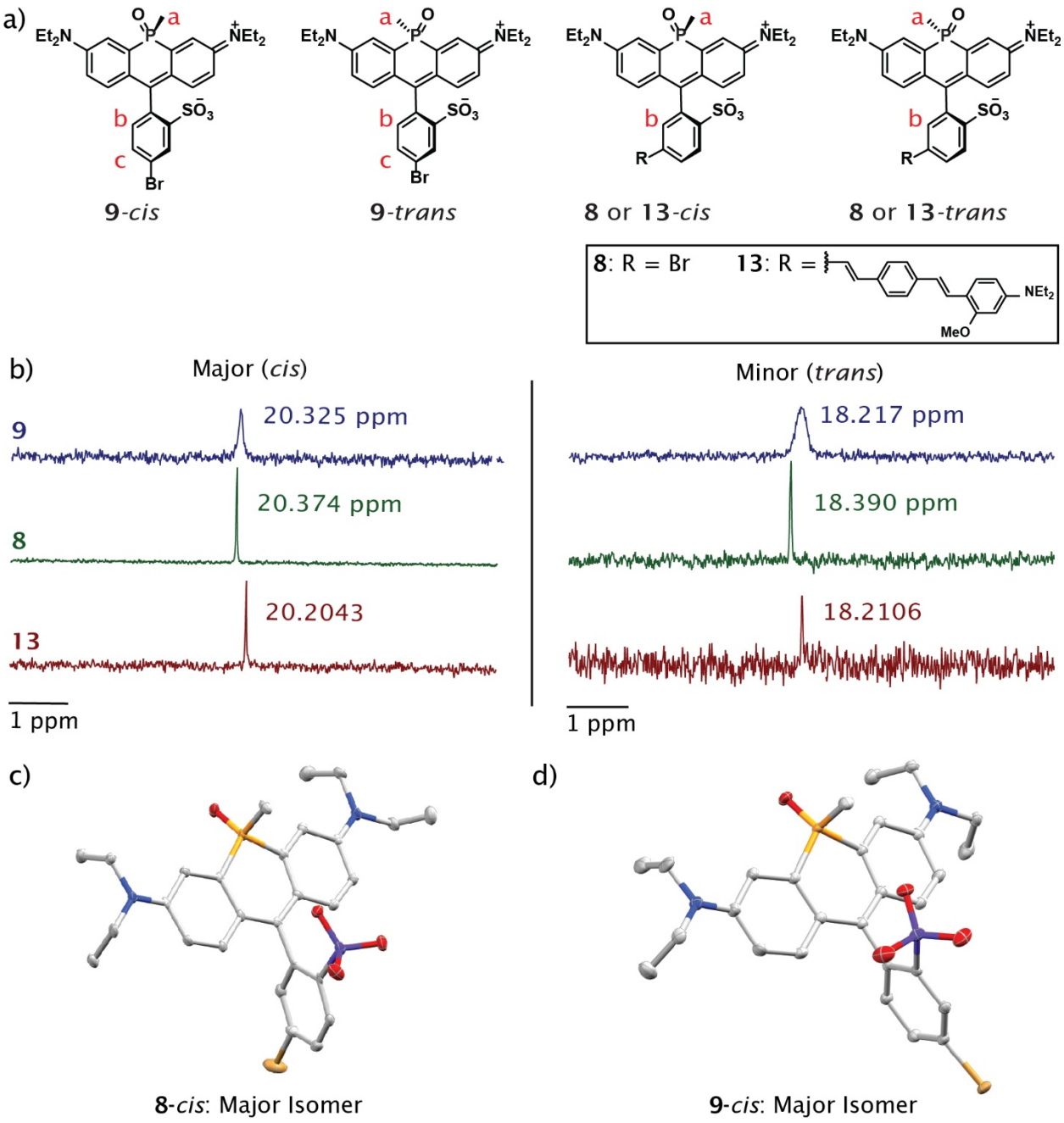

Figure 2.1.2 Chemical characterization of isomers of phosphine oxide rhodamine dyes. **a)** Proposed structures of **8**, **9**, and **13**. **b)** Decoupled ^{31}P spectra the *trans*- and *cis*- isomers of po-rhodamines **8** and **9** and for poRhoVR **13**. The structure of **8** – *cis* and **9** – *cis* were confirmed by x-ray crystallography, shown as thermal ellipsoid plots (50%) of **c) 8** and **d) 9**. Hydrogen atoms, lattice solvent molecules and resolved disordered fragments have been omitted for clarity. The structure of the major isomer of **13** is assumed to be the *cis* isomer, based on similarities in the ^{31}P NMR. ^{1}H labels on the structures (a, b, and c) refer to the indicated chemical shifts in **Table #**.

The condensation between *m*- (**6**) or *p*-bromosulfobenzaldehye (**7**) and phosphine oxide **5** produced two isomers of bromosulfo-phosphine oxide rhodamines [1, 7] in which the P-methyl

substituent and sulfonate exist in either a *cis* or *trans* relationship to one another (**Figure 2.1.2**). High pressure liquid chromatograph (HPLC) of the crude condensation mixture reveals two distinct peaks with different retention times and the same mass to charge ratio corresponding to phosphine-oxide rhodamine **8** or **9** (**Figure 2.1.2**). These two sets of isomers were separable on a basic alumina column, eluting with 0-5% methanol in dichloromethane. After this step, no further purification was necessary for the major isomer of either **8** or **9**. But for the minor isomer, preparative HPLC was required. NMRs of the purified materials revealed differences between the chemical shifts of the phosphorous bridgehead atoms, the methyl substituents on the bridgehead atom of the two isomers Major: δ 2.00 (Me ^{1}H), δ 20.20 (^{31}P); Minor δ2.01 (Me ^{1}H), δ 18.21 (^{31}P) (**Figure 2.1.2**). Furthermore, x-ray crystal structures of the major isomer of both **8** and **9** reveal a *trans* relationship between the sulfonate and the methyl group on the phosphorous bridgehead atom (**Figure 2.1.2 c** and **d**). Attempts to crystalize the minor isomer of **8** or **9** were unfruitful. Any crystals that were collected from these attempts showed a *trans* relationship. It is possible that in solution at room temperature over a period of several weeks the minor isomer slowly converts to the major isomer. In aqueous solution (phosphate buffered saline, 5 μM dye), both bromo phosphine oxide rhodamine **8** and **9** isomers (*meta* and *para*) had an absorption maximum at 704 nm and emission maxima around 728 nm (**Figure 2.1.2**) and quantum yields near 20% (22% for **8** and 19% for **9**).

	Compound	NMR Chemical Shift (ppm) ^{31}P	$^{1}H_a$	$^{1}H_b$	$^{1}H_c$
Major	**9**	20.325	2.010	7.192	7.823
	8	20.374	2.019	7.483	---
	13	20.204	1.999	6.252	---
Minor	**9**	18.217	1.948	7.232	7.800
	8	18.390	1.966	7.549	---
	13	18.211	2.006	6.255	---

Table 2.1.1 Summary of differences in NMR shifts of the isomers of **8**, **9** and **13**. The atoms shown in the table are labeled in **Figure 2.1.2 a**.

Molecular wires **10** (dimethyl aniline) or **11** (diethyl aniline and methoxy substituent) were installed onto the phosphine-oxide rhodamine fluorophore using a Pd-catalyzed Heck coupling to generate a total of four new phosphine oxide Rhodamine Voltage Reporters (poRhoVRs, **12** – **14**, **Scheme 2.1.1**). For each reaction the cross coupling was performed using the purified, major isomer (*trans*) of either **8** or **9**. However, in each case this did not prevent the formation of diastereomers: analytical HPLC/MS showed two peaks with the product mass corresponding to poRhoVR. As previously reported,[1] separation of the isomers is extremely arduous but in the case of **13**, extensive column chromatography on silica gel and preparative scale HPLC on C_{18}-functionalized silica afforded small quantities of major (9% yield) and even smaller quantities of minor isomers (1% yield). Comparison of the ^{1}H and ^{31}P NMR data for the isomers of **13** closely match the chemical shifts observed for the *cis* and *trans* isomers of **8** and **9**, suggesting that the major product is the *trans* isomer of **13** (**Figure 2.1.2**). Isomers of the other three poRhoVRs (**12**, **14**, and **15**) were not separated due to the difficulty of purification. After purification on preparative TLC, the *cis* isomer of the three

other poRhoVRs were not detected. ^{31}P NMRs showed that for poRhoVRs **12**, **14** and **15** major products isolated were *trans*. Absorption and emission spectra of poRhoVRs **12-14** in PBS showed that the photophysical properties closely matched those of phosphine oxide rhodamines **8** and **9**.

Compound number	isomer[a]	R^1	R^2	λ_{abs}[b]	λ_{em}[b]	Φ[b]
8	*meta, cis*	---	---	704	727	0.19
8	*meta, trans*	---	---	704	724	0.3
9	*para, cis*	---	---	704	729	0.22
12	*meta, cis*	H	Me	705	731	0.01
13	*meta*, mixture	OMe	Et	703	728	0.01
14	*para, cis*	H	Me	704	723	0.07
15	*para, cis*	OMe	Et	704	726	0.09

[a] relationship between fluorophore and molecular wire or bromine, relationship between methyl substiuent on phosphorous and sulfonate [b] dPBS with 0.1% DMSO, QY measured using Cy 5.5 as a standard

Table 2.1.2 Summary of photophysical properties of dyes **8-15**.

2.2 Conclusion

Synthesis of 4 poRhoVRs were completed over 6 steps (**Scheme 2.1.1**). Characterization of the phosphorous rhodamine fluorophores, **8** and **9**, revealed two distinct isomers that could be isolated via purification with flash column chromatography (**Figure 2.1.2**). X-ray crystallography revealed that the major isomer had a *cis* relationship between the methyl substituent on the phosphorous atom and the sulfonate on the pendant ring (**Figure2.1.2 c-d**). These isomers showed differences in their NMR shifts, (**Figure 2.1.2 b**) but did not have different absorption and emission properties (**Table 2.1.2**). All four poRhoVRs had maximal absorption and emission beyond 700 nm (**Table 2.1.2**).

2.3 Synthetic Details

Photophysical Characterization

Absorbance and emission spectra were collected using a Shimadzu 2501 Spectrophotometer (Shimadzu) and a Quantamaster Master 4 L-format scanning spectrofluorometer (Photon Technologies International). The fluorometer excitation source is an LPS-220B 75-W xenon lamp. The fluorometer is equipped with a power supply, A-1010B lamp housing with integrated igniter, switchable 814 photon-counting/analog photomultiplier detection unit, and MD5020 motor driver. Samples were measured in 1-cm path length quartz cuvettes (Starna Cells).

Relative quantum yields (ϕ_F) were measured via comparison to Cy5.5 ($\phi_{standard}$ = 0.23 in PBS).[1, 2] DMSO stocks of fluorophores **8-9** and poRhoVRs **12-15** were diluted in PBS with

0.1% sodium dodecyl sulfate (SDS) until the max absorbance was less than 0.1 absorbance units. Serial dilutions were made from the initial dilution into PBS with 0.1% SDS. The absorbance at 625 nm versus the total area under the fluorescence curve from 635-855 nm were plotted. The slope of the resulting linear plot was calculated for each compound and for the standard. The slope was put into the equation below where; x represents the compound being analyzed, st represents the standard, ϕ_x is the ϕ_F for compound x and η is the refractive index of the solvent in which the measurements were made. The absorbance and fluorescence measurements for fluorophores **8** and **9** were made in PBS and in PBS with 0.1% SDS for poRhoVRs **12-15**. For both solutions, the refractive index was approximated to the refractive index of water (η= 1.33).

$$\Phi_x = \Phi_{st} \left(\frac{Slope_x}{Slope_{st}}\right)\left(\frac{\eta_x^2}{\eta_{st}^2}\right)$$

General Synthesis and Characterization Information

Chemical reagents and solvents were purchased from commercial sources and used without further purification. Flash column chromatography was performed using Silicycle Silica Flash F60 (230–400 Mesh). Preparative Thin Layer Chromatography (PTLC) purification was done using glass plates coated with a layer of silica gel (Silicycle, F254, 1000 μm). Preparative High Performance Liquid Chromatography (Prep-HPLC) was done using a Waters Acquity Autopurificaitonsystem equipped with a Waters XBridge BEH 5 μm C18 column (19 mm I.D. x 250 mm) with a flow rate of 30.0 mL/min, made available by the Catalysis Facility of Lawrence Berkeley National Laboratory (Berkeley, CA). The mobile phases were MiliQ (MQ-H_2O) with 0.05% formic acid (FA) and HPLC grade acetonitrile (MeCN) with 0.05% FA. Absorbance was monitored at 350 nm over 200 min with a gradient of 10-100% of MeCN with 0.05% FA. NMR spectra were collected on one of the following instruments: Bruker AVB-400 MHz, AVQ-400 MHz, Bruker AV-600 MHz. Chemical shifts are reported in parts per million (ppm) and couplings constants are reported in Hertz (Hz). Characterization of purity and identity was also done via High Performance Liquid Chromatography (HPLC) and low resolution ESI mass spectrometry on an Agilent Infinity 1200 analytical instrument coupled to an Advion CMS-L ESI mass spectrometer. The column used for the analytical HPLC was Phenomenex Luna 5 μm C18(2) (4.6 mm I.D. × 75 mm) with a flow rate of 1.0 mL/min. The mobile phases were MQ-H_2O with 0.05% formic acid (FA) and HPLC grade MeCN with 0.05% FA. Absorbance was monitored at 254, 280, 350 and 690 nm over 10 min with a gradient of 10-100% of MeCN with 0.05% FA.

Crystallization of 8- and 9- ***cis***

Crystals were grown through vapor diffusion. The compound was dissolved in a mixture of 90% 1,2-dichloroethane, 5% ethanol, 5% methanol by volume. The resulting solution was

filtered with a 0.45 μm PTFE filter into a 60 mm test tube. The tube was placed into a 20 mL vial containing 7 mL of hexanes and capped with lid (foil inner lining). The vial was kept at room temperature away from light.

Single-crystal X-ray diffraction experiments were performed at the UC Berkeley CHEXRAY crystallographic facility. Measurements of all compounds were performed on a Bruker Quazar SMART APEX-II using Mo Kα radiation (λ = 0.71073 Å). Crystals were kept at 100(2) K throughout collection. Data collection was performed with Bruker APEX2 software (v. 2014.11). Data refinement and reduction were performed with Bruker SAINT (V8.34A). All structures were solved with SHELXT.53. Structures were refined with SHELXL-2016. Molecular graphics were computed with Mercury 4.0. All non-hydrogen atoms were refined anisotropically, and hydrogen atoms were included at the geometrically calculated positions and refined using a riding model.

	8	**9**
Chemical formula	$C_{30}H_{44}BrN_2O_8PS$	$C_{30}H_{37}BrCl_2N_2O_{4.5}PS$
Formula weight	703.61	712.27
Color, habit	Blue, plate	Blue, plate
Temperature (K)	100(2)	100(2)
Crystal system	Triclinic	Monoclinic
Space group	P -1	C 2/c
a (Å)	10.4009(5)	34.703(3)
b (Å)	12.1497(5)	10.3808(7)
c (Å)	15.2206(7)	24.3311(18)
α (°)	100.379(3)	90
β (°)	107.814(3)	133.946(6)
γ (°)	110.872(2)	90
V (Å^3)	1618.10(13)	6310.9(9)
Z	2	8
Density (Mg m^{-3})	1.444	1.499
F(000)	736	2939

Radiation Type	MoK_α	MoK_α
μ (mm^{-1})	1.435	1.629
Crystal size (mm^3)	0.19 x 0.075 x 0.035	0.20 x 0.06 x 0.03
Meas. Refl.	28286	47710
Indep. Refl.	5937	5767
R(int)	0.0739	0.0327
Final R indices [$I > 2\sigma(I)$]	R = 0.0494	R = 0.0332
	R_w = 0.0973	R_w = 0.0859
Goodness-of-fit	1.028	1.050
$\Delta\rho_{max}$, $\Delta\rho_{min}$ (e $Å^{-3}$)	1.198, -1.003	0.569, -0.481

NMR Abbreviations

s = singlet

d = doublet

dd = doublet of doublets

t = triplet

dt = doublet of triplets

td = triplet of doublets

q = quartet

qnt = quintet

dqnt = doublet of quintets

m = multiplet

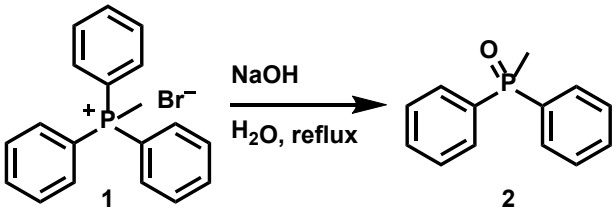

Synthesis of methyldiphenylphosphine oxide, 2:

Added 50 mL of H_2O to **1** (5.00 g, 14.0 mmol). Refluxed the solution for 30 minutes. Made a separate solution of NaOH (2.80 g, 70.0 mmol) in 25 mL of H_2O. The solution of NaOH was added to the solution of **1** and the reaction mixture became cloudy and opaque. The mixture was refluxed for an additional 2 hours. Once the mixture cooled to room temperature it was extracted with $CHCl_3$ (3X). The organic layer was washed with H_2O (3X), collected, and dried with anhydrous Na_2SO_4. The solvent was removed by rotary evaporation. Collected 3.02 g of a white solid (quantitative yield).

^{1}H NMR (400 MHz, $CDCl_3$) δ7.754-7.700 (m, 4 H); δ7.528-7.445 (m, 6 H); δ2.041-2.008 (d, J=13.2, 3 H).

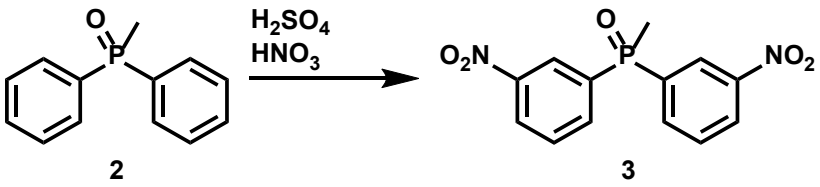

Synthesis of methylbis(3-nitrophenyl)phosphine oxide, 3:

Dissolved **2** (1.00 g, 4.63 mmol) in 5.2 mL of concentrated H_2SO_4. The solution was cooled to 0 °C. A separate solution of concentrated H_2SO_4 (1.8 mL) and HNO_3 (1.0 mL) was made while on ice. The acid mixture was added dropwise to the solution of **2**. After addition was complete the reaction mixture changed from clear to yellow. The reaction was stirred at 0 °C for two hours and then for an additional 3 hours at room temperature. The mixture was poured over ice and extracted with $CHCl_3$. The organic layer was collected and washed with a saturated $NaHCO_3$ solution (3X) and brine (1X). The organic layer was dried over anhydrous Na_2SO_4 and the solvent removed by rotary evaporation. Collected 1.40 g of a pale yellow solid (quantitative yield).

^{1}H NMR (400 MHz, $CDCl_3$) δ8.577-8.538 (dt, J=1.8 Hz, J=12.2 Hz, 2 H); δ8.441-8.414 (dqnt, J=1.1 Hz, J=8.2 Hz, 2H); δ8.154-8.107 (m, 2 H); δ7.777-7.731 (td, J=2.72 Hz, J=7.9 Hz, 2 H); δ2.221-2.188 (d, J=13.4 Hz, 3 H).

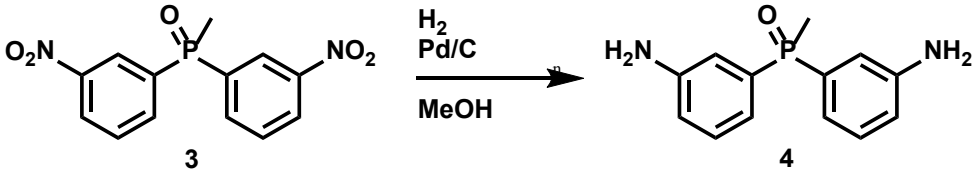

Synthesis of bis(3-aminophenyl)(methyl)phosphine oxide, 4:

Added **3** (0.25 g, 0.82 mmol) and 5% Pd/C (0.025 g, 10% wt) to a Schlenk flask. Evacuated the flask and backfilled using a balloon filled with H_2. Added 10 mL of MeOH and stirred at room temperature for 12 hours. The reaction mixture was filtered through a pad of Celite. The pad was washed with acetone and the filtrate collected. The solvent was removed by rotary evaporation. Collected 0.20 g of crude product, 99% yield.

^{1}H NMR (400 MHz, MeOD) δ7.245-7.197 (td, J=3.8 Hz, J=7.7 Hz, 2 H); δ7.016-6.936 (m, 4H); δ6.876-6.856 (dqnt, J=1.1 Hz, J=8.1 Hz, 2 H); δ2.221-2.188 (d, J=13.4 Hz, 3 H).

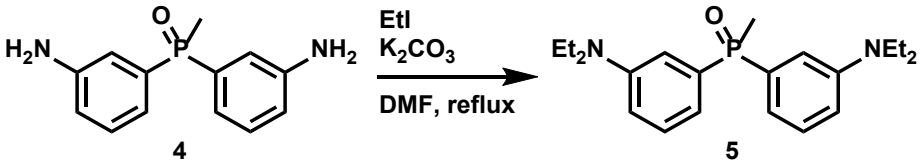

Synthesis of bis(3-(diethylamino)phenyl)(methyl)phosphine oxide, 5:

To **4** (5.83 g, 23.7 mmol) added 10 mL of dry DMF, EtI (10.0 mL, 124.4 mmol) and K_2CO_3 (16.4 g, 118.7 mmol). Refluxed for 12 hours. Removed DMF from reaction mixture by rotary evaporation. The remaining solid was redissolved in H_2O and extracted with DCM

(3X). The organics layer was dried over Na_2SO_4 and the solvent removed by rotary evaporation. The resulting residue was purified via flash column chromatography using silica as the stationary phase and 3% MeOH in DCM as the mobile phase. Collected 7.6 g of a golden oil (89% yield).

^{1}H NMR (400 MHz, $CDCl_3$) δ7.260-7.217 (m, 2 H); δ 7.108-7.073 (dm, J=13.9 Hz, 2 H); δ6.880-6.833 (m, 2 H); δ6.772-6.746 (dm, J=8.3 Hz, 2H); δ 3.378-3.326 (q, J=7.1Hz, 8 H); δ1.973-1.940 (d, J=13.1 Hz, 3 H); δ1.143-1.108 (t, J=7.0 Hz, 12 H).

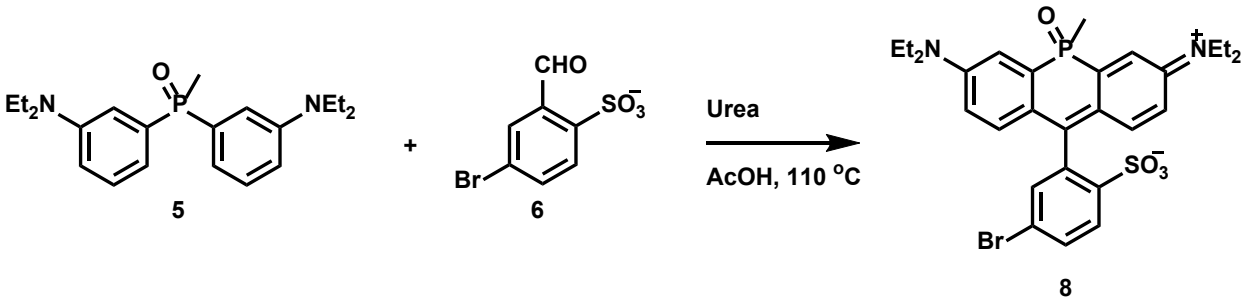

Synthesis of m-bromo tetraethylphosphourous rhodamine (mBrTEPR), 8:

Dissolved **5** (0.100 g, 0.280 mmol), **6** (0.067 g, 0.25 mmol) and urea (0.030 g, 0.50 mmol) in 2 mL of glacial acetic acid. Stirred at 110 °C for 24 hours. The reaction mixture changed from clear yellow to a dark blue green. Once the mixture had cooled to room temperature the acetic acid was removed by rotary evaporation. The blue green residue was redissolved in saturated $NaHCO_3$ and extracted with 2:1 DCM:IPA (3X). The organic layer was collected and dried over Na_2SO_4 and the solvent removed by rotary evaporation. The product was obtained by purifying first with a silica column using a gradient from 2-20% MeOH in DCM, followed by a basic alumina column using a gradient from 0-2% MeOH in DCM. The first blue green band to elute was collected which corresponds to the cis isomer of **8**. The second blue green band to elute was also collected and contained the trans isomer of **8** but required further purification. The trans isomer was obtained using reverse phase HPLC using a gradient from 0-100% MeCN in H_2O with 0.05% formic acid. Collected 0.015 g of the major *cis* isomer as a black-blue solid (10 % yield) and 1.6 mg of the minor *trans* isomer (1.1% yield).

8 (cis) ^{1}H NMR (400 MHz, MeOD) δ8.041-8.020 (d, J=8.4 Hz, 1 H); δ7.868-7.842 (dd J=2.0 Hz, J=8.4 Hz, 1 H); δ7.686-7.639 (dd J=2.8 Hz, J=16.0 Hz, 2 H); δ7.478-7.473 (d J=2.0 Hz, 1 H); δ7.111-7.073 (m, 2 H); δ6.930-6.889 (dd J=2.8 Hz, J=9.6 Hz, 2 H); δ3.838-3.722 (m, 8 H); δ2.018-1.983 (d, J=14.0 Hz, 3 H); δ1.355-1.319 (t, J=7.2 Hz, 12 H).

^{31}P NMR (400 MHz, MeOD) δ20.375.

8 (trans) ^{1}H NMR (400 MHz, MeOD) δ8.057-8.036 (d, J=8.4 Hz, 1 H); δ7.863-7.837 (dd J=2.0 Hz, J=8.4 Hz, 1 H); δ7.677-7.630 (dd J=2.8 Hz, J=16.0 Hz, 2 H); δ7.545-7.540 (d

J=2.0 Hz, 1 H); δ7.127-7.088 (m, 2 H); δ6.915-6.884 (dd J=2.8 Hz, J=9.6 Hz, 2 H); δ3.845-3.641 (m, 8 H); δ1.963-1.929 (d, J=13.6 Hz, 3 H); δ1.354-1.318 (t, J=7.2 Hz, 12 H).

^{31}P NMR (400 MHz, MeOD) δ18.389.

ESI MS, calculated for $[M+]^+$, $C_{28}H_{33}BrN_2O_4PS^+$, 603.11; found: 603.1. HR-ESI-MS, calculated for $[M+]^+$, $C_{28}H_{33}BrN_2O_4PS^+$, 603.1077, found 603.1075.

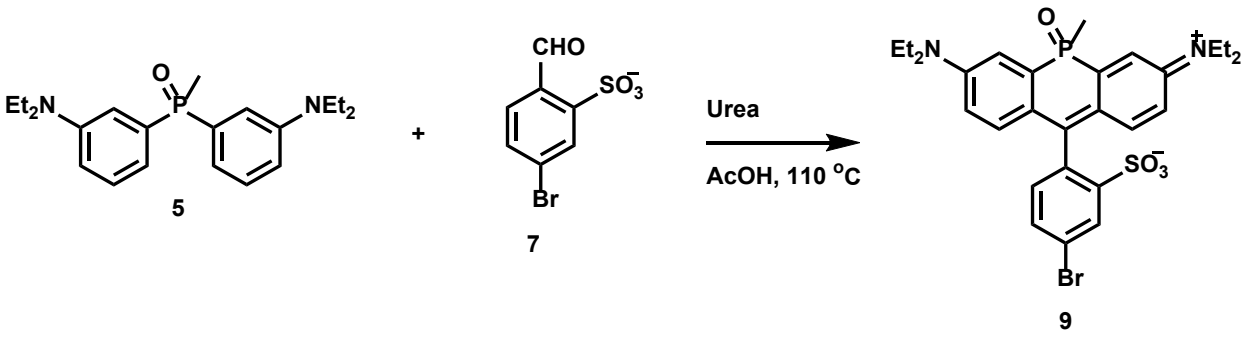

Synthesis of p-bromo tetraethylphosphourous rhodamine (pBrTEPR), 9:

Dissolved **5** (0.100 g, 0.280 mmol), **7** (0.067 g, 0.25 mmol) and urea (0.030 g, 0.50 mmol) in 2 mL of glacial acetic acid. Stirred at 110 °C for 24 hours. The reaction mixture changed from clear yellow to a dark blue green. Once the mixture had cooled to room temperature the acetic acid was removed by rotary evaporation. The blue green residue was redissolved in saturated $NaHCO_3$ and extracted with 2:1 DCM:IPA (3X). The organic layer was collected and dried over Na_2SO_4 and the solvent removed by rotary evaporation. The product was obtained by purifying first with a silica column using a gradient from 2-20% MeOH in DCM, followed by a basic alumina column using a gradient from 0-2% MeOH in DCM. The first blue green band to elute was collected which corresponds to the trans isomer of **9**. Collected 0.007 g of the cis isomer as a black-blue solid (5 % yield). The second blue green band to elute contained the minor trans isomer with an impurity that had a mass corresponding to the dibrominated product. The trans isomer further purified via reverse phase HPLC using a gradient from 0-100% MeCN in H_2O with 0.05% formic acid. Collected 0.7 mg of the minor *trans* isomer (0.46 % yield).

9 (cis) ^{1}H NMR (400 MHz, MeOD) δ8.268-8.264 (d, J=2.0 Hz, 1 H); δ7.825-7.805 (dd, J=2.0Hz, J=8.1 Hz, 1 H); δ7.678-7.640 (dd, J=2.7 Hz, J=15.9 Hz, 2 H); δ7.194-7.177 (d, J=8.1 Hz, 1 H); δ7.102-7.072 (m, 2 H); δ6.914-6.890 (dd, J=2.5 Hz, J=9.6 Hz, 2 H); δ3.797-3.725 (m, 8 H); δ2.015-1.987 (d, J=14.0 Hz, 3 H); δ 1.345-1.317 (t, J=6.9 Hz, 12 Hz).

^{31}P NMR (400 MHz, MeOD) δ20.325.

9 (trans) ^{1}H NMR (400 MHz, MeOD) δ8.286-8.281 (d, J=2.0 Hz, 1 H); δ7.800-7.775 (dd, J=2.0 Hz, J=8.2Hz, 2 H); δ7.673-7.627 (dd, J=2.6 Hz, J=16 Hz, 2 H); δ7.232-7.212 (d, J=8.2Hz, 1 H); δ7.124-7.085 (m, 2 H); δ 6.905-6.875 (dd, J=2.6 Hz, J=9.6 Hz); δ3.841-3.687 (m, 8 H); δ 1.948-1.914 (d, J=13.5 Hz); δ1.349-1.313 (t, J=7.0 Hz, 12 H).

^{31}P NMR (400 MHz, MeOD) δ18.217.

ESI MS, calculated for $[M+]^+$, $C_{28}H_{33}BrN_2O_4PS^+$, 603.11; found: 603.1. HR-ESI-MS, calculated for $[M+]^+$, $C_{28}H_{33}BrN_2O_4PS^+$, 603.1077; found 603.1079, calculated for $[M-H+Na]^+$, $C_{28}H_{32}BrN_2O_4PSNa^+$, 625.0896; found 625.0899.

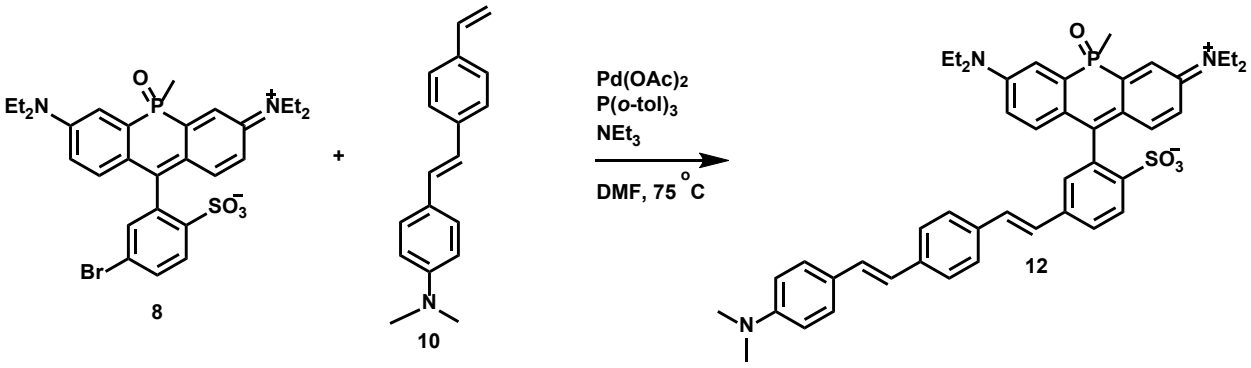

Synthesis of 12:

In an oven-dried flask added **8** (25 mg, 0.042 mmol), **10** (10 mg, 0.042 mmol), $Pd(OAc)_2$ (2.4 mg, 0.011 mmol) and P(*o*-tol)$_3$ (6.4 mg, 0.029 mmol). Evacuated and back-filled the flask with N_2 (3X). Dissolved the solids in 0.4 mL of dry DMSO and added dry NEt_3 (0.12 mL). Stirred at 75 °C for 18 hours. Once the reaction mixture cooled it was diluted with DCM and washed with H_2O (3X). The organic layer was washed with brine (1X) and dried over Na_2SO_4. The solvent was removed by rotary evaporation and the resulting residue was purified via prep TLC using 10% MeOH in DCM as the mobile phase. Further purified via reverse phase HPLC using a gradient from 0-100% MeCN in H_2O with 0.05% formic acid. Collected 1.1 mg of product (3.0 % yield).

^{1}H NMR (400 MHz, MeOD) δ8.110-8.092 (d, J=8.3 Hz, 1 H); δ7.874-7.851 (dd, J=1.4 Hz, J=8.3 Hz, 1 H); δ7.682-7.651 (dd, J=2.7 Hz, J=15.8 Hz, 2 H); δ7.543-7.529 (d, J=8.3 Hz, 2 H); δ 7.489-7.475 (d, J=8.3 Hz, 2 H); δ7.422-7.408 (m, 3 H); δ7.347-7.319 (d, J=16.4 Hz, 1 H); δ7.243-7.189 (m, 3 H); δ7.116-7.089 (d, J=16.3 Hz, 1 H); δ6.946-6.891 (m, 3 H); δ6.767-6.752 (d, J=8.9 Hz, 2 H); δ3.794-3.729 (m, 8 H); δ2.966 (s, 3.6 H); δ2.031-2.008 (d, J=14 Hz, 3 H); δ1.353-1.336 (t, J=6.9 Hz, 10 H).

ESI MS, calculated for $[M+H]^{2+}$, $C_{46}H_{52}N_3O_4PS^{2+}$, 386.67; found: 386.6.

HR-ESI-MS, calculated for $[M+]^+$, $C_{46}H_{51}N_3O_4PS^+$, 772.3332; found 772.3321, calculated for $[M-H+Na]^+$, $C_{46}H_{50}N_3O_4PSNa^+$, 794.3152; found 794.3149,

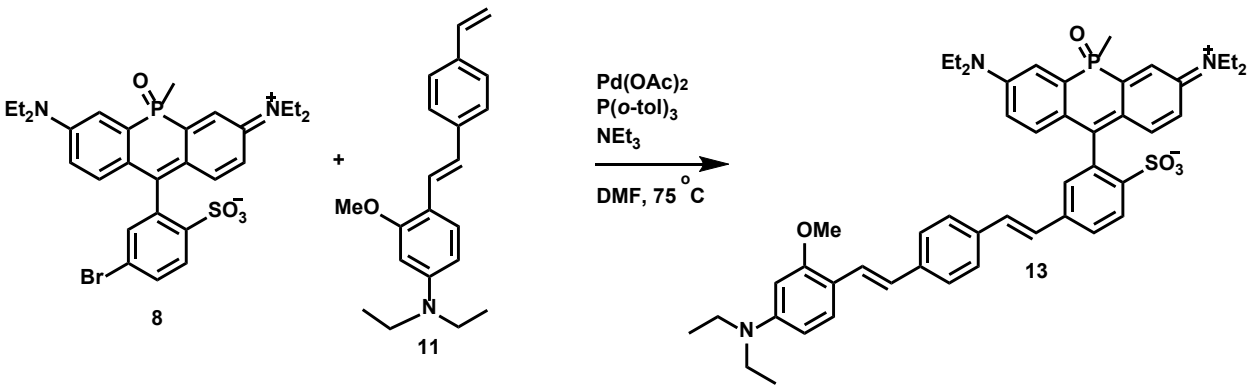

Synthesis of 13:

In an oven-dried flask added **8** (14.3 mg, 0.0237 mmol), **11** (7.3 mg, 0.024 mmol), $Pd(OAc)_2$ (2.7 mg, 0.012 mmol) and P(*o*-tol)$_3$ (7.2 mg, 0.024 mmol). Evacuated and back-filled the flask with N_2 (3X). Dissolved the solids in 1 mL of dry DMF and added NEt_3 (0.13 mL). Stirred at 75 °C for 2 hours before adding another 2.7 mg of $Pd(OAc)_2$. After the second addition of catalyst allowed the reaction to stir for an additional 12 hours. The product was obtained by purifying the reaction mixture via prep TLC using 10% MeOH in DCM as the mobile phase. Collected a green solid that was a mixture of isomers (9.8 mg, 50% yield). To separate the two isomers further purification was required. The solvent was removed from the reaction mixture and the remaining residue was first purified on an alumina column using 0-5% MeOH in DCM as the mobile phase. Two green solids were collected and are further purified via reverse phase HPLC with 0-100% MeCN in H_2O with 0.05% formic acid. Collected 1.8 mg of the major *cis* product (9.0 % yield) and 0.2 mg of the minor *trans* product (1.0 % yield).

13 (cis) ^{1}H NMR (400 MHz, MeOD) δ8.054-8.033 (d, J=8.3 Hz, 1 H); δ7.766-7.740 (dd, J=1.76 Hz, J=8.3Hz, 1 H); δ7.652-7.605 (dd, J=2.7 Hz, J=15.9 Hz, 2 H); δ7.459-7.344 (m, 7 H); δ7.266-7.226 (d, J=16.3 Hz, 1 H); δ7.163-7.100 (m, 3 H); δ6.902-6.861 (d, J=16.4 Hz, 1 H); δ6.822-6.791 (dd, J=2.7 Hz, J=9.7 Hz, 2 H); δ6.345-6.317 (dd, J=2.4 Hz, J=8.8 Hz, 1 H); δ6.253-6.247 (d, J=2.4 Hz, 1 H); δ3.873 (s, 3 H); δ3.757-3.722 (m, 8 H); δ3.444-3.392 (q, J=7.0 Hz, 4 H); δ2.002-1.967 (d, J=14.0, 3 H); δ1.339-1.303 (t, J=7.0 Hz, 12 H); δ1.205-1.170 (t, J=7.0 Hz, 6 H).

^{31}P NMR (400 MHz, MeOD) δ20.204.

13 (trans) ^{1}H NMR (400 MHz, MeOD) δ8.437 (s, 4 H); δ8.129-8.108 (d, J=8.2 Hz, 1 H); δ7.873-7.848 (dd, J=1.7 Hz, J=8.2 Hz, 1 H); δ7.687-7.640 (dd, J=2.8 Hz, J=16.0 Hz, 2 H); δ7.528-7.507 (d, J=8.4 Hz, 2 H); δ7.459-7.320 (m, 6 H); δ7.244-7.188 (m, 3 H); δ6.930-6.884 (m, 3 H); δ6.345-6.317 (dd, J=2.4 Hz, J=8.7 Hz, 1 H); δ6.256-6.250 (d, J=2.4 Hz, 1 H); δ3.874 (s, 3 H); δ3.843-3.691 (m, 8 H); δ3.446-3.394 (q, J=7.04 Hz, 4 H); δ 2.006-1.972 (d, J=13.5 Hz, 3 H); δ1.354-1.319 (t, J=6.9 Hz, 12 H); δ1.205-1.170 (t, J=7.0 Hz, 6 H).

^{31}P NMR (400 MHz, MeOD) δ18.209.

ESI MS, calculated for $[M+]^+$, $C_{49}H_{57}N_3O_5PS^+$, 830.38; found 830.4; $[M+H]^{2+}$, $C_{49}H_{58}N_3O_5PS^{2+}$, 415.69; found: 415.7.

HR-ESI-MS, calculated for $[M+]^+$, $C_{49}H_{57}N_3O_5PS^+$, 830.3751; found 830.3732, calculated for $[M-H+Na]^+$, $C_{49}H_{56}N_3O_5PSNa^+$, 852.3571; found 852.3570.

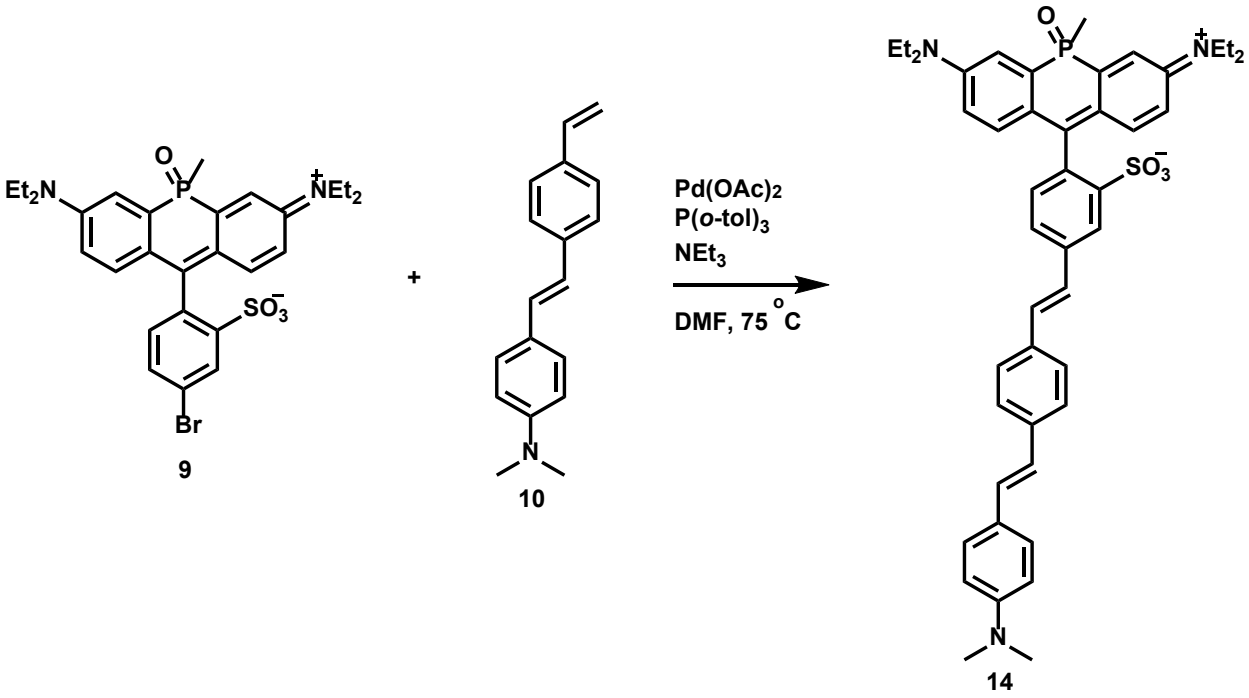

Synthesis of 14:

In an oven-dried flask added **9** (5.8 mg, 0.0096 mmol), **10** (2.5 mg, 0.0096 mmol), $Pd(OAc)_2$ (1.1 mg, 0.0048 mmol) and P(*o*-tol)$_3$ (2.9 mg, 0.0038 mmol). Evacuated and back-filled the flask with N_2 (3X). Dissolved the solids in 1 mL of dry DMF and added NEt_3 (0.05 mL). Stirred at 75 °C for 2 hours. The product was obtained by purifying the reaction mixture via prep TLC using 10% MeOH in DCM as the mobile phase. Collected 6.7 mg of a green solid (90% yield).

^{1}H NMR (600 MHz, MeOD) δ8.550 (s, 1 H, formate); δ8.313-8.311 (d, J=0.8 Hz, 1 H); δ7.833-7.818 (dd, J=0.9 Hz, J=8.8 Hz, 1 H); δ 7.672-7.642 (dd, J=2.5 Hz, J=15.8 Hz, 2 H); δ7.607-7.593 (d, J=8.2 Hz, 2 H); δ 7.537-7.524 (d, J=8.2 Hz, 2 H); δ7.440-7.426 (d, J=8.7 Hz, 2 H); δ7.409-7.381 (d, J=16.4 Hz, 1 H); δ7.346-7.319 (d, J=16.4 Hz, 1 H); δ7.223-7.173 (m, 3 H); δ7.147-7.120 (d, J=16.3 Hz, 1 H); δ6.976-6.949 (d, J=16.3 Hz, 1 H); δ6.906-6.885 (dd, J=2.6 Hz, J=9.7 Hz, 2 H); δ6.776-6.762 (d, J=8.7 Hz, 2 H); δ3.813-3.716 (m, 8 H); δ2.030-2.007 (d, J=13.9 Hz, 3 H); δ1.343-1.321 (t, J=6.5 Hz, 12 H).

^{31}P NMR (400 MHz, MeOD) δ20.359.

ESI MS, calculated for $[M+]^+$, $C_{46}H_{51}N_3O_4PS^+$, 772.33; found 772.3; $[M+H]^{2+}$, $C_{46}H_{52}N_3O_4PS^{2+}$, 386.67; found: 386.7.

HR-ESI-MS, calculated for $[M+]^+$, $C_{46}H_{51}N_3O_4PS^+$, 772.3332; found 772.3344, calculated for $[M+H]^{2+}$, $C_{46}H_{52}N_3O_4PS^{2+}$, 386.6703; found 386.6707, calculated for $[M+H+Na]^{2+}$, $C_{46}H_{51}N_3O_4PSNa^{2+}$, 397.6612; found 397.6617.

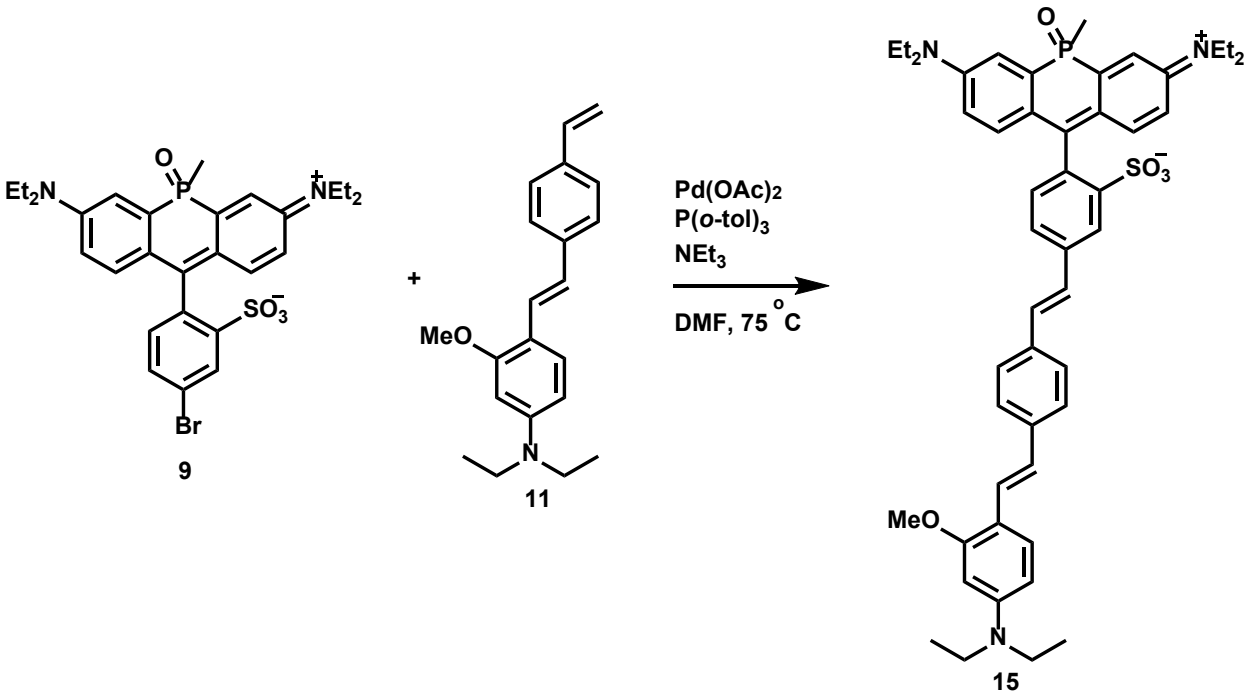

Synthesis of 15:

In an oven-dried flask added **9** (50 mg, 0.083 mmol), **11** (26 mg, 0.083 mmol), $Pd(OAc)_2$ (4.7 mg, 0.021 mmol) and P(*o*-tol)$_3$ (12.8 mg, 0.042 mmol). Evacuated and back-filled the flask with N_2 (3X). Dissolved the solids in 0.5 mL of dry DMF and added dry NEt_3 (0.02 mL). Stirred at 75 °C for 12 hours. The product was obtained by purifying the reaction mixture via prep TLC using 10% MeOH in DCM as the mobile phase. further purified via reverse phase HPLC using a gradient from 0-100% MeCN in H_2O with 0.05% formic acid. Collected 4.5 mg of a green solid (6.5% yield).

^{1}H NMR (600 MHz, MeOD) δ8.305 (s, 1 H); δ7.809-7.796 (d, J=7.92 Hz, 1 H); δ7.665-7.635 (dd, J=2.34 Hz, J=15.78 Hz, 2 H); δ7.573-7.560 (d, J=8.1 Hz, 2 H); δ7.485-7.472 (d, J=8.1 Hz, 2 H); δ7.448-7.406 (m, 2 H); δ7.387-7.360 (d, J=16.3 Hz, 1 H); δ7.318-7.291 (d, J=16.3 Hz, 1 H); δ7.203-7.167 (m, 3 H); δ6.948-6.921 (d, J=16.4 Hz, 1 H); δ6.891-6.870 (dd, J=2.5 Hz, J=12.2 Hz, 2 H); δ6.351-6.334 (dd, J=1.3 Hz, J=8.7 Hz, 1 H); δ6.266-6.264 (d, J=1.5 Hz, 1 H); δ3.801-3.709 (m, 8 H); δ3.442-3.407 (q, J=7.0 Hz, 4 H); δ3.887 (s, 3 H); δ2.026-2.002 (d, J=14.0 Hz, 3 H); δ1.339-1.316 (t, J=6.8 Hz, 12 H); δ1.206-1.83 (t, J=7.0 Hz, 6 H).

^{31}P NMR (400 MHz, MeOD) δ20.322. ESI MS, calculated for $[M+H]^{2+}$, $C_{49}H_{58}N_3O_5PS^{2+}$, 415.69; found: 415.7. HR-ESI-MS, calculated for $[M+]^{+}$, $C_{49}H_{57}N_3O_5PS^{+}$, 830.3751; found 830.3729, calculated for $[M+Na]^{+}$, $C_{49}H_{56}N_3O_5PSNa^{+}$, 852.3571; found 852.3570,

Synthesis of 6, 7, 10 & 11:

Synthesis of these compounds can be found in Kulkarni, R.U.; Yin, H.; Pourmandi, N.; James, F.; Adil, M.M.; Schaffer, D.V.; Wang, Y.; Miller, E.W.; *ACS Chem. Biol.* **12**, 407−413 (2017)

2.4 NMR and LCMS Data

Spectrum S1. ^{1}H NMR methyldiphenylphosphine oxide, 2

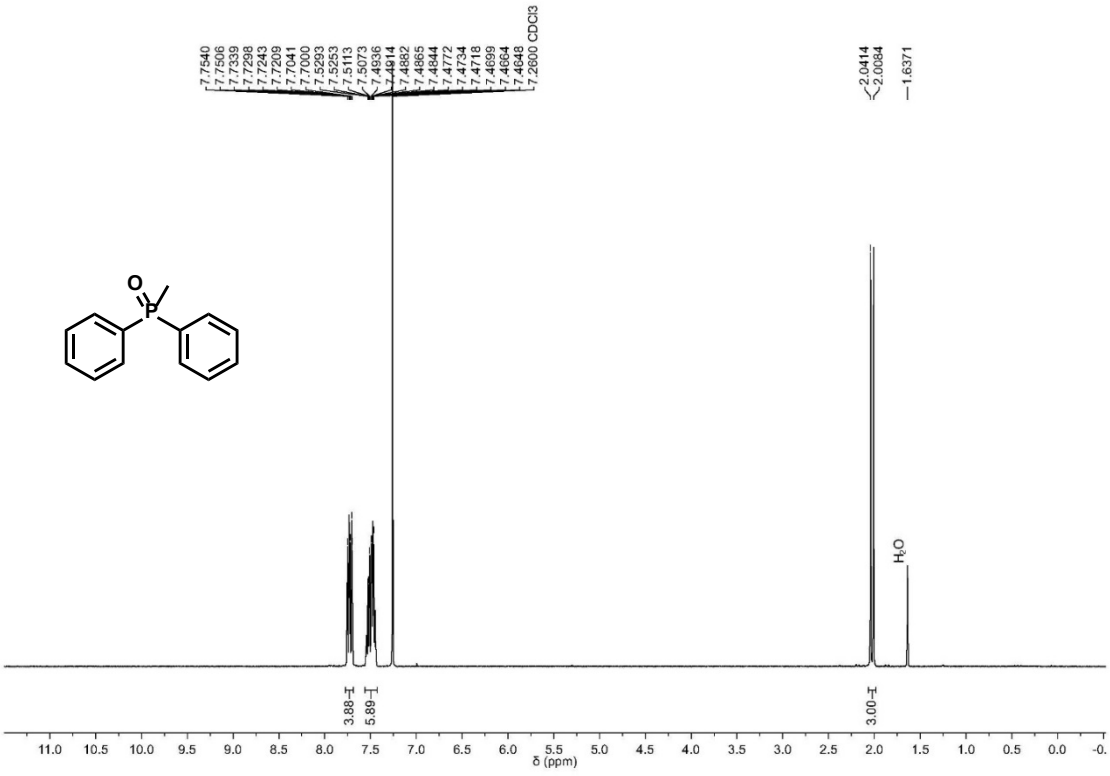

Spectrum S2. ^{1}H NMR methylbis(3-nitrophenyl)phosphine oxide, 3

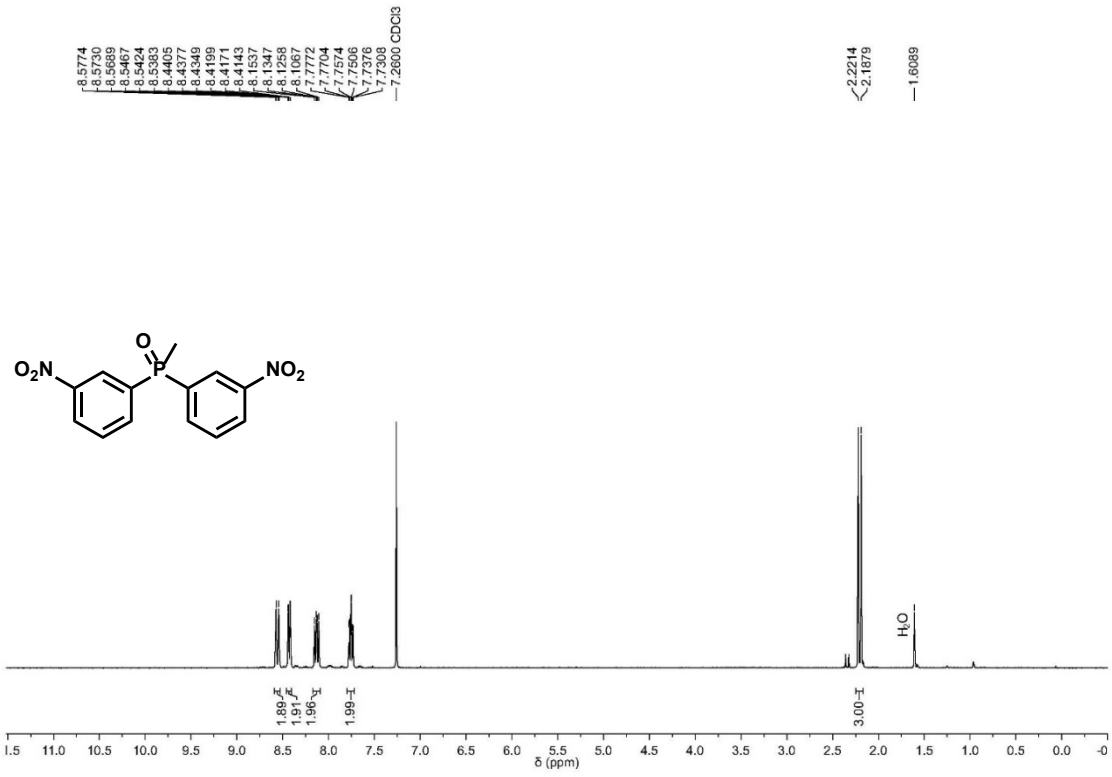

Spectrum S3. ^{1}H NMR bis(3-aminophenyl)(methyl)phosphine oxide, 4

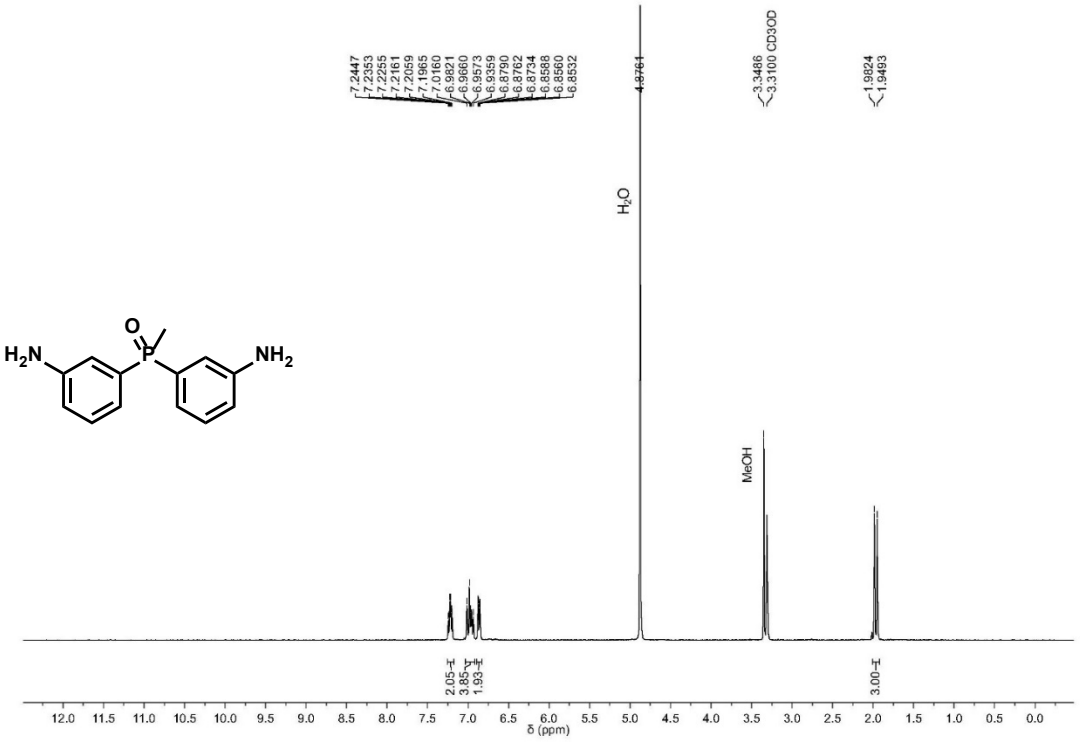

Spectrum S4. ^{1}H NMR bis(3-(diethylamino)phenyl)(methyl)phosphine oxide, 5

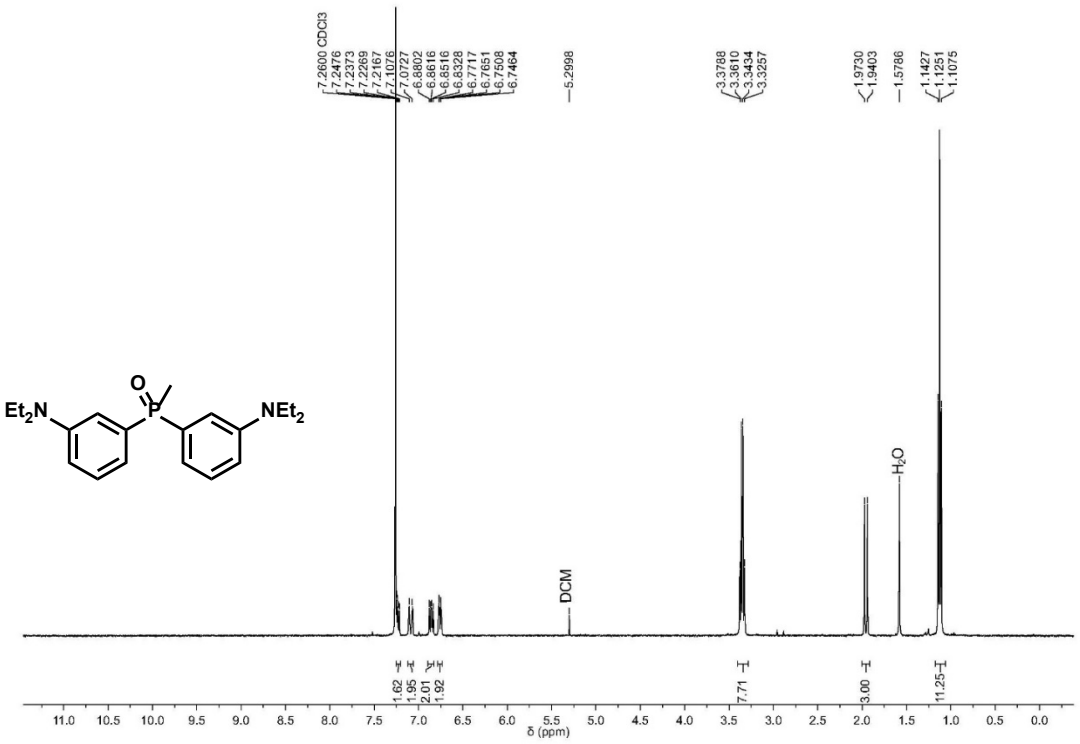

Spectrum S5. ^{1}H NMR m-bromosulfo-phosphine oxide rhodamine (cis), 8

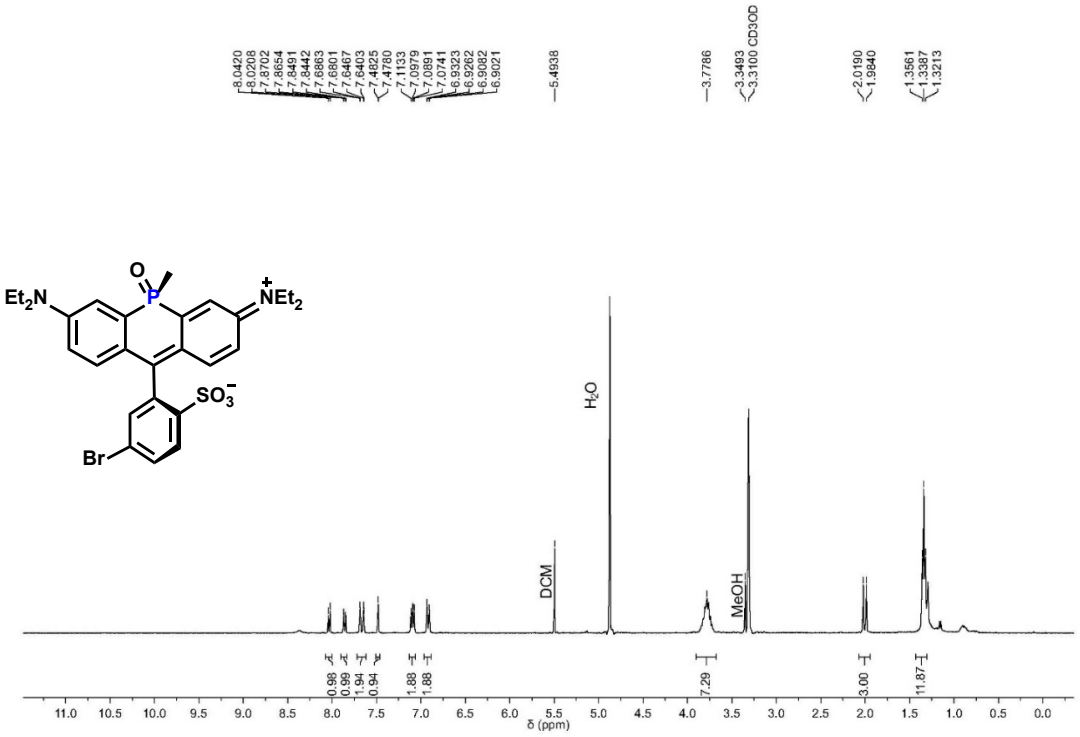

Spectrum S6. ^{31}P NMR m-bromosulfo-phosphine oxide rhodamine (cis), 8

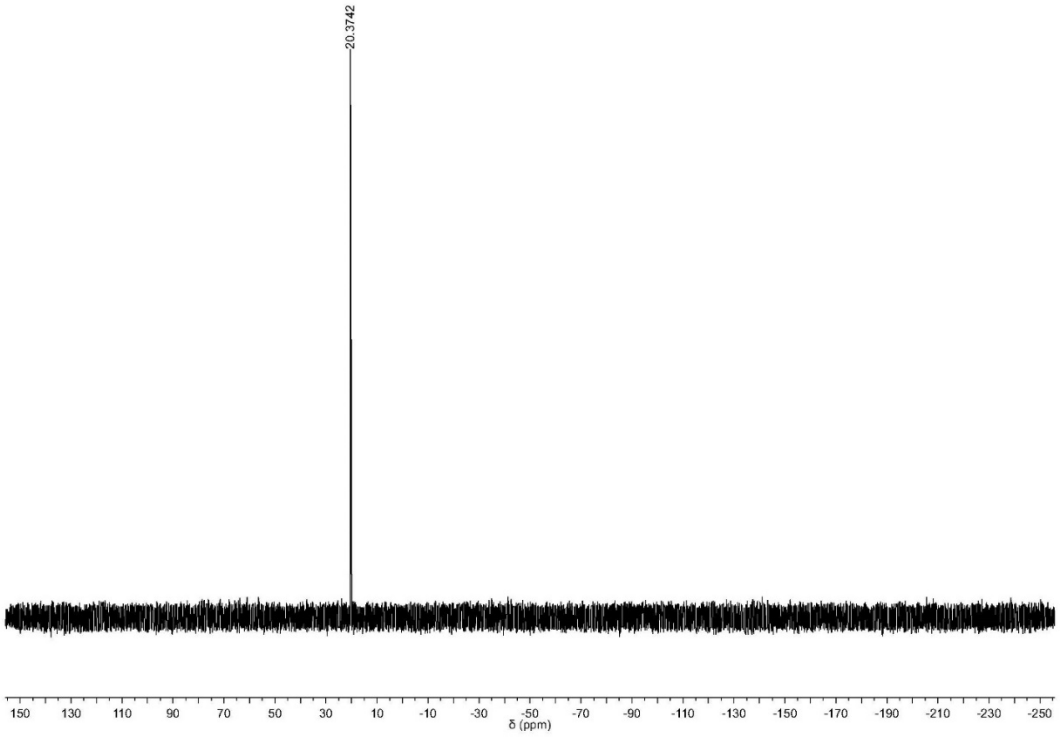

Spectrum S7. LC/MS traces m-bromosulfo-phosphine oxide rhodamine (cis), 8

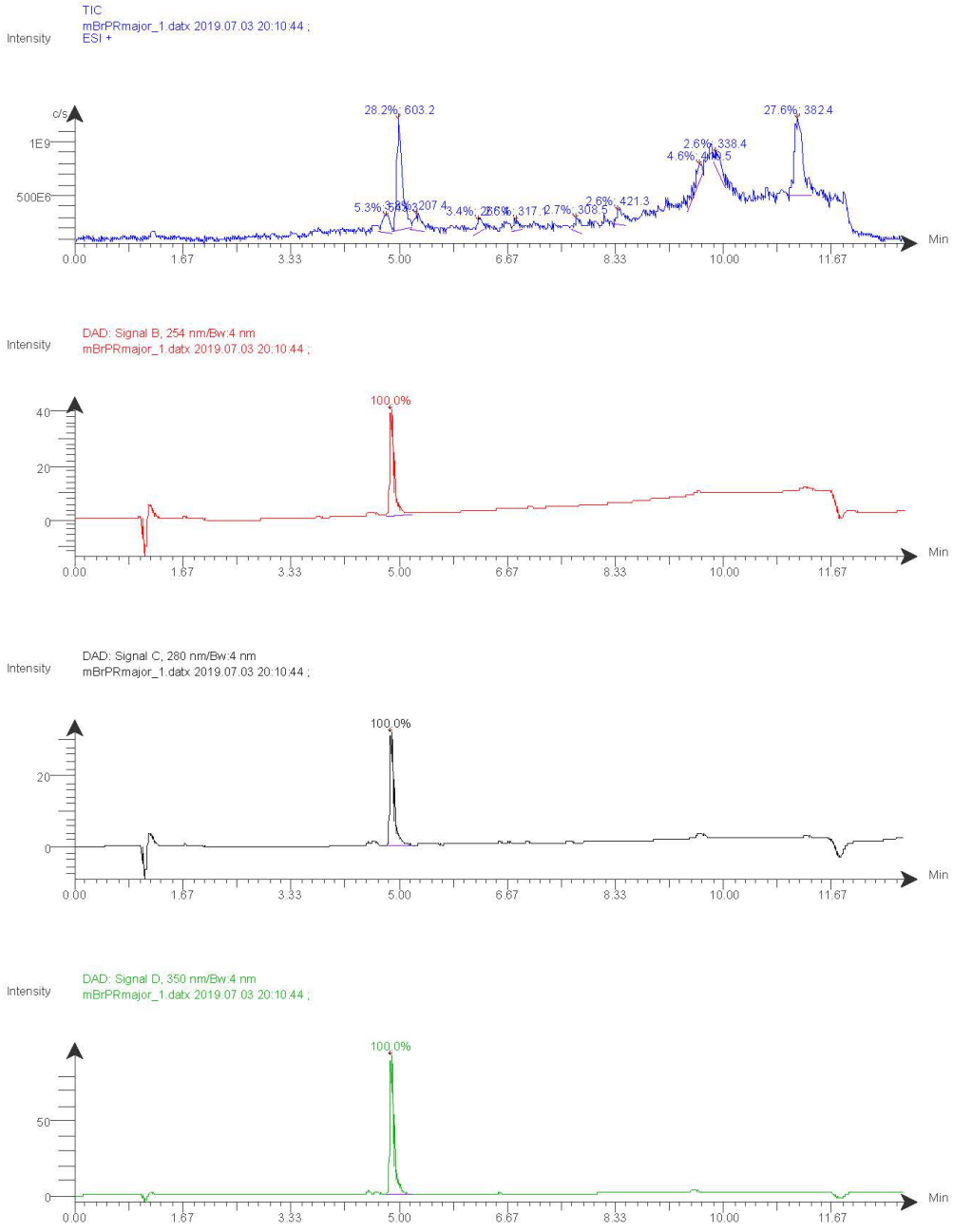

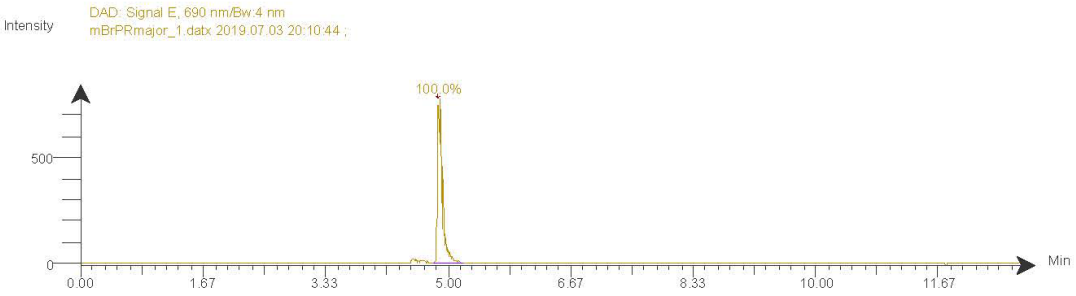
Intensity
DAD: Signal E, 690 nm/Bw:4 nm
mBrPRmajor_1.datx 2019.07.03 20:10:44 ;
100.0%
500
0
0.00
1.67
3.33
5.00
6.67
8.33
10.00
11.67
Min

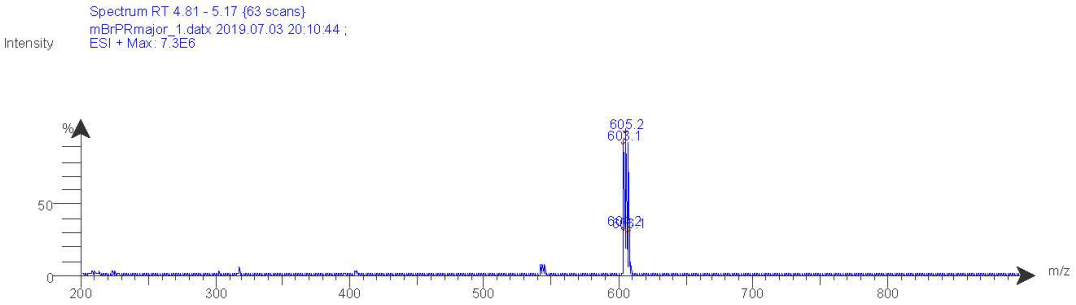
Intensity
Spectrum RT 4.81 - 5.17 {63 scans}
mBrPRmajor_1.datx 2019.07.03 20:10:44 ;
ESI + Max: 7.3E6
%
50
0
605.2
605.1
200
300
400
500
600
700
800
m/z

Spectrum S8. ^{1}H NMR m-bromosulfo-phosphine oxide rhodamine (trans), 8

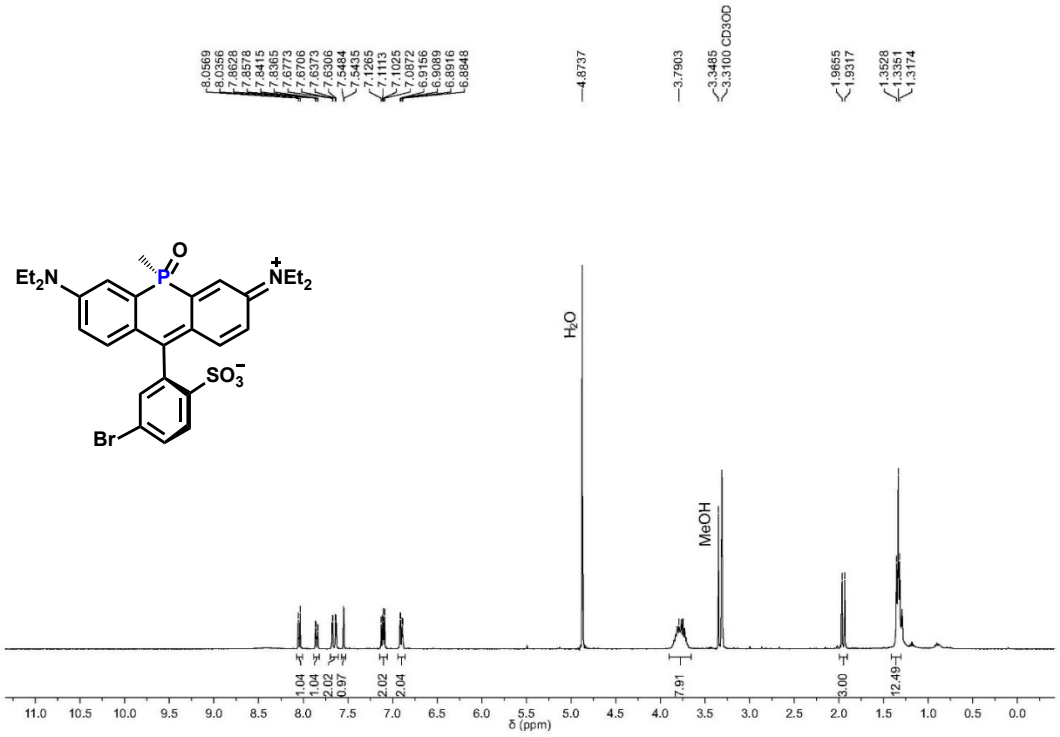

Spectrum S9. ^{31}P NMR m-bromosulfo-phosphine oxide rhodamine (trans), 8

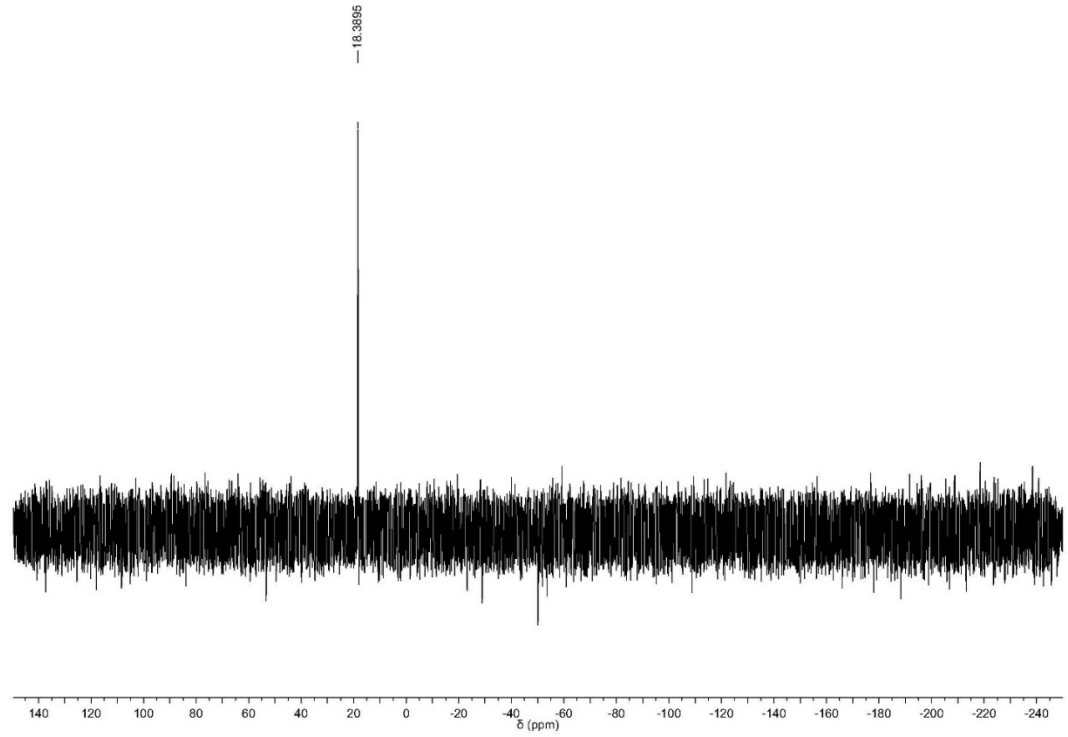

Spectrum S10. LC/MS traces m-bromosulfo-phosphine oxide rhodamine (trans), 8

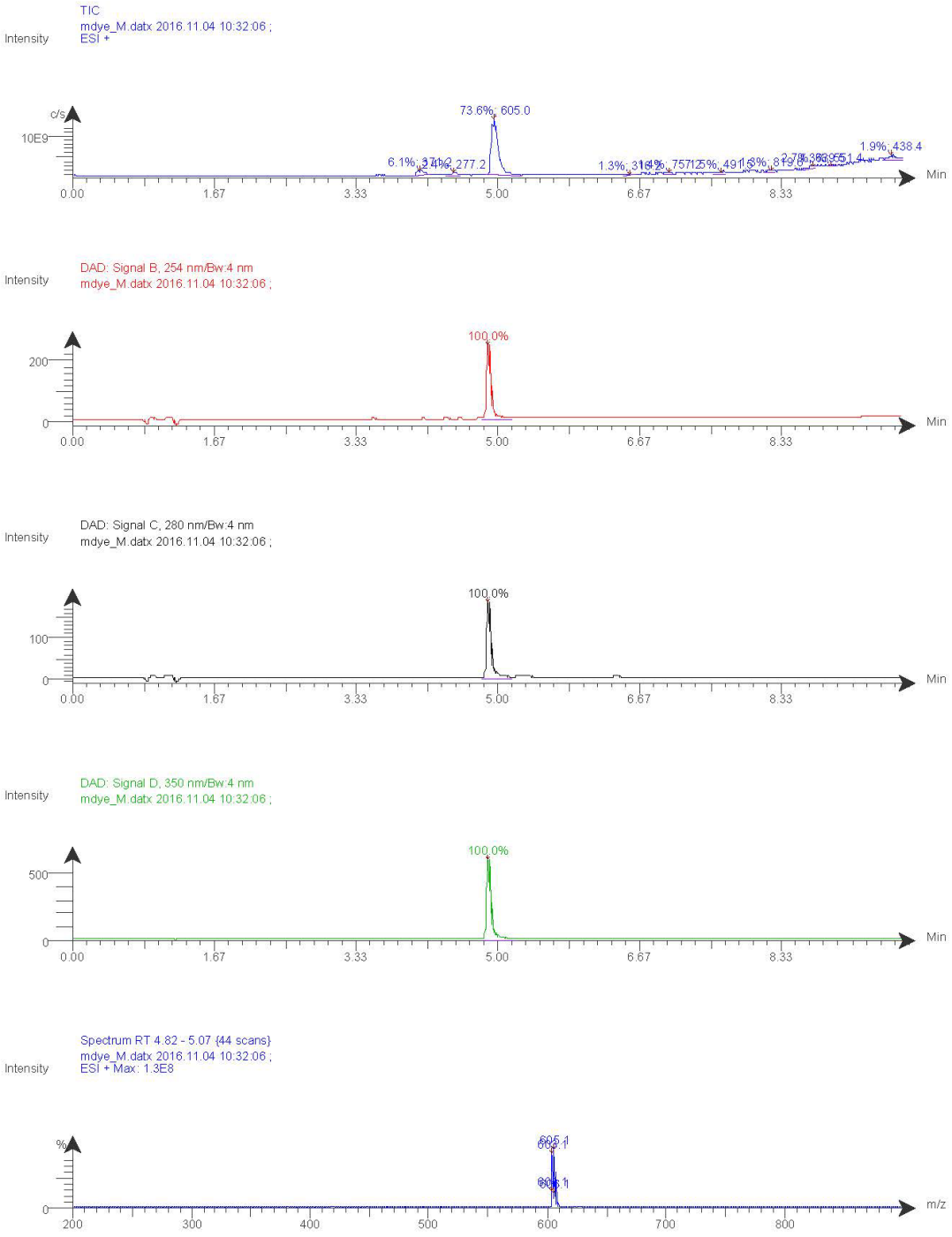

Spectrum S11. ^{1}H NMR p-bromosulfo-phosphine oxide rhodamine (cis), 9

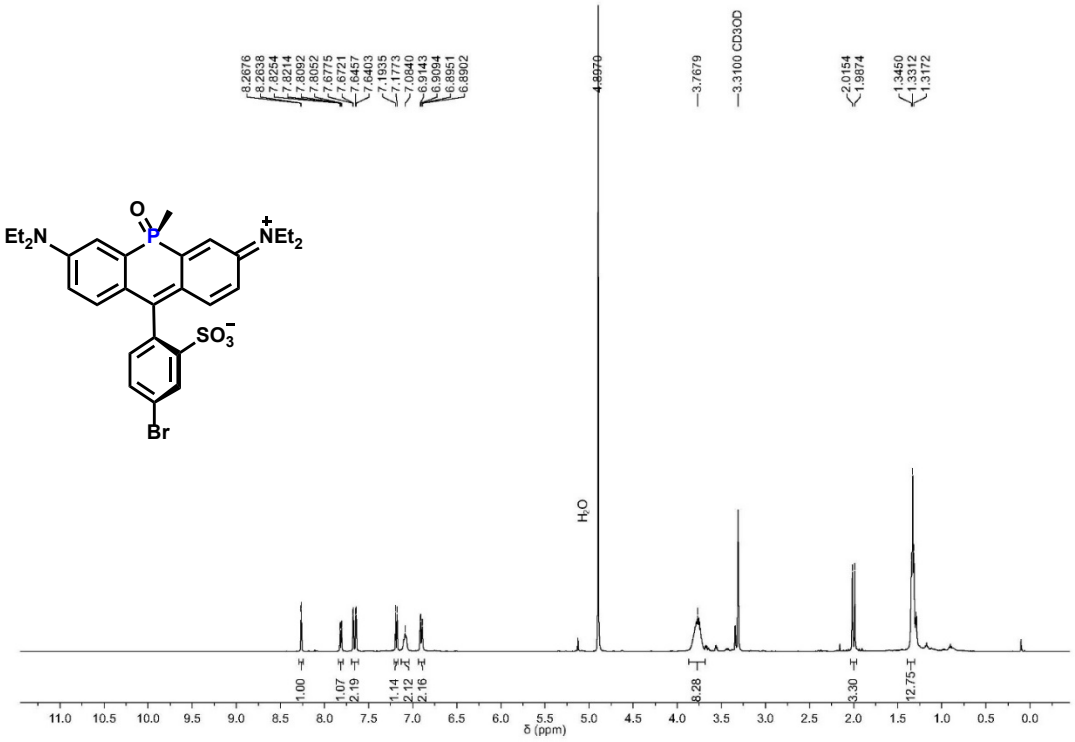

Spectrum S12. ^{31}P NMR p-bromosulfo-phosphine oxide rhodamine (cis), 9

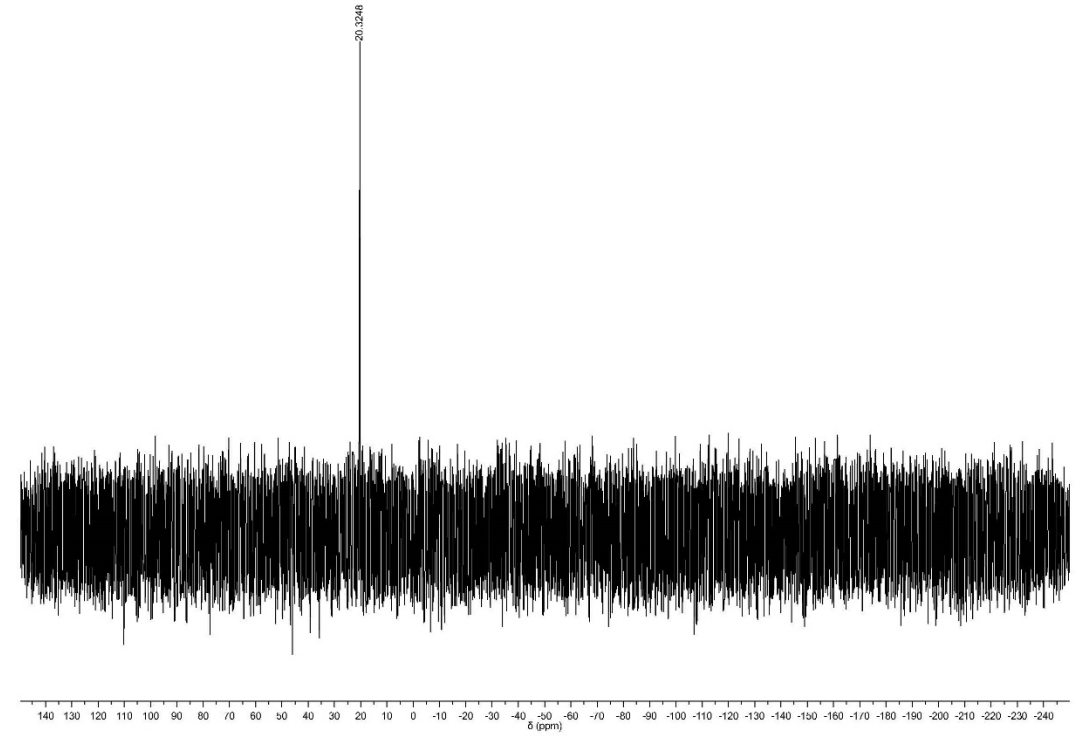

Spectrum S13. LC/MS traces p-bromosulfo-phosphine oxide rhodamine (cis), 9

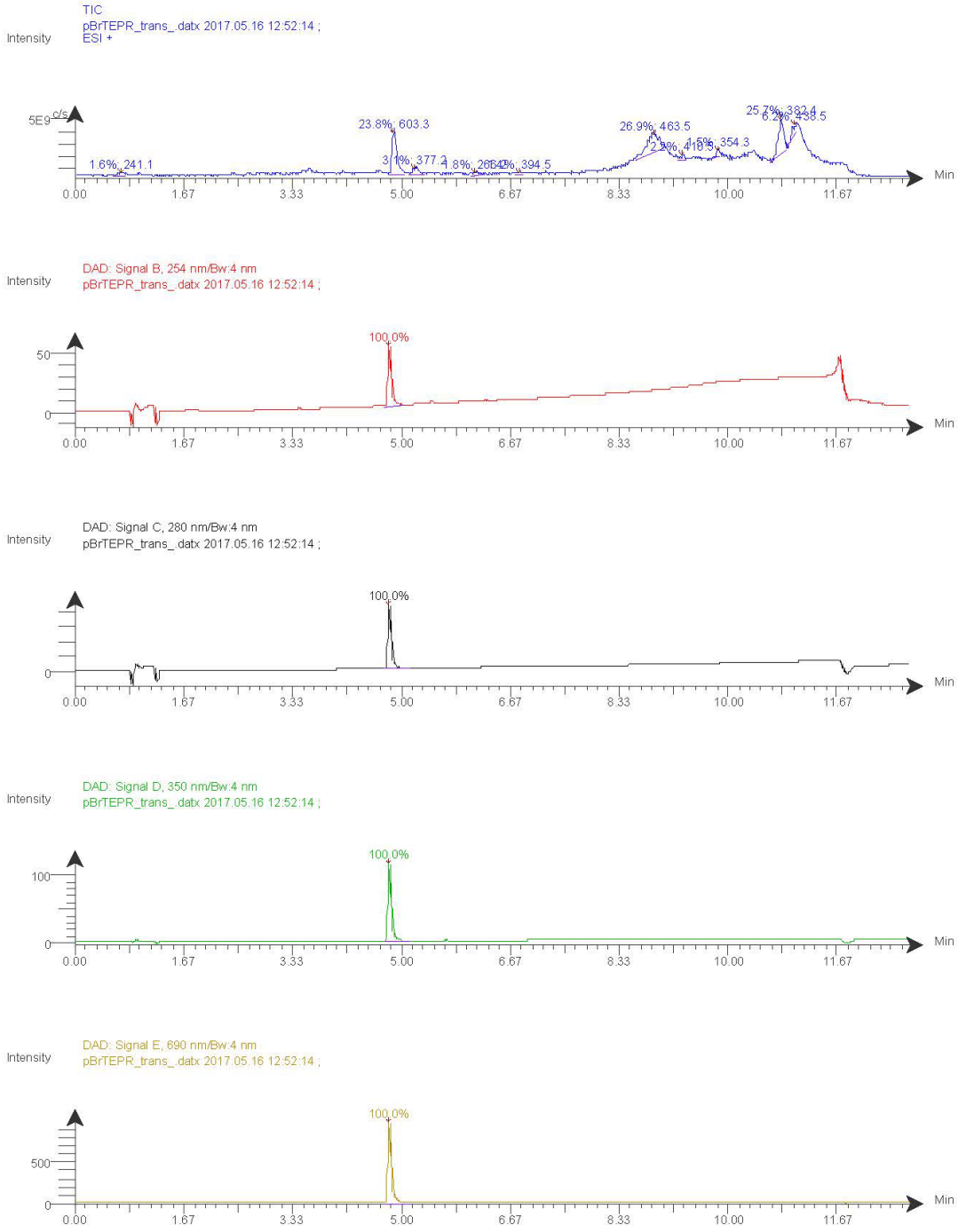

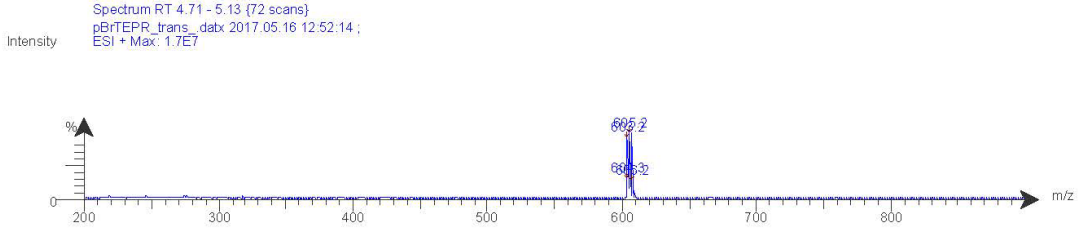
Spectrum RT 4.71 - 5.13 {72 scans}
pBrTEPR_trans_.datx 2017.05.16 12:52:14 ;
Intensity
ESI + Max: 1.7E7
%
0
605.2
606.2
200
300
400
500
600
700
800
m/z

Spectrum S14. ^{1}H NMR p-bromosulfo-phosphine oxide rhodamine (trans), 9

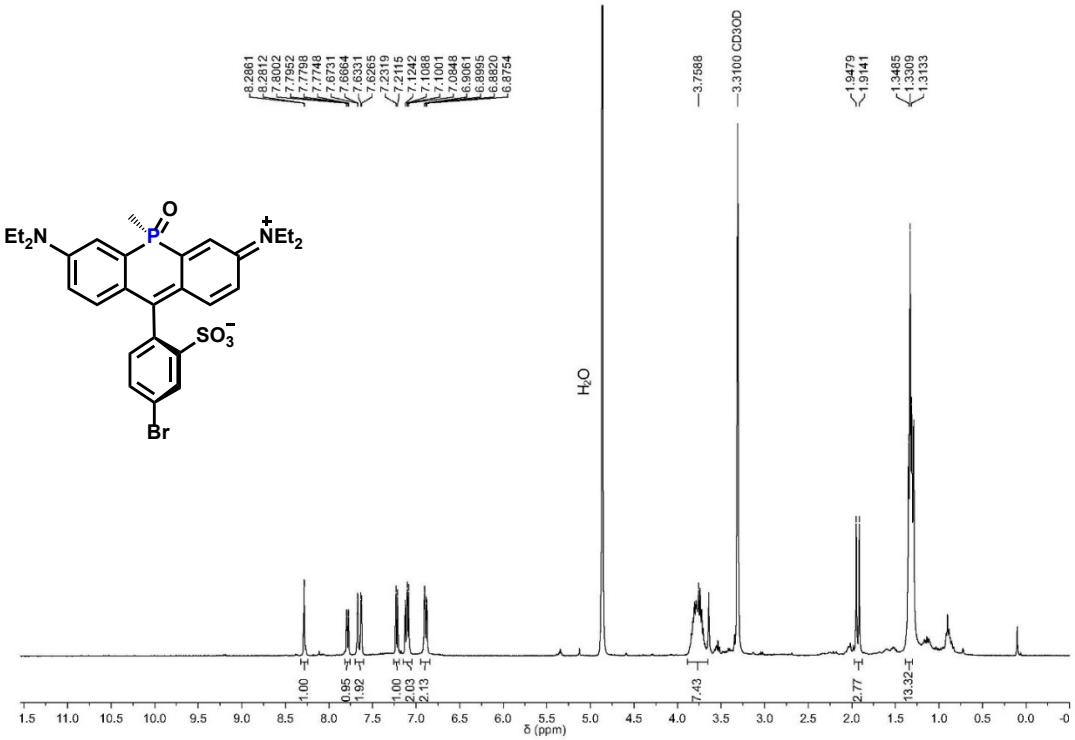

Spectrum S15. ^{31}P NMR p-bromosulfo-phosphine oxide rhodamine (trans), 9

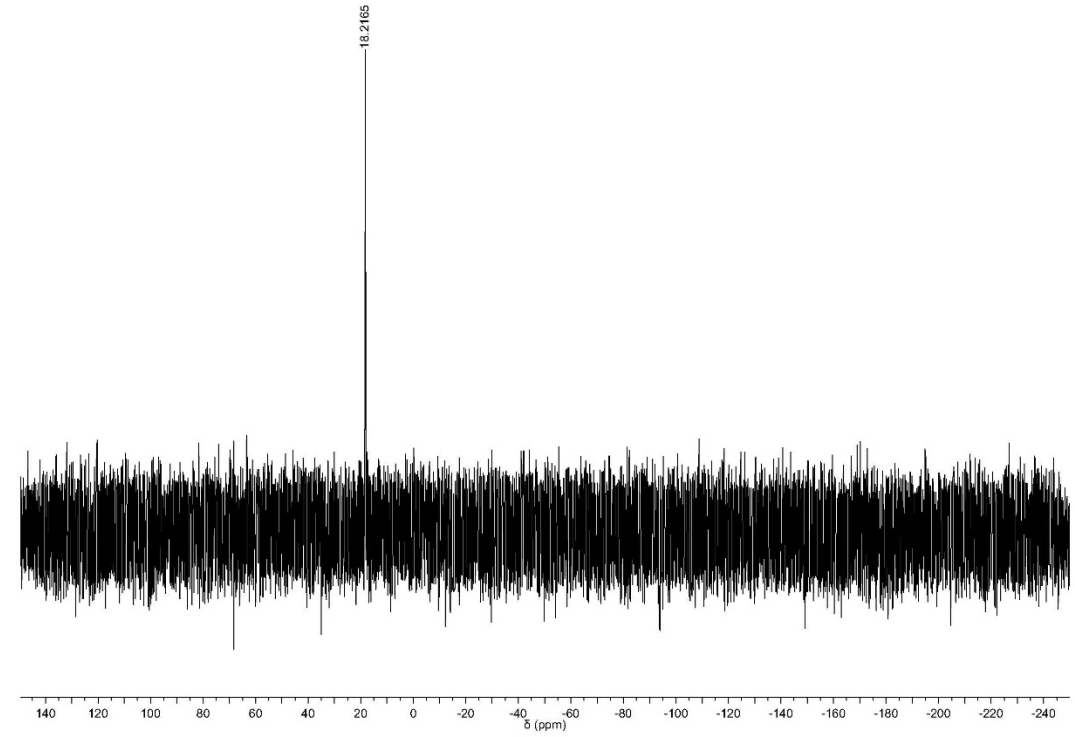

Spectrum S16. LC/MS traces p-bromosulfo-phosphine oxide rhodamine (trans), 9

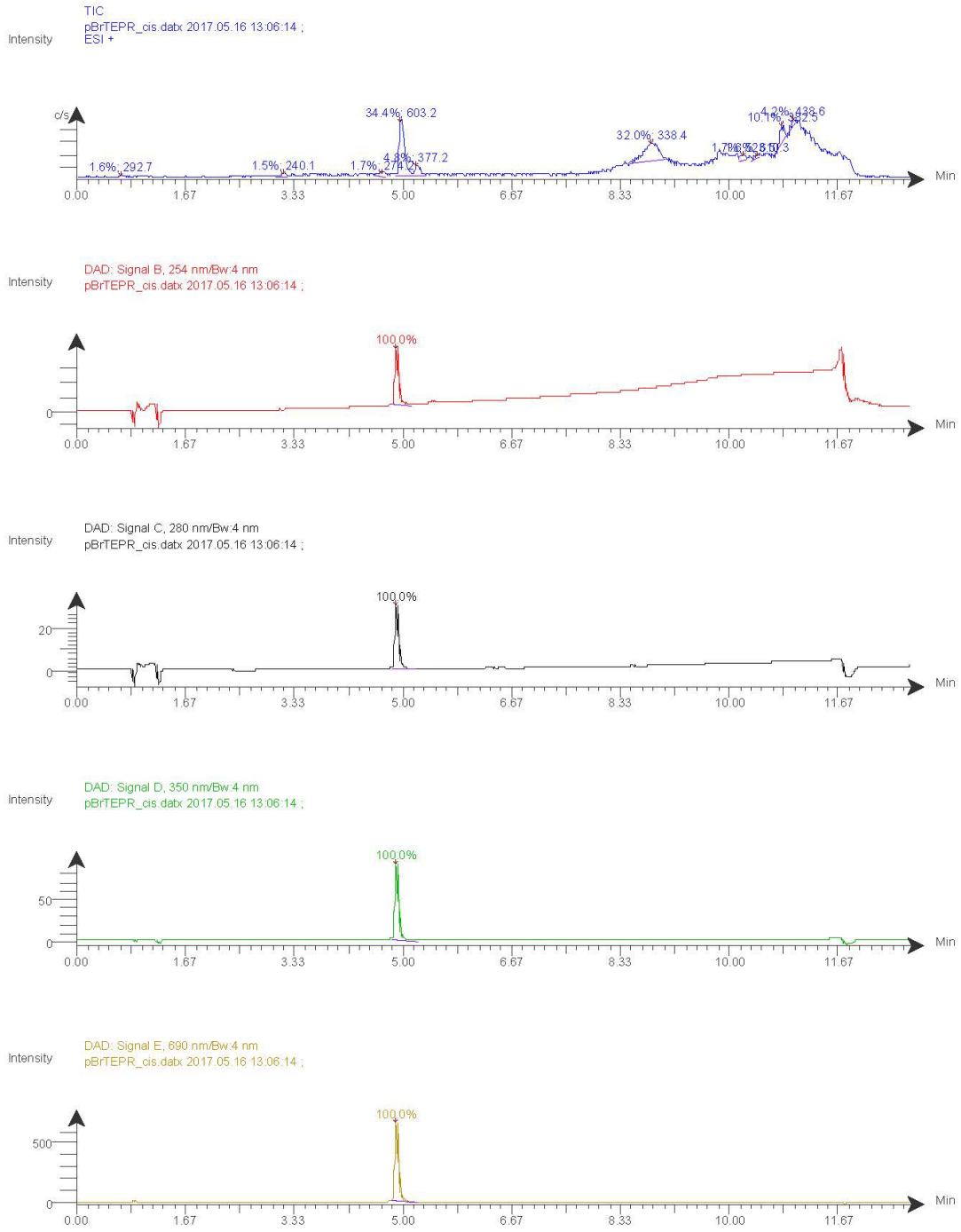

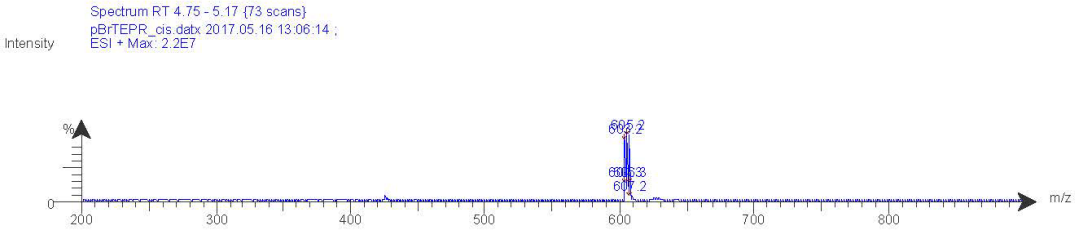
Spectrum RT 4.75 - 5.17 {73 scans}
pBrTEPR_cis.datx 2017.05.16 13:06:14 ;
Intensity
ESI + Max: 2.2E7
%
0
200
300
400
500
600
700
800
m/z

Spectrum S17. ^{1}H NMR poRhoVR (cis), 12

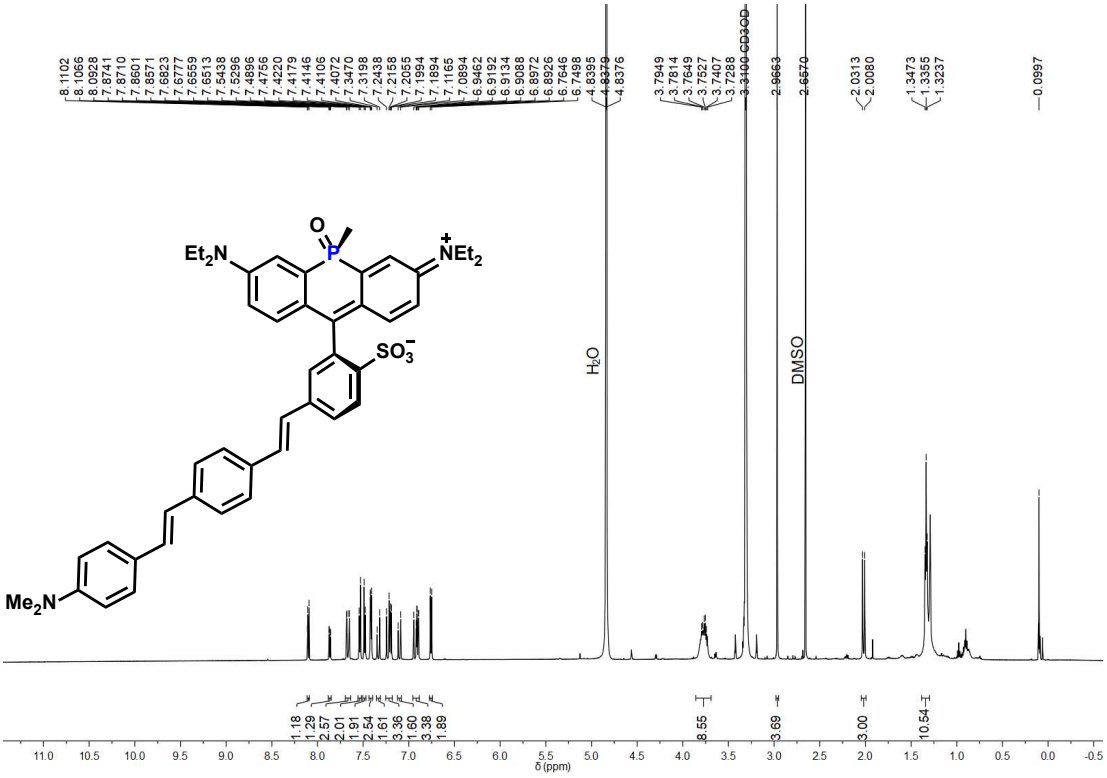

Spectrum S18. ^{31}P NMR poRhoVR (cis), 12

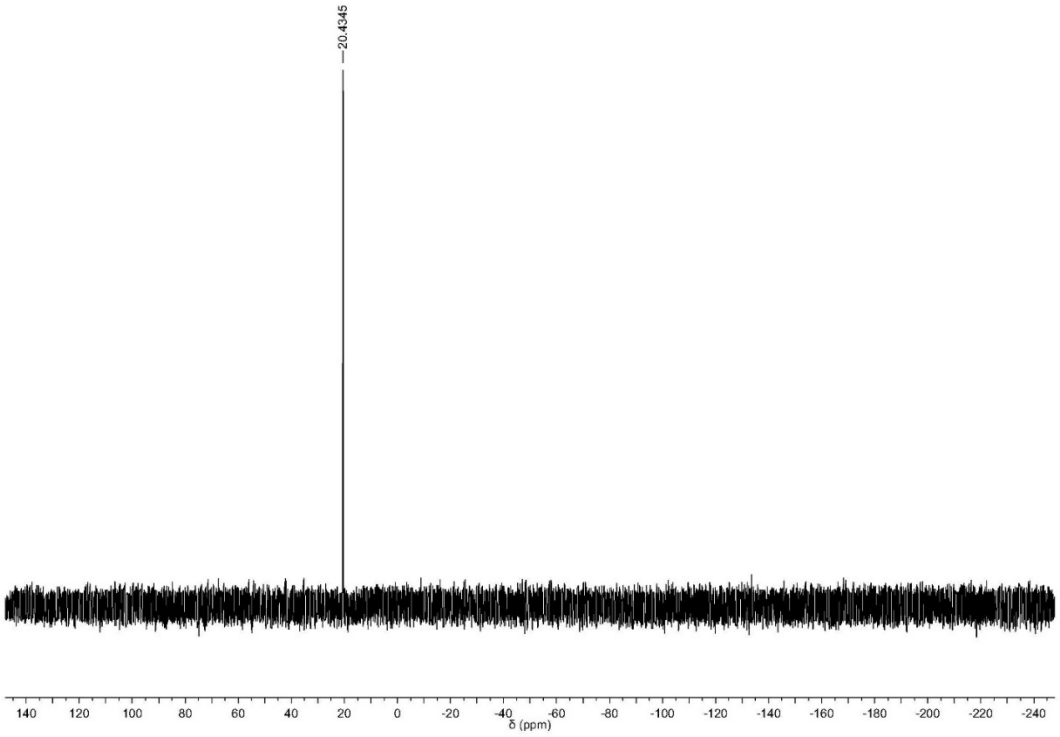

Spectrum S19. LC/MS traces poRhoVR (cis), 12

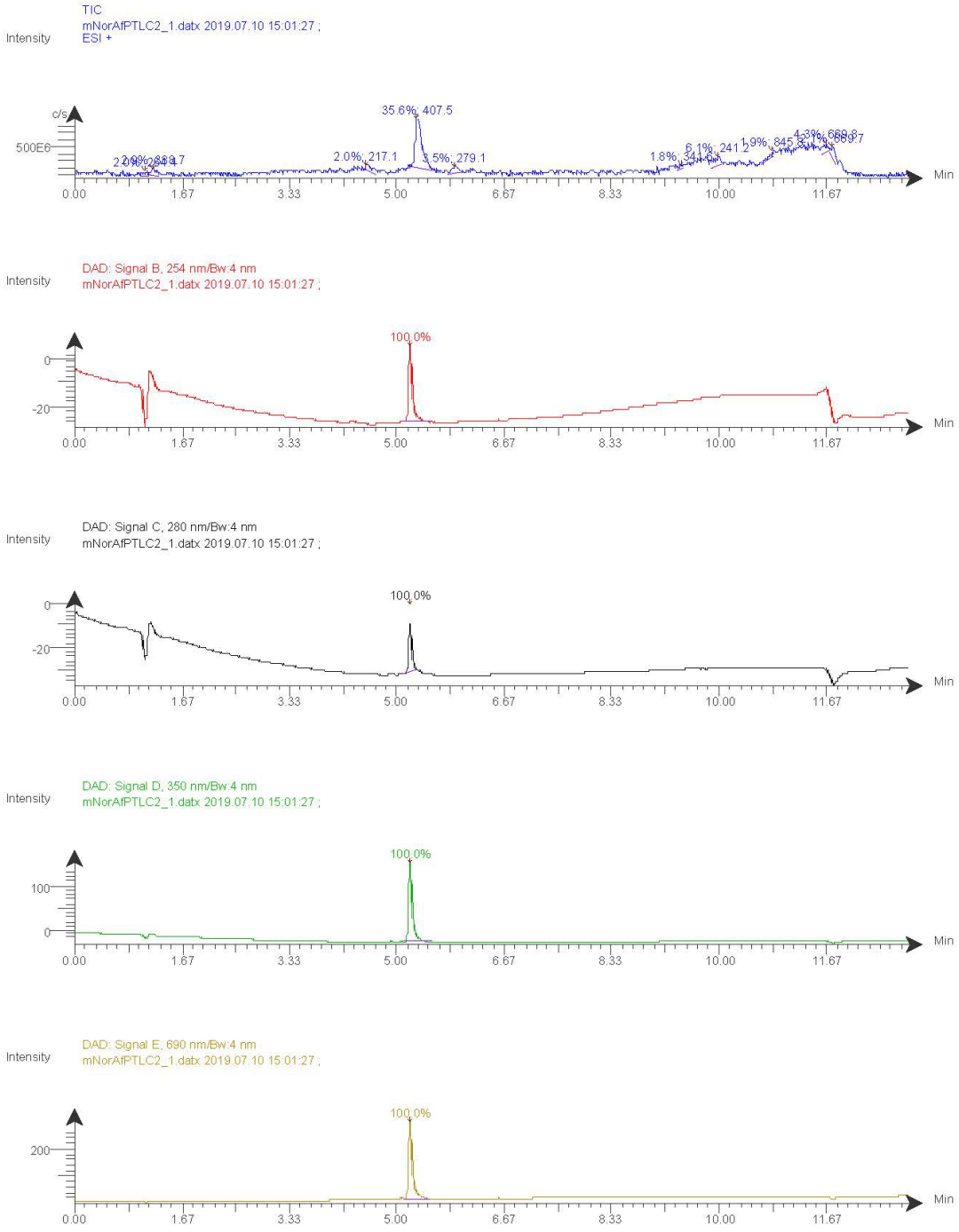

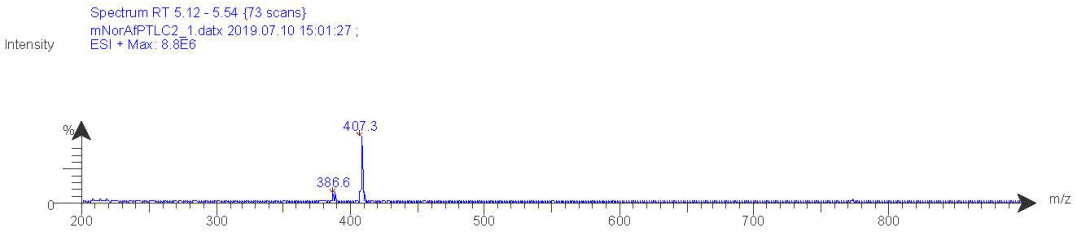
Spectrum RT 5.12 - 5.54 {73 scans}
mNorAfPTLC2_1.datx 2019.07.10 15:01:27 ;
ESI + Max: 8.8E6
Intensity
%
0
407.3
386.6
200
300
400
500
600
700
800
m/z

Spectrum S20. ^{1}H NMR poRhoVR (cis), 13

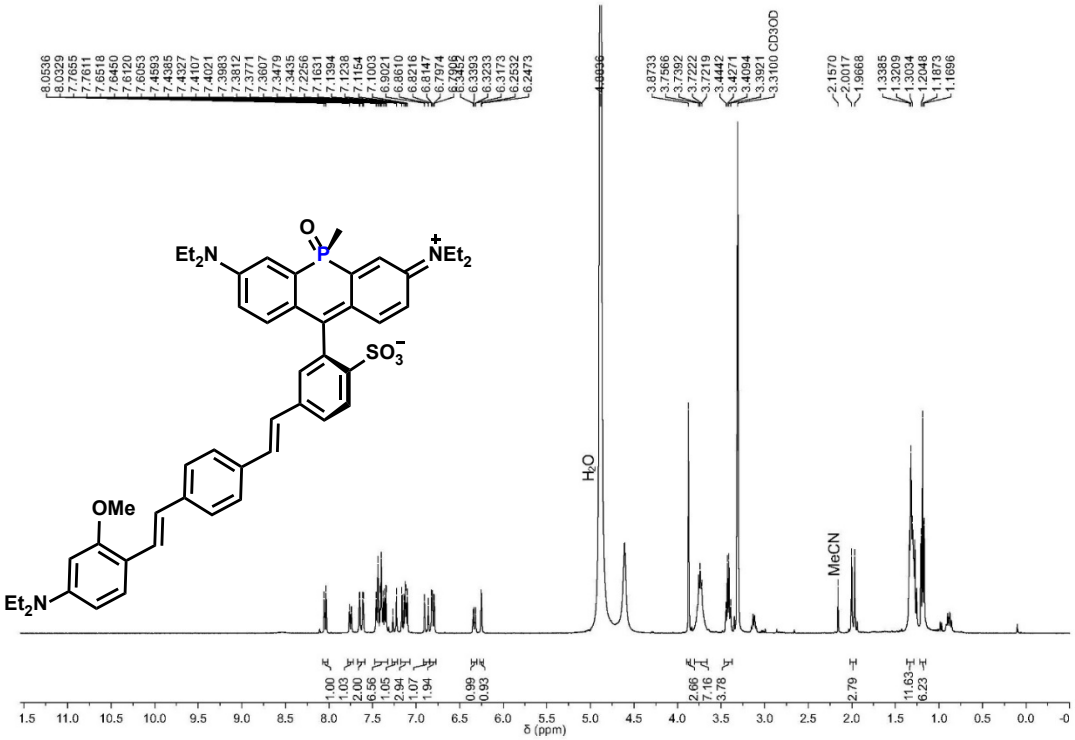

Spectrum S21. ^{31}P NMR poRhoVR (cis), 13

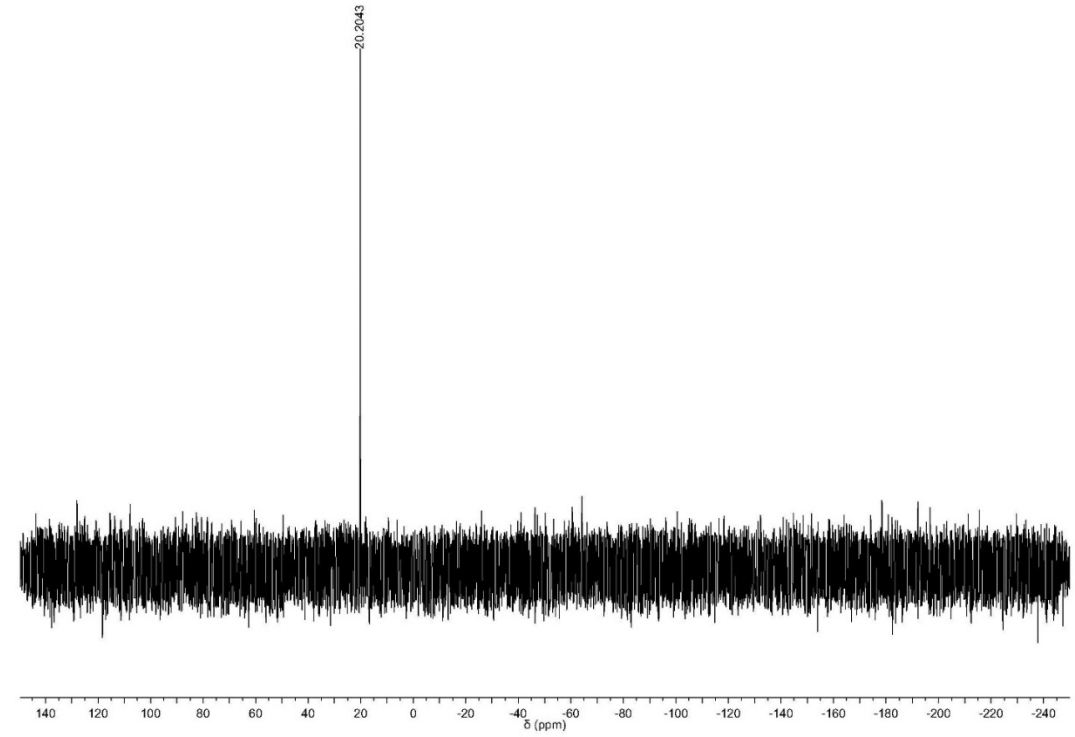

Spectrum S22. LC/MS traces poRhoVR (cis), 13

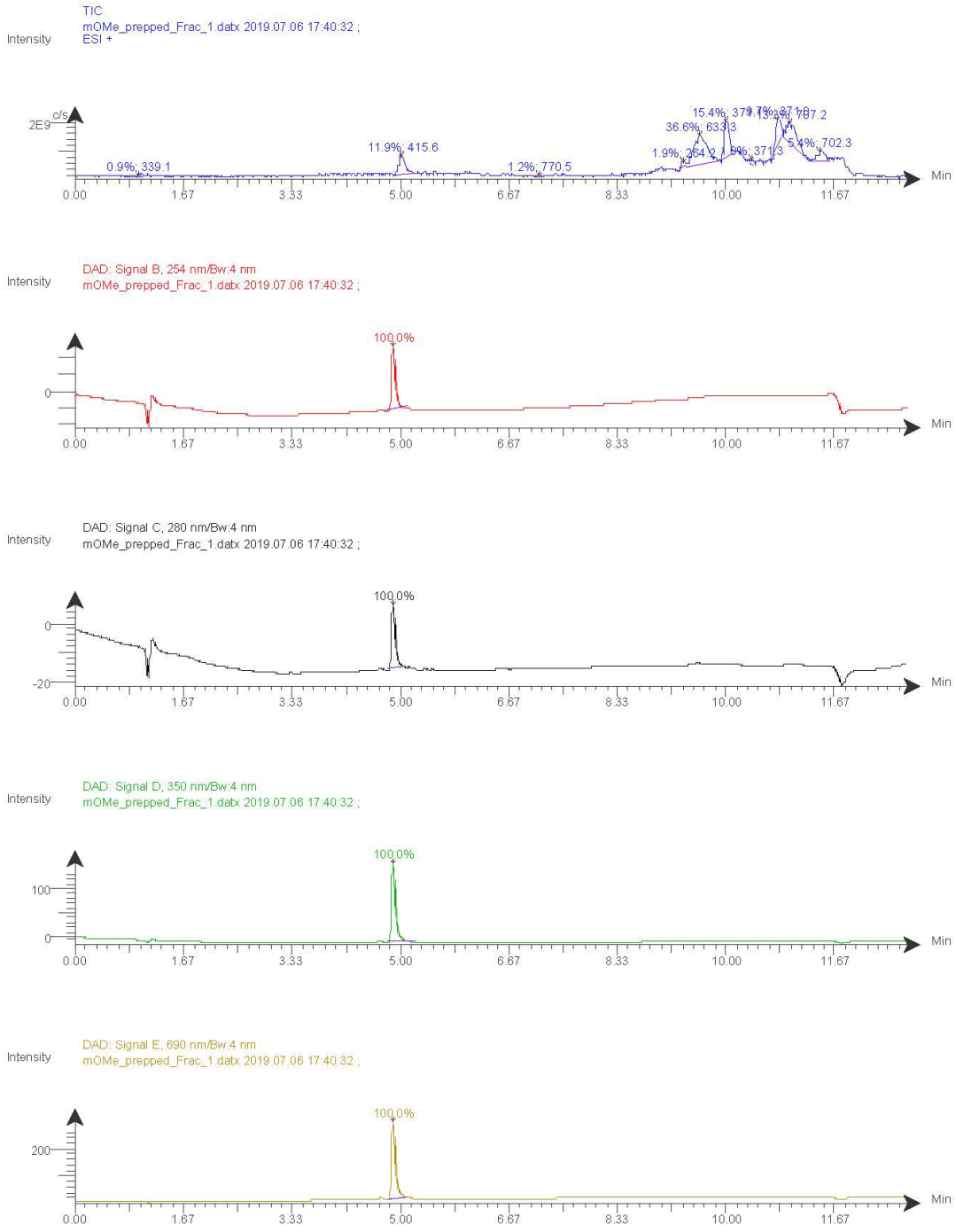

Intensity

Spectrum RT 4.82 - 5.16 {59 scans}
mOMe_prepped_Frac_1.datx 2019.07.06 17:40:32 ;
ESI + Max: 6.1E6

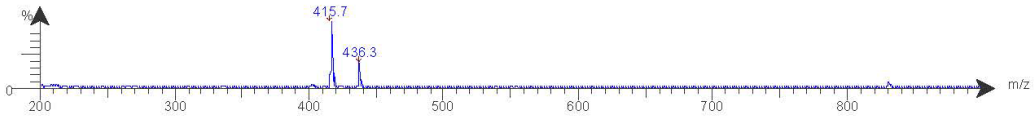

Spectrum S23. ^{1}H NMR poRhoVR (trans), 13

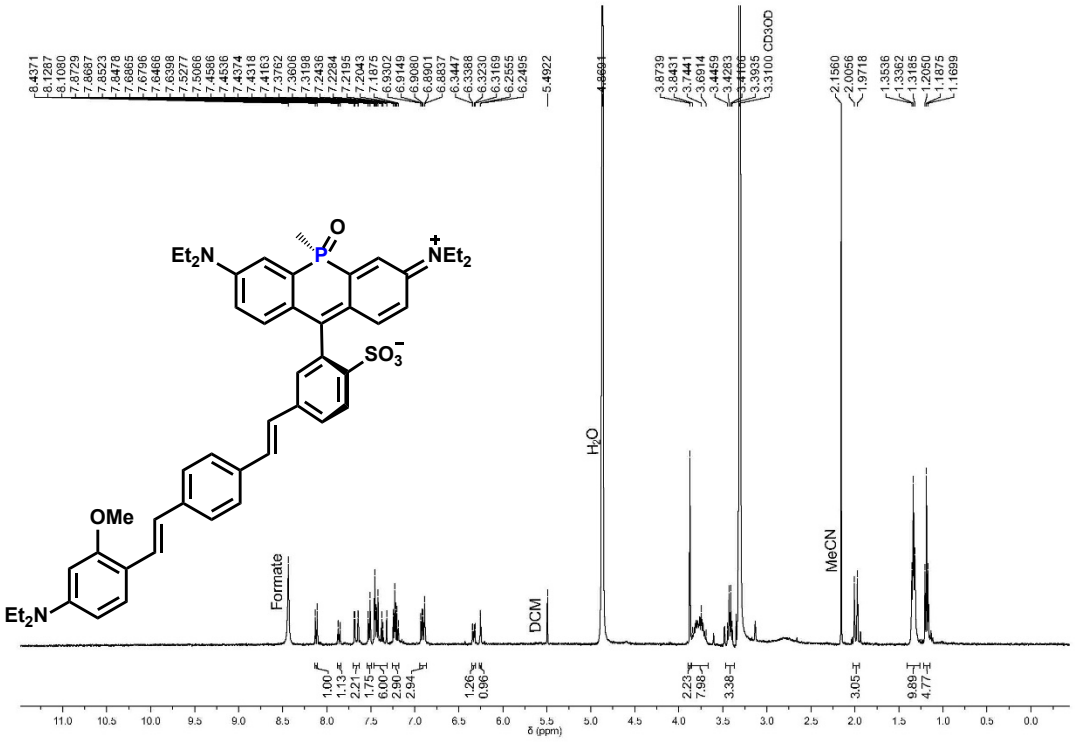

Spectrum S24. ^{31}P NMR poRhoVR (trans), 13

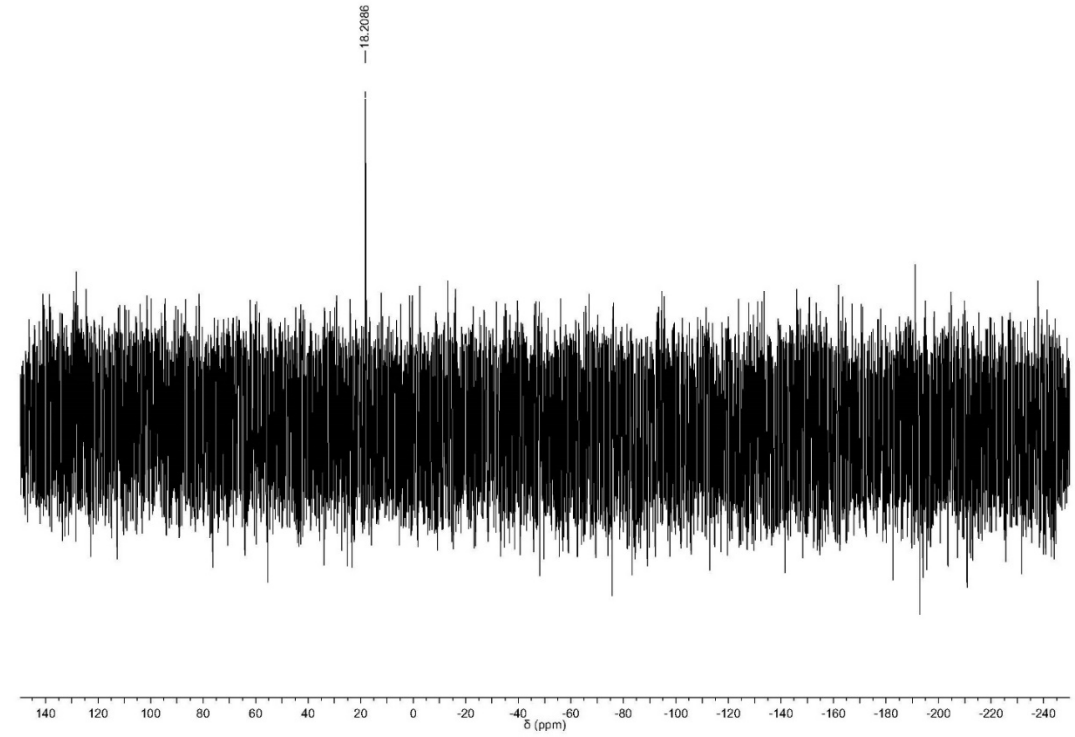

Spectrum S25. LC/MS traces poRhoVR (trans), 13

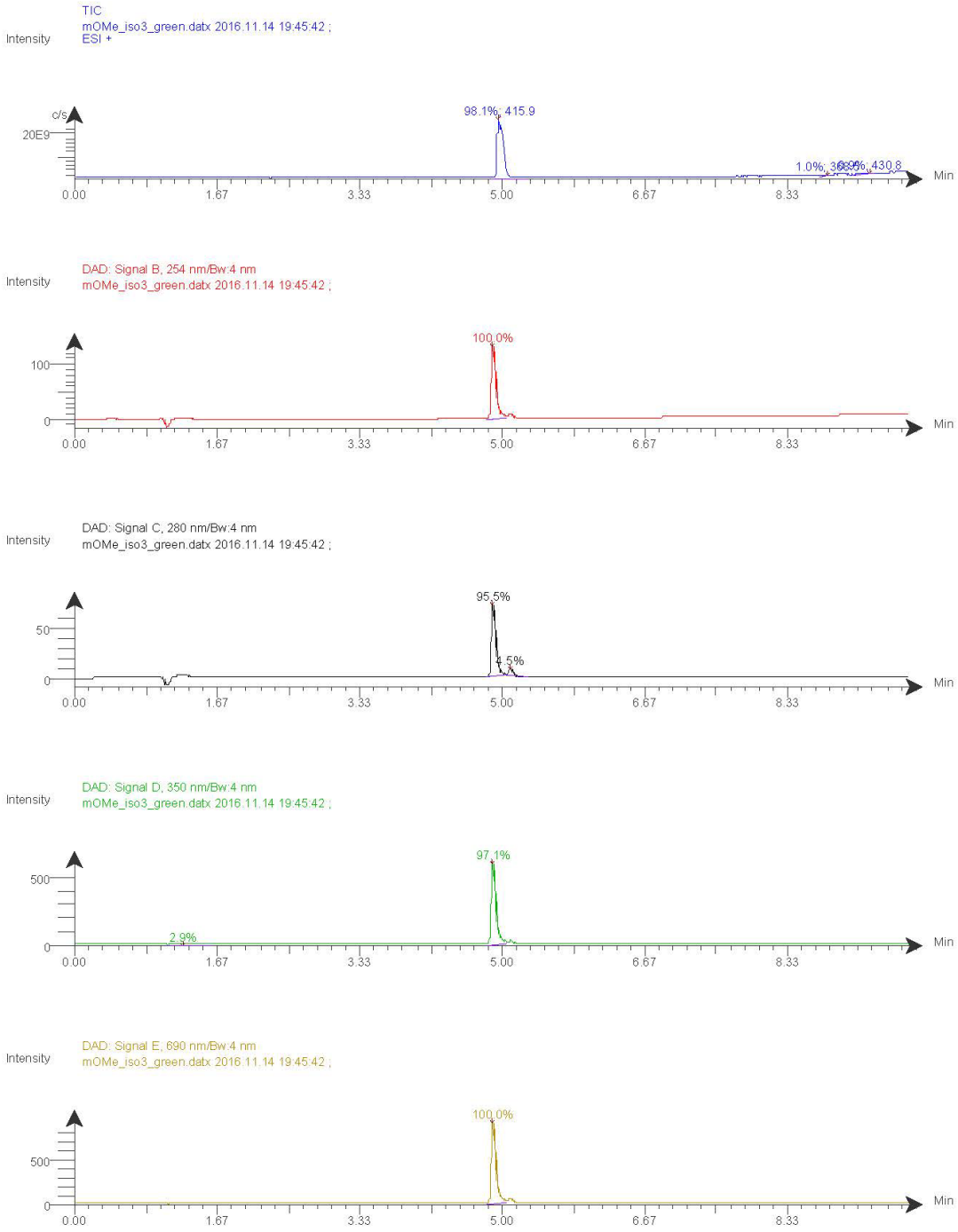

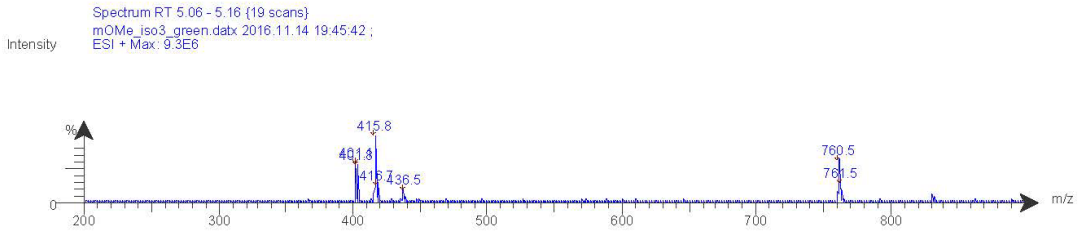
Spectrum RT 5.06 - 5.16 {19 scans}
mOMe_iso3_green.datx 2016.11.14 19:45:42 ;
ESI + Max: 9.3E6
Intensity
%
0
415.8
401.8
416.7
436.5
760.5
761.5
200
300
400
500
600
700
800
m/z

Spectrum S26. ^{1}H NMR poRhoVR (cis), 14

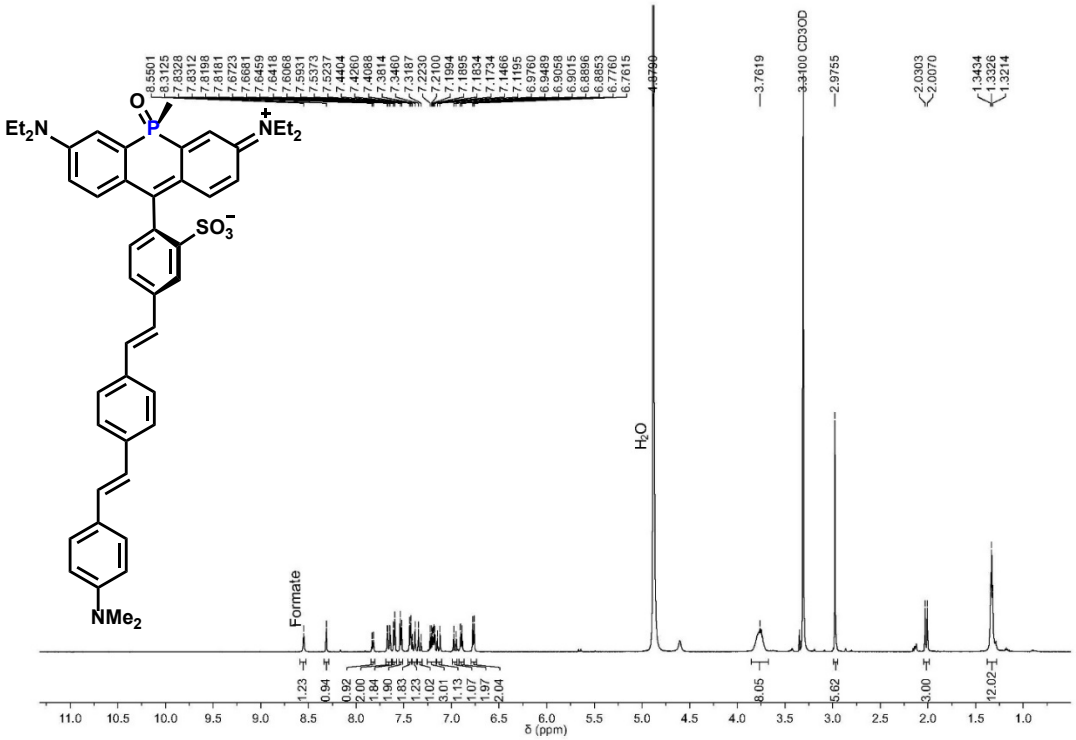

Spectrum S27. ^{31}P NMR poRhoVR (cis), 14

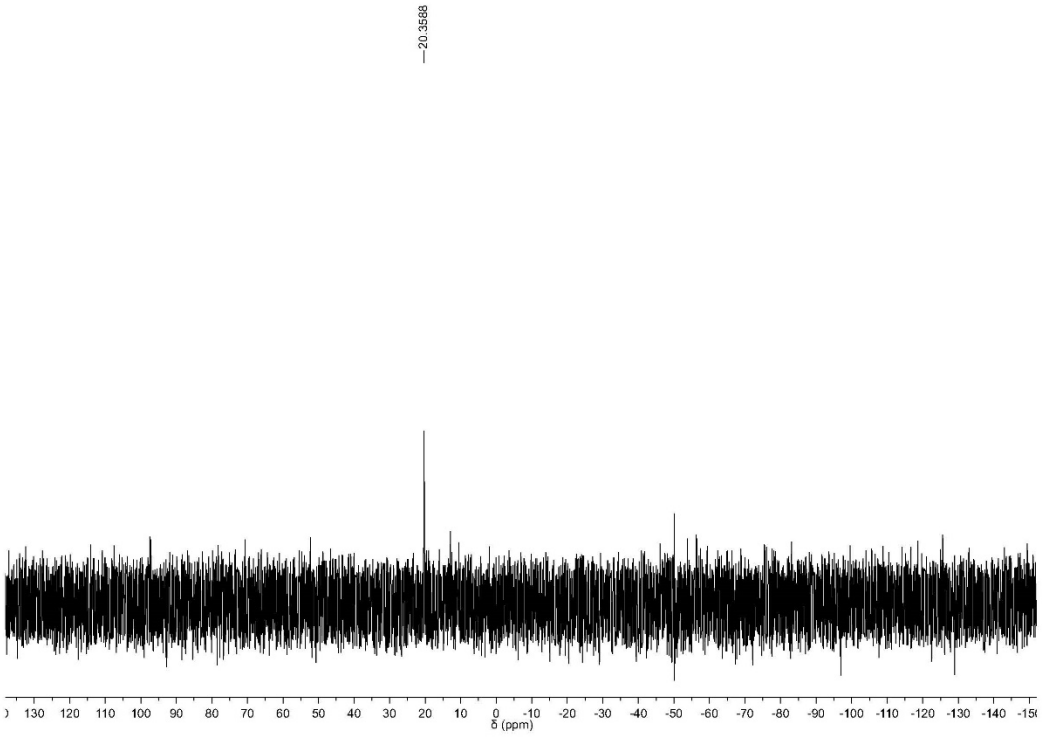

Spectrum S28. LC/MS traces poRhoVR (cis), 14

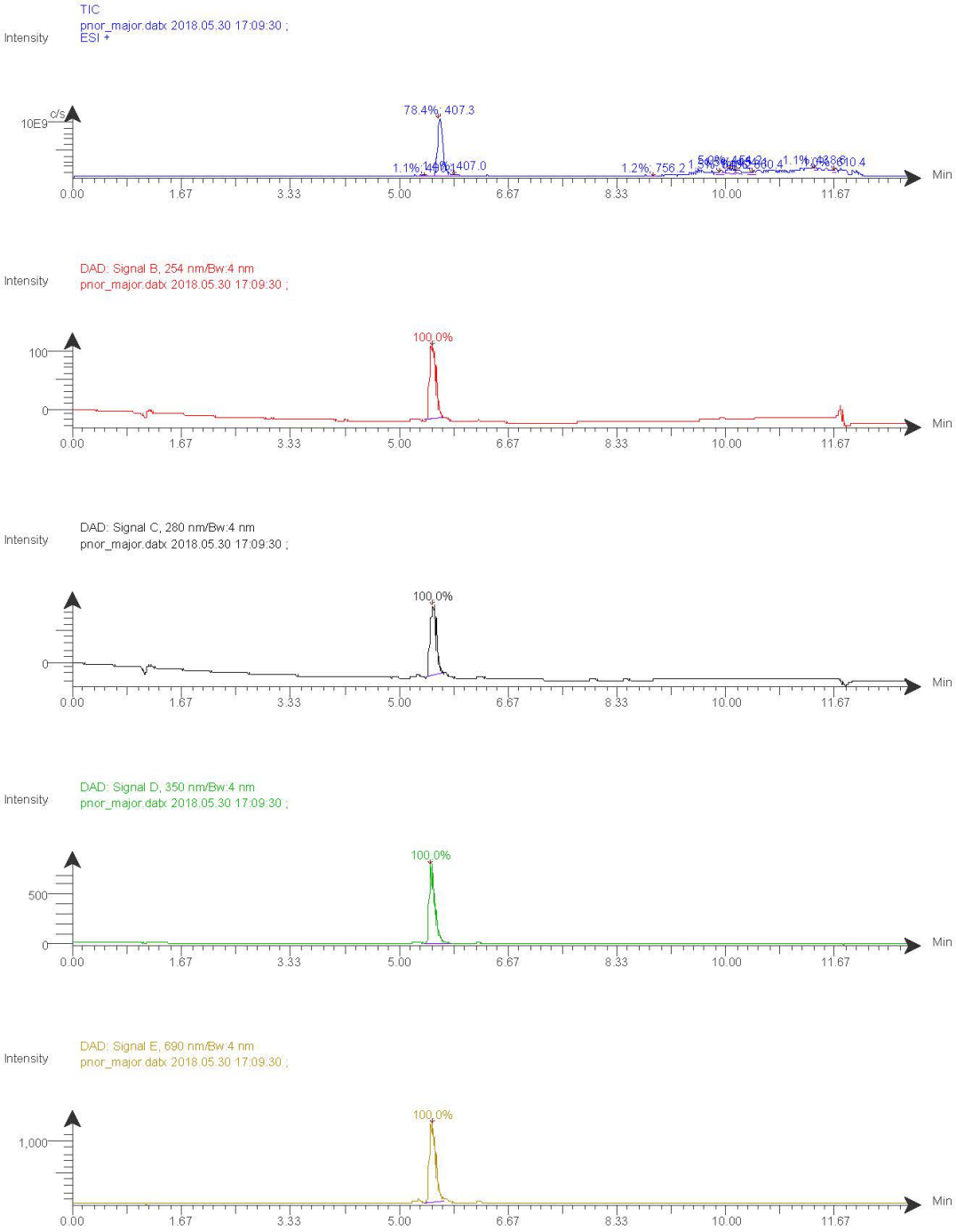

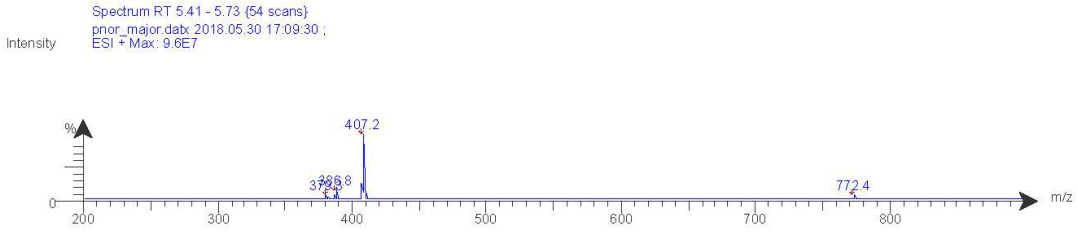
Spectrum RT 5.41 - 5.73 {54 scans}
pnor_major.datx 2018.05.30 17:09:30 ;
ESI + Max: 9.6E7
Intensity
%
0
407.2
388.8
772.4
200
300
400
500
600
700
800
m/z

Spectrum S29. ^{1}H NMR poRhoVR (cis),15

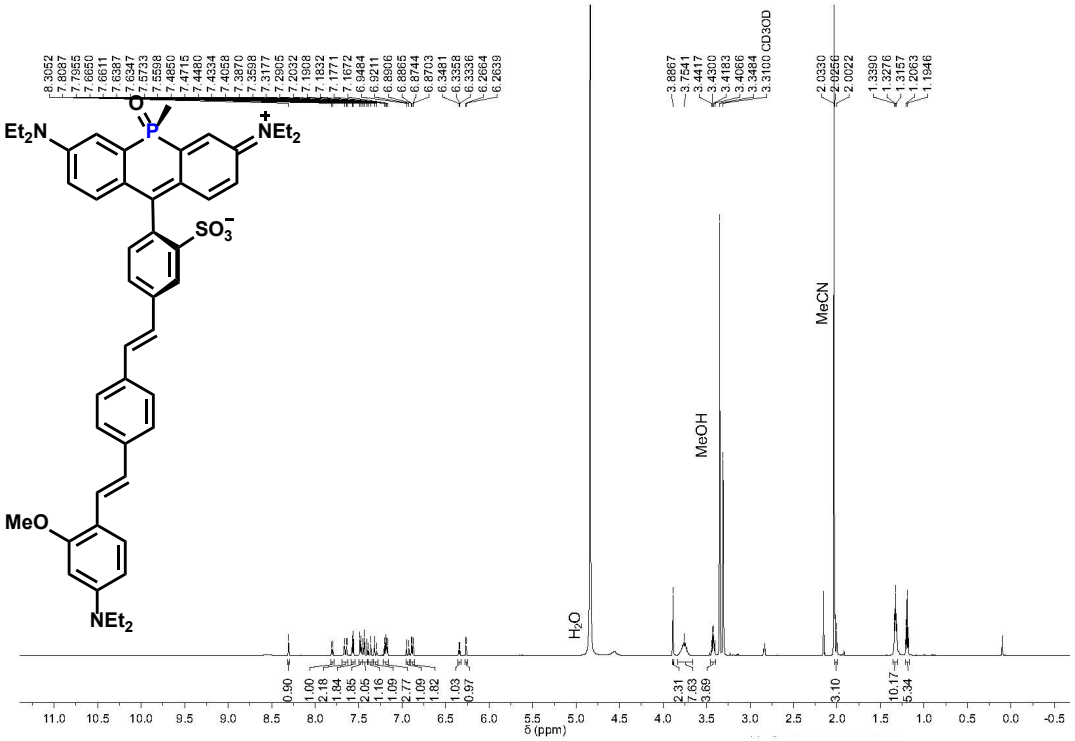

Spectrum S30. ^{31}P NMR poRhoVR (cis),15

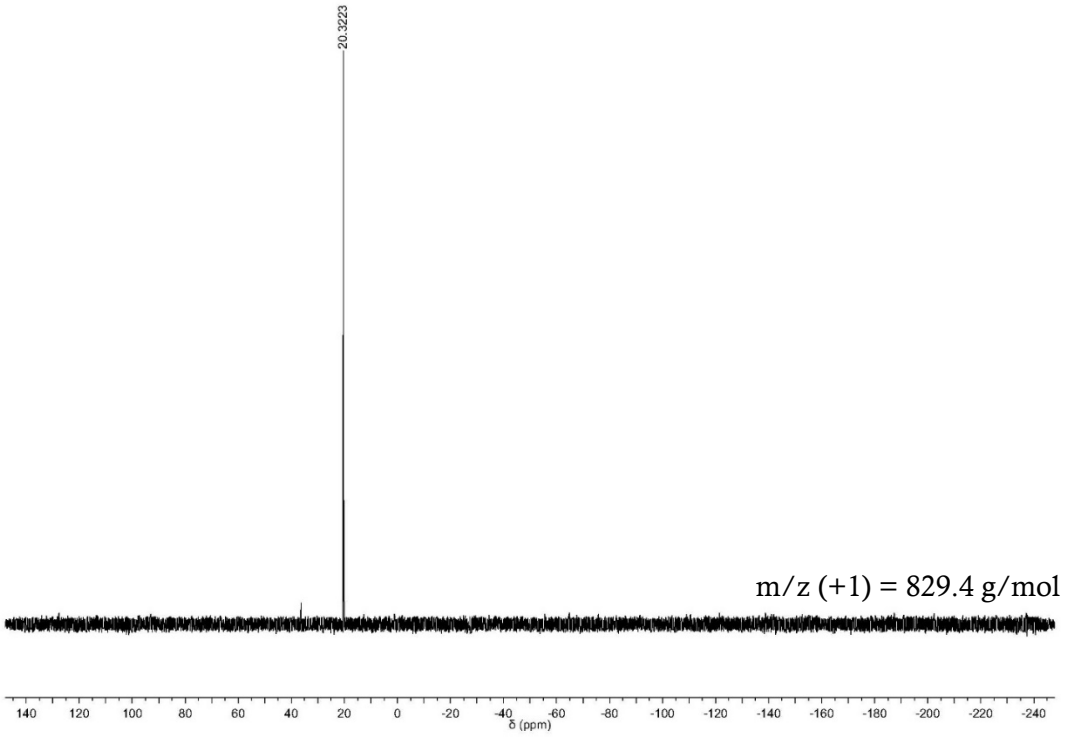

Spectrum S31. LC/MS traces poRhoVR (cis),15

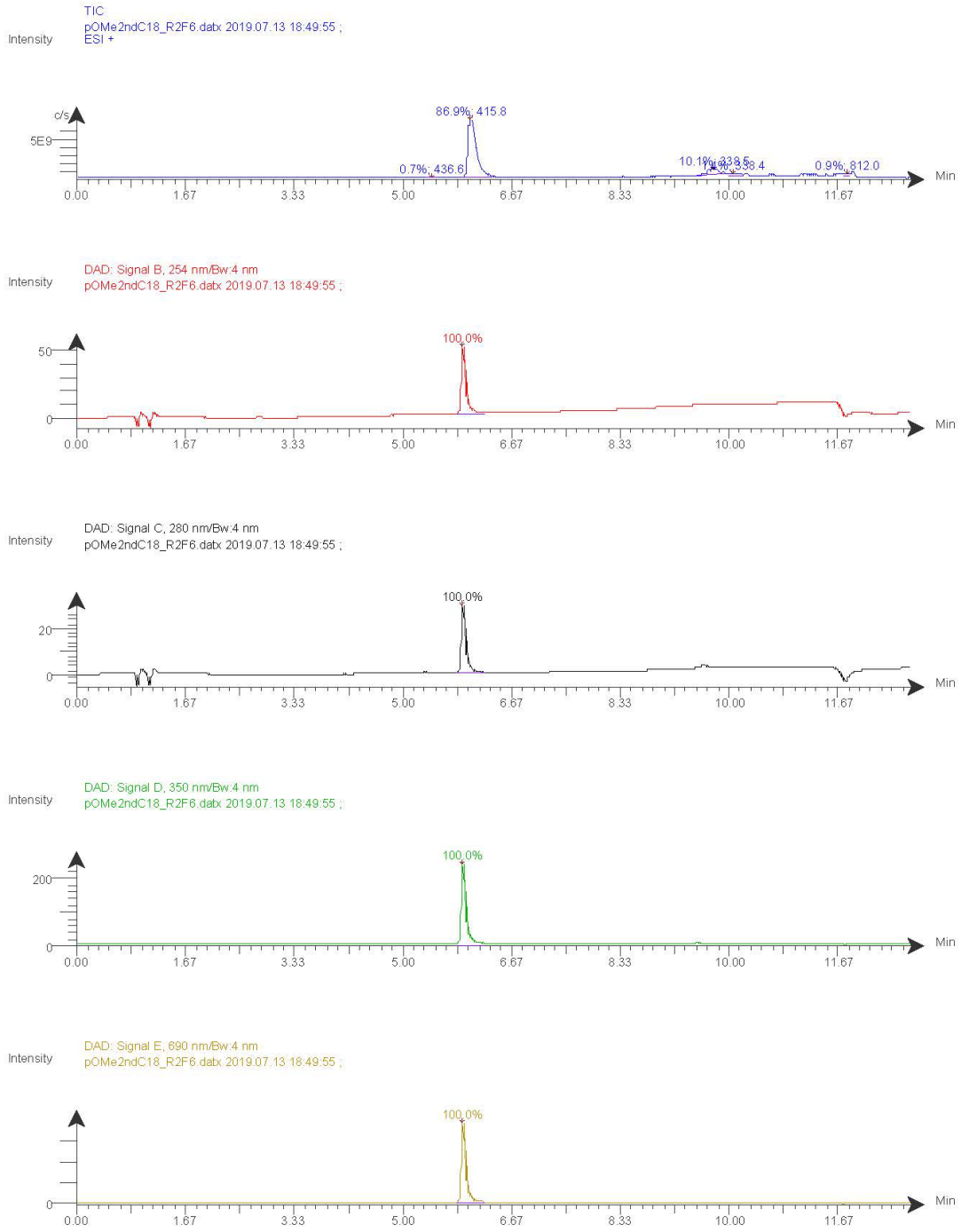

Spectrum RT 6.07 {1 scans}
pOMe2ndC18_R2F6.datx 2019.07.13 18:49:55 ;
Intensity ESI + Max: 1.8E8

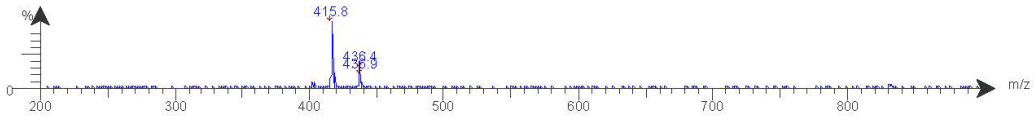

2.5 References

1) Chai, X.; Cui, X.; Wang, B.; Yang, F.; Cai, Y.; Wu, Q.; Wang, T., Near-Infrared Phosphorus-Substituted Rhodamine with Emission Wavelength above 700 nm for Bioimaging. *Chemistry – A European Journal* **2015,** *21* (47), 16754-16758.

2) Fery-Forgues, S.; Lavabre, D., Are Fluorescence Quantum Yields So Tricky to Measure? A Demonstration Using Familiar Stationery Products. *J Chem Educ* **1999**, *76*, 1260-1264

3) Grzybowski, M.; Taki, M.; Senda, K.; Sato, Y.; Ariyoshi, T.; Okada, Y.; Kawakami, R.; Imamura, T.; Yamaguchi, S., A Highly Photostable Near-Infrared Labeling Agent Based on a Phospha-rhodamine for Long-Term and Deep Imaging. *Angewandte Chemie International Edition* **2018,** *57* (32), 10137-10141.

4) Kulkarni, R. U.; Vandenberghe, M.; Thunemann, M.; James, F.; Andreassen, O. A.; Djurovic, S.; Devor, A.; Miller, E. W., In Vivo Two-Photon Voltage Imaging with Sulfonated Rhodamine Dyes. *ACS Cent Sci* **2018,** *4* (10), 1371-1378.

5) Miller, E. W., Lin, J. Y., Frady, E. P., Steinbach, P. A., Kristan, W. B., & Tsien, R. Y. Optically monitoring voltage in neurons by photoinduced electron transfer through molecular wires. *Proceedings of the National Academy of Sciences of the United States of America* **2012**, *109*(6), 2114–2119. https://doi.org/10.1073/pnas.1120694109
6) Smith, A. M., Mancini, M. C., & Nie, S. Bioimaging: Second window for in vivo imaging. *Nature Nanotechnology* **2009**, *4*(11), 710–711. https://doi.org/10.1038/nnano.2009.326.

7) Tan, B.; Tchatchoua, C. N.; Dong, L.; McGrath, J. E., Synthesis and characterization of arylene ether imide reactive oligomers and polymers containing diaryl alkyl phosphine oxide groups. *Polym Advan Technol* **1998,** *9* (1), 84-93.

Chapter 3

Cellular Characterization of poRhoVRs

Portions of this work appeared as a preprint:

Gonzalez, M. A.; Walker, A. S.; Cao, K. J.; Lazzari-Dean, J. R.; Settineri, N.; Kong, E.-J.; Kramer, R. H.; Miller, E. W.; Voltage imaging with a NIR-absorbing phosphine oxide rhodamine voltage reporter. *ChemRxiv.* **2019**, Preprint: DOI: 10.26434/chemrxiv.10025789.v1.

Portions of this work were performed in collaboration with the following people:

Alison Walker assisted with imaging and performed imaging in neurons with OGB-AM and channel rhodopsin.

Julia Lazzari-Dean performed patch clamp electrophysiology experiments in HEK cells.

3.0 Introduction

Because poRhoVRs absorb and emit light beyond 700 nm, they are suitable for multicolor imaging. Optogenetic actuators, like ChannelRhodopsin-2, require the use of cyan light to activate transfected neurons[1,2]. Fluorescent sensors for Ca^{2+} are among the most widely used optical sensors. Despite some three decades since the initial reports of fluorescent indicators for this critical intracellular messanger,[3,4] most Ca^{2+} indicators utilize excitation and emission profiles firmly centered in the blue/green region of the visible spectrum (for example, Oregon Green BAPTA (OGB)[3] and the GCaMP family of genetically encoded indicators).[5] Although promising new Ca^{2+} indicators, both synthetic[6–9] and genetically encoded,[10–13] possess red-shifted excitation and emission spectra, circularly-permuted (cp) GFP-based indicators, like the GCaMP family[5], dominate the landscape of functional imaging.[14,15] Therefore, fluorescent voltage indicators with orthogonal wavelengths are required. Before imaging with these tools can be done, initial characterizations in HEK cells must be completed to ensure membrane localization and measure voltage sensitivity. After these initial characterizations, simultaneous calcium and voltage imaging can be done as well as all-optical electrophysiology with ChannelRhodopsin-2.

3.1 Initial Characterization in HEK 293T Cells

All four poRhoVR dyes (**12** – **15**) localize to the cell membrane and display differing cellular brightness when applied to HEK cells under identical experimental conditions (**Figure 3.1.1**). Although all poRhoVRs localize to the membrane, poRhoVRs **13** and **15**, with N,N-diethyl, methoxy-aniline substituents, are approximately 10-fold dimmer in cell membranes than poRhoVR **12** and **14** (N,N-dimethyl aniline) (**Table 3.1.1, Figure 3.1.1**). The long wavelength excitation and emission of poRhoVRs enables multi-color imaging with organelle specific dyes.

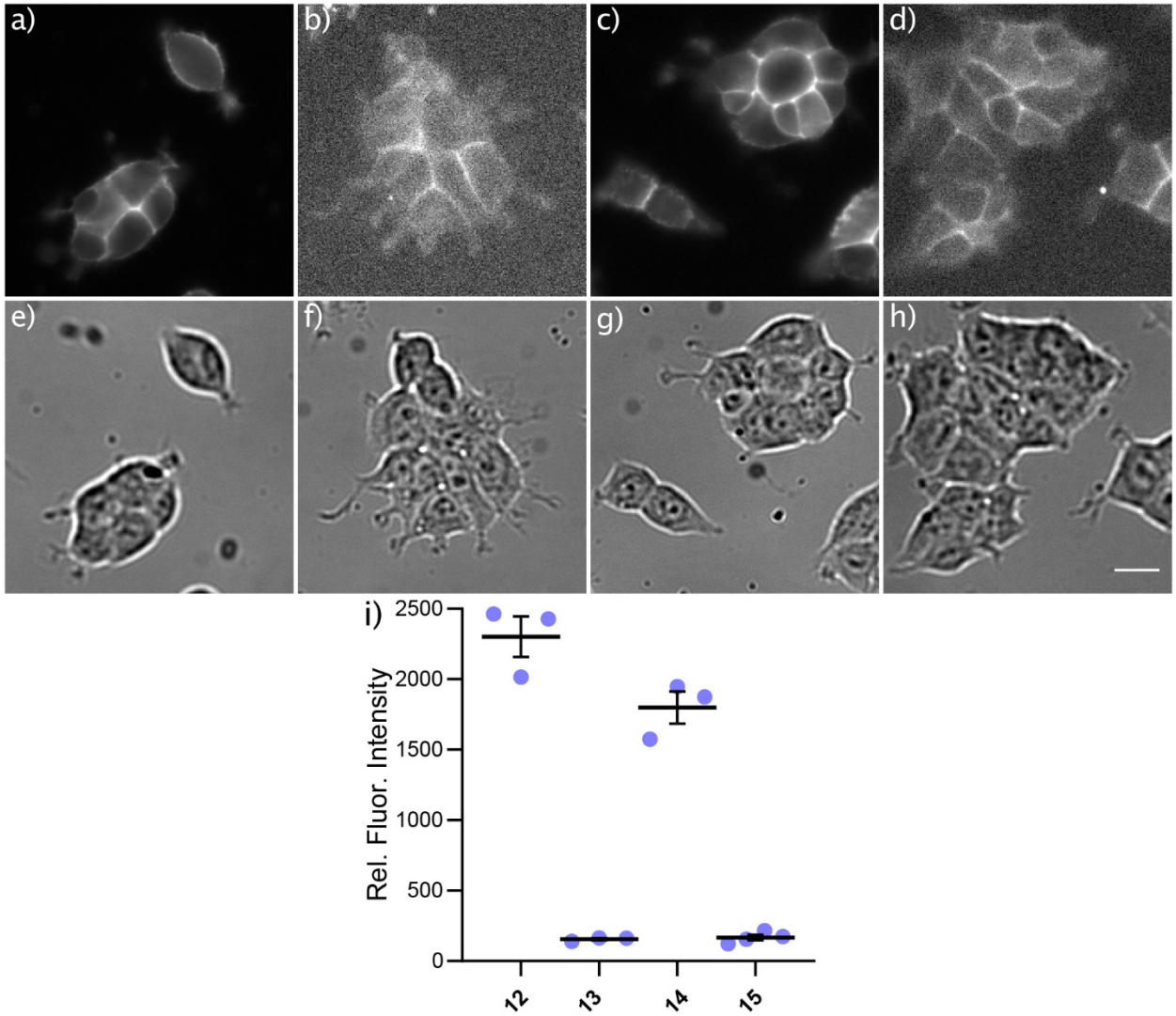

Figure 3.1.1 Quantification of poRhoVR brightness in HEK cells. **(a-d)** Widefield epifluorescence images and **(e-h)** differential interference contrast (DIC) images of poRhoVR indicators in HEK cells (2 μM); **a,e)** poRhoVR **12**, **b,f)** poRhoVR **13**, **c,g)** poRhoVR **14**, and **d,h)** poRhoVR **15**. Scale bar for (**a-h**) is 20 μm. **i)** Plot of fluorescence intensity of HEK cells stained with 2 μM poRhoVR dyes (**12** – **15**). Bars represent mean fluorescence intensity for n = 3 independent coverslips of HEK cells. The average value for a coverslip of HEK cells stained with poRhoVR is shown as a blue dot. Each coverslip contained 30 to 60 individual cells/regions of interest (ROIs) that were used to determine the mean fluorescence. Error bars depict standard deviation (n = 3).

Live-cell imaging[16] of poRhoVR 14 (1 μM, **Figure 3.1.2 a**) in HEK cells co-stained with rhodamine 123[17] (the methyl ester of rhodamine 110),[18] which localizes to the mitochondria on account of its overall positive charge (**Figure 3.1.2 b**) and Hoechst 33342,[1920] a bisbenzimidazole dye which binds to nucleic acid, labeling the nuclei of cells, (**Figure 3.1.2 c**) demonstrate good membrane localization for poRhoVRs along with compatibility with simultaneous, multi-color imaging (**Figure 3.1.2 d**).

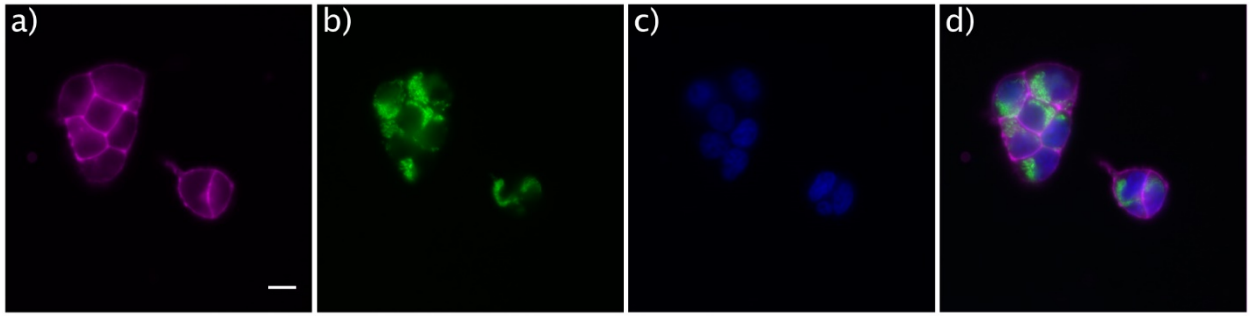

Figure 3.1.2 Multi-color imaging with poRhoVR **14**. **(a-d)** Widefield, epifluorescence images of **a)** poRhoVR **14** (1 μM) in HEK cells. Cells are counter-stained with **b)** rhodamine 123 (1 μM) and **c)** Hoechst 33342 (1 μM) to visualize mitochondria and nuclei, respective. **d)** An overlay of poRhoVR **14**, rhodamine 123, and Hoechst 33342. Scale bar for **(a-d)** is 10 μm.

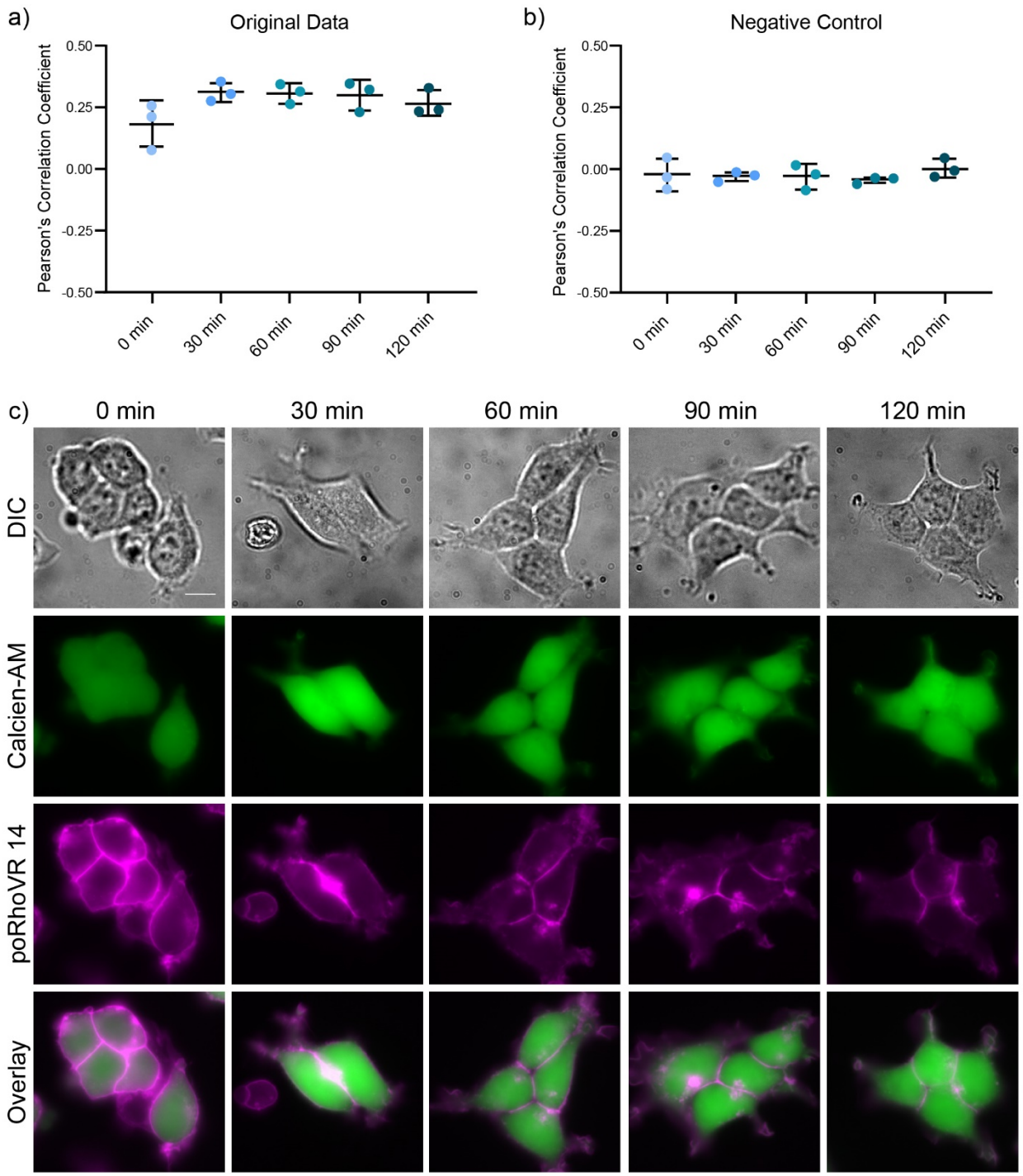

Figure 3.1.3 Extent of endocytosis in HEK293T cells. **a)** Graph of the average Pearson's correlation coefficient (PCC) per timepoint. Error bars show standard deviation. Each point represents an independent replicate (a coverslip). The PCC for each coverslip was calculated as the average PCC of 4 imaged areas per coverslip. The PCC for each area was calculated as the average PCC for all ROIs in the area imaged. Dunnett's multiple comparisons test of 0 min versus all other time points gave the following P-values: 0.0772 (0 vs. 30 min), 0.0894 (0 vs. 60 min), 0.1138 (0 vs. 90 min), 0.3039 (0 vs. 120 min). A P-value below 0.05 is considered statistically

significant. **b)** Graph of the average PCC for the negative control. Data points were calculated in the same manner as in a). The negative control values were obtained by rotating the Calcein-AM image 90° and rerunning the analysis. Dunnett's multiple comparisons test of 0 min versus all other time points gave the following P-values: 0.9981 (0 vs. 30 min), 0.9979(0 vs. 60 min), 0.9118 (0 vs. 90 min), 0.8743 (0 vs. 120 min). **c)** Representative images at each time point displaying the poRhoVR **14** and Calcein-AM staining. Scale bar is 10 μm.

Next the internalization rate, toxicity and photostability of poRhoVR **14** were examined. The persistence of poRhoVR **14** on the cell membrane in HEK cells was measured over the course of two hours (**Figure 3.1.3**). The extent of poRhoVR **14** internalization was determined by measuring the degree of colocalization between poRhoVR **14**, which stains only membranes and Calcien-AM[20], a cytosolic stain that becomes fluorescent and is retained inside living cells. Since Calcein-AM is only fluorescent in live cells, dead cells, which readily internalize poRhoVR **14** were excluded from the colocalization analysis. Increased colocalization values indicates a higher degree of internalization of the membrane-associated poRhoVR **14**. There is a low degree of colocalization between poRhoVR **14** signal and cytosolic Calcein-AM after an initial 20 minutes of loading (the Pearson's correlation coefficient is 0.22 ± 0.2, mean ± S.E.M. for n = 3 coverslips) (**Figure 3.1.3 a**). There is an increase in the degree of colocalization, to approximately 0.26, after additional observation for up to 2 hours (**Figure 3.1.3 a**), but the changes are not statistically significant ($P > 0.05$, Dunnett's multiple comparisons test, see **Figure 3.1.3**).

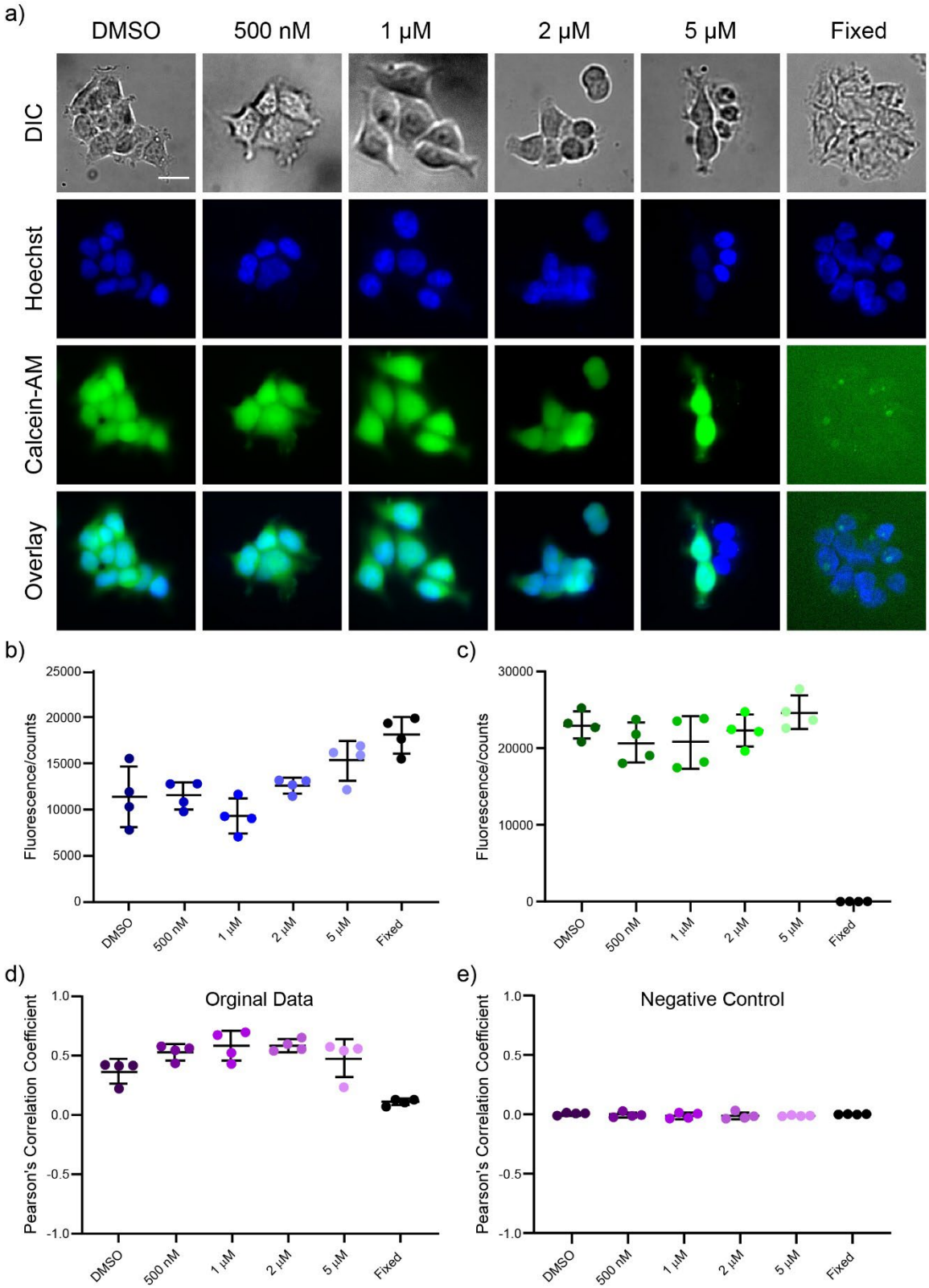
a)
DMSO
500 nM
1 µM
2 µM
5 µM
Fixed
DIC
Hoechst
Calcein-AM
Overlay
b)
Fluorescence/counts
25000
20000
15000
10000
5000
0
DMSO
500 nM
1 µM
2 µM
5 µM
Fixed
c)
Fluorescence/counts
30000
20000
10000
0
DMSO
500 nM
1 µM
2 µM
5 µM
Fixed
d)
Orginal Data
Pearson's Correlation Coefficient
1.0
0.5
0.0
-0.5
-1.0
DMSO
500 nM
1 µM
2 µM
5 µM
Fixed
e)
Negative Control
Pearson's Correlation Coefficient
1.0
0.5
0.0
-0.5
-1.0
DMSO
500 nM
1 µM
2 µM
5 µM
Fixed

Figure 3.1.4 Toxicity of poRhoVR **14** in HEK 293T cells. **a)** Images of HEK 293T cells that have been loaded DMSO or with varying concentrations of poRhoVR **14** or fixed with formaldehyde and then stained with Hoechst 33342 and Calcein-AM. Scale bar 20 μM. **b)** Background subtracted Hoechst 33342 fluorescence. Each data point represents a single coverslip. A total of four coverslips were imaged per condition (the value of each coverslip was determined from 4 distinct areas that had approximately 20 to 50 cellular regions of interest). The error bars represent the standard deviation. Dunnett's multiple comparisons test of DMSO, the positive control, versus poRhoVR **14** treated and fixed cells gave the following P-values: 0.9999 (DMSO vs. 500 nM), 0.4617 (DMSO vs. 1 μM), 0.8729 (DMSO vs. 2 μM), 0.0600 (DMSO vs. 5 μM) and 0.0010 (DMSO vs. Fixed). A P-value below 0.05 constitutes a statistically significant difference. **c)** Background subtracted Calcein-AM fluorescence. Each data point represents an area of a coverslip. The error bars represent the standard deviation. Dunnett's multiple comparisons test of DMSO versus poRhoVR **14** treated and fixed cells gave the following P-values: 0.4672 (DMSO vs. 500 nM), 0.5116 (DMSO vs. 1 μM), 0.9852 (DMSO vs. 2 μM), 0.7441 (DMSO vs. 5 μM) and <0.0001 (DMSO vs. Fixed). **d)** Pearson's correlation coefficient for Hoechst 3332 and Calcein-AM fluorescence for each area. The error bars represent the standard deviation. Dunnett's multiple comparisons test of DMSO versus poRhoVR **14** treated and fixed cells gave the following P-values: 0.1231 (DMSO vs. 500 nM), 0.0298 (DMSO vs. 1 μM), 0.0261 (DMSO vs. 2 μM), 0.4247 (DMSO vs. 5 μM) and 0.0071 (DMSO vs. Fixed). **e)** Pearson's correlation coefficient for Hoechst 3332 and Calcein-AM fluorescence, rotated 90° for each area. The error bars represent the standard deviation. Dunnett's multiple comparisons test of DMSO versus poRhoVR **14** treated and fixed cells gave the following P-values: 0.9752 (DMSO vs. 500 nM), 0.7539 (DMSO vs. 1 μM), 0.7280 (DMSO vs. 2 μM), 0.7544 (DMSO vs. 5 μM) and 0.9986 (DMSO vs. Fixed).

Toxicity of poRhoVR **14** was assayed using Calcein-AM. Comparison of the colocalization of Hoechst 33342 fluorescence, which stains the nuclei of dead and alive cells, and Calcein-AM fluorescence across various conditions revealed no difference in colocalization, and therefore toxicity, between vehicle-treated HEK293T cells (DMSO) and up to 5 μM poRhoVR 14 (**Figure 3.1.4**).

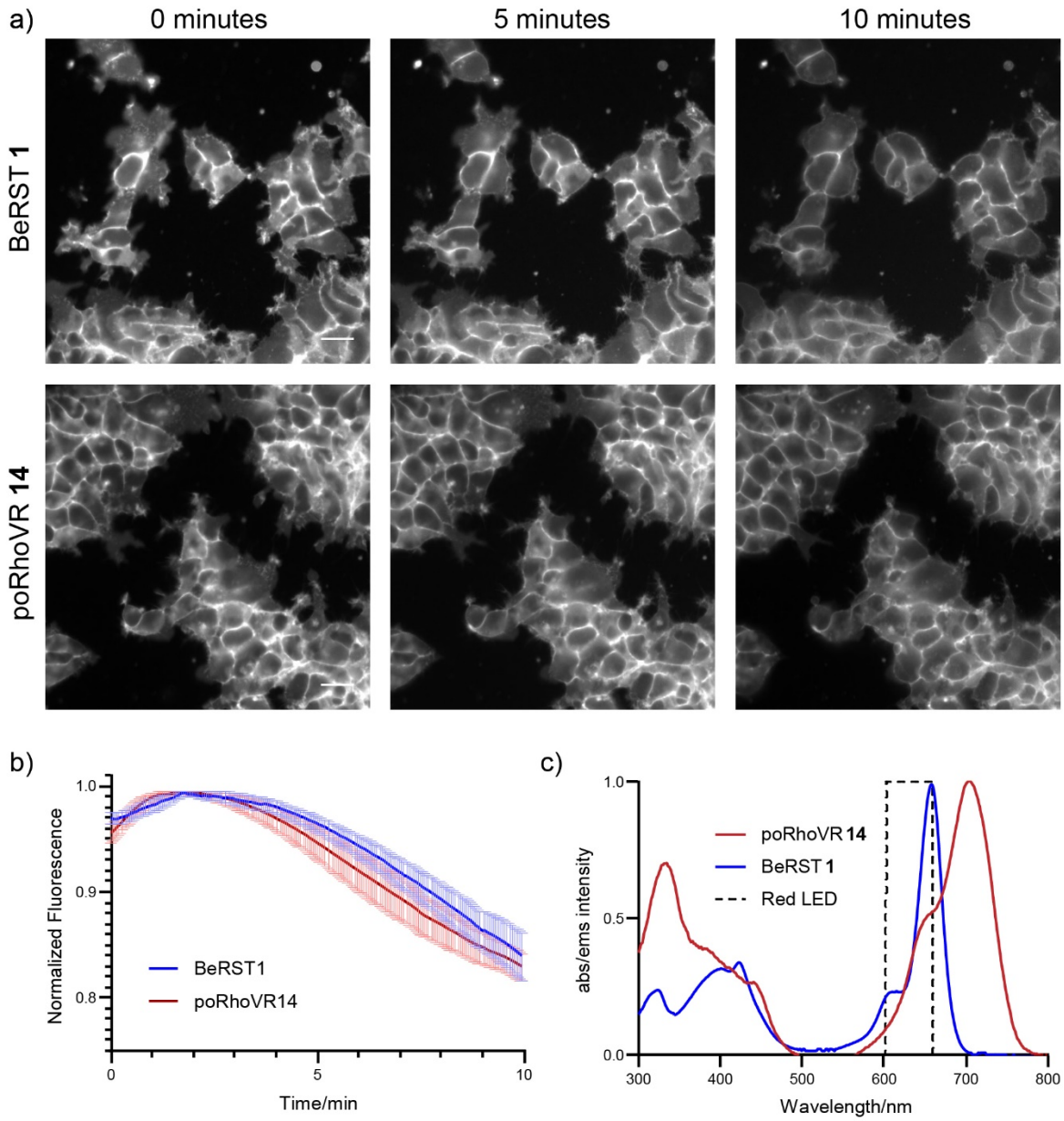

Figure 3.1.5 Photostability comparison between poRhoVR **14** and BeRST **1**. **a)** Widefield fluorescence images of HEK293T stained with 300 nM BeRST **1** and 500 nM poRhoVR **14** at timepoints 0, 5, 10 minutes of continuous illumination with a red LED (78.6 mW/mm^2). Scale bar is 20 μm. **b)** Plot of photobleaching curve of BeRST**1** (blue) and poRhoVR **14** (red). The bold line represents the background subtracted average cellular fluorescence at each time point (6 coverslips each) and the error bars represent the standard error of the mean. **c)** Absorption spectra for poRhoVR **14** (solvent: dPBS with 1% DMSO) and BeRST **1** (solvent: solvent: dPBS with 0.1% sodium dodecyl sulfate)

The photostability of poRhoVR **14** is comparable to the photostability exhibited by BeRST **1**.[21] To account for differences in absorption of light from the red LED used to illuminate the

cells, the absorbances of the dyes were matched at 631nm. As a result, cells were stained with either 300 nM BeRST **1** or 500 nM poRhoVR **14**.

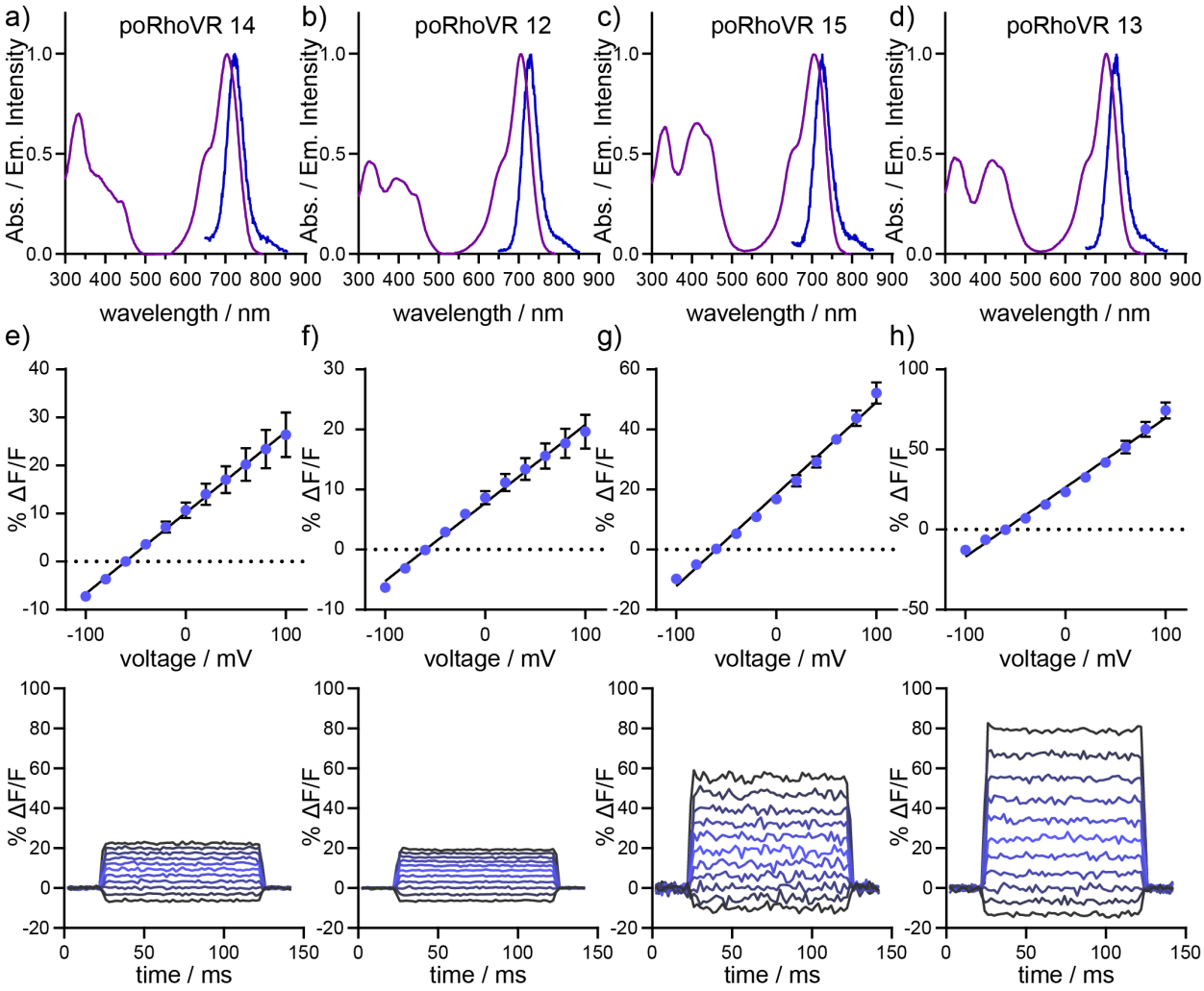

Figure 3.1.6 Absorption/Emission Spectra and Voltage sensitivity of poRhoVR dyes. Plot of normalized absorption (purple) and emission (blue) for poRhoVR dyes **a) 14**, **b**), **12**, **c) 15**, and **d) 13**. Spectra were acquired at 1 μM (0.1 % DMSO) in PBS buffer. For emission spectrum, excitation was provided at 625 nm. Voltage sensitivity plots for poRhoVR dyes **e) 14**, **f**), **12**, **g) 15**, and **h) 13**. Upper row depicts plots of ΔF/F vs. final membrane potential (mV) in HEK cells loaded with 1 μM poRhoVR dye and subjected to whole-cell voltage-clamp conditions. Error bars represent standard deviation for n = 6, 5, 5, and 4 cells, respectively. Lower row depicts plots of ΔF/F (%) vs time for HEK cells loaded with 1 μM poRhoVR and held at -60 mV under whole-cell voltage-clamp and stepped to hyper- and depolarizing potentials in increments of 20 mV (±100 mV).

The cellular fluorescence of poRhoVRs is voltage sensitive. Simultaneous fluorescence microscopy during sequential depolarizing and hyperpolarizing steps from a holding potential of -60 mV in HEK cells under whole-cell voltage-clamp conditions reveals linear fluorescence vs. voltage relationships for poRhoVR dyes **12** – **14** (**Figure 3.1.6**). Voltage sensitivities range from 13% (poRhoVR **12**) to 43% (poRhoVR **13**) per 100 mV (**Table 3.1.1**). The sensitivity of

poRhoVR **13**, at 43%, is nearly 2-fold the sensitivity of the most red-shifted voltage indicator to date, the Si-rhodamine based BeRST 1 (24% ΔF/F per 100 mV)[21] and is comparable to the sensitivity of our previously reported, tetra-methyl rhodamine based RhoVR (47% ΔF/F per 100 mV).[22] However, the low cellular brightness of poRhoVR **13** (more than 10x dimmer than poRhoVRs **12** and **14**) means that indicators like poRhoVR 14, with intermediate voltage sensitivity (17% ΔF/F per 100 mV), but high cellular brightness (12x brighter, compared to **13**) are also attractive for monitoring voltage dynamics in living systems. This is because, in a shot-noise-limited system, SNR scales with the square root of the number of collected photons, or the cellular brightness.[23,24] Therefore, even indicators with only middling ΔF/F values can be quite effective detectors of rapid voltage changes.[16,25]

Compound number	isomer[a]	R^1	R^2	relative cell brightness[b]	ΔF/F[c]
12	*meta*	H	Me	15 ± 0.9	13 ± 0.3%
13	*meta*	OMe	Et	1.0 ± 0.1	43 ± 0.9%
14	*para*	H	Me	12 ± 0.1	17 ± 0.5%
15	*para*	OMe	Et	1.3 ± 0.03	31 ± 0.5%

[a]Relationship between fluorophore and molecular wire. [b]Relative cellular brightness, in HEK cells [c]per 100 mV, in HEK cells. Data are mean ± S.E.M. for at least 3 separate determinations.

Table 3.1.1 Cellular Properties of poRhoVR indicators.

3.2 Characterization in Neurons

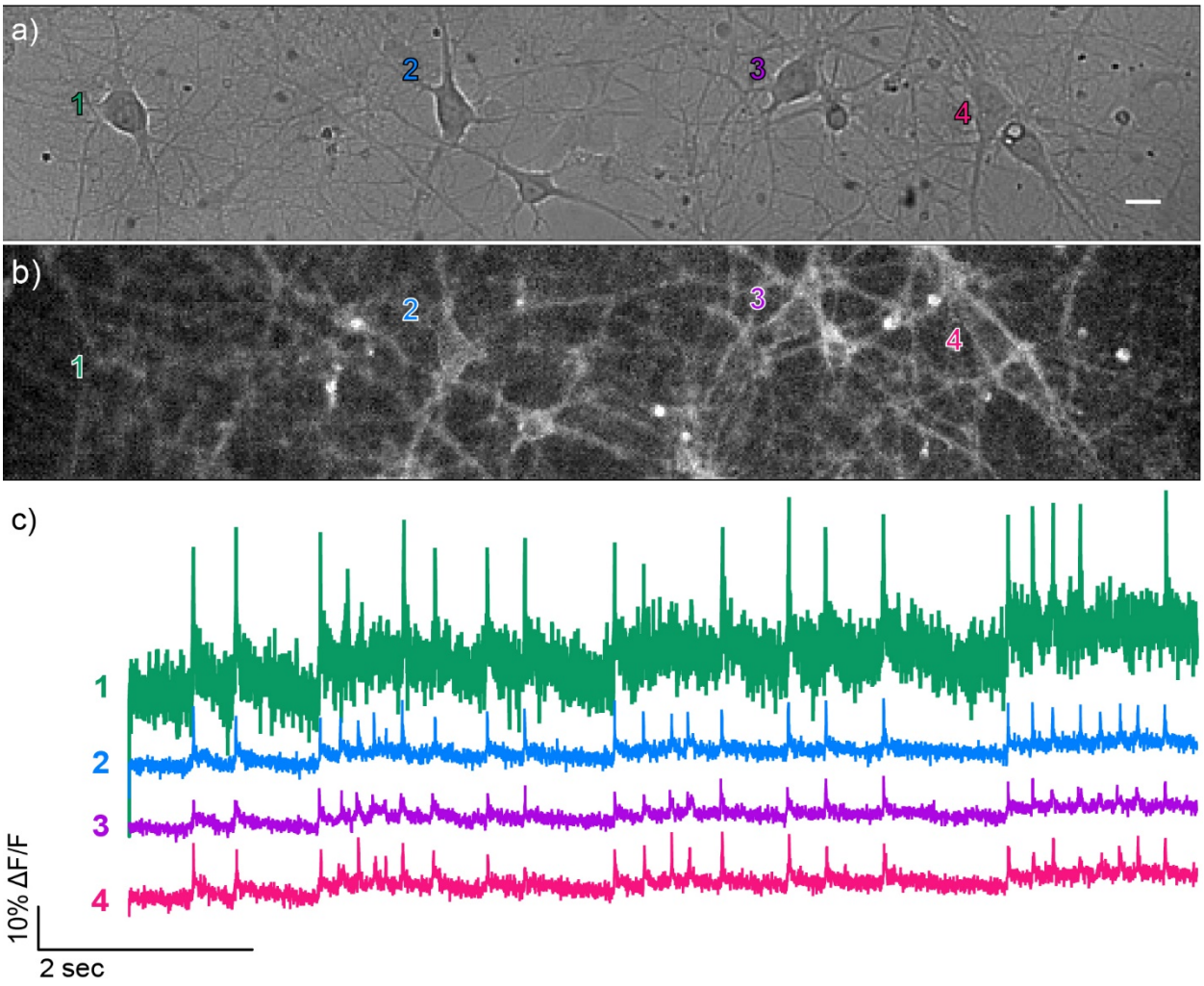

Figure 3.2.1 Traces of spontaneously fired action potentials from cultured neurons recorded with poRhoVR **13**. Transmitted light image of neurons loaded with **a)** poRhoVR **13** (500 nM). **b)** Epifluorescence image of neurons showing poRhoVR **13** staining. Scale bars are 20 μm. **c)** Plot of fractional change in poRhoVR **13** fluorescence (ΔF/F) vs time emanating from cells 1-4 in image (b). Optical sampling rate is 500 Hz.

Both poRhoVR **13** and **14** were evaluated in cultured hippocampal neurons isolated from rat embryos. Both poRhoVR **13** (**Figure 3.2.1**) and **14** (**Figure 3.2.2**) localize well to cellular membranes and readily report on spontaneously-firing action potentials in single-trial acquisitions.

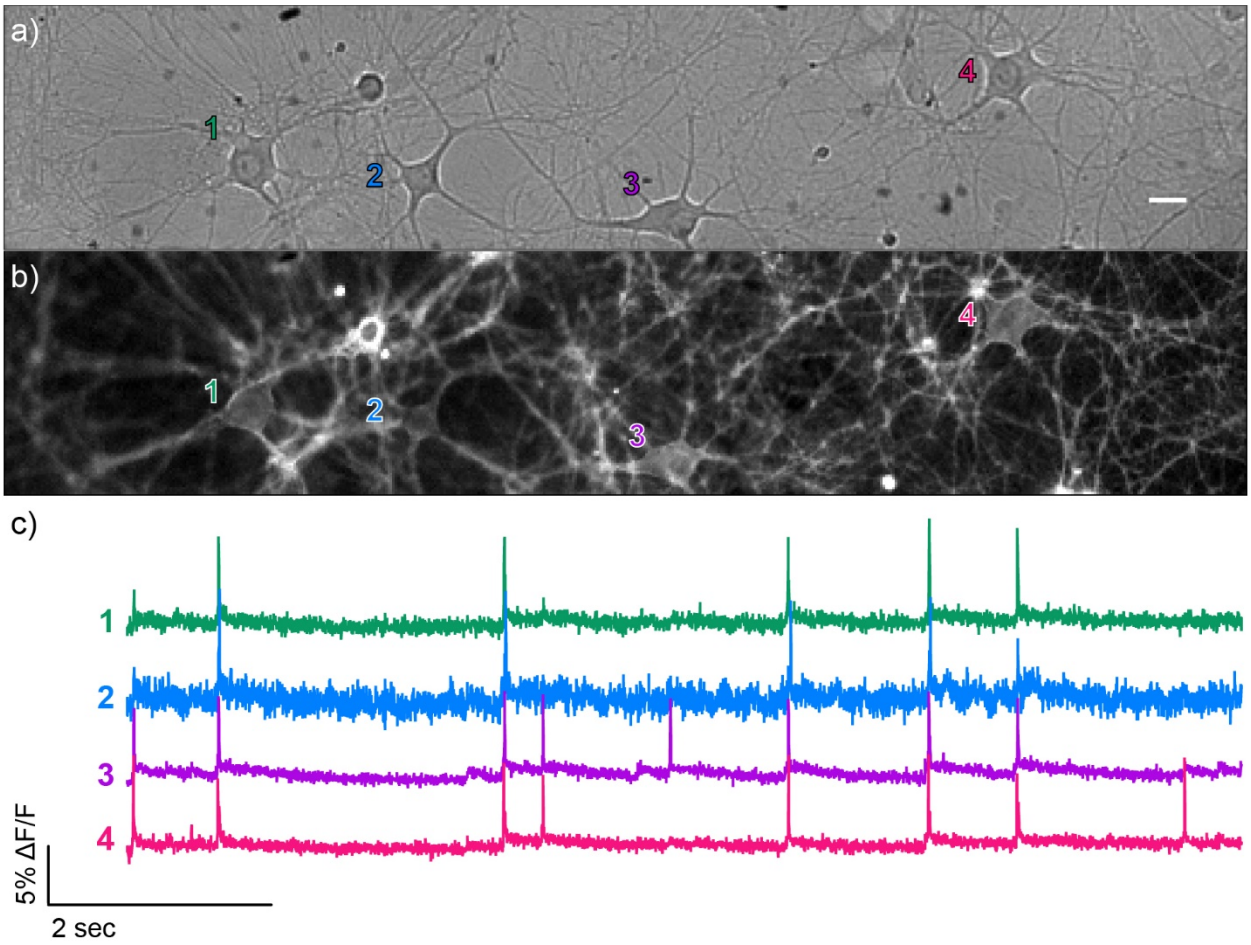

Figure 3.2.2 Traces of spontaneously fired action potentials from cultured neurons poRhoVR **14**. Transmitted light image of neurons loaded with **a)** poRhoVR **14** (500 nM). **b)** Epifluorescence image of neurons showing poRhoVR **14** staining. Scale bars are 20 μm. **c)** Plot of fractional change in poRhoVR **14** fluorescence (ΔF/F) vs time emanating from cells 1-4 in image (b). Optical sampling rate is 500 Hz. Asterisks indicate subthreshold voltage changes.

Consistent with its performance in HEK cells, poRhoVR **14** was approximately 8 to 12-fold brighter than 13 under identical experimental conditions (**Figure 3.2.3**). In a complementary fashion, the %ΔF/F value per spike/action potential for **13** was larger than for **14** (12% vs 6%, **Figure 3.2.3**) but with lower overall signal-to-noise ratio (SNR, 20:1 vs 40:1, **Figure 3.2.3**). Because of the higher brightness and SNR for detecting action potentials, we used poRhoVR **14** for subsequent experiments.

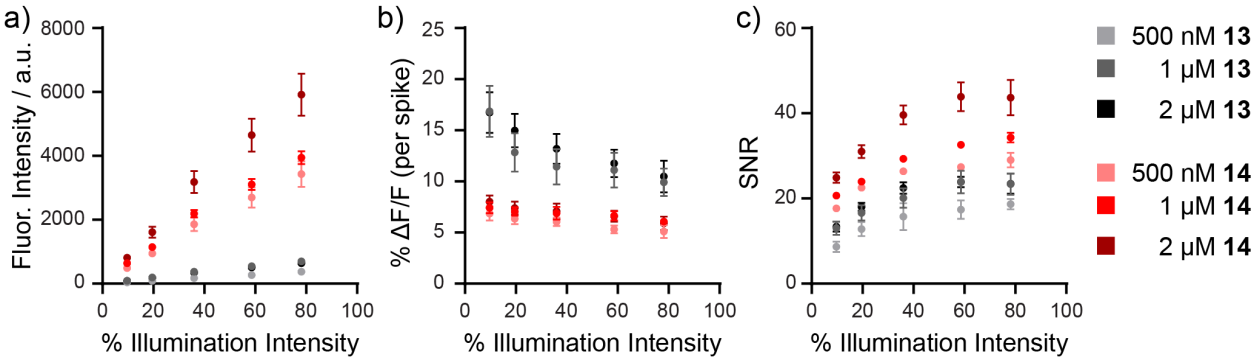

Figure 3.2.3 Quantification of brightness, voltage sensitivity and signal to noise of poRhoVR **13** and **14** in neurons. Plots of **a)** fluorescence intensity, **b)** fractional change in fluorescence in response to evoked action potentials (ΔF/F), and **c)** and signal-to-noise ratios (SNR) for these action potentials vs. illumination intensity in neurons. Hippocampal rat neurons were stained with poRhoVR **13** (grey) or **14** (red) at concentrations of 500 nM (light red/light grey), 1 μM (red/grey), or 2 μM (dark red/dark grey) poRhoVR dye and imaged at 500 Hz. Data represent mean values ± S.E.M. for n = 4 images, comprising approximately 10-20 neurons per image.

poRhoVR **14** can be used in multicolor experiments, not only for tracking static fluorescence associated with distinct organelles (**Figure 3.1.2**), but also in concert with commonly employed optogenetic actuators and sensors. The blue light-activated opsin, ChannelRhodopsin-2 (ChR2),[1,2] fused to yellow fluorescent protein (YFP) was expressed in a subset of hippocampal neurons isolated from rat embryos (**Figure 3.2.4**). Bath application of poRhoVR **14** to these same neurons results in membrane-localized fluorescence (**Figure 3.2.4 c**) that is spectrally isolated from the YFP signal (**Figure 3.2.4 d**).

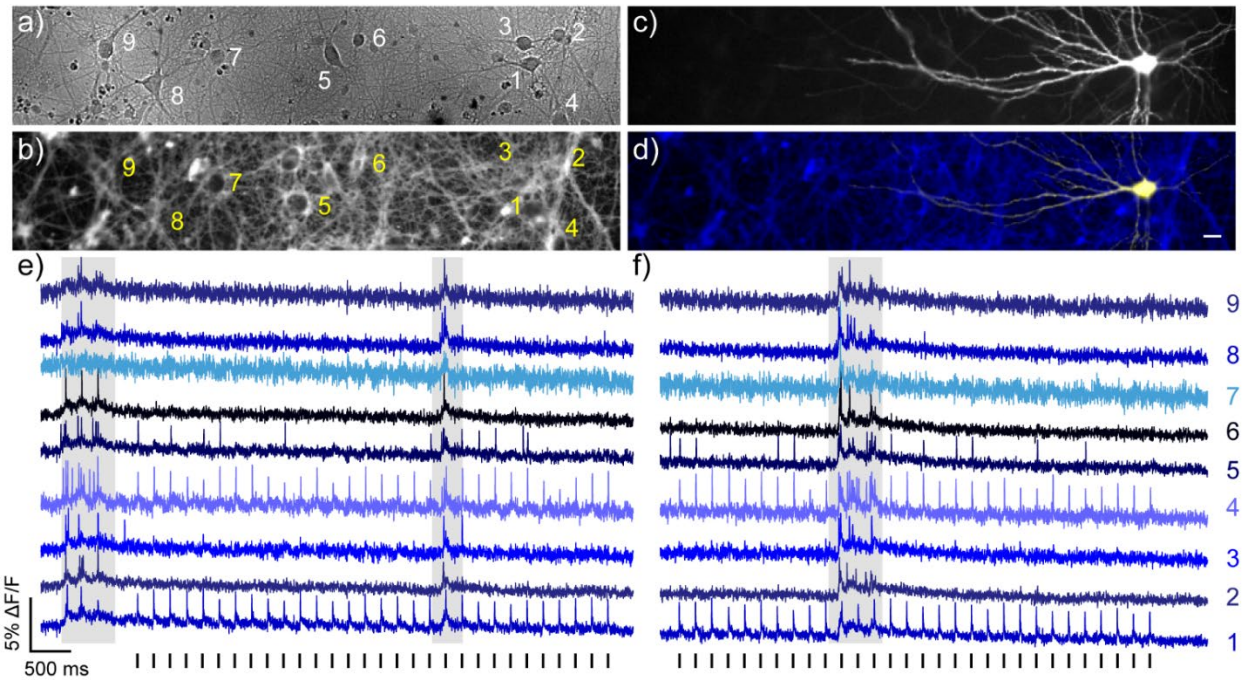

Figure 3.2.4 All-optical electrophysiology using poRhoVR 14 and ChR2. **a)** Transmitted light image of dissociated rat hippocampal neurons stained with poRhoVR 14 (500 nM). **b)** Epifluorescence image of neurons stained with poRhoVR 14. **c)** Epifluorescence image of neuron displaying YFP marker of ChR2 expression. **d)** Composite image depicting poRhoVR 14 labeling and ChR2-YFP expression. Scale bar is 20 µm. **e)** Recording of ΔF/F from the cell bodies of neurons indicated in panels (a-d). **f)** Plot of %ΔF/F from the cell bodies of neurons indicated in panels (a-d), recorded 90 seconds after the data shown in panel (e). Optical sampling rate was 500 Hz. The entire field was stimulated optically with flashes of cyan light (475 nm, 5 ms, 1.92 mW/mm^2) as indicated by the vertical bars below the blue optical recording in panels e and f. Optical voltage recordings are single trials.

The combined use of ChR2 and poRhoVR allows dissection of functional connectivity across many neurons. Optical stimulation of cell **1** (475 nm, 5 ms, 1.92 mW/mm^2) results in ChR2-evoked action potentials optically recorded at cell **1** (**Figure 3.2.4 e** and **f**). Cells 4 and 5 appear monosynaptically coupled to ChR2-positive cell 1 with action potential latencies of 6.7 ms ± 1.5 ms (S.D. n = 60 pairs of spikes) and 5.6 ms ± 1.3 ms (S.D., n = 20 out of 60 spikes), respectively. However, the data reveals differences in the relative strengths of these connections with cell **1** triggering firing in cell **4** for 100% of action potentials, and only 33% for cell **5**. Interestingly, bursts of spontaneous activity indicate strong recurrent connectivity between all neurons (**Figure 3.2.4 e** and **f**, grey shaded areas), but firing initiated in the ChR2-expressing neuron (cell **1**, **Figure 3.2.4 a-d**) activates only a subset of these neurons (**Figure 3.2.4 e** and **f**): notably, cell **4**, nearly 50 µm away from cell **1**, and cell **5**, over 120 µm distant from ChR2-expressing cell **1**. The use of cyan light to stimulate ChR2 does not cross-excite poRhoVR **14**, as indicated by the lack of stimulus artifact in the ChR2-negative cells in the same field of view (**Figure 3.2.4 d** and **e**). Together, these experiments establish poRhoVR **14** as a powerful complement for all-optical electrophysiology utilizing NIR absorbing indicators.

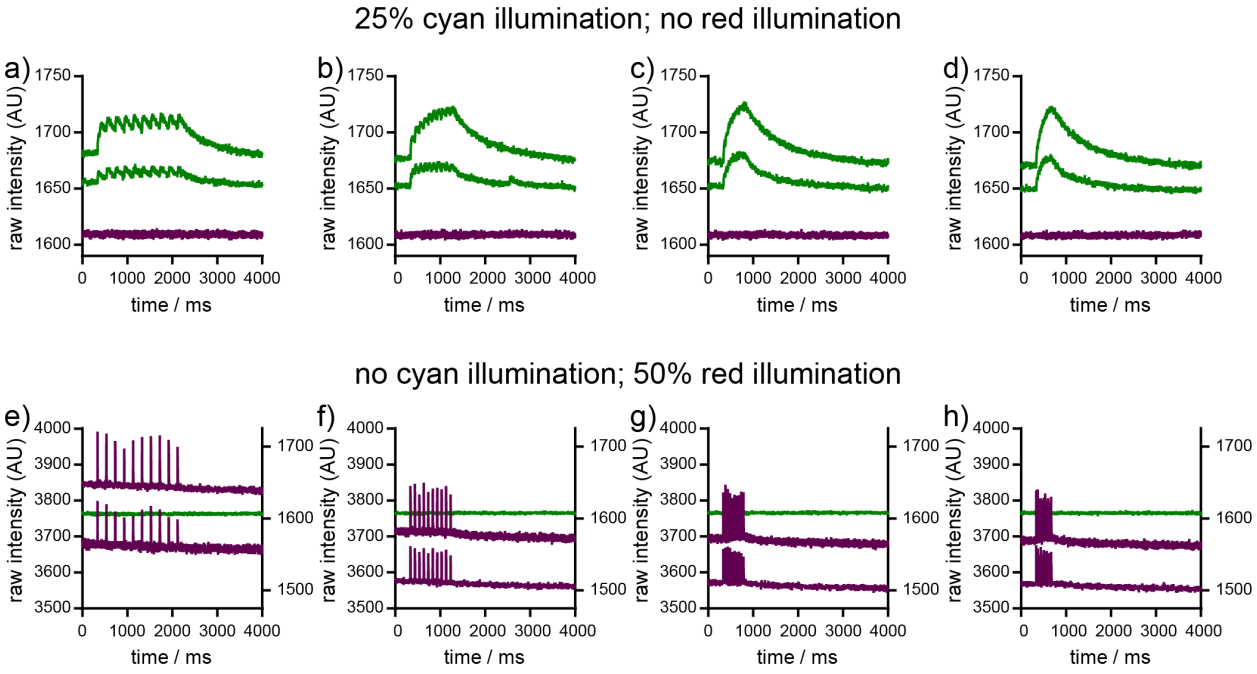

Figure 3.2.5 Compatibility of poRhoVR **14** with OGB Ca^{2+} imaging in rat hippocampal neurons. Rat hippocampal neurons with stained with poRhoVR **14** (1 μM) and OGB (1 μM) and imaged using an image-splitter to enable acquisition of simultaneous NIR (poRhoVR) and green (OGB) fluorescence, as in **Figure 5** (main text). **a-d**) Plots of fluorescence intensity vs time for OGB (green traces) and poRhoVR **14** (magenta traces) vs. time (ms) with cyan illumination only (17.6 mW/mm^2). Under single wavelength (cyan) illumination, field stimulation was provided at **a)** 5, **b)** 10, **c)** 20, and **d)** 30 Hz. **e-h)** Plots of fluorescence intensity vs. time for poRhoVR **14** (magenta traces) and OGB (green traces) vs. time with red illumination only (50%, 49.7 mW/mm^2). Under single wavelength (red) illumination, field stimulation was provided at **e)** 5, **f)** 10, **g)** 20, and **h)** 30 Hz. Each plot shows the responses of two neurons (recorded simultaneously in red and green channels).

Two-color, simultaneous voltage and Ca^{2+} imaging was performed in the same cells using poRhoVR **14** and the synthetic Ca^{2+} indicator, OGB (**Figure 3.2.6 a-c**). We treated hippocampal neurons with both poRhoVR **14** (500 nM) and OGB (1 μM) simultaneously and imaged using an emission-splitter to project both emission wavelengths onto the same camera chip. This resulted in a separate image for OGB and poRhoVR **14** fluorescence. Under these conditions, we observe clear membrane-associated fluorescence for poRhoVR **14** (**Figure 3.2.6 a**) and cytosolic fluorescence for OGB (**Figure 3.2.6 b**). We established that no cross-excitation exists under these conditions (**Figure 3.2.5**). Using field-stimulation electrodes, we evoked a series of 10 action potentials, across a range of frequencies, and simultaneously recorded voltage (**Figure 3.2.6 c**, magenta traces) and Ca^{2+} (**Figure 3.2.6 c**, green traces) dynamics.

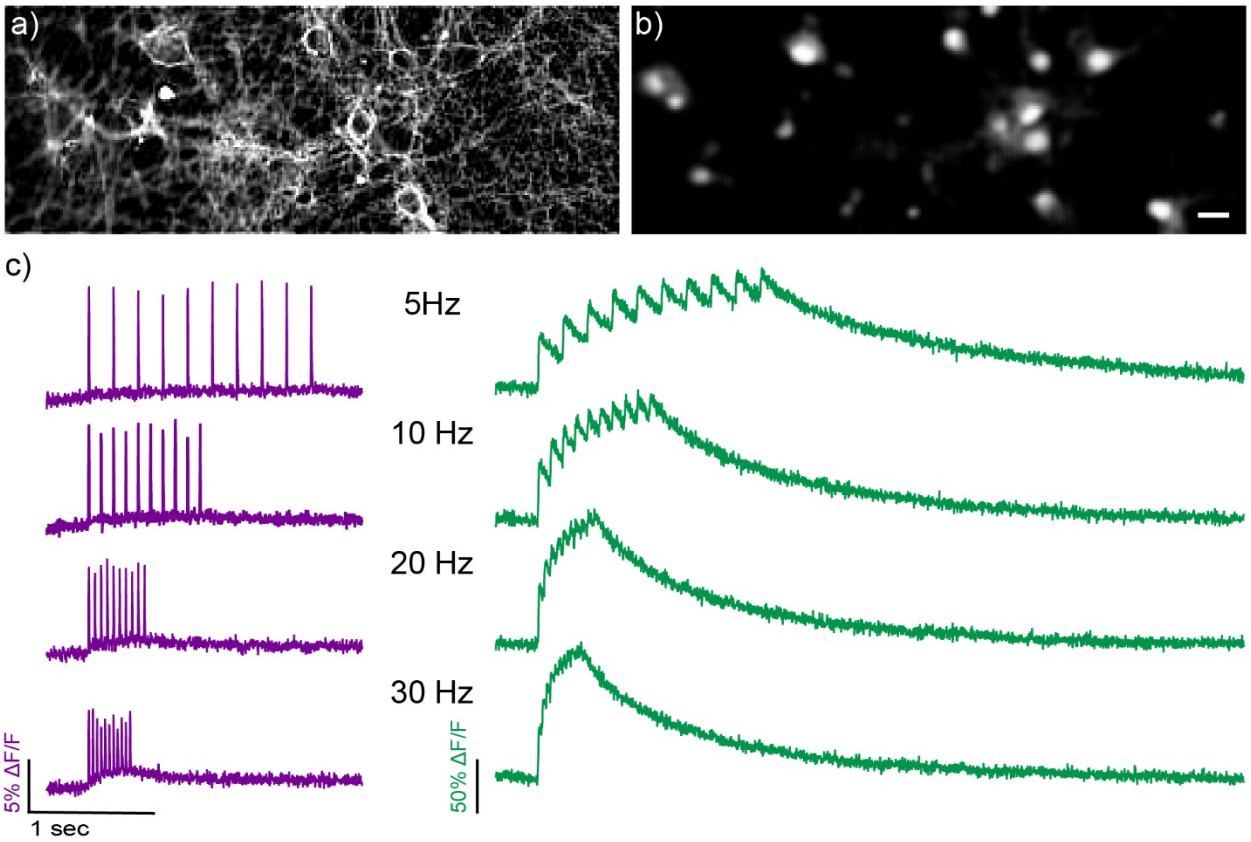

Figure 3.2.6 Simultaneous voltage and calcium imaging with poRhoVR **14** and Oregon Green BAPTA 1 AM. Epifluorescence image of neurons stained with both **a)** poRhoVR **14** (1 μM) and **b)** Oregon Green BAPTA 1 AM (OGB, 1 μM). **c)** Plots of %ΔF/F for voltage (poRhoVR **14**, purple) and Ca^{2+} transients (OGB, green) in response to field stimulation driven at 5, 10, 20, and 30 Hz.

Both poRhoVR **14** and OGB clearly resolve single action potentials when activity is evoked at rates of either 5 or 10 Hz. poRhoVR **14** clearly resolves action potentials at firing rates of 20 and 30 Hz (**Figure 3.2.6 c**). OGB, despite its fast Ca^{2+} response kinetics (<5 ms to action potential peak)[5] compared to GCaMP6f (~45 ms to peak)[5] and other genetically encoded indicators,[26–28] fails to accurately report individual action potential-evoked Ca^{2+} transients at firing frequencies higher than 10 Hz (**Figure 3.2.6 c**). Neurons in the brain and retina can fire action potentials at rates up to several hundred Hz, for example in interneurons of the hippocampus,[29] Purkinje cells of the cerebellum,[30] and ganglion cells of the retina,[31] emphasizing the need for indicators with fast response kinetics.

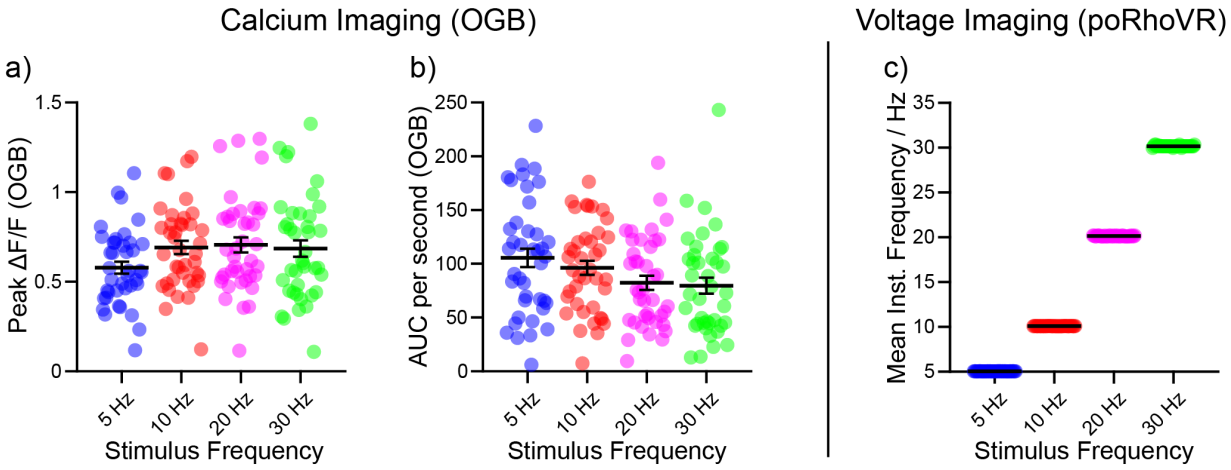

Figure 3.2.7 Quantification of evoked activity in neurons using poRhoVR **14** and Oregon Green BAPTA. Analysis of data presented in **Figure 5** of main text. Ca^{2+} imaging data with OGB was quantified as **a)** peak ΔF/F or **b)** integrated area under the curve per second vs stimulus frequency, in Hz. For Ca^{2+} imaging data, black bars represent the mean ± S.E.M. for n = 40 cells. Data points represent individual cells. There are no statistically significant differences between stimulus frequency when analyzing peak ΔF/F or AUC per second (one-way ANOVA + Tukeys comparisons). Voltage imaging data with poRhoVR **14** was quantified as **c)** the mean instantaneous frequency (Mean Inst. Frequency), in Hz, vs stimulus frequency, in Hz. For voltage imaging data, black bars represent the mean ± S.E.M. for n = 40 cells. Data points represent the mean instantaneous frequency between spikes for each analyzed cell (10 spikes, 9 intra-spike intervals). For voltage imaging, all the differences between stimulus frequencies are significant ($p < 0.0001$, one-way ANOVA Kruskal-Wallis test + Dunns comparison).

Ca^{2+} indicators are often characterized against varying numbers of action potentials arriving at a constant frequency. However, neural information is often encoded in the form of spike rates. Therefore, resolution of individual spikes and firing frequency is critical for understanding the underlying physiology of the system under observation. Even with very fast OGB, estimating spike frequency using Ca^{2+} imaging traces alone was unsuccessful. Neither peak Ca^{2+} ΔF/F (**Figure 3.2.7 a**) nor integrated area under the curve (**Figure 3.2.7 b**)

were able to resolve differences at 5, 10, 20, or 30 Hz firing rates. In contrast, the optically recorded voltage transients revealed by poRhoVR **14** clearly discriminates between firing frequencies of 5, 10, 20, and 30 Hz (**Figure 3.2.7 c**).

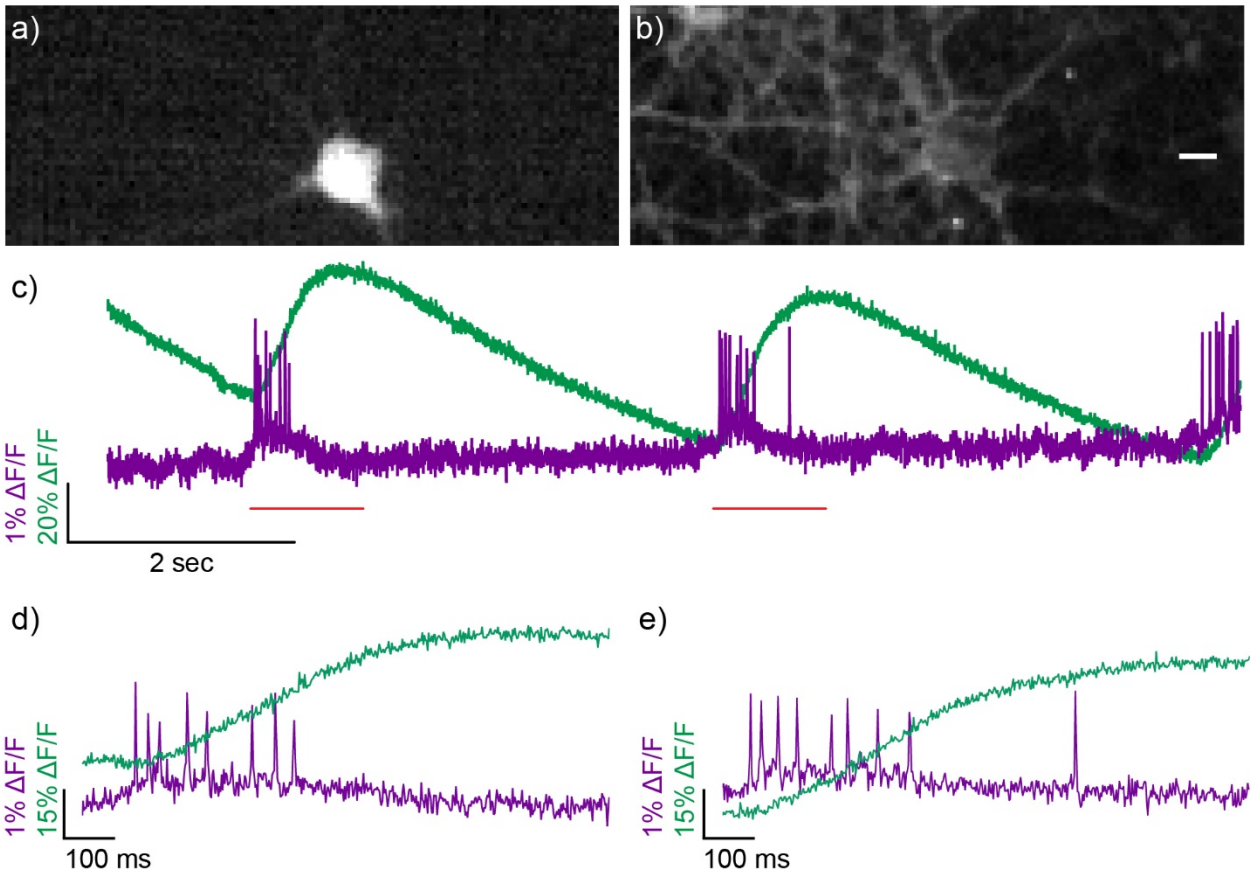

Figure 3.2.8 Simultaneous voltage and calcium imaging with poRhoVR **14** and GCaMP 6s. **a)** Epifluorescence image of a neuron transfected with GCaMP6s. **b)** This same GCaMP6s (+) neuron is also stained with poRhoVR **14** and imaged simultaneously. Scale bar is 10 μm. **c)** Simultaneously recorded traces of voltage and calcium activity from neuron in panels (a) and (b). Activity was evoked using field stimulation at a rate of 16 Hz. **d)** and **e)** The insets show that the onset and decay of voltage signals imaged with poRhoVR **14** precede that of the calcium signal visualized from the same cell with GCaMP6s. The red lines underneath the traces in (c) indicate the zoomed in sections showed in panels (d) (the first train of action potentials) and (e) (the second train of action potentials).

Simultaneous voltage and Ca^{2+} imaging in the same cells can also be achieved alongside genetically encoded indicators, like GCaMP6. We again stained neurons with poRhoVR **14** (1 μM). This time, a subset of hippocampal neurons expressed GCaMP6s. Again, poRhoVR localizes to membranes (**Figure 3.2.8 b**), while GCaMP6s fluorescence appears cytosolic (**Figure 3.2.8 a**). Simultaneous voltage and Ca^{2+} imaging of spontaneous activity in hippocampal neurons reveals fast-spiking bursts resolved in voltage (**Figure 3.2.8 c-e**, magenta trace), followed by slower, sustained increases in GCaMP6-associated fluorescence (**Figure 3.2.8 c-e**, green trace). Notably, voltage imaging with poRhoVR **14** exhibits sufficiently high temporal resolution to distinguish individual action potentials in spike

volleys (**Figure 3.2.8 d**, 8 spikes; **Figure 3.2.8 e**, 9 spikes), while Ca^{2+} imaging does not. Together, these experiments establish the utility of poRhoVR dyes for monitoring fast spiking in neurons alongside commonly used synthetic and genetically encoded Ca^{2+} indicators and emphasizes the care needed when interpreting Ca^{2+} imaging data.

3.3 Conclusion

Experiments in HEK cells, showed that all poRhoVRs localized to the cell membrane and were voltage sensitive (**Figure 3.1.6**). poRhoVR **13** had the highest voltage sensitivity (43 %ΔF/F) and poRhoVR **14** had a good combination of brightness and sensitivity (17 %ΔF/F) (**Table 3.1.1**). For these reasons poRhoVR **13** and **14** were further characterized in dissociated rat hippocampal neurons. When monitoring spontaneous action potentials in neuron cultures, poRhoVR **13** had a higher fractional change in fluorescence per action potential than poRhoVR **14** across various concentrations and light powers (**Figure 3.2.3 b**). In contrast poRhoVR **14**, was brighter and reported action potentials with a greater signal to noise ratio (**Figure 3.2.3 a** and **c**). For this reason, poRhoVR **14** was used in continued experiments in neurons. When poRhoVR **14** was used in combination with ChR2 it was possible to activate a single neuron in the field of view and watch its effect on the all the neurons in the field of view, (**Figure 3.2.4**). Dual calcium and voltage imaging of evoked activity in neurons, showed that OGB-AM did not faithfully report firing frequency in the way that poRhoVR **14** did (**Figure 3.2.6-7**). This experiment underscores the limitations of calcium indicators to accurately characterize spiking behavior in neurons and further demonstrates the important role of voltage sensing dyes.

3.4 Imaging Details

HEK293T Cell Culture Information

HEK293T cells were obtained from the UC Berkeley Cell Culture Facility. Cells were passaged and plated onto 12 mm glass coverslips coated with Poly-D-Lysine (PDL; 1 mg/mL; Sigma-Aldrich) to a confluency of approximately 15% and 50% for electrophysiology and imaging, respectively. HEK293T cells were plated and maintained in Dulbecco's modified eagle medium (DMEM) supplemented with 4.5 g/L D-glucose, 10% fetal bovine serum (FBS), and 1% GlutaMax. Cells were maintained at 37 °C in a humidified incubator with 5 % CO_2.

Preparation of Primary Neuron Cultures

Hippocampi were dissected from embryonic day 19 Sprague Dawley rats (Charles River Laboratory) in cold sterile HBSS (zero Ca^{2+}, zero Mg^{2+}). Hippocampal tissue was treated with trypsin (2.5%) for 15 min at 37 °C. The tissue was triturated using fire polished Pasteur pipettes, in minimum essential media (MEM) supplemented with 5% FBS, 2% B-27, 2% 1M dextrose and 1% GlutaMax. The dissociated cells were plated onto 12 mm diameter coverslips

(Fisher Scientific) pre-treated with PDL at a density of 25,000-30,000 cells per coverslip in MEM supplemented media (as above). Neurons were maintained at 37 °C in a humidified incubator with 5 % CO2. After 1 day in vitro (DIV) half of the MEM supplemented media was removed and replaced with Neurobasal media containing 2% B-27 supplement and 1% GlutaMax. Functional imaging was performed on mature neurons 13-20 DIV.

General Imaging Parameters

Imaging experiments were performed on either an upright or an inverted epifluorescence microscope, AxioExaminer Z-1 (Zeiss), equipped with a Spectra-X Light engine LED light (Lumencor), and an OrcaFlash4.0 sCMOS camera (Hamamatsu). The following LED light sources were used; red (631/28 nm bandpass), teal LED (510/25 nm bandpass), cyan (475/34 nm bandpass), violet (390/22 nm bandpass). The microscope was controlled via Slidebook (v6, Intelligent Imaging Innovations) or MicroManager (Studio Version 1.4.22). Imaging was done with a W-Plan-Apo 20x/1.0 objective (20x; Zeiss) or a W-Plan-Apo 63x/1.0 objective (63x; Zeiss). The QUAD emission filter set, a quadruple dichroic mirror (432/38, 509/22, 586/40, 654 nm LP) combined with a quadruple emission filter (430/32 nm, 508/14 nm, 586/30 nm, 708/98 nm), was routinely used. For experiments with simultaneous voltage and calcium imaging a Dual View emission splitter (Optical Insights) was used. The Dual-View contained a 585dcxr dichroic and two emission filters (520/28 nm and 723/68 nm) which separated the calcium (GCaMP or Oregon Green BAPTA-AM) and poRhoVR fluorescence signals.

Voltage Sensitivity Measurements

HEK293T cells were incubated at 37 °C for 20 minutes in an HBSS solution containing 1 μM poRhoVRs. Voltage sensitivity data was acquired using a 20X water immersion objective on an upright epifluorescence microscope. Recordings were binned 4X4 and recorded at an optical sampling rate of 500 Hz. poRhoVRs were imaged with a red LED (ND 75, 30.8 mW/mm^2) and emission was collected with the QUAD filter set (see *General Imaging Parameters*). For electrophysiological experiments in HEK293T cells, pipettes were pulled from borosilicate glass (Sutter Instruments, BF150-86-10), with a resistance of 4–7 MΩ, and were filled with an internal solution; 125 mM potassium gluconate, 1 mM EGTA, 10 mM HEPES, 5 mM NaCl, 10 mM KCl, 2 mM ATP disodium salt, 0.3 mM GTP trisodium salt (pH 7.25, 285 mOsm). Recordings were made with an Axopatch 200B amplifier (Molecular Devices) at room temperature. The signals were digitized with a Digidata 1440A, sampled at 50 kHz and recorded with pCLAMP 10 software (Molecular Devices) on a PC. Fast capacitance was compensated in the on-cell configuration. Recordings were only pursued if series resistance in voltage clamp was less than 30 MΩ. Cells were held at -60 mV and hyper- and de- polarizing steps applied from +100 to -100 mV in 20 mV increments. Analysis of voltage sensitivity in HEK cells was performed using custom MATLAB routines in which a

region of interest (ROI) was automatically selected based on changes in fluorescence intensity. The ROI is then applied as a mask to all frames in the image stack. Fluorescence intensity values were calculated at known baseline and voltage step epochs and used to calculate a percent change in baseline fluorescence (% ΔF/F) per 100 mV change in membrane potential.

Image Analysis

Analysis of voltage sensitivity in HEK cells was performed using custom MATLAB routines in which a region of interest (ROI) was automatically selected based on changes in fluorescence intensity. The ROI is then applied as a mask to all frames in the image stack. Fluorescence intensity values were calculated at known baseline and voltage step epochs and used to calculate a percent change in baseline fluorescence (% ΔF/F) per 100 mV change in membrane potential.

Optical traces of neuronal calcium and voltage activity were obtained by drawing ROIs around the cell bodies of neurons, transfected with GCaMP6s or stained with poRhoVR or OGB-AM, in ImageJ and extracting the mean cellular fluorescence from each frame in the image stack. The mean background fluorescence was subtracted from the mean cellular fluorescence of each frame. ΔF/F values were calculated by first subtracting a mean background value from all raw fluorescence frames to give a background subtracted trace (bkgsub). A baseline fluorescence value (F_{base}) is calculated by averaging the fluorescence of 10 to 20 frames that show no activity. F_{base} was subtracted from each timepoint of the bkgsub trace to yield a ΔF trace. The ΔF was then divided by F_{base} to give ΔF/F traces.

Figure 3.1.1 Quantification of poRhoVR Brightness in HEK Cells.

HEK 293T cells were incubated in a 2 μM HBSS solution of one of poRhoVRs **12**-**15** for 20 min at 37 °C. A mixture of *cis* and *trans* poRhoVR **13** isomers was used. Images were taken using 20x water immersion objective on an upright epifluorescence microscope. poRhoVRs were imaged using a red LED (ND 75, 30.8 mW/mm^2) as the excitation source and 50 ms exposure. Emission was collected with the QUAD filter set (see **General Imaging Parameters**). The median fluorescence of cell ROIs were compared across all four dyes.

Figure 3.1.2 Cellular Characterization of poRhoVR Indicators in HEK Cells.

HEK293T cells were incubated at 37 °C for 20 minutes in an HBSS solution containing the following dyes at 1 μM concentrations: poRhoVR, Rhodamine 123 and Hoechst 33342. Images were taken using W-Plan-Apo 63x/1.0 objective (Zeiss) on an upright epifluorescence microscope. poRhoVR was imaged using a red LED (Neutral Density Setting, ND, 75; 30.8 mW/mm^2) as the excitation source and 100 ms exposure. Emission was collected with a

single emission filter (723/68 nm) after passing through a quadruple dichroic mirror (432/38, 509/22, 586/40, 654 nm LP). Rhodamine 123 was imaged using a cyan LED (ND 75, 51.5 mW/mm^2) and 100 ms exposure. Emission was collected with a single emission filter (540/50 nm) after passing through a dichroic mirror (510 nm LP). Hoechst 33342 was imaged using a violet LED (ND 75, 6.7 mW/mm^2) and 100 ms exposure. Emission was collected using a triple emission filter (473/22 nm, 543/19 nm, 648/98 nm) after passing through a triple dichroic mirror (475/30 nm, 540/25 nm, 642/96 nm).

Figure 3.1.3 Extent of Endocytosis in HEK Cells.

A 1 μM solution of poRhoVR **14** in HBSS was bath applied to HEK293T cells for 20 minutes at 37 °C. The poRhoVR **14** solution was removed and replaced with a 250 nM Calcein-AM solution with 0.1% pluronic in HBSS. The cells were incubated at 37 °C for one of the following times 30, 60, 90 or 120 minutes. For the 0-minute time point poRhoVR **14** and Calcein-AM were coloaded together for 20 minutes. Four areas were imaged for each coverslip. Cells were imaged using a 63X water objective on an upright epifluorescence microscope. Cells were illuminated with a red LED (1.22 mW/mm^2) or a cyan LED (0.82 mW/mm^2). Images were taken at 100 ms exposure setting. Emission was filtered with a QUAD dichroic.

For each coverslip, a total of four images were taken. Each image was analyzed by circling ROIs on the poRhoVR **14** image. The ROIs included only live cells as was determined by the presence of cytosolic Calcein-AM fluorescence. The Pearson's correlation coefficient (PCC) for each ROI in the poRhoVR**14** Calcein-AM images were calculated via MATLAB. As a negative control the Calcein-AM image was rotated 90°, the same ROIs were applied to the rotated image and the PCCs were calculated for each ROI in the unrotated poRhoVR **14** image and the rotated Calcein-AM image. The average PCC for each image was calculated by averaging the PCCs of all the ROIs in the image. The average PCC for each coverslip was calculated by averaging all the areas imaged for each of the coverslips. Dunnett's multiple comparisons test was performed to determine if the differences between the means of the 0-minute time point, and other time points were statistically significant. If the P-values of the pairwise comparisons were less than 0.05 the difference between the means was considered statistically significant. One-way ANOVA followed by Dunnett's multiple comparisons test was performed in GraphPad Prism version 8.4.3. for Windows, GraphPad Software, San Diego, California USA, www.graphpad.com.

Figure 3.1.4 Toxicity of poRhoVR 14 in HEK Cells

A solution of poRhoVR **14**, concentrations ranged from 500 nM to 5 μM, in HBSS was bath applied to HEK293T cells for 20 minutes at 37 °C. Cells were incubated in 0.25% v/v DMSO HBSS solution as a positive control. The first solution was removed and replaced with an HBSS solution of 250 nM Calcein-AM with 0.1% pluronic in HBSS and 1 μM Hoechst 33342. The cells were incubated at 37 °C for an additional 20 minutes. As a negative control cells

were fixed with 4% formaldehyde for 20 minutes and then permeabilized with 0.1% TritonX-100 for 5 minutes. Cells were then stained with Hoechst 33342 and Calcein-AM in the same manner as the other conditions. Four areas were imaged for each coverslip. A total of 4 coverslips were imaged per condition. Cells were imaged using a 20X water objective on an upright epifluorescence microscope. Cells were illuminated with a violet LED (6.68 mW/mm^2) or a cyan LED (7.87 mW/mm^2). Images were taken at 100 ms exposure setting. Emission was filtered with a QUAD dichroic.

1. Use Hoechst 33342 fluorescence to create a binary mask

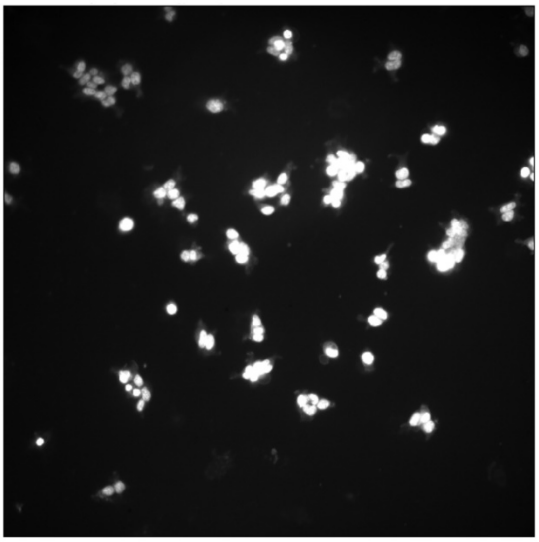

Hoechst 33342 fluorescence image

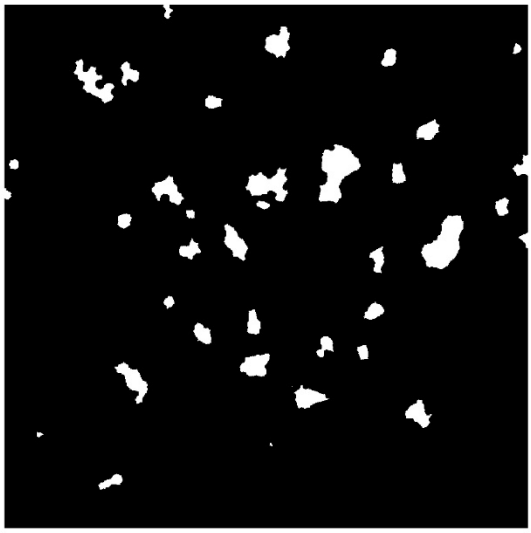

Binary mask generated from Hoechst 33342 image

2. Use the binary mask to generated ROIs that are applied to Hoechst 33342 and Calcein-AM images. The background subtracted fluorescence and PCC coeffcient are determined and averaged for each image.

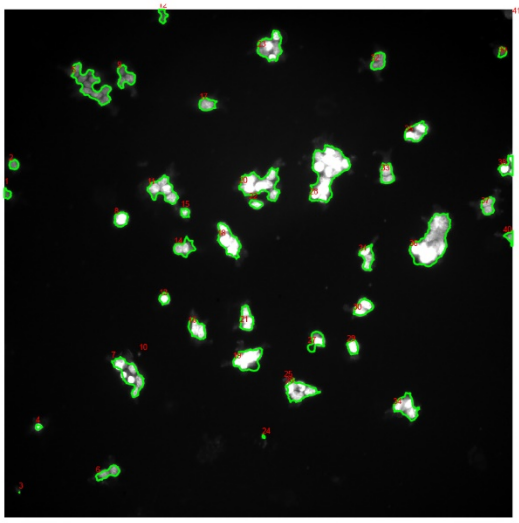

Hoechst 33342 image with ROIs

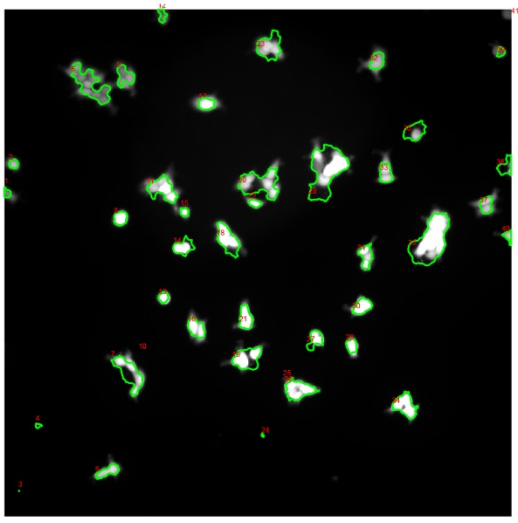

Calcein-AM image with ROIs

Figure 3.4.1 ROI selection for poRhoVR 14 toxicity assay.

During image analysis ROIs were selected as described in **Figure 3.3.1**. For each ROI, the background subtracted fluorescence was calculated for Hoechst 33342 and Calcein-AM images. The PCC value for Hoechst 33342 and Calcein-AM images were also calculated for each ROI. In live cells Hoechst 33342 and Calcein-AM fluorescence overlaps and a PCC of 1 is expected. In dead cells, Hoechst 33342 fluorescence is still visible, but Calcein-AM

fluorescence is not present, and this inverse correlation would lead to an expected PCC value of -1. As a negative control, where a PCC of 0 indicates no correlation, the Calcein-AM image was rotated 90° and PCC values were recalculated for each ROI. ROIs that were smaller than 10 pixels were excluded from the analysis as well as those that did not appear to encompass a nucleus as determined visually. The remaining ROIs were averaged for each image to generate a single value for background subtracted fluorescence and PCC values. Dunnett's multiple comparisons test was performed to determine if the differences between the mean of the control, DMSO treated cells, and the mean of poRhoVR **14** treated cells or fixed cells are statistically significant. If the P-values of the pairwise comparison were less than 0.05 the difference between the means was considered statistically significant. One-way ANOVA followed by Dunnett's multiple comparisons test was performed in GraphPad Prism version 8.4.3. for Windows, GraphPad Software, San Diego, California USA, www.graphpad.com.

Figure 3.1.5 Photostability Comparison Between poRhoVR 14 and BeRST 1.

Due to differences in absorption spectra the absorbances of poRhoVR **14** (λ_{max} = 703 nm) and BeRST **1** (λ_{max} = 658 nm) were matched at 631 nm (central emission wavelength of red LED used for imaging). As a result, HEK293T cells, seeded at 75,000 cells per 12 mm coverslip, were incubated at 37 ˚C in either a 500 nM HBSS solution of poRhoVR or a 300 nM HBSS solution of BeRST **1**. The cells were imaged using a 20X water objective on an upright epifluorescence microscope. Cells were continuously illuminated with a red LED (78.6 mW/mm^2) for 10 minutes and images were taking at 3 second intervals with 50 milliseconds exposure. Emission was collected using a long pass filter (732/68 nm).

For each 10-minute time-lapse three cellular ROIs and a background ROI were circled. The average fluorescence intensity from each ROI was plotted for each frame. The background fluorescence trace was subtracted from each cellular ROI fluorescence trace. The resulting background subtracted trace was normalized by dividing each value by the largest fluorescence value. In order to determine the photobleaching curve for each coverslip, the normalized background subtracted traces for each ROI were averaged. The final graphical representation of the data is the average of the six coverslips analyzed for each dye.

Figure 3.2.1-2 Voltage Imaging in Dissociated Rat Hippocampal Neurons with poRhoVR 13 and 14.

Dissociated rat hippocampal neurons were incubated at 37 ºC for 20 min in an HBSS solution containing 500 nM poRhoVR **13** or **14**. Spontaneous neuronal activity was monitored using a 20X water immersion objective on an upright epifluorescence microscope. The field of view was binned 4X4 and recorded at an optical sampling rate of 500 Hz. poRhoVR **13** and **14** were imaged using a red LED (ND 50, 21.2 mW/mm^2). Emission was collected with the QUAD filter set (see **General Imaging Parameters**).

Figure 3.2.4 All-optical Electrophysiology Using poRhoVR 14 and ChR2.

Dissociated rat hippocampal neurons previously transfected with Channelrhodopsin-2-YFP (ChR2-YFP) were incubated at 37 °C for 20 minutes in an HBSS solution containing 500 nM poRhoVR **14**. ChR2 positive cells were identified by locating YFP expressing neurons using a teal LED (50% max power, 9.2 mW/mm^2). YFP emission was collected via a triple emission filter (473/22 nm, 543/19 nm, 648/98 nm) after passing through a triple dichroic mirror (475/30 nm, 540/25 nm, 642/96 nm). ChR2 was activated by 5 ms pulses of cyan light (2% of max power, 1.92 mW/mm^2). poRhoVR **14** was imaged with a red LED (100% of max power, 78.5 mW/mm^2) and emission was collected with the QUAD filter set (see **General Imaging Parameters**). The field of view was binned 4X4 and recorded at an optical sampling rate of 500 Hz using a 20X water immersion objective on an upright epifluorescence microscope.

Figure 3.2.6-8. Simultaneous Voltage and Calcium Imaging with poRhoVR 14.

Dissociated rat hippocampal neurons previously transfected with GCaMP6s were incubated at 37 °C for 20 minutes in an HBSS solution containing 500 nM poRhoVR **14**. Separately, neurons were loaded with 1 μM OGB-AM and 500 nM poRhoVR with 0.01% pluronic. A red LED (50% of max power, 49.7 mW/mm^2) was the source of excitation light for poRhoVR **14** and a cyan LED was used for GCaMP6s (10% of max power, 7.9 mW/mm^2). Emission from GCaMP6s or OGB-AM and poRhoVR **14** was collected simultaneously with the QUAD filter set and a Dual-View emission splitter (see **General Imaging Parameters**). Extracellular field stimulation was delivered by a Grass Stimulator connected to a recording chamber containing two platinum electrodes (Warner), with triggering provided through a Digidata 1440A digitizer and pCLAMP 10 software (Molecular Devices). Action potentials were triggered by 1 ms 80 V field potentials delivered at 5 Hz. To prevent recurrent activity the HBS bath solution was supplemented with synaptic blockers 10 μM 2,3-Dioxo-6-nitro-1,2,3,4-tetrahydrobenzo[f]quinoxaline-7-sulfonamide (NBQX; Santa Cruz Biotechnology) and 25 μM DL-2-Amino-5-phosphonopentanoic acid (APV; Sigma-Aldrich).

3.5 References

(1) Nagel, G.; Szellas, T.; Huhn, W.; Kateriya, S.; Adeishvili, N.; Berthold, P.; Ollig, D.; Hegemann, P.; Bamberg, E. Cation-Selective Membrane Channel. *Pnas* **2003**, *100* (24), 13940–13945.

(2) Boyden, E. S.; Zhang, F.; Bamberg, E.; Nagel, G.; Deisseroth, K. Millisecond-Timescale, Genetically Targeted Optical Control of Neural Activity. *Nat. Neurosci.* **2005**, *8* (9), 1263–1268. https://doi.org/10.1038/nn1525.

(3) Gee, Kyle; Poot, Martin; Klaubert, Dieter H.; Sun, Wei-Chuan; Mao, F. Fluorinated Xanthene Devrivatives. WO 97/39064, 1997.

(4) Minta, A.; Kao, J. P. Y.; Tsien, R. Y. Fluorescent Indicators for Cytosolic Calcium Based on Rhodamine and Fluorescein Chromophores. *J. Biol. Chem.* **1989**, *264* (14), 8171–8178.

(5) Chen, T. W.; Wardill, T. J.; Sun, Y.; Pulver, S. R.; Renninger, S. L.; Baohan, A.; Schreiter, E. R.; Kerr, R. A.; Orger, M. B.; Jayaraman, V.; Looger, L. L.; Svoboda, K.; Kim, D. S. Ultrasensitive Fluorescent Proteins for Imaging Neuronal Activity. *Nature* **2013**, *499* (7458), 295–300. https://doi.org/10.1038/nature12354.

(6) Collot, M.; Wilms, C. D.; Bentkhayet, A.; Marcaggi, P.; Couchman, K.; Charpak, S.; Dieudonné, S.; Häusser, M.; Feltz, A.; Mallet, J. M. CaRuby-Nano: A Novel High Affinity Calcium Probe for Dual Color Imaging. *Elife* **2015**, *2015* (4), 1–18. https://doi.org/10.7554/eLife.05808.

(7) Diwu, Z.; Guo, H.; Peng, R.; Zhao, Q.; Liu, J.; Liao, J. Carbofluorescein Lactone Ion Indicators and Their Applications. **2014**, *1* (13).

(8) Egawa, T.; Hirabayashi, K.; Koide, Y.; Kobayashi, C.; Takahashi, N.; Mineno, T.; Terai, T.; Ueno, T.; Komatsu, T.; Ikegaya, Y.; Matsuki, N.; Nagano, T.; Hanaoka, K. Red Fluorescent Probe for Monitoring the Dynamics of Cytoplasmic Calcium Ions. *Angew. Chemie* **2013**, *125* (14), 3966–3969. https://doi.org/10.1002/ange.201210279.

(9) Ogasawara, H.; Grzybowski, M.; Hosokawa, R.; Sato, Y.; Taki, M.; Yamaguchi, S. A Far-Red Fluorescent Probe Based on a Phospha-Fluorescein Scaffold for Cytosolic Calcium Imaging. *Chem. Commun.* **2018**, *54* (3), 299–302. https://doi.org/10.1039/c7cc07344e.

(10) Dana, H.; Mohar, B.; Sun, Y.; Narayan, S.; Gordus, A.; Hasseman, J. P.; Tsegaye, G.; Holt, G. T.; Hu, A.; Walpita, D.; Patel, R.; Macklin, J. J.; Bargmann, C. I.; Ahrens, M. B.; Schreiter, E. R.; Jayaraman, V.; Looger, L. L.; Svoboda, K.; Kim, D. S. Sensitive Red Protein Calcium Indicators for Imaging Neural Activity. *Elife* **2016**, *5* (MARCH2016), 1–24. https://doi.org/10.7554/eLife.12727.

(11) Inoue, M.; Takeuchi, A.; Manita, S.; Horigane, S. ichiro; Sakamoto, M.; Kawakami, R.; Yamaguchi, K.; Otomo, K.; Yokoyama, H.; Kim, R.; Yokoyama, T.; Takemoto-

Kimura, S.; Abe, M.; Okamura, M.; Kondo, Y.; Quirin, S.; Ramakrishnan, C.; Imamura, T.; Sakimura, K.; Nemoto, T.; Kano, M.; Fujii, H.; Deisseroth, K.; Kitamura, K.; Bito, H. Rational Engineering of XCaMPs, a Multicolor GECI Suite for In Vivo Imaging of Complex Brain Circuit Dynamics. *Cell* **2019**, *177* (5), 1346-1360.e24. https://doi.org/10.1016/j.cell.2019.04.007.

(12) Qian, Y.; Piatkevich, K. D.; Mc Larney, B.; Abdelfattah, A. S.; Mehta, S.; Murdock, M. H.; Gottschalk, S.; Molina, R. S.; Zhang, W.; Chen, Y.; Wu, J.; Drobizhev, M.; Hughes, T. E.; Zhang, J.; Schreiter, E. R.; Shoham, S.; Razansky, D.; Boyden, E. S.; Campbell, R. E. A Genetically Encoded Near-Infrared Fluorescent Calcium Ion Indicator. *Nat. Methods* **2019**, *16* (2), 171–174. https://doi.org/10.1038/s41592-018-0294-6.

(13) Kalko, E. K. V; Dukas, R.; Ratcliffe, J. M.; Teeling, E. C.; Haven, N.; Fattu, J. M.; Bates, M. E.; Simmons, J. a; Riquimaroux, H.; Surlykke, A.; Bouffard, F. H.; Lee, D. N.; Dear, S. P.; Horiuchi, T. K.; Krishnaprasad, P. S.; Moss, C. F.; Schuller, G.; Brudzynski, S. M.; Syme, D. a; Hollingworth, S.; Lindstedt, S. L.; Baylor, S. M.; Mead, a F.; Rome, L. C.; Goller, F.; Spierts, I. L. Y.; Leeuwen, J. L. Van; Schachat, F.; Rossmanith, G. H.; Hoh, J. F. Y.; Kelley, D. B.; Vater, M. a; Zhao, Y.; Kalko, E. K. V; Dukas, R.; Ratcliffe, J. M.; Teeling, E. C.; Haven, N.; Fattu, J. M.; Bates, M. E.; Simmons, J. a; Riquimaroux, H.; Surlykke, A.; Bouffard, F. H.; Lee, D. N.; Dear, S. P.; Horiuchi, T. K.; Krishnaprasad, P. S.; Moss, C. F.; Schuller, G.; Brudzynski, S. M.; Syme, D. a; Hollingworth, S.; Lindstedt, S. L.; Baylor, S. M.; Mead, a F.; Rome, L. C.; Goller, F.; Spierts, I. L. Y.; Leeuwen, J. L. Van; Schachat, F.; Rossmanith, G. H.; Hoh, J. F. Y.; Kelley, D. B.; Vater, M. a. An Expanded Palette of Genetically Encoded Calcium Indicators. *Cell* **2011**, *557* (September), 1888–1891.

(14) Marvin, J. S.; Borghuis, B. G.; Tian, L.; Cichon, J.; Harnett, M. T.; Akerboom, J.; Gordus, A.; Renninger, S. L.; Chen, T.; Cornelia, I.; Orger, M. B.; Schreiter, E. R.; Demb, J. B.; Gan, W.; Hires, A.; Looger, L. L. An Optimized Fluorescent Probe Fo Visualizing Glutamat Neurotransmission. *Nat. Methods* **2013**, *10* (2), 162–170. https://doi.org/10.1038/nmeth.2333.An.

(15) Patriarchi, T.; Cho, J. R.; Merten, K.; Howe, M. W.; Marley, A.; Xiong, W. H.; Folk, R. W.; Broussard, G. J.; Liang, R.; Jang, M. J.; Zhong, H.; Dombeck, D.; von Zastrow, M.; Nimmerjahn, A.; Gradinaru, V.; Williams, J. T.; Tian, L. Ultrafast Neuronal Imaging of Dopamine Dynamics with Designed Genetically Encoded Sensors. *Science (80-.).* **2018**, *360* (6396). https://doi.org/10.1126/science.aat4422.

(16) Schindelin, J.; Arganda-Carreras, I.; Frise, E.; Kaynig, V.; Longair, M.; Pietzsch, T.; Preibisch, S.; Rueden, C.; Saalfeld, S.; Schmid, B.; Tinevez, J. Y.; White, D. J.; Hartenstein, V.; Eliceiri, K.; Tomancak, P.; Cardona, A. Fiji: An Open-Source Platform for Biological-Image Analysis. *Nat. Methods* **2012**, *9* (7), 676–682. https://doi.org/10.1038/nmeth.2019.

(17) Johnson, L. V.; Walsh, M. L.; Chen, L. B. Localization of Mitochondria in Living Cells with Rhodamine 123. *Proc. Natl. Acad. Sci. U. S. A.* **1980**, *77* (2 II), 990–994.

https://doi.org/10.1073/pnas.77.2.990.

(18) Cooksey, C. J. Quirks of Dye Nomenclature. 5. Rhodamines. *Biotech. Histochem.* **2016**, *91* (1), 71–76. https://doi.org/10.3109/10520295.2015.1074287.

(19) Hospital, L.; Division, C. G. SPECTRAL STUDIES ON FOR FLUORESCENT ACID AND SYNTHESIS RELATED DETECTION OF Absorption , Fluorescence and Circular Dichroism Deoxyribonucleic Acid (DNA) Complexes Are Consistent of Dye-Binding One Type , Which Persists Is Highly Specific for Adenine-Thy. **1976**, 24–33.

(20) Wiederschain, G. Y. The Molecular Probes Handbook. A Guide to Fluorescent Probes and Labeling Technologies: (I. Johnson and M. Spence (Eds.) 11th Edition, Life Technologies, 2010, 1060 p., $100). *Biochem.* **2011**. https://doi.org/10.1134/S0006297911110101.

(21) Huang, Y. L.; Walker, A. S.; Miller, E. W. A Photostable Silicon Rhodamine Platform for Optical Voltage Sensing. *J. Am. Chem. Soc.* **2015**. https://doi.org/10.1021/jacs.5b06644.

(22) Deal, P. E.; Kulkarni, R. U.; Al-Abdullatif, S. H.; Miller, E. W. Isomerically Pure Tetramethylrhodamine Voltage Reporters. *J. Am. Chem. Soc.* **2016**, *138* (29), 9085–9088. https://doi.org/10.1021/jacs.6b05672.

(23) Homma, R.; Baker, B. J.; Jin, L.; Garaschuk, O.; Konnerth, A.; Cohen, L. B.; Zecevic, D. Wide-Field and Two-Photon Imaging of Brain Activity with Voltage- and Calcium-Sensitive Dyes. *Philos. Trans. R. Soc. B Biol. Sci.* **2009**, *364* (1529), 2453–2467. https://doi.org/10.1098/rstb.2009.0084.

(24) Xu, Y.; Zou, P.; Cohen, A. E. Voltage Imaging with Genetically Encoded Indicators. *Curr. Opin. Chem. Biol.* **2017**, *39*, 1–10. https://doi.org/10.1016/j.cbpa.2017.04.005.

(25) Wilt, B. A.; Fitzgerald, J. E.; Schnitzer, M. J. Photon Shot Noise Limits on Optical Detection of Neuronal Spikes and Estimation of Spike Timing. *Biophys. J.* **2013**, *104* (1), 51–62. https://doi.org/10.1016/j.bpj.2012.07.058.

(26) Hendel, T.; Mank, M.; Schnell, B.; Griesbeck, O.; Borst, A.; Reiff, D. F. Fluorescence Changes of Genetic Calcium Indicators and OGB-1 Correlated with Neural Activity and Calcium in Vivo and in Vitro. *J. Neurosci.* **2008**, *28* (29), 7399–7411. https://doi.org/10.1523/JNEUROSCI.1038-08.2008.

(27) Lock, J.T; Parker, I. F. A Comparison of Ca2+ Indicators for Imaging Local Ca2+ Signals Cultured in Cells. *Cell Calcium* **2015**, *58* (6), 638–648. https://doi.org/10.1117/12.2549369.Hyperspectral.

(28) Tang, S.; Reddish, F.; Zhuo, Y.; Yang, J. J. Fast Kinetics of Calcium Signaling and Sensor Design. *Curr. Opin. Chem. Biol.* **2015**, *27*, 90–97. https://doi.org/10.1016/j.cbpa.2015.06.014.

(29) Lapray, D.; Lasztoczi, B.; Lagler, M.; Viney, T. J.; Katona, L.; Valenti, O.;

Hartwich, K.; Borhegyi, Z.; Somogyi, P.; Klausberger, T. Behavior-Dependent Specialization of Identified Hippocampal Interneurons. *Nat. Neurosci.* **2012**, *15* (9), 1265–1271. https://doi.org/10.1038/nn.3176.

(30) Llinas, B. Y. R.; Sugimori, M. Electrophysiological Properties of in Vitro Purkinjie Cell Somata in Mammalian Cerebellar Slices. *J. Physiol.* **1980**, *305* (1), 171–195.

(31) Tochitsky, I.; Polosukhina, A.; Degtyar, V. E.; Gallerani, N.; Smith, C. M.; Friedman, A.; Van Gelder, R. N.; Trauner, D.; Kaufer, D.; Kramer, R. H. Restoring Visual Function to Blind Mice with a Photoswitch That Exploits Electrophysiological Remodeling of Retinal Ganglion Cells. *Neuron* **2014**, *81* (4), 800–813. https://doi.org/10.1016/j.neuron.2014.01.003.

Chapter 4

Use of poRhoVR in a Mouse Model for Retinal Degeneration

Portions of this work appeared as a preprint:

Gonzalez, M. A.; Walker, A. S.; Cao, K. J.; Lazzari-Dean, J. R.; Settineri, N.; Kong, E.-J.; Kramer, R. H.; Miller, E. W.; Voltage imaging with a NIR-absorbing phosphine oxide rhodamine voltage reporter. *ChemRxiv.* **2019**, Preprint: DOI: 10.26434/chemrxiv.10025789.v1.

Portions of this work were performed in collaboration with the following people:

Alison Walker and Kevin Cao assisted with imaging.

4.0 Introduction

The NIR (>700 nm) excitation and emission spectra of poRhoVR dyes, along with their good voltage sensitivity and compatibility with commonly used optogenetic sensors and actuators, makes poRhoVR **14** a promising candidate for mapping voltage dynamics in intact neural tissue like retinas. The retina is a highly organized and accessible outpost of the central nervous system. Light responses initiated in rods and cones are synaptically transmitted to bipolar cells, which activate retinal ganglion cells (RGCs). RGCs generate the action potentials that carry visual information to the brain. In normally functioning retinas, the intrinsic light sensitivity of photoreceptors in rods and cones complicates optical imaging of both voltage and Ca^{2+} transients in RGCs. We applied poRhoVR to investigate membrane potential dynamics in retinas from a mouse model of retina degeneration.

In particular, retinas from *rd1* mice are an attractive model system in which functional imaging can be applied to explore mechanisms occurring in inherited visual disorders, including the degenerative disorder retinitis pigmentosa (RP).[1] Lacking a functional β subunit of rod cGMP phosphodiesterase (βPDE), *rd1* mice suffer rapid loss of rod cells, followed by a delayed loss of cone cells. As a result, these mice lack rods and cones and are therefore blind, yet still retain functional RGCs in the ganglion cell layer (GCL). Therefore, apart from the rare melanopsin-expressing, intrinsically sensitive RGC (<2% of the RGCs) the surviving RGCs in *rd1* retinas have no light response and continue to receive synaptic input from bipolar cells. RGCs in *rd1* mice develop hyperactivity, firing spontaneous bursts of spikes in darkness. This phenomenon has been observed only through electrophysiological recordings that sample only a fraction of cells, or by Ca^{2+} imaging with GCaMP expressed in RGCs, which is indirect and has low temporal resolution.[2,3] The precise mechanisms underlying hyperactivity are not understood, and voltage imaging could reveal where in the retinal circuitry this activity originates and how it propagates from neuron to neuron.

4.1 poRhoVR 14 Staining of Mice Retina

To explore the interplay between neuronal voltage and Ca^{2+} signaling in this model of retinopathy, we prepared *ex vivo*, flat-mount retinas from *rd1* mice that express GCaMP6f in retinal ganglion cells (RGCs). Bath application of poRhoVR **14** (5 μM, in oxygenated ACSF) results in diffuse poRhoVR staining throughout the tissue, as assessed by widefield fluorescence microscopy (**Figure 4.4.1**, **Figure 4.4.2**) and confocal microscopy (**Figure 4.1.1**). Retina staining by BeRST 1 and poRhoVR **14** were compared using confocal microscopy. BeRST 1 is another voltage sensing dye whose absorption and emission are slightly blue shifted to that of poRhoVR **14**.

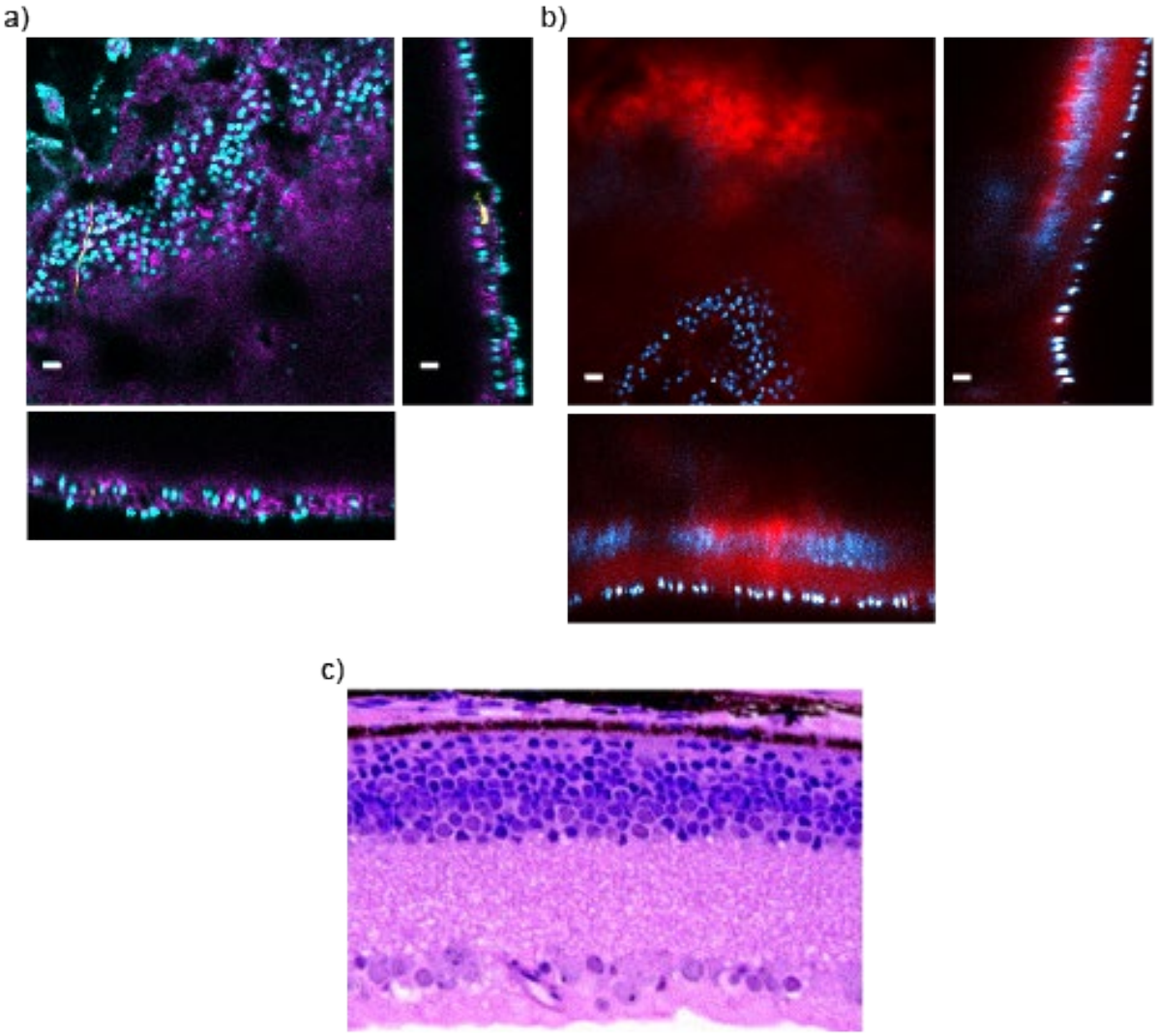

Figure 4.1.1 Depth of poRhoVR **14** staining in *rd1* Thy1-YFP mouse retina. **a)** Confocal images of a 2-hour loading with poRhoVR **14**, 5 μM, and Hoechst 33342, 10 μM, bath applied to a section of *rd1* Thy1-YFP mouse retina showing the XZ and YZ cross sections. Scale bars are 20 μM. **b)** Confocal images of a 4-hour loading of BeRST **1**, 5 μM, and Hoechst 33342, 10 μM, bath applied to a section of *rd1* Thy1-YFP mouse retina showing the XZ and YZ cross sections. Scale bars are 20 μM. **c)** Histology staining of *rd1* mouse retina at 21 days of age (Chang, B.; *et al. Vision Research*, 42, 517-525 (2002)).

Z-stacks obtained via confocal microscopy showed that 4 hours of staining with BeRST **1** labels multiple retinal cell layers (**Figure 4.1.1 b**) whereas 2 hours of loading with poRhoVR **14** labelled one layer (**Figure 4.1.1 a**). BeRST **1** staining permeated through the retinal ganglion cell layer and the bipolar and amacrine cell layer. This was possibly a result of the longer loading times for BeRST **1**, around 4 hours, and the shorter poRhoVR **14** times, around 2 hours. Better staining can possible be achieved with poRhoVR **14** with longer loading times.

4.2 BENAQ and poRhoVR 14

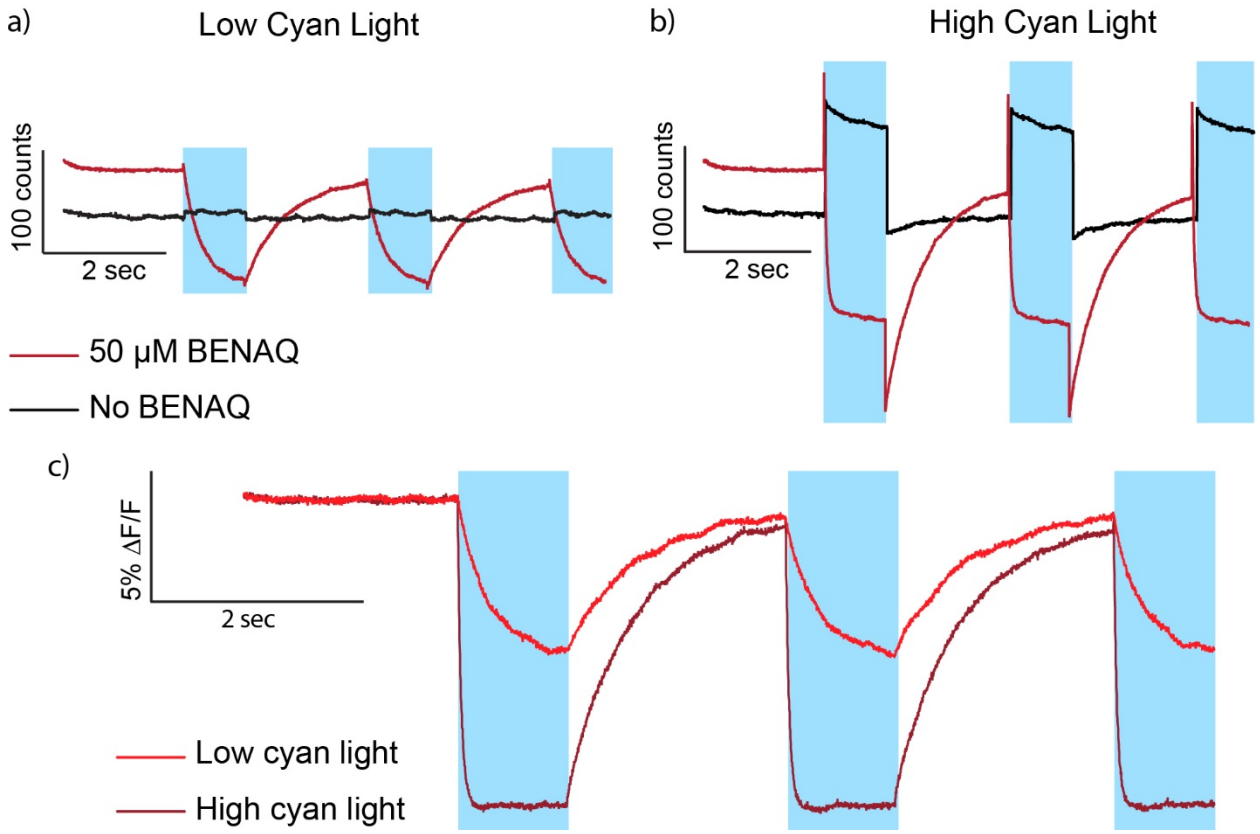

Figure 4.2.1 poRhoVR 14 traces from *rd1* retina treated with BENAQ. poRhoVR **14** traces recorded from sections of *rd1* retina stained with 5 µM poRhoVR **14** and/or 50 µM BENAQ while irradiated with **a)** low (0.99 mW/mm^2) or **b)** high (8.77 mW/mm^2) levels of cyan light (475 nm) at the times indicated by the blue rectangles. The y-axis is labeled as fluorescence counts. poRhoVR **14** traces from retina without BENAQ were subtracted from poRhoVR **14** traces recorded in the presence of BENAQ at **c)** low and high levels of cyan light. The y-axis is labeled as the fractional change in poRhoVR **14** fluorescence.

Due to the lack of photoceptors, *rd1* retina lack sensitivity to light. This sensitivity can be partially restored using photoswitch compounds based on an azobenzene scaffold.[3–5] BENAQ is an azobenzene photoswitch that in the absence of cyan light exists in a *trans* configuration and blocks hyperpolarization-activated cyclic nucleotide-gated (HCN) channels in RGCs.[4,5] Blockage of HCN channels prevents the depolarization of RGCs resulting in inhibition of action potentials. Upon irradiation with cyan light, BENAQ converts to the *cis* configuration and no longer blocks HCN channels. This leads to RGC depolarization and increased firing. We sought to take advantage of BENAQ to record activity in the retina evoked by cyan light. During this experiment, retinal tissue was stained with 5 µM poRhoVR **14** and then treated with 50 µM BENAQ for 30 minutes. The retinal tissue was constantly illuminated with red light and flashed with a second of cyan light every 2 seconds over the course of imaging experiment. Imaging lasted for 10 seconds total. The poRhoVR **14** fluorescence traces showed

sharp decreases in fluorescence in the presence of cyan light that slowly recovered once the cyan light was shut off (**Figure 4.2.1 a**). At high levels of cyan light cross excitation of poRhoVR **14** leads to a small increase in fluorescence (**Figure 4.2.1 b**, No BENAQ). As a result, there is an additional drop in fluorescence after cyan light is shut off in retinal tissue imaged with BENAQ (**Figure 4.2.1 b**). At low levels of cyan light, cross excitation of poRhoVR **14** does not lead to a detectable increase in fluorescence (**Figure 4.2.1 a**, No BENAQ). Cross excitation of poRhoVR **14** can be accounted for by subtracting the traces recorded with poRhoVR **14** only from those recorded in the presence of BENAQ (**Figure 4.2.1 c**). The resulting traces show activity that does not match the expected bursts of action potentials that have been recorded with multielectrode arrays previously and instead seemed to show a rapid hyperpolarization under cyan light followed by a gradual depolarization under red light.

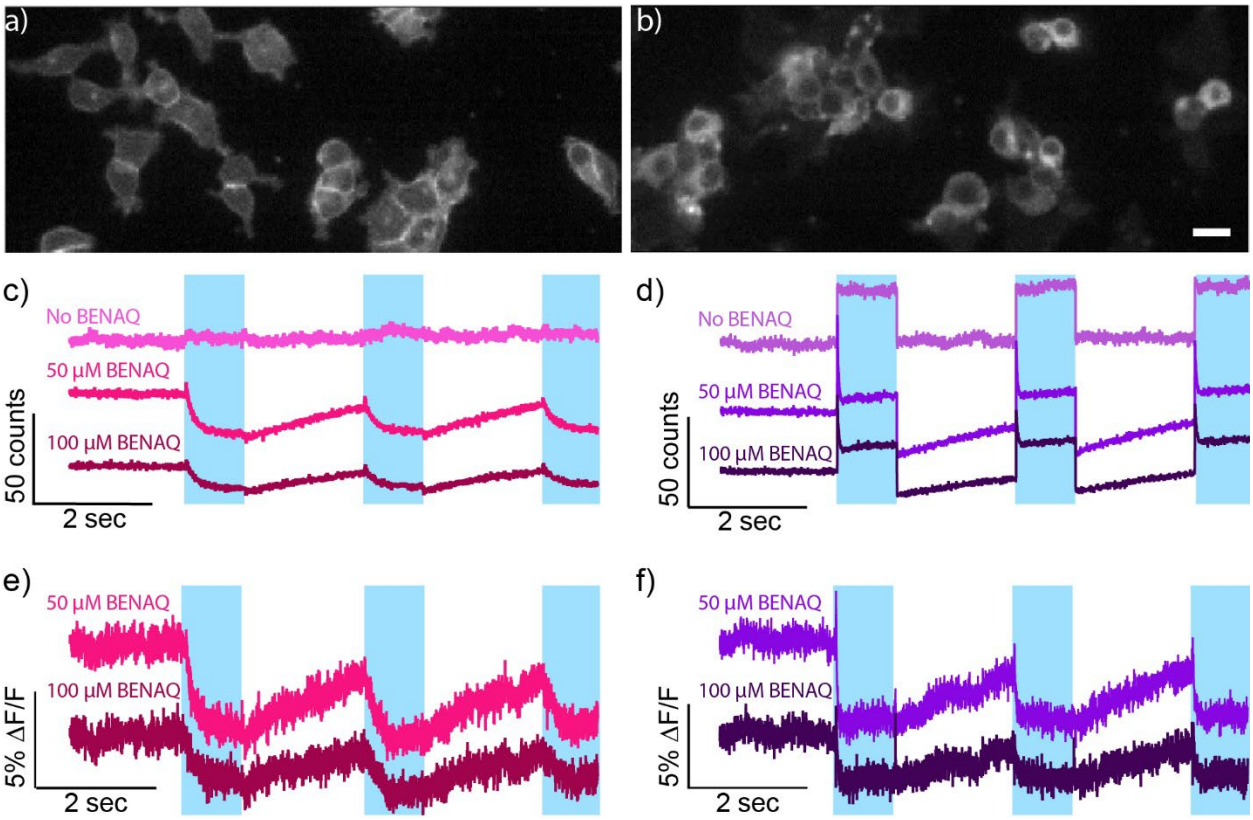

Figure 4.2.2. BENAQ in HEK cells. **a)** Widefield epifluorescence images of HEK cells loaded with 1 µM poRhoVR **14 b)** and 50 µM BENAQ. Scale bar 20 µm. **c)** poRhoVR **14** traces from samples that were illuminated with low (0.99 mW/mm^2) or **d)** high (8.72 mW/mm^2) levels of cyan light at the times indicated by the blue rectangles. The y-axis is labeled as fluorescence counts. poRhoVR **14** traces from HEK cells without BENAQ were subtracted from poRhoVR **14** traces in the presence of BENAQ at **e)** low and **f)** high levels of cyan light.

The same experiment was repeated in HEK cells to confirm that the changes in poRhoVR **14** fluorescence corresponded to changes in RGC activity evoked by BENAQ. Since HEK cells are non-excitable cells that do not express HCN channels,[6] BENAQ should have no effect on

cellular membrane potential and as a result there should be no changes in the fluorescence of poRhoVR **14**. However, as shown in **Figure 4.2.2**, the fluorescence of poRhoVR **14** decreased upon irradiation with cyan light both at low and high levels so long as BENAQ was present. As mentioned before, high levels of cyan light cross excitation of poRhoVR **14** leads to a small increase in fluorescence (**Figure 4.2.2 d**, No BENAQ). Consequently, there is an additional drop in fluorescence after cyan light is shut off in HEK cells imaged with BENAQ (**Figure 4.2.2 d**). Once poRhoVR **14** traces recorded in the absence of BENAQ are subtracted from those collected in the presence of BENAQ, it becomes clear that the combination of cyan light and BENAQ quench poRhoVR **14** fluorescence. The quenching effects of BENAQ prevented us from using it to stimulate RGC activity, therefore we turned to pharmacological manipulations of activity.

4.3 Ivabradine and poRhoVR 14

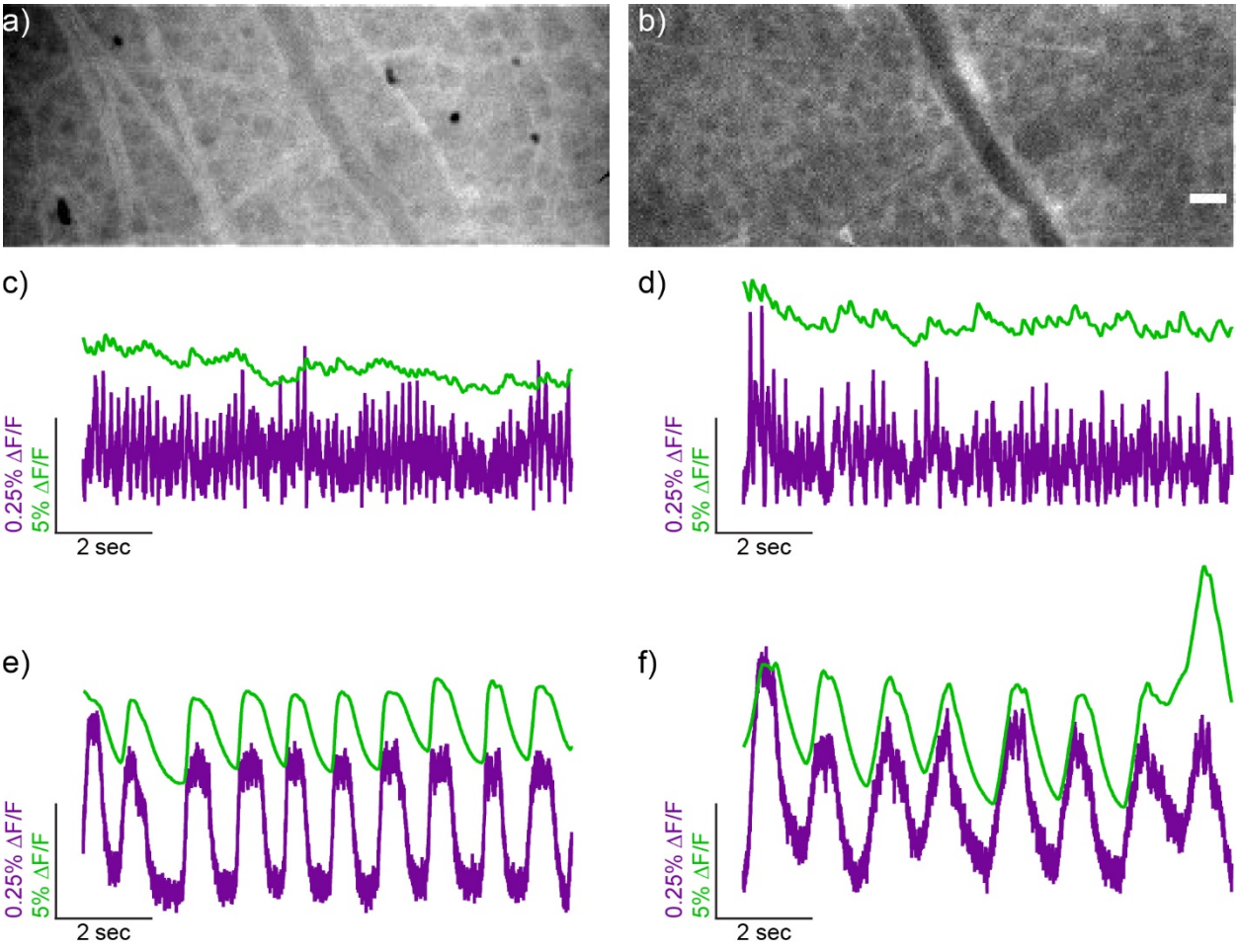

Figure 4.3.1 Ivabradine in *rd1* retina. Widefield epifluorescence image of a section of *rd1* retina stained with **a)** 5 μM poRhoVR **14** and expresses **b)** GCaMP 6f under a synapsin promotor. Scale bar 20 μm. poRhoVR **14** and

GCaMP6f traces from **c)** untreated tissue, control, **d)** tissue that has been treated with 50 μM ivabradine, **e)** synaptic blockers or **f)** ivabradine and synaptic blockers.

Ivabradine is an HCN channel antagonist that causes burst like firing in RGCs.[5,7] We used ivabradine to evoke activity in retina but when compared to an untreated control sample we did not detect major changes in activity using poRhoVR **14** (**Figure 4.3.1 c** and **d**). In contrast, retinal tissue treated with synaptic blockers (**Figure 3.3.1 e**) showed major waves of activity and addition of ivabradine only slightly altered the activity induced by synaptic blockers (**Figure 4.3.1 f**). In each condition, poRhoVR **14** traces correlated well to the GCaMP6f traces that were recorded simultaneously. From this data we concluded that synaptic blockers produced a more robust response when compared to ivabradine. We went on to confirm the changes in activity from synaptic blockers using a multi-electrode array.

4.4 Voltage and Ca2+ Imaging and Electrode Recording in a Mouse Model of Retina Degeneration

In retinas from *rd1* mice, we observed spontaneous oscillations of poRhoVR **14** fluorescence (**Figure 4.4.1 d-h**, magenta traces). To confirm that these changes in poRhoVR **14** dynamics correspond to voltage changes in RGCs, we paired voltage imaging with multi-electrode array (MEA) recordings of extracellular potential.

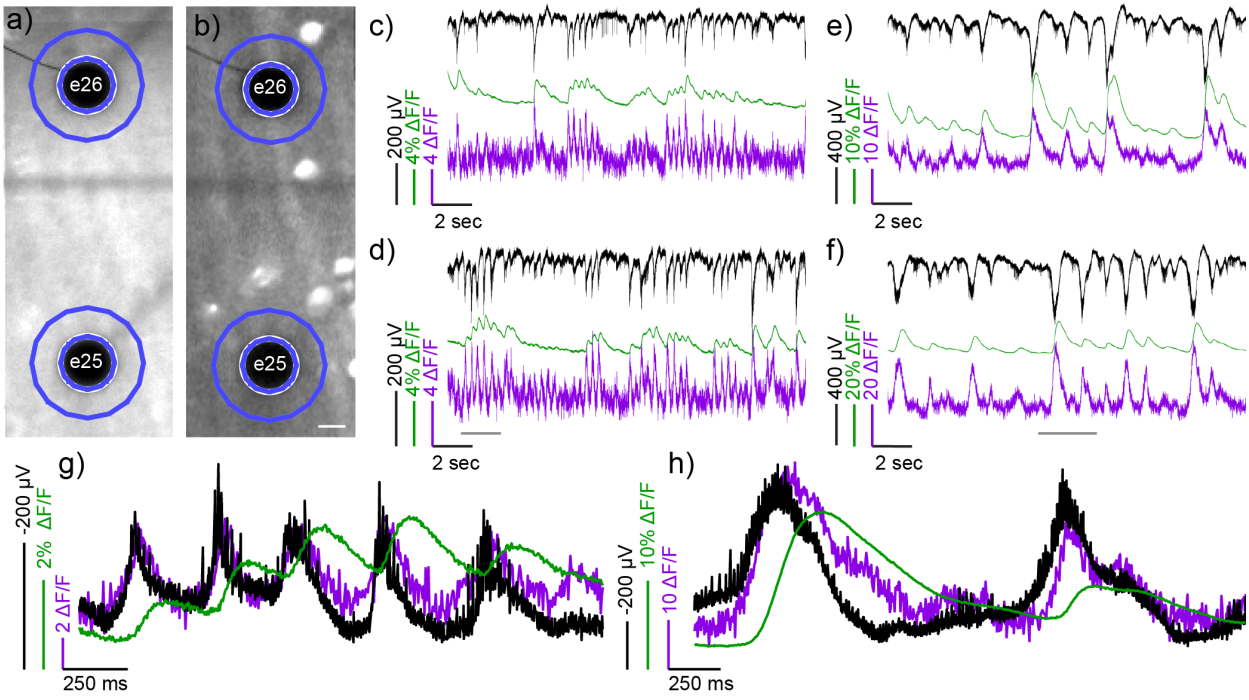

Figure 4.4.1 Simultaneous mapping of electrical and Ca^{2+} activity using poRhoVR, GCaMP6f and multi-electrode arrays (MEA) in *ex vivo* retinas from *rd1* mice. Widefield fluorescence micrographs of retina stained with **a)** poRhoVR **14**; the retinal ganglion cells (RGCs) express **b)** GCaMP6f. The black dots are MEA

electrodes, labeled numerically, underneath the retina. Scale bar is 20 μm. Recordings **(c-f)** depict MEA, GCaMP6f, and poRhoVR **14** signals vs. time. Traces are as follows: raw MEA electrical signal (black), bleach corrected poRhoVR **14** ΔF/F (arbitrary units) (magenta), and GCaMP6f ΔF/F (%) (green). Optical signals are from the regions of interest (ROIs) indicated in blue in panels (a) and (b). Panels (c) and (d) depict the spontaneous activity in the retina prior to addition of synaptic blockers. Panels (e) and (f) show MEA, GCaMP6f, and poRhoVR **14** signals 15 min. after the addition of synaptic blockers. Panels c and e correspond to signals associated with electrode 26 (e26), and panels (d) and (f) correspond to signals associated with electrode 25 (e25). Panels (g) and (h) show zoomed-in regions of e25, from the period of time indicated by a grey bar in panel (d) and f, respectively. In panels g and h, the MEA signal (black) is inverted to facilitate comparison with optical voltage recordings with poRhoVR **14** (magenta).

The poRhoVR **14**-stained retinas were mounted on a 64-channel MEA to simultaneously record transmembrane potential (poRhoVR **14**), extracellular potential (MEA), and Ca^{2+} transients (GCaMP6f) in many RGCs. Simultaneous transmembrane voltage imaging and MEA recording of extracellular potentials (black traces) confirms that poRhoVR **14** (magenta traces) accurately reports changes in transmembrane potential in RGCs of the retina (**Figure 4.4.1 c-f**). The time courses of the MEA signals (black) and poRhoVR **14** signals (magenta) match well, establishing that poRhoVR **14** senses voltage changes in mouse retina. The signs of the MEA and poRhoVR **14** signals are inversely related (**Figure 4.4.1 c-f**): poRhoVR measures transmembrane potential, while MEA records extracellular potentials. A zoomed-in view of poRhoVR and MEA signals (**Figure 4.4.1 g** and **h**), where the black MEA signals have been inverted to enable better comparisons, show excellent correspondence between the optically recorded transmembrane potential measured with poRhoVR (magenta) and the MEA recording (black).

Voltage imaging reveals spontaneous membrane potential depolarizations that appear clustered in bursts throughout the imaging session (**Figure 4.4.1 c** and **d**, magenta). These optically-recorded oscillatory bursts are, to our knowledge, the first direct imaging of membrane potential dynamics in *rd1* retinas, and are consistent with previous MEA recordings in *rd1* retinas.[8,9] GCaMP6f recordings from the same areas revealed slower, Ca^{2+} transients that were delayed relative to increases in the transmembrane potential measured by poRhoVR **14** fluorescence (**Figure 4.4.1 c** and **d**, green). This lag between Ca^{2+} and voltage is like our observations of simultaneous Ca^{2+} / voltage imaging in hippocampal neurons (**Figure 4.4.1 c-e**) and provides the first direct and simultaneous observation of voltage and Ca^{2+} in the mouse retina.

Voltage imaging with poRhoVR **14** enables dissection of the temporal evolution of neuronal activity in *rd1* retina. Synaptic isolation of RGCs via blockade of all major forms of excitatory and inhibitory synaptic transmission results in evolution of activity from short, unsynchronized firing patterns (**Figure 4.4.1 c**, **d**, and **g**) to synchronous and sustained firing (**Figure 4.4.1 e**, **f**, and **h**), consistent with the idea that the driver of this behavior is presynaptic. {Stasheff, 2008 #98} Voltage imaging with poRhoVR also allows investigation of the spatial differences in voltage dynamics with the retina. Fluorescence was recorded from a region of interest (ROI) composed of a ring with a width approximately matching that of an RGC (~10 μm) around the MEA electrode (**Figure 4.4.1 a** and **b**). This enables a direct

comparison to extracellular potentials recorded by the MEA (**Figure 4.4.1 c** and **d**, black). For the two electrodes visible in the recording image (**Figure 4.4.1 a** and **b**), the MEA recording is closely matched by the poRhoVR dynamics (**Figure 4.4.1 c** and **d**, black vs. magenta).

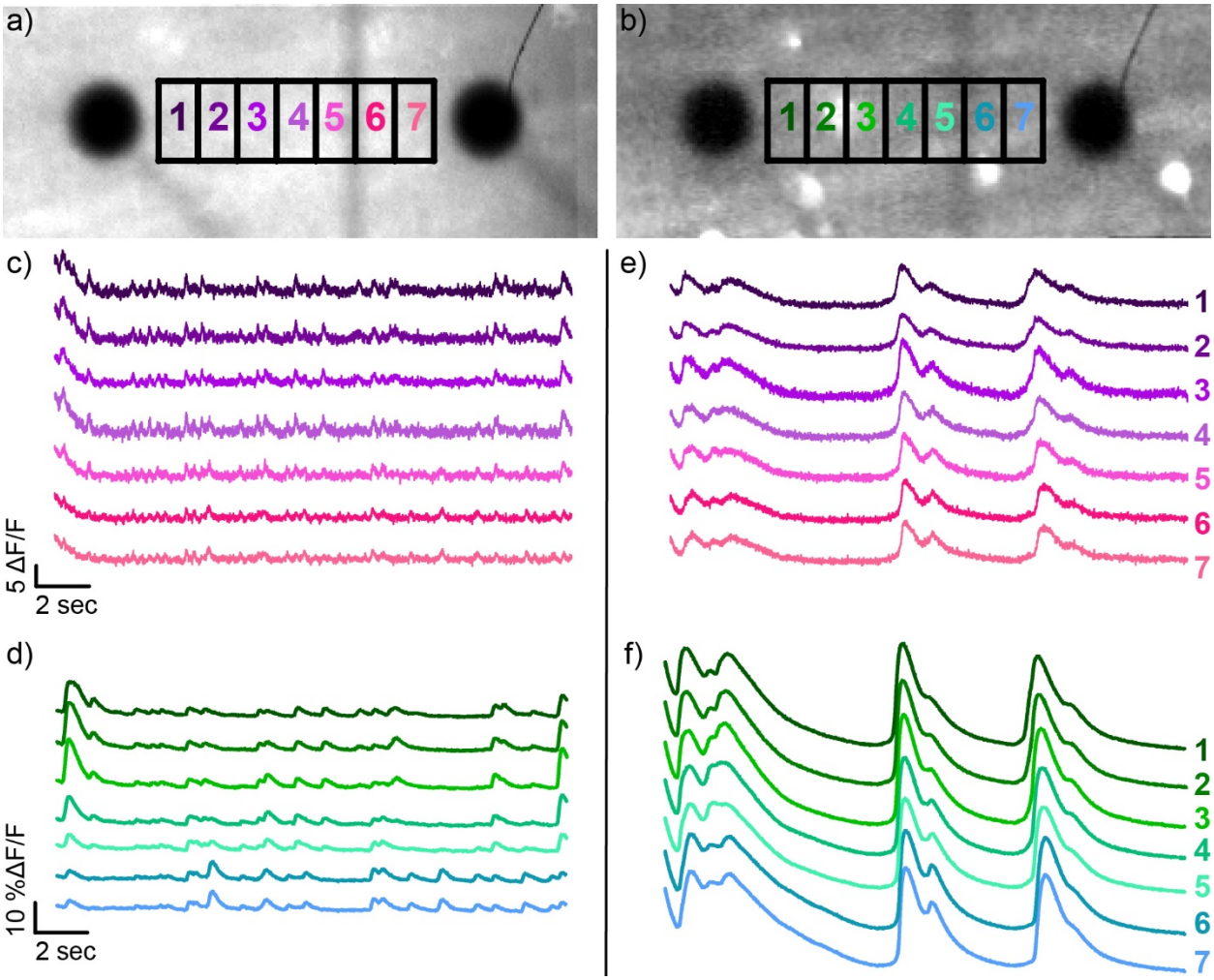

Figure 4.4.2 Spatial evolution of voltage signals in *rd1* mouse retina, monitored by poRhoVR **14**. **a)** Widefield, epifluorescence image of *rd1* mouse retina stained with poRhoVR **14** and expressing **b)** GCaMP6f. The black circles are the electrodes, labeled "e25" and "e26". Rectangles, outlined in black, indicate regions of interest. Plots of relative change in fluorescence (arbitrary units) from either **c)** poRhoVR **14** or **d)** GCaMP6 vs time for the ROIs indicated in panel (a) before blocking synaptic transmission pharmocologically. Fluorescence traces after the addition of synaptic blockers from **e)** poRhoVR **14** and **f)** GCaMP6f.

The use of poRhoVR allows examination of the spatial relationships of voltage changes at locations distant from electrodes (**Figure 4.4.2**). Imaging of poRhoVR **14** signals recorded in ROIs in between electrodes reveal a unique activity profile that is not fully recapitulated by ROIs near the respective electrodes (**Figure 4.4.2**), highlighting the ability of poRhoVR **14** to map the spatial extent of voltage dynamics in retina. Once synaptic transmission is blocked pharmacologically, (**Figure 4.4.2**), its activity across the field of view becomes synchronous

and indistinguishable in the across the various ROIs. This methodology could prove a promising starting point for mapping the dendritic fields of RGCs by probing where voltage dynamics become convoluted with additional signals.

4.5 Conclusion

poRhoVR **14** can be bath applied to *rd1* mice retina, (**Figure 4.1.1**). Confocal imaging showed that over the course of 2 hours, poRhoVR **14** stained only one layer of cells (**Figure 4.1.1 a**). Compared to wild type retina, *rd1* retina have only two primary layers of cells because they lack photoreceptors. Over the course of 4 hours, BeRST 1 was able to stain both layers of cells (**Figure 4.1.1 b**). To improve labeling, incubation time with poRhoVR **14** should be extended to 4 hours. Various attempts were made to evoke activity in retinal ganglion cells (RGCs). The first involved the use of the photoswitch BENAQ[4], (**Figure 4.2.1**). This approach led to the quenching of poRhoVR **14** fluorescence (**Figure 4.2.2**). Since poRhoVR **14** has been shown to work well alongside ChannelRhodopsin-2 (ChR2)[10,11] in neurons (**Figure 3.2.4**) future experiments can be done with retinal tissue expressing ChR2. In this way light can be used to activate RGCs in a time specific manner, allowing us to directly correlate activity caused by ChR2 activation to changes in poRhoVR **14** fluorescence. Both BENAQ and ChR2 require the use of cyan light for activation, making them incompatible with GCaMP6f and highlighting the need for redshifted voltage indicators such as poRhoVR **14**. We next focused on inducing changes in RGC activity pharmacologically with ivabradine (**Figure 4.3.1**). In this experiment we found that synaptic blockers alone produced a more robust response than ivabradine (**Figure 4.3.1**). To confirm that the changes in poRhoVR **14** fluorescence correlated with changes in membrane potential, we recorded electrical signals and fluorescence emission simultaneously using a multi-electrode array (MEA) alongside poRhoVR**14** and GCaMP6f (**Figure 4.4.1**). MEA recordings aligned with poRhoVR **14** traces from regions of interest (ROIs) surrounding the electrodes (**Figure 4.4.1**). In the area between the electrodes, poRhoVR **14** was able detect differences in activity providing greater spatial resolution than is possible with an MEA (**Figure 4.4.2**) and greater temporal resolution than is possible with GCaMP6f (**Figure 4.4.1 g** and **h**).

4.6 Imaging Details

Figure 4.4.1-2 Simultaneous mapping of electrical and Ca2+activity using poRhoVR, GCaMP6s and multi-electrode 370arrays (MEA) in ex vivo retinas from rd1 mice

Retinas were dissected from 3-month-old heterozygous rd1-GCaMP6f mouse in artificial cerebral spinal fluid (ACSF). ACSF was prepared with the following: NaCl (119 mM), KCl (2.5 mM), $MgCl_2$ (1.3 mM), $CaCl_2$ (2.5), $NaHCO_3$ (26.2 mM), D-glucose (20 mM) and KH_2PO_4 (1 mM). GCaMP6f was expressed under a synapsin promotor. Each retina was cut into four pieces and placed into an ACSF solution of 5 μM poRhoVR **14**. The solution was bubbled continuously for approximately 2 hours at room temperature with carbogen (95% O_2 and 5% CO_2). A piece of retina was placed on to an MEA chip (Multichannel Systems 60 pin ThinMEA chip, 200 μm interelectrode distance, 30 μm electrode diameter, 180 μm thickness)

with the RGC layer in direct contact with the electrodes. The electrode pins on the MEA chip are made of titanium nitride (TiN) and the chip itself is made of indium tin oxide (ITO). Electrical data from the MEA was recorded on a Multichannel Systems USB-64 system at a sampling rate of 20kHz. The retina was imaged on an inverted epifluorescence microscope equipped with an OracFlash4.0 sCMOS camera (Hamamatsu) via a 20X air objective. The field of view was binned 4X4 and recorded at an optical sampling rate of 500 Hz. A red LED (20% of max power, 8.85 mW/mm^2) was used as the excitation source for poRhoVR **14** and a cyan LED (20% of max power, 8.77 mW/mm^2) was used for GCaMP6f. Emission from GCaMP6f and poRhoVR 14 was collected simultaneously with the QUAD filter set alongside a Dual-View emission splitter (Optical Insights). The Dual-View contained a 585dcxr dichroic and two emission filters (520/28 nm and 723/68 nm) which separated the GCaMP6f and poRhoVR **14** fluorescence signals. After a few initial recordings the ACSF solution was replaced by a solution of synaptic blockers. The solution of synaptic blockers was prepared in ACSF with the following: DNQX (40 μM), D-AP5 (30 μM), Curare (50 μM), Strychnine (10 μM), TPMPA (50 μM), Gabazine (10 μM) and L-AP4 (10 μM). Recordings of pharmacologically isolated ganglion cells were taken approximately 10-15 minutes after blocker treatment.

A custom ImageJ macro aligned and spilt the image stack into two, one for the GCaMP6s signal and the other for the poRhoVR **14** signal. Custom MATLAB routines were used to extract raw fluorescence traces of retinal activity (see **Appendix 5**). Either ring-shaped ROIs 16 pixels (20.8 μm) wide or a series of 7 rectangular ROIs each 16 pixels (20.8 μm) by 32 pixels (41.6 μm) were drawn around or between the electrodes. These ROIs were applied as masks to all frames in the image stack. poRhoVR **14** traces were bleach corrected by approximating the bleach curve via asymmetric least squares and subtracting the resulting curve from the raw poRhoVR **14** signal. A baseline fluorescence value (F_{base}) is calculated by averaging the fluorescence of 10 to 20 frames that show no activity. F_{base} was subtracted from each timepoint of the bleach corrected poRhoVR **14** traces or the raw GCaMP6f traces to yield a ΔF trace. The ΔF was then divided by F_{base} to give $\Delta F/F$ traces.

Figure 4.3.1-2 poRhoVR 14 and BENAQ

In experiments with BENAQ retina were loaded with 5 μM poRhoVR **14** in ACSF as described above. After staining with poRhoVR **14**, a 50 μM solution of BENAQ in ACSF was bath applied to retinal tissue for 15 minutes. Control samples were only treated with poRhoVR **14**. The tissue was then placed into an imaging dish with fresh ACSF.

In BENAQ experiments involving HEK cells, the cells were bathed in an HBSS solution containing 1 μM poRhoVR **14** BENAQ at a low (50 μM) or a high concentration (100 μM). Controls samples were only stained with poRhoVR **14**. Cells were incubated at 37 °C for 30 minutes before being imaged in an imaging dish with a fresh solution of HBSS.

Samples were imaged on an inverted epifluorescence microscope equipped with an OracFlash4.0 sCMOS camera (Hamamatsu) via a 20X air objective. The field of view was binned 4X4 and recorded at an optical sampling rate of 500 Hz. A red LED (20% of max power, 8.85 mW/mm2) was used as the excitation source for poRhoVR **14**. A cyan LED was shone intermittently for 1 second every 2 seconds at high (20% of max power, 8.77 mW/mm2) or low (2% of max power, 0.99 mW/mm^2) levels to cause BENAQ isomerization. poRhoVR **14** emission was collected with the QUAD filter set.

Fluorescence traces were averaged for the entire field of view and extracted using ImageJ. For traces showing the changes in counts of fluorescence in retina, raw unaltered traces were reported. In HEK cell experiments the raw fluorescence traces were background subtracted. To account for increases in poRhoVR **14** fluorescence due to cross excitation with cyan light, traces from the control samples not treated with BENAQ were subtracted from traces derived from samples treated with BENAQ. A baseline fluorescence value (F_{base}) was calculated by averaging the fluorescence of 10 to 20 frames that showed no changes in fluorescence. F_{base} was subtracted from each timepoint of the control subtracted traces to yield a ΔF trace. The ΔF was then divided by F_{base} to give $\Delta F/F$ traces.

Figure 4.2.1 Ivabradine and poRhoVR 14.

In experiments with ivabradine, sections of retina were treated with a 50 μM solution of ivabradine in ACSF for 15 minutes. When used with synaptic blockers both ivabradine and the synaptic blockers were applied simultaneously for 15 minutes. Imaging settings were the same as above for **Figure 3.4.1-2**.

Fluorescence traces were averaged for the entire field of view for poRhoVR **14** and GCaMP 6f. poRhoVR **14** traces were bleach corrected by approximating the bleach curve via asymmetric least squares and subtracting the resulting curve from the raw poRhoVR **14** signal. This bleach correction served as the baseline fluorescence (F_{base}) and was used to calculate $\Delta F/F$ by dividing the bleach corrected poRhoVR **14** (ΔF) trace by the corresponding bleach correction cure (F_{base}). For GCaMP 6f traces, a baseline fluorescence value (F_{base}) is calculated by averaging the fluorescence of 10 to 20 frames that show no activity. F_{base} was subtracted from each timepoint of the raw GCaMP6f traces to yield a ΔF trace. The ΔF was then divided by F_{base} to give $\Delta F/F$ traces.

Figure 4.1.1 poRhoVR 14 Retina Staining Procedure- Confocal.

Retinas were dissected from *rd1* Thy1-YFP mice in ACSF. YFP was under a thy1 promotor. Each retina was cut into four pieces and placed in to an ACSF solution of either 5 μM poRhoVR **14** and 10 μM Hoechst 33342 or 5 μM BeRST1 **1** and 10 μM Hoechst 33342. The solution was bubbled continuously for a minimum of 2 hours at room temperature with

carbogen (95% O2 and 5% CO2). The pieces of retina were mounted onto a piece of Whatman filter paper and placed into an imaging dish filled with ACSF. Z-stacks of the stained retina were collected using an upright confocal microscope, Zeiss LSM 780 AxioExaminer, and a W-Plan-Apo 20x/1.0 water objective. Retina tissue was illuminated with HeNe 633 nm laser (laser power 5), a diode 405 nm laser (laser power 30) and an argon 458 nm laser (laser power 25). Emission light was collected within the following ranges: 415-511 nm (Hoechst 33342 emission), 525-623 nm (YFP emission) and 643-758 nm (poRhoVR **14** and BeRST 1 emission).

4.7 References

(1) Lapray, D.; Lasztoczi, B.; Lagler, M.; Viney, T. J.; Katona, L.; Valenti, O.; Hartwich, K.; Borhegyi, Z.; Somogyi, P.; Klausberger, T. Behavior-Dependent Specialization of Identified Hippocampal Interneurons. *Nat. Neurosci.* **2012**, *15* (9), 1265–1271. https://doi.org/10.1038/nn.3176.

(2) Tang, S.; Reddish, F.; Zhuo, Y.; Yang, J. J. Fast Kinetics of Calcium Signaling and Sensor Design. *Curr. Opin. Chem. Biol.* **2015**, *27*, 90–97. https://doi.org/10.1016/j.cbpa.2015.06.014.

(3) Tochitsky, I.; Polosukhina, A.; Degtyar, V. E.; Gallerani, N.; Smith, C. M.; Friedman, A.; Van Gelder, R. N.; Trauner, D.; Kaufer, D.; Kramer, R. H. Restoring Visual Function to Blind Mice with a Photoswitch That Exploits Electrophysiological Remodeling of Retinal Ganglion Cells. *Neuron* **2014**, *81* (4), 800–813. https://doi.org/10.1016/j.neuron.2014.01.003.

(4) Tochitsky, I.; Trautman, J.; Gallerani, N.; Malis, J. G.; Kramer, R. H. Restoring Visual Function to the Blind Retina with a Potent, Safe and Long-Lasting Photoswitch. *Sci. Rep.* **2017**, *7*, 1–8. https://doi.org/10.1038/srep45487.

(5) Tochitsky, I.; Helft, Z.; Meseguer, V.; Fletcher, R. B.; Vessey, K. A.; Telias, M.; Denlinger, B.; Malis, J.; Fletcher, E. L.; Kramer, R. H. How Azobenzene Photoswitches Restore Visual Responses to the Blind Retina. *Neuron* **2016**, *92* (1), 100–113. https://doi.org/10.1016/j.neuron.2016.08.038.

(6) Kase, D.; Imoto, K. The Role of HCN Channels on Membrane Excitability in the Nervous System. *J. Signal Transduct.* **2012**, *2012*, 1–11. https://doi.org/10.1155/2012/619747.

(7) Postea, O.; Biel, M. Exploring HCN Channels as Novel Drug Targets. *Nat. Rev. Drug Discov.* **2011**, *10* (12), 903–914. https://doi.org/10.1038/nrd3576.

(8) Euler, T.; Hausselt, S. E.; Margolis, D. J.; Breuninger, T.; Castell, X.; Detwiler, P. B.; Denk, W. Eyecup Scope-Optical Recordings of Light Stimulus-Evoked Fluorescence Signals in the Retina. *Pflugers Arch. Eur. J. Physiol.* **2009**, *457* (6), 1393–1414. https://doi.org/10.1007/s00424-008-0603-5.

(9) Farber, D. B.; Flannery, J. G.; Bowes-Rickman, C. The Rd Mouse Story: Seventy Years of Research on an Animal Model of Inherited Retinal Degeneration. *Prog. Retin. Eye Res.* **1994**, *13* (1), 31–64. https://doi.org/10.1016/1350-9462(94)90004-3.

(10) Boyden, E. S.; Zhang, F.; Bamberg, E.; Nagel, G.; Deisseroth, K. Millisecond-Timescale, Genetically Targeted Optical Control of Neural Activity. *Nat. Neurosci.* **2005**, *8* (9), 1263–1268. https://doi.org/10.1038/nn1525.

(11) Nagel, G.; Szellas, T.; Huhn, W.; Kateriya, S.; Adeishvili, N.; Berthold, P.; Ollig, D.; Hegemann, P.; Bamberg, E. Cation-Selective Membrane Channel. *Pnas* **2003**, *100* (24), 13940–13945.

Acknowledgements

Confocal imaging experiments were conducted at the CRL Molecular Imaging Center, supported by NSF DBI-1041078.

Thank you to Benjamin Smith for assistance with the ImageJ macro.

Appendix 1

Optimization of the Reduction of Compound 3

Portions of this work were performed in collaboration with the following person:

Synthesis was done with the assistance of Jeremy Dworkin

A1.1 Optimization of Nitro Reduction, Synthesis of 4

a)

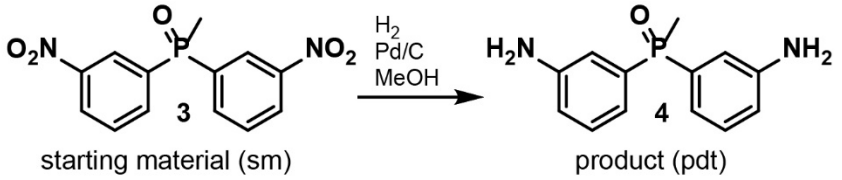

starting material (sm) product (pdt)

b)

Reaction	Initial Hydrogen Pressure (atm)	Equiv of H_2	Equiv of Pd/C (% by wt)	Time (hr)
1	3.0	2.4	10	24
2	4.5	3.6	10	24
3	6.0	4.8	10	24
4	7.5	6.0	10	24
5	7.5	6.0	20	24
6	7.5	6.0	10	24
7	7.5	6.0	20	48
8	7.5	6.0	10	48

c)

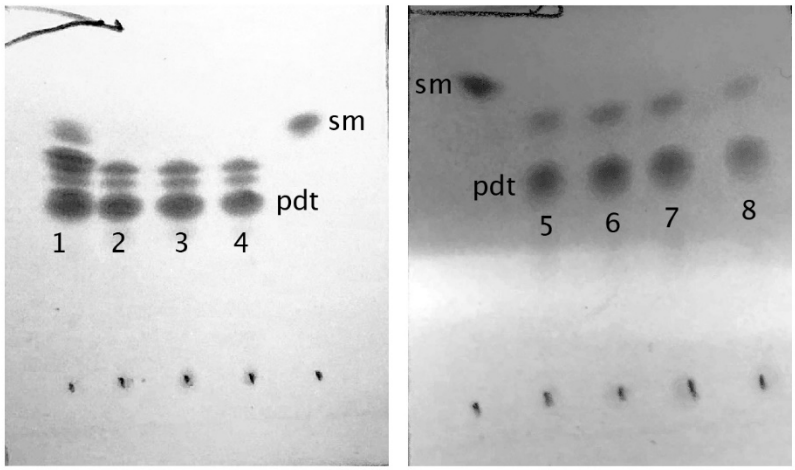

Figure A1.1.1. Hydrogenation optimization. **a)** Nitro reduction conditions. The reactions were carried out in an Endeavor Catalyst Screening System pressure reactor. Each reaction began with 125 mg of starting material (sm). **b)** This table details the various reaction conditions that were tested. The initial pressure of hydrogen was varied in reactions 1-4. In reactions 5-8 the amount of catalyst and time that the reaction stirred for was varied. **c)** Images of thin-layer chromatography (TLC) silica plates labeled with the reaction number. The spots pertaining to product (pdt) and sm have also been labeled. The remaining spots are from incomplete hydrogenation in reactions 1-4 and an unidentified impurity in reactions 1-8. These plates were run in a 1:9 DCM/MeOH mobile phase and visualized under UV light.

Synthesis of **4** (**Figure A1.1.1a**) was done via a palladium catalyzed hydrogenation at room temperature. This hydrogenation resulted in complete consumption of starting material **3**, but aside from product an unidentified impurity was also produced. Hydrogen was supplied to the reaction through a balloon filled with the gas. Overtime the balloon would deflate and there would no longer be a positive pressure of hydrogen gas being supplied to the reaction.

For this reason, the impurity was thought to arise from incomplete reduction of compound **3**. To address this issue test reactions were done in a pressurized multi-reactor, shown in **Figure A1.1.1**. In reactions 1 through 4 the initial pressure of hydrogen was incrementally increased. In the TLC plates of these first 4 reactions increasing equivalents of hydrogen gas did not stop the production of impurities. In reactions 5 through 8, the length of reaction time and the amount of catalyst were varied. Increased reaction time and catalyst also did not stop the production of impurities as evidenced by the TLC plates of those test reactions.

The impurity was ultimately isolated using preparative TLC purification techniques. The LCMS of the impurity showed a mass to charge ratio (m/z) that matched that of a diaryl phosphine oxide that had just one amine on the aryl rings, **Figure A1.1.2**. This was possibly do to over reduction that ultimately resulted in deamination. Another potential source of this impurity may have come from the starting material, **3**. It is possible that incomplete nitration of **2** resulted in a mononitrated product. However, there was no evidence of a mononitrated product in the NMRs of **3** isolated from the nitration reaction. This leads to deamination as the most likely source of the impurity.

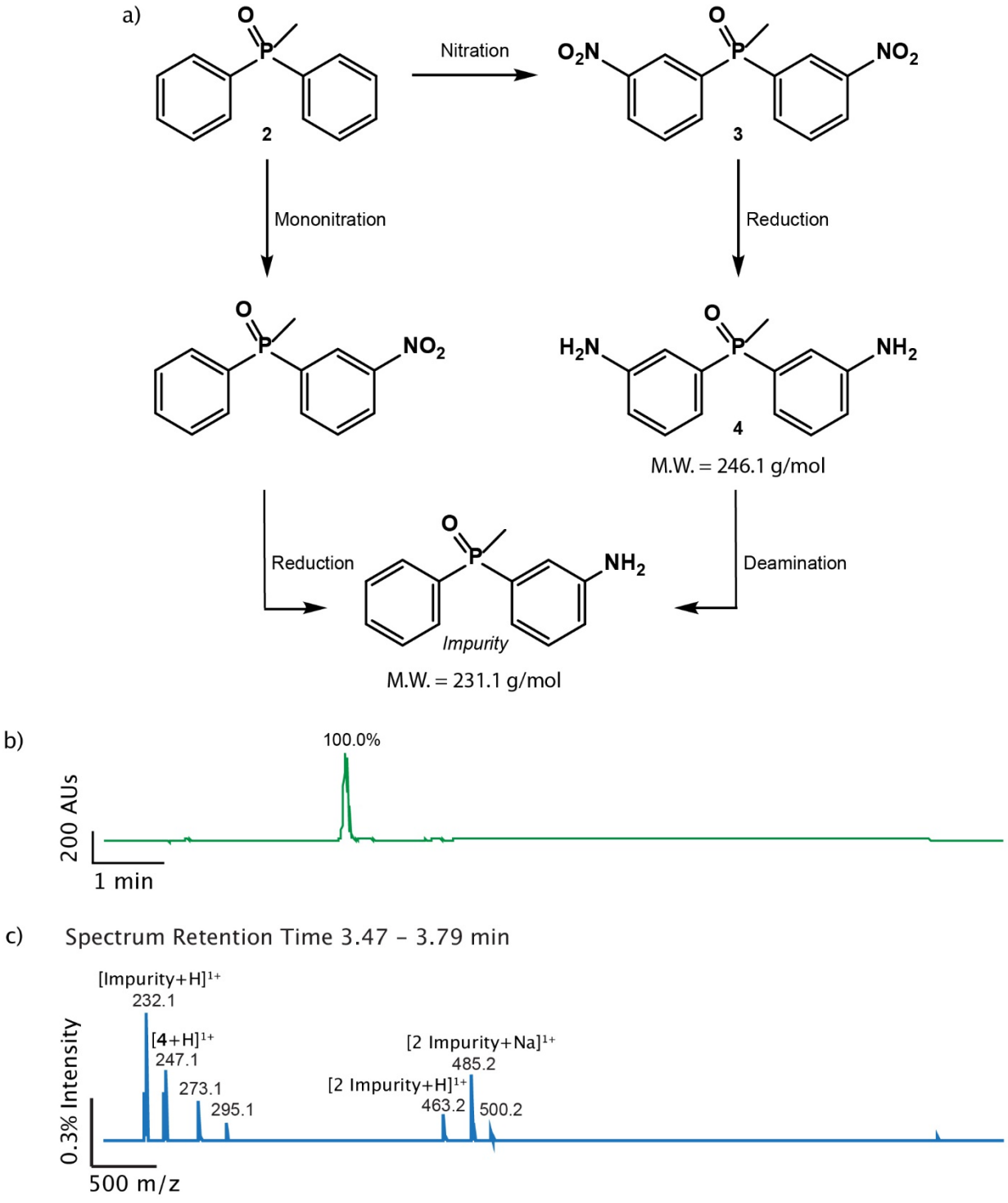

Figure A1.1.2 Sources and identification of reduction impurity. **a)** There are two potential sources of the monamine impurity. The first is from the incomplete nitration of **2**, resulting in a mononitrated impurity that becomes reduced in the subsequent reaction. The second source is from the deamination of **4**. **b)** After attempted purification of deamination impurity,

collected a Liquid Chromatography (LC) trace of compound that eluted and absorbed at 254 nm. **c)** Mass Spectrometry (MS) trace corresponding to the LC trace showing the mass to charge ratios (m/z) corresponding to the monoamine impurity as well as product, **4**.

A variety of reducing agents can be used in the reduction of nitro groups. These include metals such as zinc and iron. Different reducing agents were explored with the aim of decreasing deamination during the reduction reaction. **Table A1.1.1** shows the data from these efforts.

Reducing Agent	Equivalents	Temperature (°C)	Time (Days)	Starting Material, **3** (% by LCMS)	Product, **4** (% by LCMS)	Deamination (% by LCMS)	Product:Deamination
$Fe_{(s)}$	4.0	80	5	22.6	13.6	7.0	1.9
$Fe_{(s)}$	16.0	80	5	1.9	78.4	14.5	5.4
$Fe_{(s)}$	16.0	65	3	0.0	61.5	29.3	2.1
$Zn_{(s)}$	16.0	25	3 hrs	0.0	67.9	28.2	2.4
$Zn_{(s)}$	16.0	25	3	0.0	83.4	13.1	6.4
B_2Pin_2	6.2	80	1	0.0	79.4	14.1	5.6

Table A1.1.1. Optimization of reduction of **3** with different reducing agents.

All the reducing agents used in **Table A1.1** resulted in the deamination of product. Across the $Fe_{(s)}$ series, a lower temperature, 65 °C resulted in increased deamination compared to higher temperatures, 80 °C. This is consistent with what has been noted previous, wherein lower reaction temperatures result in increased deamination.[1] In the future, optimization of this reaction should focus on exploring higher reaction temperatures when possible to reduce deamination.

A1.2 Synthetic Details

Synthesis of bis(3-aminophenyl)(methyl)phosphine oxide, 4, Iron Reduction

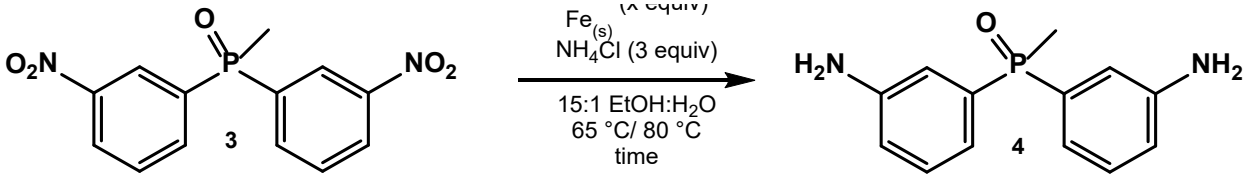

To a 20 mL scintillation vial, added **3**, (50 mg, 0.163 mmol), varied equivalents of Fe(s) (4 equivalents, 0.65 mmol; 16 equivalents, 2.6 mmol) and NH_4Cl (26 mg, 0.49 mmol) then covered with a septum cap. Evacuated and backfilled with N_2 twice. Added 2 mL of EtOH and 0.18 mL of H_2O. Stirred at varied temperatures and reaction times (80°C for 5 days or 65°C for 3 days). Checked reaction progress by TLC at 30 min and 60 min with a 10% MeOH:DCM mobile phase. Reaction mixture was run through a celite column with EtOH into a round bottom flask to remove the Fe. The solvent was removed by evaporation. An LCMS sample was prepared with 0.2 mL 1:1 H_2O:ACN and 2 drops of a saturated solution of the purified solid and MeOH.

Synthesis of bis(3-aminophenyl)(methyl)phosphine oxide, 4, Zinc Reduction

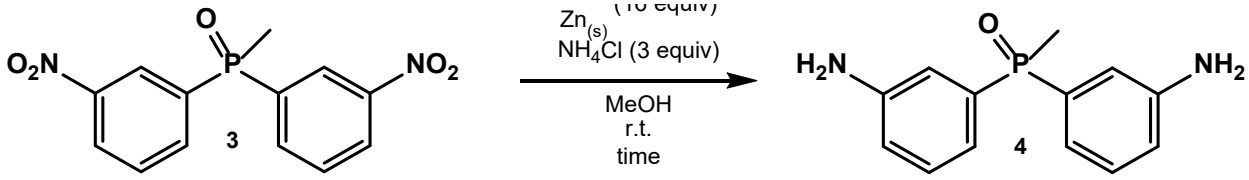

In a 20 mL scintillation vial, **3** (50 mg, 0.163 mmol) and NH_4Cl (26 mg, 0.49 mmol) were dissolved in 1.63 mL of MeOH and stirred for 20 minutes. Then Zn(s) (17 mg, 2.6 mmol) was added, and the reaction was stirred at 25ºC for various time periods (3 hours or 3 days). Reaction progress was checked periodically by TLC with a 10% MeOH:DCM mobile phase. The Zn was removed with a silica column and MeOH as the mobile phase. An LCMS sample was prepared with 0.2 mL 1:1 H_2O:ACN and 2 drops of the filtered solution.

A1.3 References

(1) Guttieri, M. J.; Maier, W. F. Selective Cleavage of Carbon-Nitrogen Bonds with Platinum. *J. Org. Chem.* **1984**, *49* (16), 2875–2880. https://doi.org/10.1021/jo00190a006.

Appendix 2

Investigating the Effects of Dantrolene and Ryanodine on Calcium and Voltage Dynamics in Neurons

A.1 Effects of Dantrolene and Ryanodine on Calcium Release

In neurons calcium transients often accompany an action potential as part of the signaling cascade. These increases in cytosolic calcium can be achieved in two ways: through uptake of extracellular calcium or release of calcium ions from internal stores.[1] Calcium is most often stored with the endoplasmic or sarcoplasmic reticula (ER, SR) within the cell.[1] By opening calcium release channels on the in these organelles neurons can rapidly increase cytosolic calcium levels. Among these channels are the ryanodine receptors (RyR). Ryanodine receptors are named after the plant alkaloid ryanodine which has a high affinity for RyR.[2] Ryanodine at high concentrations can block RyR and prevent release of calcium and at low concentrations it can lock RyR in a half open state leading to the depletion of calcium from internal stores.[1,3,4] Dantrolene, is another compound that has been found to act on RyR and inhibit calcium release.[5,6] Dantrolene inhibits channel activation of RyR by calmodulin.[7]

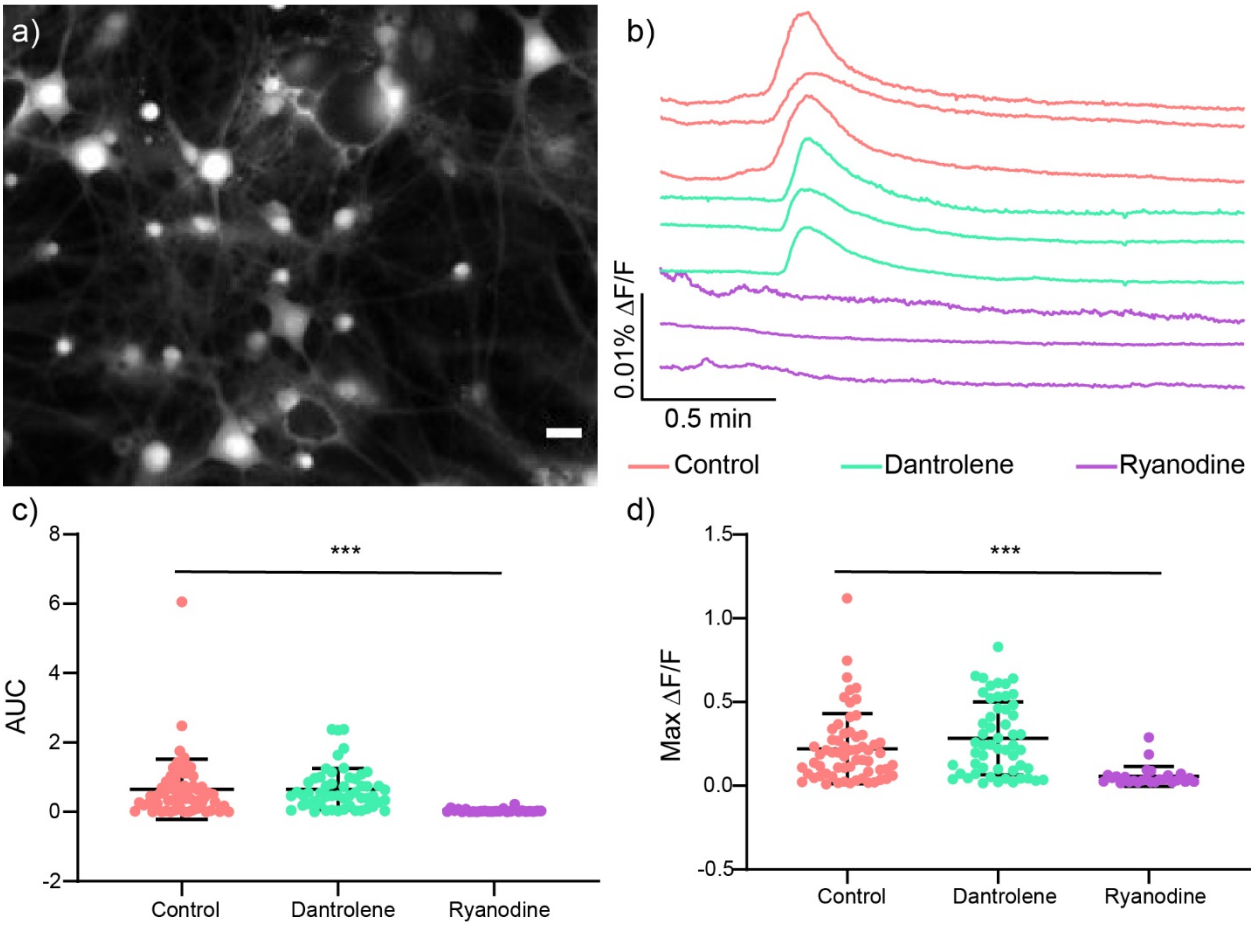

Figure A2.1.1 Ryanodine blocks calcium release caused by caffeine. **a)** Representative widefield image of dissociated rat hippocampal neurons stained with OGB-AM. Scale bar is 20 µm. **b)** Example OGB-AM fluorescence traces from neurons that have been perfused with 10 µM caffeine in the presence of either synaptic blockers, 10 µM NBQX and 20 µM APV, (control) or synaptic blockers and dantrolene or ryanodine. Quantification of calcium fluctuations recorded from neurons after treatments mentioned in (b). Two parameters were measured the **c)** area under the curve (AUC) or **d)** the maximum fractional change in fluorescence (Max

ΔF/F). A total of 62 cells across 3 coverslips were analyzed for the control. A total of 54 cells across 2 coverslips were analyzed for dantrolene. A total of 26 cell across 1 coverslip were analyzed for ryanodine. One-way ANOVA followed by Dunnett's multiple comparisons test was performed in GraphPad Prism. A P-value <0.05 was considered statistically significant. In the analysis of (c), Dunnett's multiple comparisons test of the control versus all other time points gave the following P-values: 0.9996 (control vs. dantrolene), 0.0003 (control vs. ryanodine). In the analysis of (d), Dunett's multiple comparisons test of the control versus all other time points gave the following P-values: 0.1607 (control vs. dantrolene), 0.0008 (control vs. ryanodine).

In our experiments, we sought to highlight the differences in calcium and voltage activity by using ryanodine and dantrolene to significantly reduce cytosolic calcium concentrations following an action potential. We first confirmed that the concentrations of ryanodine and dantrolene we used in our experiments were effective at blocking release of calcium from internal stores.[8] Caffeine cause a large increase in the cytosolic concentrations of neurons by releasing calcium from internal stores by acting on RyR.[8,9] To determine if this effect could be blocked by ryanodine or dantrolene we preincubated dissociated rat hippocampal neurons with either of the two drugs at 20 μM concentrations. At the same time the cells were stained with the calcium sensor Oregon-Green BAPTA-AM (OGB-AM) (**Figure A2.1.1 a**). A 10 mM caffeine solution was perfused onto cells that led to a large increase in OGB-AM fluorescence in the control and dantrolene treated cells (**Figures A2.1.1 b**). In the ryanodine treated cells there was no detectable increase in OGB-AM fluorescence (**Figure A2.1.1 b**). After quantifying OGB-AM signal (**Figure A2.1.1 c** and **d**) it was clear that ryanodine effectively blocked release of calcium from, most likely through the depletion of calcium from internal stores prior to imaging.[4] Since dantrolene may be acting indirectly on RyR it is possible that it is not as effective as ryanodine in preventing a release of calcium caused by caffeine.

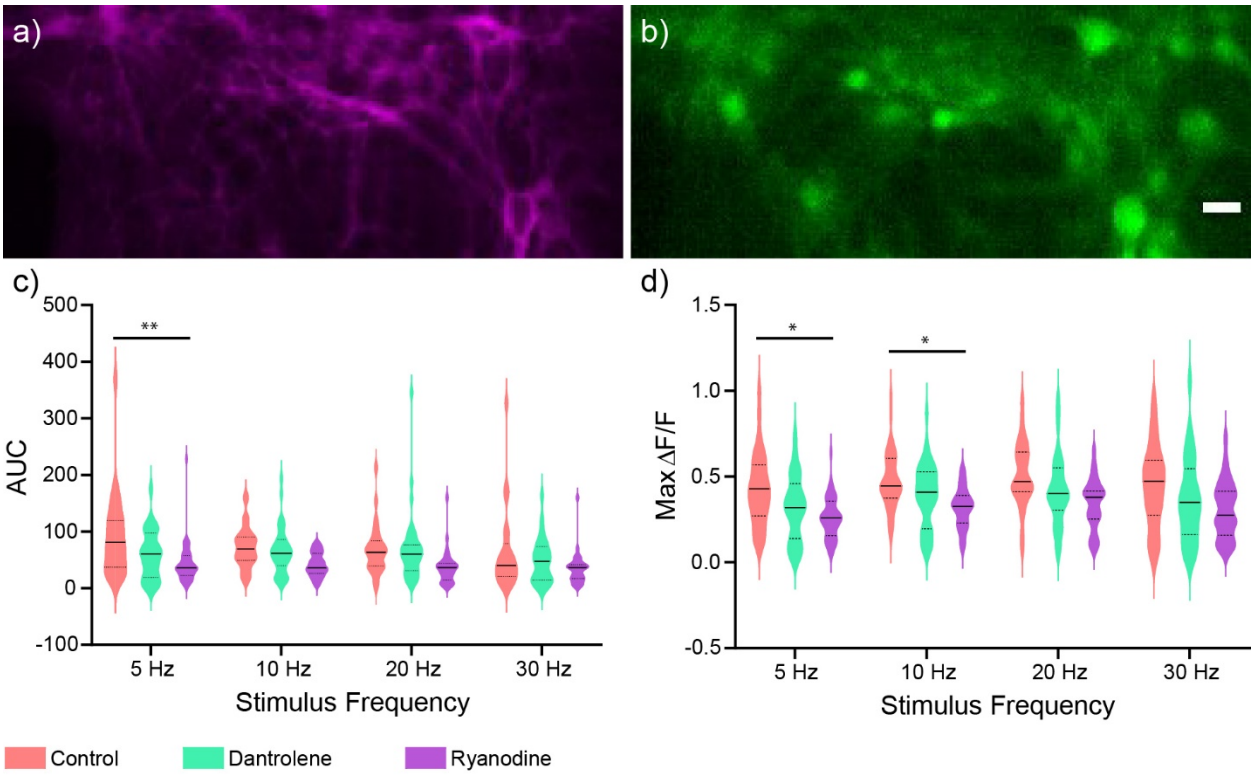

Figure A2.1.2 Ryanodine partially blocks calcium release at low firing frequencies. Representative images of dissociated rat hippocampal neuron stained with **a)** poRhoVR **14** or **b)** OGB-AM. Scale bar 20 µM. Neurons were electrically stimulated to fire action potentials at the following frequencies: 5, 10, 20, 30 Hz, with or without dantrolene or ryanodine. To ensure that only neurons that were firing at the appropriate frequencies were analyzed, the instantaneous firing frequencies of neurons was measured by counting the number of action potentials recorded by poRhoVR **14**. Calcium transients simultaneously recorded from OGB-AM were quantified using two parameters **c)** the area under the curve (AUC) or **d)** the maximum fractional change in fluorescence (Max ΔF/F). These values were plotted as violin plots where the center line represents the median and the upper and lower lines represent the 1st and 3rd quartiles. About 20 to 30 cells were analyzed per treatment (control, dantrolene, ryanodine). Two-way ANOVA followed by Tukey's multiple comparisons test was performed in GraphPad Prism. A P-value <0.05 was considered statistically significant. A summary of the P-values can be found under A#.2 Imaging Details.

In the next experiment we looked at the effects of dantrolene and ryanodine on the calcium transients associated with action potentials in neurons (**Figure A2.1.2**). Action potentials were evoked with an electrical stimulus at various frequencies (**Figure A2.1.2**). Using an emission splitter, simultaneous imaging of changes in transmembrane potential and calcium transients were visualized with poRhoVR **14** (**Figure A2.1.2 a**) and OGB-AM (**Figure A2.1.2 b**) respectively. Since stimulus frequency and the firing frequency reported by poRhoVR **14** correlate well (**Figure 3.2.7 c**), cells firing at the appropriate frequencies were identified using poRhoVR **14** signals and the calcium signals corresponding to those cells were quantified (**Figure A2.1.2 c** and **d**). At low firing frequencies, 5 and 10 Hz, ryanodine appeared to influence calcium release during the transients following action potentials (**Figure A2.1.2 c**). At higher frequencies, however, this effect was not detectable. Cells treated with dantrolene

did not show diminished calcium signal when compared to the control (**Figure A2.1.2 d**). Intracellular calcium is believed to play a role in calcium transients evoked by action potentials.[10] Further experiments with different calcium indicators and with different extracellular concentrations of calcium can be done to confirm the effects seen with ryanodine and dantrolene (**Figure A2.1.2**). This will help determine if the type of calcium sensor used plays a role in the observed effects of dantrolene and ryanodine. It may also be useful to try a combination of drugs that target internal stores of calcium via various targets to amplify the effects on calcium transients.

A2.2 Imaging Details

Preparation of Primary Neuron Cultures

Hippocampi were dissected from embryonic day 19 Sprague Dawley rats (Charles River Laboratory) in cold sterile HBSS (zero Ca^{2+}, zero Mg^{2+}). Hippocampal tissue was treated with trypsin (2.5%) for 15 min at 37 °C. The tissue was triturated using fire polished Pasteur pipettes, in minimum essential media (MEM) supplemented with 5% FBS, 2% B-27, 2% 1M dextrose and 1% GlutaMax. The dissociated cells were plated onto 12 mm diameter coverslips (Fisher Scientific) pre-treated with PDL at a density of 25,000-30,000 cells per coverslip in MEM supplemented media (as above). Neurons were maintained at 37 °C in a humidified incubator with 5 % CO2. After 1 day in vitro (DIV) half of the MEM supplemented media was removed and replaced with Neurobasal media containing 2% B-27 supplement and 1% GlutaMax. Functional imaging was performed on mature neurons 13-20 DIV.

General Imaging Parameters

Imaging experiments were performed on an upright epifluorescence microscope, AxioExaminer Z-1 (Zeiss), equipped with a Spectra-X Light engine LED light (Lumencor), and an OrcaFlash4.0 sCMOS camera (Hamamatsu). The following LED light sources were used; red (631/28 nm bandpass) and cyan (475/34 nm bandpass). The microscope was controlled via Slidebook (v6, Intelligent Imaging Innovations) or MicroManager (Studio Version 1.4.22). Imaging was done with a W-Plan-Apo 20x/1.0 objective (20x; Zeiss). The QUAD emission filter set, a quadruple dichroic mirror (432/38, 509/22, 586/40, 654 nm LP) combined with a quadruple emission filter (430/32 nm, 508/14 nm, 586/30 nm, 708/98 nm), was used. For experiments with simultaneous voltage and calcium imaging a Dual View emission splitter (Optical Insights) was used. The Dual-View contained a 585dcxr dichroic and two emission filters (520/28 nm and 723/68 nm) which separated the calcium (Oregon Green BAPTA-AM) and poRhoVR **14** fluorescence signals.

Image Analysis

Optical traces of neuronal calcium and voltage activity were obtained by drawing ROIs around the cell bodies of neurons stained with poRhoVR or OGB-AM, in ImageJ and extracting the mean cellular fluorescence from each frame in the image stack. The mean background fluorescence was subtracted from the mean cellular fluorescence of each frame. $\Delta F/F$ values were calculated by first subtracting a mean background value from all raw fluorescence frames to give a background subtracted trace (bkgsub). A baseline fluorescence value (F_{base}) is calculated by averaging the fluorescence of 10 to 20 frames that show no activity. F_{base} was subtracted from each timepoint of the bkgsub trace to yield a ΔF trace. The ΔF was then divided by F_{base} to give $\Delta F/F$ traces.

Max $\Delta F/F$ and area under the curve (AUC) were calculated using a custom MATLAB script. Instantaneous firing frequencies were calculated using a second custom MATLAB script, SpikeNet, from poRhoVR **14** fluorescence traces.

Figure A2.1.1 Ryanodine Blocks Calcium Release Caused by Caffeine

Neurons were loaded with 1 μM OGB-AM and 0.01% pluronic. A cyan LED (0.05 mW/mm^2) was used as the excitation source for OGB-AM. The HBS imaging solution was supplemented with synaptic blockers 10 μM 2,3-Dioxo-6-nitro-1,2,3,4-tetrahydrobenzo[f]quinoxaline-7-sulfonamide (NBQX; Santa Cruz Biotechnology) and 25 μM DL-2-Amino-5-phosphonopentanoic acid (APV; Sigma-Aldrich) to prevent any spontaneous firing. In the case of cells treated with drugs, the imaging solution contained either 20 μM dantrolene or ryanodine. Cells were also preincubated with the drugs for 20 minutes before imaging. After a minute of imaging, a solution containing 10 mM caffeine with or without drugs was perfused on. A time-lapse of the cells during perfusion was taken. An image was recorded every 200 ms with a 50 ms exposure for a total of 2.2 minutes. One-way ANOVA followed by Dunnett's multiple comparisons test was performed in GraphPad Prism version 8.4.3. for Windows, GraphPad Software, San Diego, California USA, www.graphpad.com.

Figure A2.1.2 Ryanodine Partially Blocks Calcium Release at Low Firing Frequencies.

Neurons were loaded with 1 μM OGB-AM and 500 nM poRhoVR with 0.01% pluronic. A red LED (50% of max power, 49.7 mW/mm^2) was the source of excitation light for poRhoVR **14** and a cyan LED was used for OGB-AM (10% of max power, 7.9 mW/mm^2). Emission from OGB-AM and poRhoVR **14** was collected simultaneously with the QUAD filter set and a Dual-View emission splitter (see **General Imaging Parameters**). Extracellular field stimulation was delivered by a Grass Stimulator connected to a recording chamber containing two platinum electrodes (Warner), with triggering provided through a Digidata 1440A

digitizer and pCLAMP 10 software (Molecular Devices). Action potentials were triggered by 1 ms 80 V field potentials delivered at 5, 10 20 or 30 Hz. In the case of cells treated with drugs, the imaging solution contained either 20 μM dantrolene or ryanodine. To prevent recurrent activity the HBS bath solution was supplemented with synaptic blockers 10 μM 2,3-Dioxo-6-nitro-1,2,3,4-tetrahydrobenzo[f]quinoxaline-7-sulfonamide (NBQX; Santa Cruz Biotechnology) and 25 μM DL-2-Amino-5-phosphonopentanoic acid (APV; Sigma-Aldrich). Cells were also preincubated with the drugs for 20 minutes before imaging. Two-way ANOVA followed by Tukey's multiple comparisons test was performed in GraphPad Prism version 8.4.3. for Windows, GraphPad Software, San Diego, California USA, www.graphpad.com.

AUC			
Stimulus Frequency (Hz)	Comparison	P-Value	Summary
5	Control vs. Dantrolene	0.3453	ns
	Control vs. Ryanodine	0.0043	**
10	Control vs. Dantrolene	>0.9999	ns
	Control vs. Ryanodine	0.2073	ns
20	Control vs. Dantrolene	>0.9999	ns
	Control vs. Ryanodine	0.3995	ns
30	Control vs. Dantrolene	0.9861	ns
	Control vs. Ryanodine	0.5209	ns

Table A2.2.1 Summary of P-value for graph in Figure A#1.2 c. A P-value below 0.05 is considered significant.

Max DF/F			
Stimulus Frequency (Hz)	Comparison	P-Value	Summary
5	Control vs. Dantrolene	0.529	ns
	Control vs. Ryanodine	0.0133	*
10	Control vs. Dantrolene	0.4835	ns
	Control vs. Ryanodine	0.0243	*
20	Control vs. Dantrolene	0.8257	ns
	Control vs. Ryanodine	0.0522	ns
30	Control vs. Dantrolene	0.9522	ns
	Control vs. Ryanodine	0.3213	ns

Table A2.2.2 Summary of P-value for graph in Figure A#1.2 d. A P-value below 0.05 is considered significant.

A2.3 References

(1) Santulli, G.; Marks, A. Essential Roles of Intracellular Calcium Release Channels in Muscle, Brain, Metabolism, and Aging. *Curr. Mol. Pharmacol.* **2015**, *8* (2), 206–222. https://doi.org/10.2174/1874467208666150507105105.

(2) Rogers, E. F.; Koniuszy, F. R.; Shavel, J.; Folkers, K. Plant Insecticides. I. Ryanodine, A New Alkaloid from Ryania Speciosa Vahl. *J. Am. Chem. Soc.* **1948**, *70* (9), 3086–3088. https://doi.org/10.1021/ja01189a074.

(3) Fairhurst, A. S.; Hasselbach, W. Calcium Efflux from a Heavy Sarcotubular Fraction: Effects of Ryanodine, Caffeine and Magnesium. *Eur. J. Biochem.* **1970**, *13* (3), 504–509. https://doi.org/10.1111/j.1432-1033.1970.tb00953.x.

(4) Murayama, T.; Oba, T.; Katayama, E.; Oyamada, H.; Oguchi, K.; Kobayashi, M.; Otsuka, K.; Ogawa, Y. Further Characterization of the Type 3 Ryanodine Receptor (RyR3) Purified from Rabbit Diaphragm. *J. Biol. Chem.* **1999**, *274* (24), 17297–17308. https://doi.org/10.1074/jbc.274.24.17297.

(5) Snyder, H. R.; Davis, C. S.; Bickerton, R. K.; Halliday, R. P. 1-[5-Arylfurfurylidene)Amino]Hydantoins. A New Class of Muscle Relaxants. *J. Med. Chem.* **1967**, *10* (5), 807–810. https://doi.org/10.1021/jm00317a011.

(6) Ellis, K. O.; Castellion, A. W.; Honkomp, L. J.; Wessels, F. L.; Carpenter, J. F.; Halliday, R. P. Dantrolene, a Direct Acting Skeletal Muscle Relaxant. *J. Pharm. Sci.* **1973**, *62* (6), 948–951. https://doi.org/10.1002/jps.2600620619.

(7) Fruen, B. R.; Mickelson, J. R.; Louis, C. F. Dantrolene Inhibition of Sarcoplasmic Reticulum Ca2+ Release by Direct and Specific Action at Skeletal Muscle Ryanodine Receptors. *J. Biol. Chem.* **1997**, *272* (43), 26965–26971. https://doi.org/10.1074/jbc.272.43.26965.

(8) Usachev, Y.; Shmigol, A.; Pronchuk, N.; Kostyuk, P.; Verkhratsky, A. Caffeine-Induced Calcium Release from Internal Stores in Cultured Rat Sensory Neurons. *Neuroscience* **1993**, *57* (3), 845–859. https://doi.org/10.1016/0306-4522(93)90029-F.

(9) Mcpherson, P. S.; Kim, Y.; Valdivia, H.; Knudson, C. M.; Takekura, H.; Franzini-armstrong, C.; Coronado, R.; Campbell, K. P. The Brain Ryanodine Receptor. *Neuron* **1991**, *7*, 17–25.

(10) Jacobs, J. M.; Meyer, T. Control of Action Potential-Induced Ca2+ Signaling in the Soma of Hippocampal Neurons by Ca2+ Release from Intracellular Stores. *J. Neurosci.* **1997**, *17* (11), 4129–4135. https://doi.org/10.1523/jneurosci.17-11-04129.1997.

Appendix 3

Multi-Wire Voltage Reporters

A3.1 Design and Synthesis of Multi-Wire Voltage Reporters

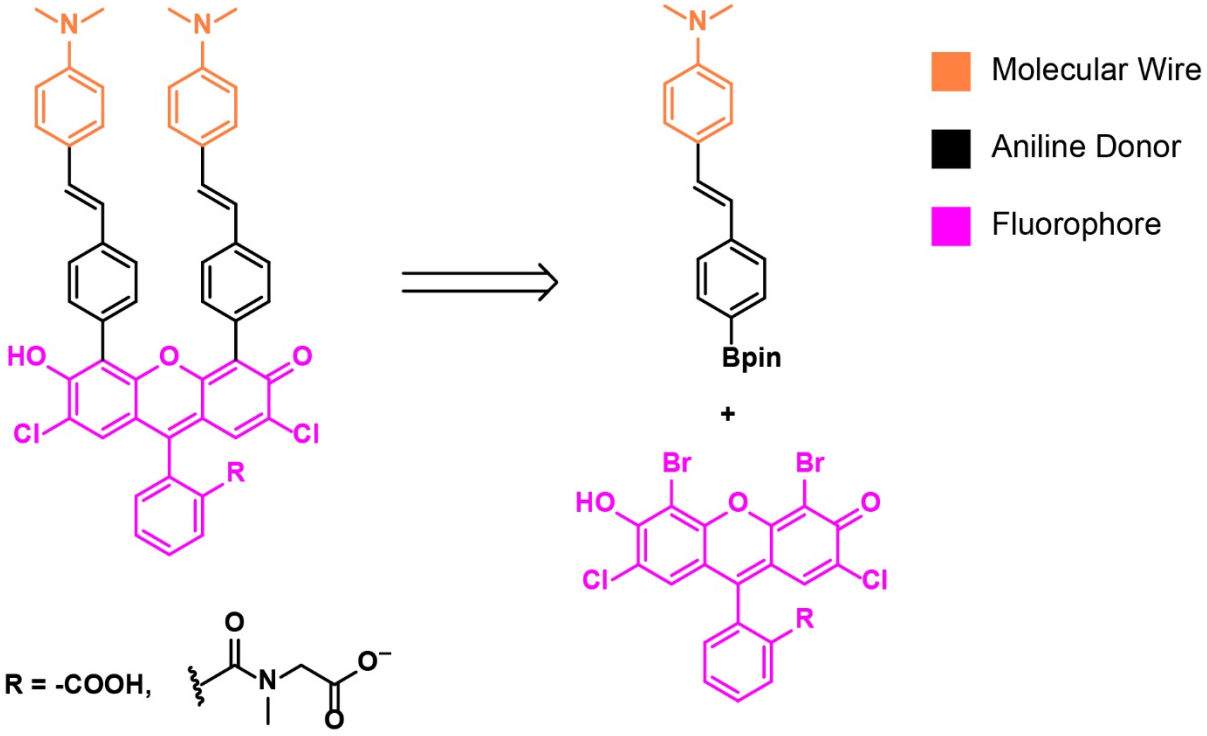

Figure A.3.1.1 Retrosynthetic scheme for the synthesis of multi-wire voltage reporters (MuVRs).

The general scaffold contains a single aniline donor that through a molecular wire and photoinduced electron transfer (PeT) impart voltage sensitivity to the voltage reporters (VRs). It is therefore possible that addition of a second wire and aniline donor could increase the sensitivity of VRs. Synthesis of these multi-wire voltage reporters (MuVRs) can be made by attaching the molecular wire to the 4' and 5' positions on a xanthene-based fluorophore (**Figure A3.1.1**). The carboxy group on the pendant ring can be modified with sarcosine to prevent possible internalization by cells.[1]

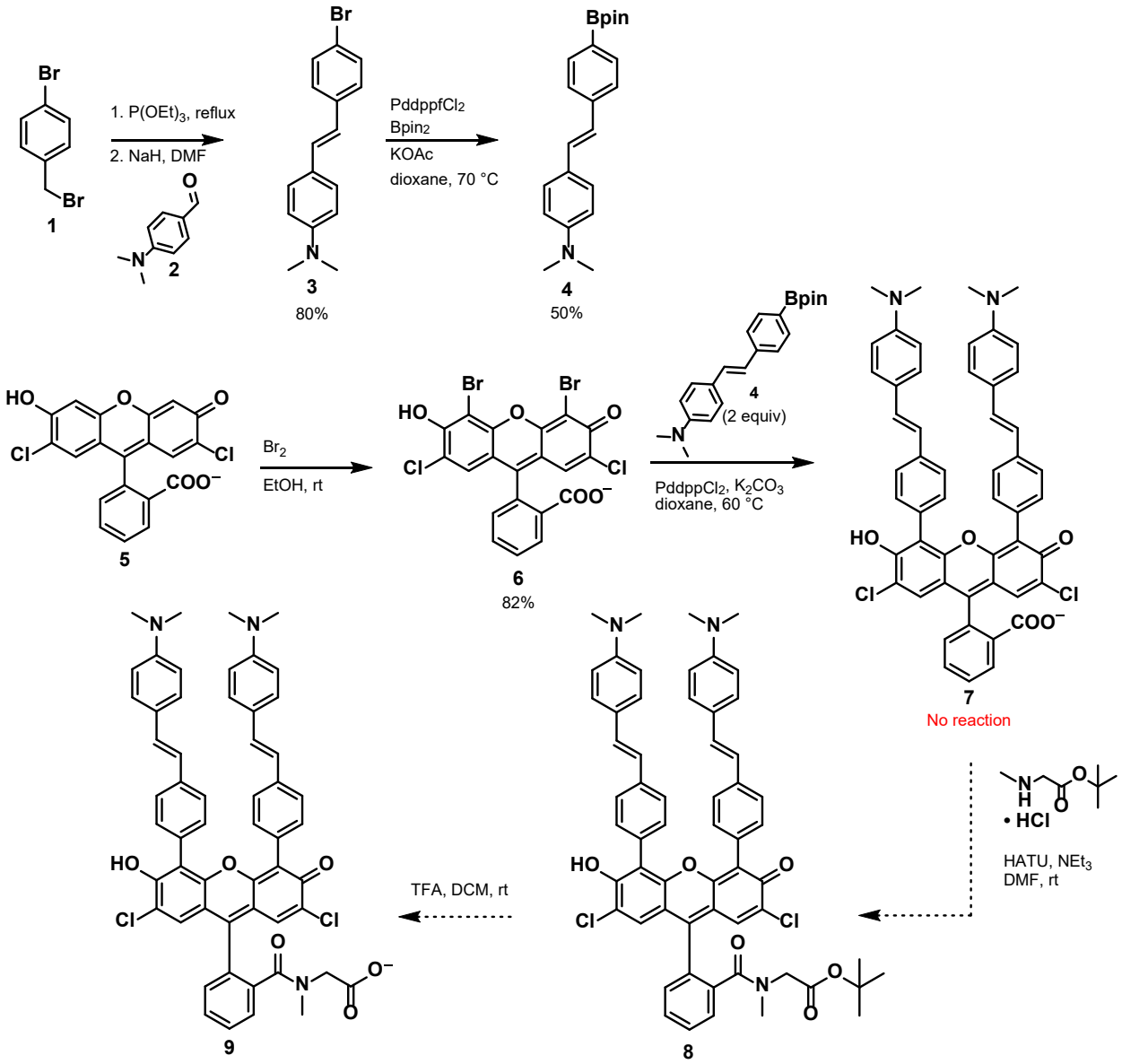

Scheme A3.1.1 Synthesis of MuVRs.

Synthesis of the wire, **4**, was relatively straight forward. Using a Wadsworth-Emmons reaction, **3** was prepared according to literature[2] after first preparing a stabilized ylide from **1** before adding it to **2**. The bromine handle was modified via a Miyaura reaction to install the pinacol borane needed for the subsequent Suzuki coupling with **6**. Bromination of dichlorofluorescien, **5**, proceeded smoothly since the chlorines prevented any bromination at the 2' and 7' positions. Bromination of the pendant ring is not energetically favorable.[3] After obtaining **6** in relatively high yield (82%), Suzuki coupling was attempted with 2 equivalents of **4**. This reaction did not proceed, and LCMS analysis showed unreacted **4** and **6**. Suzuki couplings are sensitive to air and solvents need to be degassed before attempting the reaction.[4] I had hoped to circumvent this step by using fresh anhydrous bottles of solvent and bubbling

the K_2CO_3 solution with N_2 overnight. However, these attempts were most likely unsuccessful and possibly led the failure of the reaction to. Aside from completely degassing all solutions, Suzuki couplings have been run successfully in air and water.[4] This is another option that can be explored further

A3.2 Synthetic Details

Synthesis of 3:

Synthesis of this compound can be found in Hayne, D. J.; North, A. J.; Fodero-Tavoletti, M.; White, J. M.; Hung, L. W.; Rigopoulos, A.; Mclean, C. A.; Adlard, P. A.; Ackermann, U.; Tochon-Danguy, H.; Villemagne, V. L.; Barnham, K. J.; Donnelly, P. S. Rhenium and Technetium Complexes That Bind to Amyloid-β Plaques. *Dalt. Trans.* **2015**, *44* (11), 4933–4944. https://doi.org/10.1039/c4dt02969k.

Synthesis of 4:

To a 10 mL flame-dried Schlenk flask added **3** (500.0 mg, 1.66 mmols), $Pd(dppf)Cl_2 \cdot CHCl_2$ (67.0 mg, 0.083 mmol), B_2pin_2 (506.0 mg, 1.99 mmols) and KOAc (488.0 mg, 4.98 mmols). Evacuated and back-filled the flask with N_2 (3X). Dissolved the solids in 3.3 mL of anhydrous 1,4-dioxane. Stirred at 70 °C for 24 hours. After the reaction was complete the mixture was diluted in EtOAc and the organic solution was washed with water (3X). The organic layer was collected and further washed with a saturated solution of NH_4Cl (1X) and brine (1X). The solvent was removed by rotary evaporation and the resulting residue was purified via flash column chromatography using silica as the stationary phase and 10% EtOAc in hexanes as the mobile phase. Collected 145.1 mg of a golden yellow solid (50% yield).

^{1}H NMR (400 MHz, $CDCl_3$) δ7.773-7.753 (d, J = 8.1 Hz, 2 H); δ7.483-7.463 (d, J = 8.1 Hz, 2 H); δ7.431-7.409 (d, J = 8.8 Hz, 2H); δ7.137-7.097 (d, J = 16.2H Hz, 1 H); δ6.935-6.895 (d, J = 16.2 Hz, 1 H); δ6.724-6.702 (d, J = 8.8 Hz, 2 H); δ2.989 (s, 6 H); δ1.348 (s, 12 H).

Synthesis of 6:

Dissolved **5** (50.00 mg, 0.125 mmols) in 2.4 mL of EtOH. Using a syringe added bromine (0.2 mL) dropwise. The reaction was stirred at room temperature for 24 hours. After the reaction was complete the reaction mixture was diluted in DCM and washed with 1 M Na_2SO_3 (1X). The solvent was removed by rotary evaporation. Collected 62.7 mg of a red orange solid (82% yield). Product was confirmed by LCMS.

ESI MS, calculated for $[M+H]^+$, $C_{20}H_8Br_2Cl_2O_5^+$, 556.8; found: 556.9

Attempted Synthesis of 7:

To a 10 mL flame-dried Schlenk flask added **6** (57.52 mg, 0.103 mmol), **4** (71.88 mg, 0.206 mmol), $PddppfCl_2$•$CHCl_2$(8.41 mg, 0.010 mmol). Evacuated and back-filled the flask with N_2 (3X) and added 2 mL of anhydrous DMF. Added 0.1 mL of an aqueous 5 M K_2CO_3 solution to the flask. The aqueous 5 M K_2CO_3 solution had been previously bubbled overnight with N_2. The reaction was stirred for 24 hours at 60 °C. LCMS analysis showed $[M-H]^+$ that matched **6** and **4** only. No product was detected.

A3.3 NMR and LCMS Data

Spectrum S26. ^{1}H NMR Compound 4

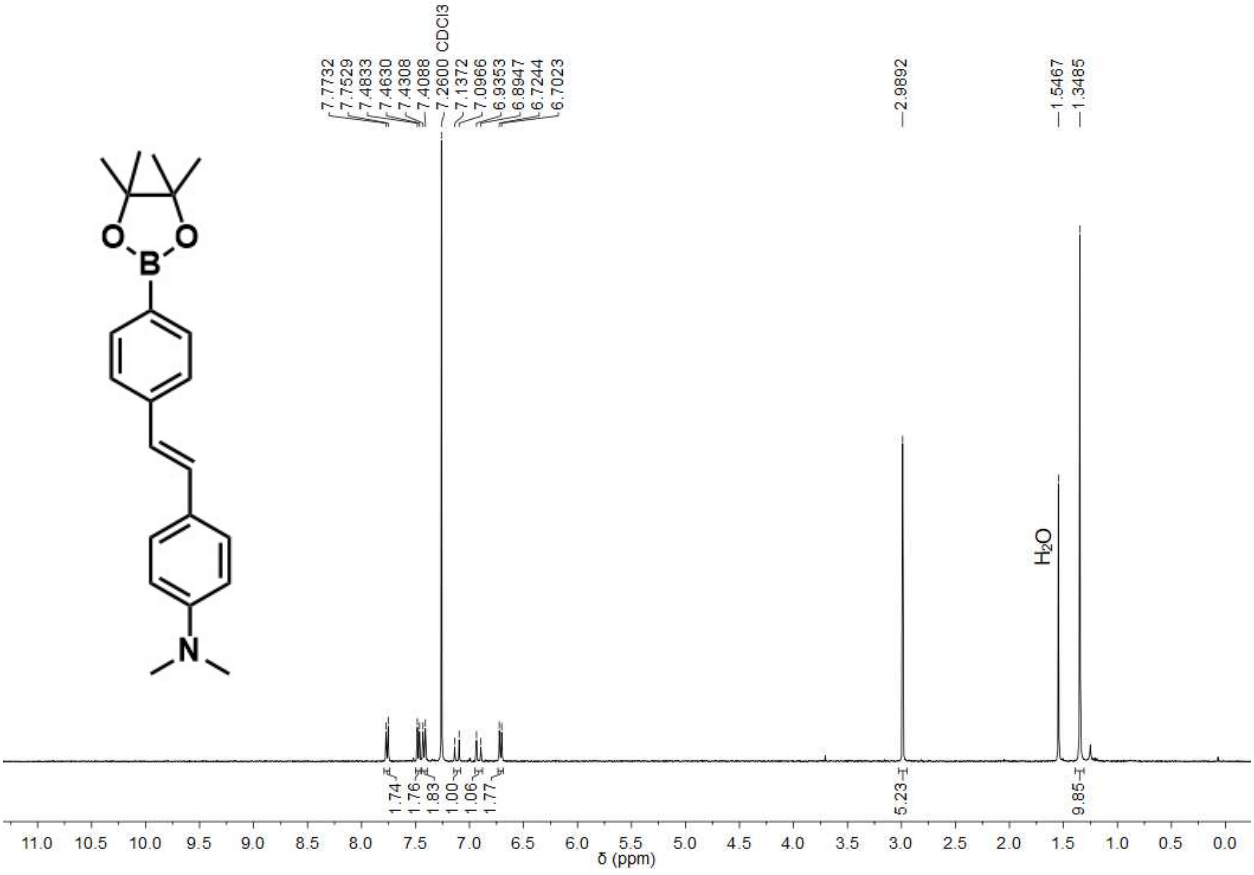

Spectrum A3.2 LC/MS traces Compound 6

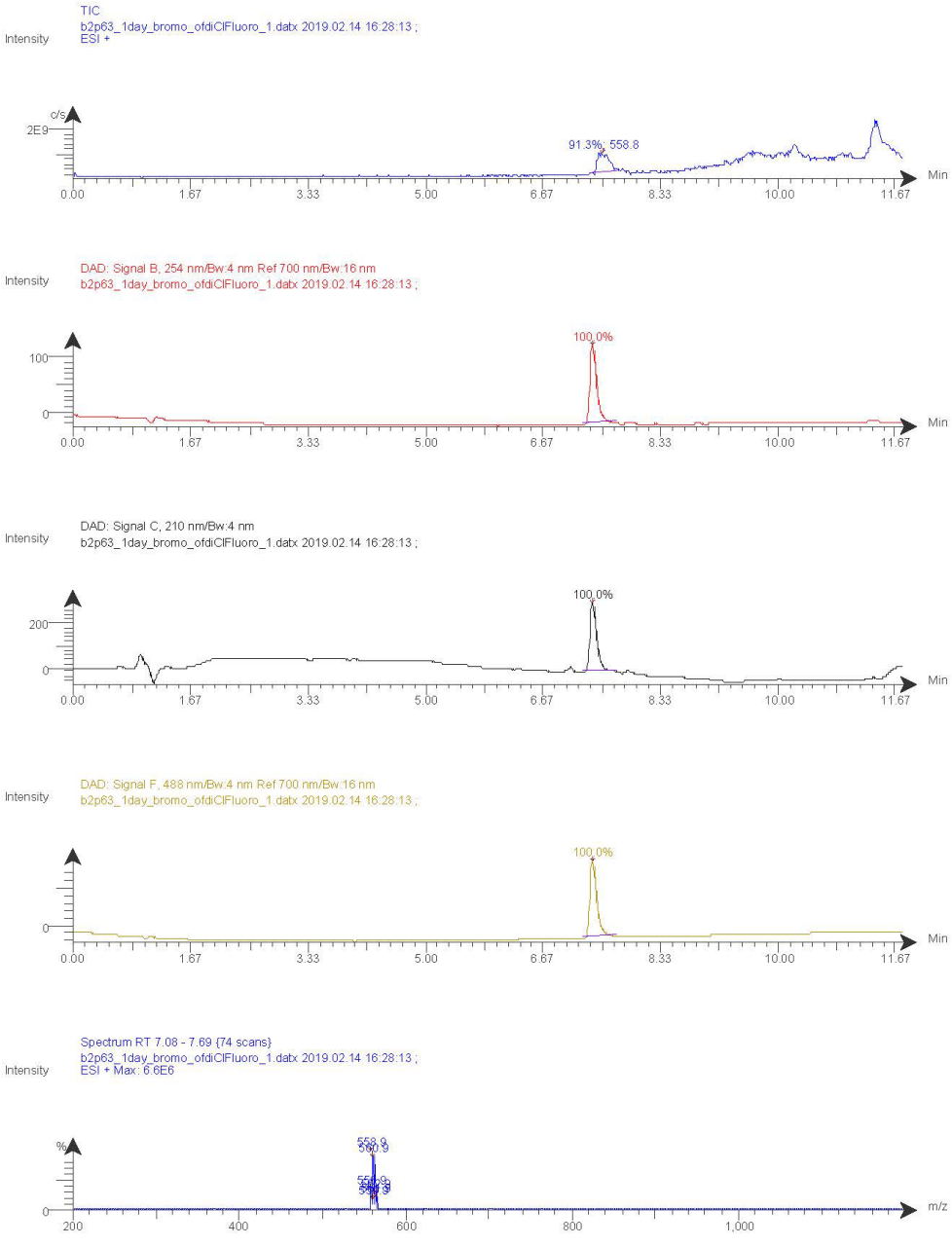

A3.4 References

(1) Deal, P. E.; Kulkarni, R. U.; Al-Abdullatif, S. H.; Miller, E. W. Isomerically Pure Tetramethylrhodamine Voltage Reporters. *J. Am. Chem. Soc.* **2016**, *138* (29), 9085–9088. https://doi.org/10.1021/jacs.6b05672.

(2) Hayne, D. J.; North, A. J.; Fodero-Tavoletti, M.; White, J. M.; Hung, L. W.; Rigopoulos, A.; Mclean, C. A.; Adlard, P. A.; Ackermann, U.; Tochon-Danguy, H.; Villemagne, V. L.; Barnham, K. J.; Donnelly, P. S. Rhenium and Technetium Complexes That Bind to Amyloid-β Plaques. *Dalt. Trans.* **2015**, *44* (11), 4933–4944. https://doi.org/10.1039/c4dt02969k.

(3) Sandin, R. B.; Orvis, R. L. Some Properties of Fluorescein. *J. Org. Chem.* **1958**, *23* (8), 1234–1235. https://doi.org/10.1021/jo01102a623.

(4) Liu, S.; Lv, M.; Xiao, D.; Li, X.; Zhou, X.; Guo, M. A Highly Efficient Catalyst of a Nitrogen-Based Ligand for the Suzuki Coupling Reaction at Room Temperature under Air in Neat Water. *Org. Biomol. Chem.* **2014**, *12* (25), 4511–4516. https://doi.org/10.1039/c3ob42517g.

Appendix 4

Methionine Proximity-Activated Imaging Reporter

Portions of this work were published in the following scientific journal:

Ohata, J.; Krishnamoorthy, L.; Gonzalez, M. A.; Xiao, T.; Iovan, D. A.; Toste, F. D.; Miller, E. W.; Chang, C. J. An Activity-Based Methionine Bioconjugation Approach to Developing Proximity-Activated Imaging Reporters. *ACS Central Science*. 2020.

This work was done in collaboration with the following person:

Jun Ohata performed the PLA assays in neurons and the analysis of those images.

A4.0 Introduction

Many calcium activity reporters provide real time fluorescent data of calcium fluctuations within a cell. These calcium indicators are either small molecules or genetically encoded fluorescent proteins that have been modified to change their fluorescence based on calcium levels within the cell. Some commonly known small molecule indicators are Oregon Green 488 BAPTA-AM and the Cal-X series. These small molecule reporters are typically comprised of a xanthene fluorophore bonded to a chelator such as BAPTA. In the presence of calcium, fluorescence increases once the chelating agent binds to Ca^{2+}. AM esters mask these charged molecules and allow them to enter the cell and detect changes in intracellular calcium levels. These are especially useful for cultured cells since they can be bath applied but much more difficult to use in tissue unlike their genetically encoded counterparts, most widely known GCaMP.[1] While genetic targeting allows genetically encoded calcium indicators (GECIs) to be expressed in animals, like small molecule indicators, GECIs require continuous monitoring of signal which can be difficult to achieve in live and moving animals. Constant illumination is also detrimental to cell health and restricts the length of time in that calcium levels can be monitored. In these situations, calcium indicators known as integrators can be particularly useful. Integrators record the cumulative calcium activity of cells over time. Before the development of photo convertible calcium integrators, researcher quantified the transcription levels of immediate early genes (IEGs) such as c-fos, whose expression is affected in part by the amount of intracellular calcium present.[2] However, IEGs have been shown to be weakly correlated to fluctuations in Ca^{2+} levels since a variety of factors can influence their transcription.[3,4] CaMPARI is an example of a photoactivatable calcium integrators that contains a photoconvertible protein which redshifts is fluorescence from green to red upon simultaneous exposure to UV light (405 nm) and rises in calcium levels.[5] The changes in the CaMPARI protein are permanent, the samples can be fixed and the green to red fluorescent ratio quantified at a later time albeit with significant loss in fluorescent signal (~50%). Although this system is usable in a wide variety of biological systems (cultured neurons, drosophila, zebrafish and mice) it still requires illumination with high energy photoconverting light. The amount of photoconverting light can vary greatly from one sample to another (2s to 10s at intensities of 1.5 W/cm^2 to 400 mW/cm^2) and requires careful titration in order to achieve an accurate relative quantification of calcium levels. Cal-Light, another photosensitive calcium integrator, uses simultaneous illumination with blue light and high levels of intracellular calcium to drive expression of a reporter protein.[6] Therefore, highly active cells will express greater amounts of the reporter protein. This system requires expression of two proteins one of which contains five protein domains. Both proteins must be available in the correct stoichiometric amounts within the cell in order to avoid calcium buffering. FLARE, another calcium integrator similar to Cal-Light, also uses illumination with blue light and calcium to drive expression of a desired protein (fluorescent protein or opsin; 10-15 min at 467nm, 400 mW/cm^2).[7] However temporal resolution of FLARE is limited to greater than 1 minute and requires exogenous proteins whose expression must be optimized before use in a new cell line. In all three cases these protein-based integrators

require optimization of expression in each system as well as the use of high energy light for periods of time that has the potential to affect cell viability.

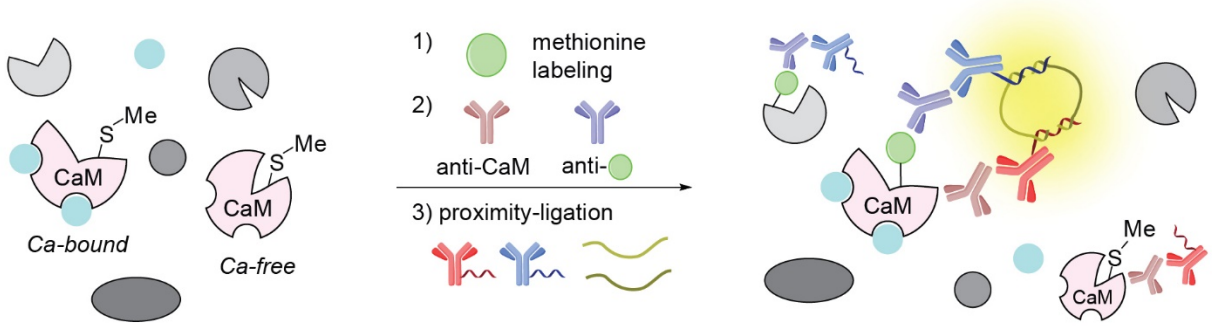

Figure A4.0.1 A schematic illustration of Met-PAIR on CaM. Blue ball: calcium ions in live cells.

The Methionine Proximity-Activated Imaging Reporter (Met-PAIR) can monitor calcium changes in samples over a period without the need for constant illumination or use of high energy photoconverting or photoactivating light. This strategy also employs the use of native calmodulin for the detection of calcium and does not require expression of non-endogenous proteins or making this technique widely applicable. Calmodulin (CaM) is a ubiquitous calcium-binding protein expressed in all eukaryotic cells with a highly conserved amino acid sequence among species. Upon binding to calcium, CaM undergoes a dynamic structural change which exposes hydrophobic pockets in the protein structure, thereby enabling a slew of subsequent protein-protein interactions to propagate signaling cascades.[8] In particular, human CaM possesses a total of 10 methionine residues, 8 of which are located in the two calcium-binding domains (4 each in N- and C-terminal domain) and become surface-exposed upon calcium binding (**Figure A4.0.1**). This dynamic, calcium-dependent conformational change led us to pursue a calcium-sensing strategy in which the extent of methionine modification on CaM would be sensitive to calcium binding, where increased accessibility of these methionine sites upon metal coordination would lead to increased labeling by a methionine reactive oxaziridine. Labeling of methionine residues with oxaziridine has been previously reported as a redox-activated chemical tagging (ReACT) method for chemoselective modification of methionine residues.[9,10]

Since analyte recognition relies on the native activity of proteins in the cell at endogenous levels, calcium buffering effects, seen with chelation-based sensors, would be minimized through this method. Signal is generated by an AND-type logic gate, where an amplified response will occur if and only if both the methionine activity label and methionine-sensing protein label bind to the same protein target, which minimizes background signal from off-target binding. We establish this approach, which we term proximity-activated imaging reporter (PAIR), by applying an oxaziridine reagent, **Ox4**, bearing a bioorthogonal alkyne functional group to label functional methionine sites on endogenous CaM (**Figure A4.1.1**). Increases in calcium release cause an increase in **Ox4** methionine labeling. Antibody labeling of the calcium-responsive protein in conjunction with a proximity ligation assay (PLA) [11–13]

provides a proxy for the relative levels of the calcium, as well as a method for imaging integrated snapshots of the calcium activity of neurons with spatial resolution.

A4.1 Assessing Ox4 Effects on Neuron Activity

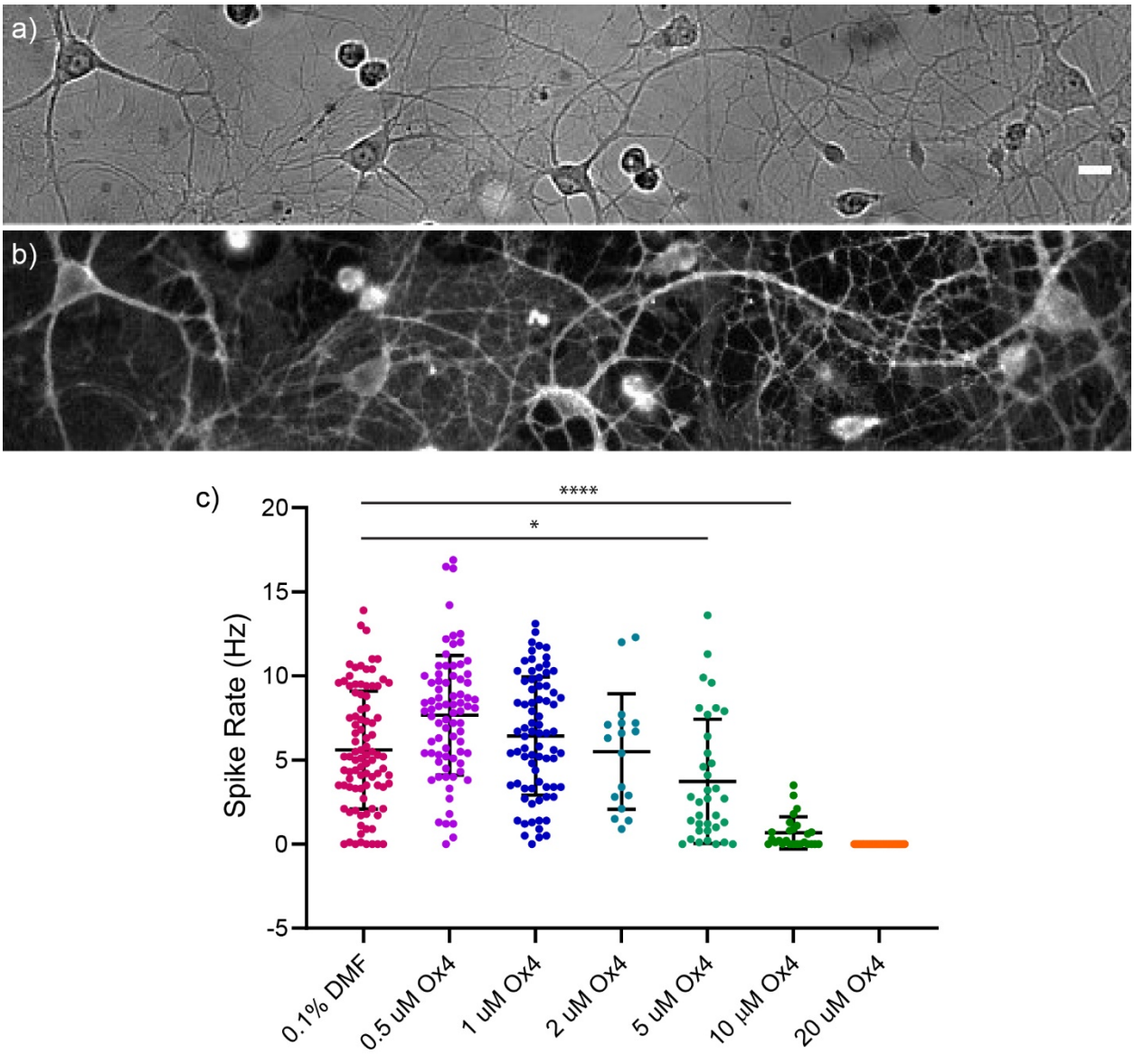

Figure A4.1.1 Fluorescence analysis of voltage response of rat hippocampal neuron stained by a voltage-sensitive fluorophore, BeRST1 in the presence or absence of **Ox4**. 0.1% dimethylformamide was applied for the "no **Ox4**" control conditions. Representative neuron images for the experiments. **a)** DIC channel, scale bar 20 µm, and **b)** BeRST1 fluorescence (bottom). Neurons in these images were treated with 20 µM **Ox4**. **c)** Quantification of spike rates of neurons imaged with BeRST 1 in the presence of a DMF control or **Ox4** (0.5 – 20 µM). Each dot represents the firing frequency of the cell bodies of each neuron. The error bars and center line represent the standard deviation and mean intensity, respectively. The quantification was conducted with imaging of 4 regions in each of 1-5 independent biological replicates (total 8 images). The number of neurons

quantified per condition: 92 (no **Ox4**), 78 (0.5 µM **Ox4**), 76 (1 µM **Ox4**), 17 (2 µM **Ox4**), 35 (5 µM **Ox4**), 26 (10 µM **Ox4**) and 37 (20 µM **Ox4**). Statistical significance differences among conditions were determined using one-way ANOVA followed by Dunnett's multiple comparisons test was performed in GraphPad Prism version 8.4.3. for Windows, GraphPad Software, San Diego, California USA, www.graphpad.com. P-values of the pairwise comparisons that were less than 0.05 considered statistically significant. (*) = significant, (****) = very significant. Dunnett's multiple comparisons test of 0.1% DMF versus all other time points gave the following P-values: 0.0002 (0.1% DMF vs. 0.5 µM **Ox4**), 0.4099 (0.1% DMF vs. 1 µM **Ox4**), 0.9999 (0.1% DMF vs. 2 µM **Ox4**), 0.0223 (0.1% DMF vs. 5 µM **Ox4**), <0.0001 (0.1% DMF vs. 10 µM **Ox4**), <0.0001 (0.1% DMF vs. 20 µM **Ox4**).

To understand how **Ox4** affected neuron activity, dissociated rat hippocampal neurons were stained with voltage sensing dye BeRST1[14] and treated with varying concentrations of **Ox4** for 20 minutes. A concentration of 20 µM was choosen as a starting point because that was the concentration necessary for HEK and Jurkat cells. At this concentration we noted that neurons had a firing frequency of 0 Hz in the two independent biological replicates analyzed (**Figure A4.1.1 c**). Firing frequency was determined by identifying the number of action potentials recorded by BeRST1 over the period of imaging. At 5 and 10 µM **Ox4**, the dampening effect of **Ox4** on firing frequency was still significant. At 1 and 2 µM the effects were no longer significant (**Figure A4.1.1 c**). There is a slight significant increase in firing frequency at 0.5 µM **Ox4** when compared to the DMF control (**Figure A4.1.1 c**). Since we were mostly concerned in the inhibition of spontaneous neuron activity and slightly higher concentration s of **Ox4** did not show any significant effects, we used a concentration of 0.5 µM for neuron experiments.

A4.2 Detecting Changes in Calcium Release Using MetPAIR

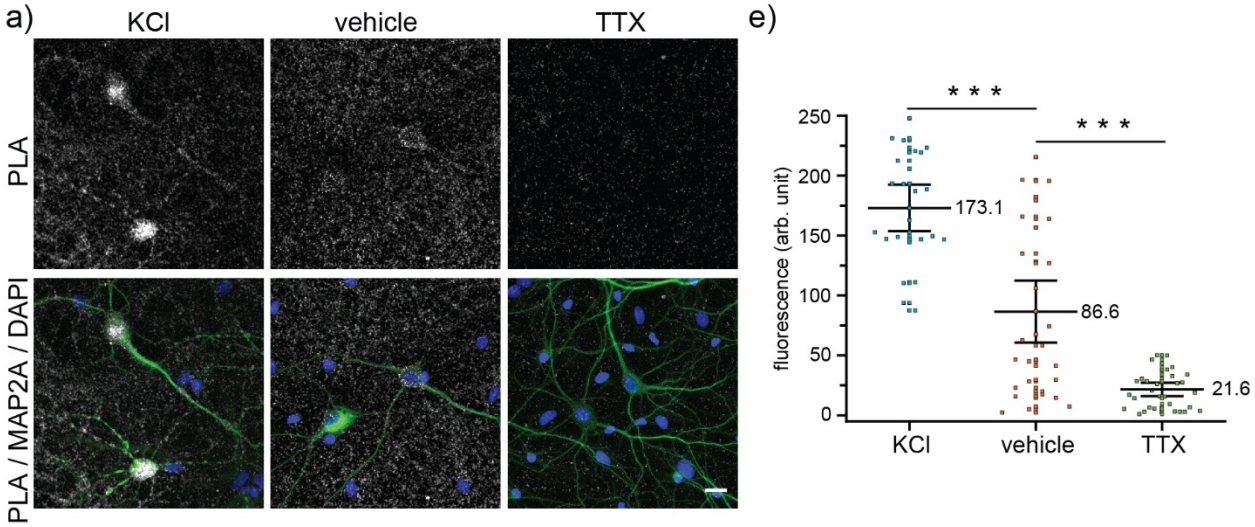

Figure A4.2.1 "Turn-on" detection of changes in calcium levels in cells by applying the Methionine Proximity-Activated Imaging Reporter (Met-PAIR) method to the native calcium regulatory protein calmodulin (CaM) at endogenous levels. Oxaziridine labeling in live cells was conducted in the presence of various reagents in Hanks' balanced salt solution (HBSS) with alkyne-tagged oxaziridine **Ox4** (0.5 µM) at 37 °C for 5 min in hippocampal

neurons. PLA staining was performed with mouse anti-CaM antibody and rabbit anti-biotin antibody (neuron). Gray: PLA staining. Blue: DAPI nuclear staining. Scale bar: 20 μm. d) Confocal images of rat hippocampal neuron stained by Met-PAIR with activation (KCl: 90 mM) or deactivation (tetrodotoxin, TTX: 10 μM) to increase or decrease calcium transients, respectively. Anti-MAP2A antibody (green) was used to identify neurons. e) Whisker plots for the confocal images in d) neurons. Each dot represents the fluorescence intensity of neuronal cell bodies. Whisker and center line represent 95% confidence interval and mean intensity, respectively. The mean value is shown near the center line. The quantification was conducted by imaging 5 regions in each of 2 independent biological replicates (total 10 images) were used for the quantification of neuronal cell bodies identified by the MAP2A staining. The number of quantified cells: 24 (KCl), 30 (neuron vehicle), and 32 (TTX). ***$P < 0.001$, Student's t test.

Met-PAIR can also be utilized to image calcium status of cultured rat hippocampal neurons, where neuronal activation is typically accompanied by an increase in intracellular calcium levels. Potassium chloride is known to activate calcium signaling through a depolarization mechanism,[15] and the Met-PAIR method visualized the calcium increase under these conditions as compared to vehicle control (**Figure A4.2.1**). In turn, tetrodotoxin (TTX), a known sodium channel blocker that inhibits action potentials and consequently leads to decreases in intracellular calcium,[16] was successfully visualized by the Met-PAIR method as well. Overall, the data indicate that Met-PAIR is a suitable tool for calcium detection across various cell types.

A6.3 Imaging Details

Preparation of Primary Neuron Cultures

Hippocampi were dissected from embryonic day 19 Sprague Dawley rats (Charles River Laboratory) in cold sterile HBSS (zero Ca2+, zero Mg2+). All dissection products were supplied by Invitrogen, unless otherwise stated. Hippocampal tissue was treated with trypsin (2.5%) for 15 min at 37 °C. The tissue was triturated using fire polished Pasteur pipettes, in minimum essential media (MEM) supplemented with 5% fetal bovine serum (FBS; Thermo Scientific), 2% B-27, 2% 1M dextrose (Fisher Scientific) and 1% GlutaMax. The dissociated cells were plated onto 12 mm diameter coverslips (Fisher Scientific) pre-treated with PDL (as above) at a density of 25,000-20,000 cells per coverslip in MEM supplemented media (as above). Neurons were maintained at 37 °C in a humidified incubator with 5 % CO2. After 1 day in vitro (DIV) half of the MEM supplemented media was removed and replaced with Neurobasal media containing 2% B-27 supplement and 1% GlutaMax. Functional imaging was performed on mature neurons 13-20 DIV. Treatment with Ox4 and fixation of neurons were done after 12-15 DIV.

MetPAIR Labeling Procedure

For PAIR experiment of CaM, cells in culture medium or buffer were washed with HBSS (+Ca, +Mg) once and incubated with **Ox4** (20 μM) in HBSS at 37 °C for 5 minutes. For

treated cells, HBSS (+Ca, +Mg) containing KCl (90 mM) or tetrodotoxin (10 μM) were used. The cells were washed with the HBSS containing acetylmethionine (0.2 mM) once, and then fixed with 4% formaldehyde in PBS at rt for 15 min.

The fixed cells were washed with PBS once and permeabilized in PBS containing triton-100X at rt (0.25% triton for 5 min). After wash with PBS twice, the cells were incubated at rt for 30 min in TBS buffer containing $CuSO_4$ (4 mM), Na ascorbate (10 mM), and Oregon green azide (50 μM, Click Chemistry Tools, #1264). The cells were washed with PBS once, incubated at rt in PBS containing 5 mM EDTA at least for 15 min, and washed twice again with PBS. After the click chemistry process, each coverslip was taken from a 6-well plate, and its edge was delineated with the hydrophobic pen (neuron on the edge was briefly removed by kimwipe beforehand to facilitate the delineation process). The drawn hydrophobic boundary was dried at rt for 5~10 min (minimum amount of PBS was applied to cells during this drying process to prevent dryness of cells), and the entire slide or coverslip was washed with PBS once.

After the whole delineation process, 20 μL incubation volume per well was used for the rest of the Met-PAIR procedures. The cells were blocked in Duolink blocking medium for 1 h at 37 °C (neuron) and incubated with anti-protein antibody (1:500) and anti-Oregon green or in Duolink antibody diluent at 37 °C for 1 h (neuron), followed by wash with PBS at rt for 5 min twice. Secondary antibody incubation with anti-mouse PLUS antibody (1:5) and anti-rabbit MINUS antibody (1:5) were conducted in in Duolink antibody diluent at 37 °C for 1 h (neuron). After wash with Duolink wash A buffer, ligation, and polymerization processes as well as mounting process were performed following the Duolink PLA protocol from Sigma Aldrich. For neuron, neuronal staining was performed at rt for 30 min in Duolink antibody diluent containing anti-MAP2A antibody–AlexaFluor™488 conjugate (1:100) after the polymerization process. After the mounting process, the coverslip was sealed with nail polish, air-dried at least for 20 min, and analyzed by confocal microscopy.

Effect of Ox4 on Neuron Activity with Voltage-Sensitive Fluorophore BeRST1

Neurons were incubated at 37 °C with a 500 nM BeRST1 solution in HBSS for 20 minutes. BeRST1 is a fluorescent voltage indicator whose fluorescence changes in response to changes in cellular membrane potential.[14] The coverslip was transferred to an imaging dish containing one of the following HBSS solutions; 500 nM **Ox4**, 1 μM **Ox4** or 0.1% DMF. Spontaneous neuronal activity was recorded optically for approximately 10 seconds using an epifluorescence microscope, AxioExaminer Z-1 (Zeiss), equipped with a Spectra-X Light engine LED light (Lumencor) and controlled with MicroManager (Studio Version 1.4.22). Imaging data was acquired with a W-Plan-Apo 20x/1.0 water objective (20x, Zeiss) and an OracFlash4.0 sCMOS camera (Hamamatsu) at an optical sampling rate of 500 Hz. BeRST1 was excited with a red LED (631/28 nm bandpass, 4.64 W/cm^2) and emission was collected with a quadruple emission filter (430/32, 508/14, 586/30, 708/98 nm) after passing through

a quadruple dichroic mirror (432/38, 509/22, 586/40, 654 nm LP). A total of 4 areas per coverslip were imaged. Spiking frequency was determined by counting spikes from ROIs associated with cells bodies.

A6.4 References

(1) Yang, Y.; Liu, N.; He, Y.; Liu, Y.; Ge, L.; Zou, L.; Song, S.; Xiong, W.; Liu, X. Improved Calcium Sensor GCaMP-X Overcomes the Calcium Channel Perturbations Induced by the Calmodulin in GCaMP. *Nat. Commun.* **2018**, *9* (1). https://doi.org/10.1038/s41467-018-03719-6.

(2) Sheng, M.; McFadden, G.; Greenberg, M. E. Membrane Depolarization and Calcium Induce C-Fos Transcription via Phosphorylation of Transcription Factor CREB. *Neuron* **1990**, *4* (4), 571–582. https://doi.org/10.1016/0896-6273(90)90115-V.

(3) Greer, P. L.; Greenberg, M. E. From Synapse to Nucleus: Calcium-Dependent Gene Transcription in the Control of Synapse Development and Function. *Neuron* **2008**, *59* (6), 846–860. https://doi.org/10.1016/j.neuron.2008.09.002.

(4) Fields, R. D.; Eshete, F.; Stevens, B.; Itoh, K. Action Potential-Dependent Regulation of Gene Expression: Temporal Specificity in Ca2+, CAMP-Responsive Element Binding Proteins, and Mitogen- Activated Protein Kinase Signaling. *J. Neurosci.* **1997**, *17* (19), 7252–7266. https://doi.org/10.1523/jneurosci.17-19-07252.1997.

(5) Fosque, B. F.; Sun, Y.; Dana, H.; Yang, C. T.; Ohyama, T.; Tadross, M. R.; Patel, R.; Zlatic, M.; Kim, D. S.; Ahrens, M. B.; Jayaraman, V.; Looger, L. L.; Schreiter, E. R. Labeling of Active Neural Circuits in Vivo with Designed Calcium Integrators. *Science (80-.).* **2015**, *347* (6223), 755–760. https://doi.org/10.1126/science.1260922.

(6) Lee, D.; Hyun, J. H.; Jung, K.; Hannan, P.; Kwon, H. B. A Calcium- A Nd Light-Gated Switch to Induce Gene Expression in Activated Neurons. *Nat. Biotechnol.* **2017**, *35* (9), 858–863. https://doi.org/10.1038/nbt.3902.

(7) Wang, W.; Wildes, C. P.; Pattarabanjird, T.; Sanchez, M. I.; Glober, G. F.; Matthews, G. A.; Tye, K. M.; Ting, A. Y. A Light- A Nd Calcium-Gated Transcription Factor for Imaging and Manipulating Activated Neurons. *Nat. Biotechnol.* **2017**, *35* (9), 864–871. https://doi.org/10.1038/nbt.3909.

(8) Johnson, C. K. Calmodulin, Conformational States, and Calcium Signaling. A Single-Molecule Perspective. *Biochemistry*. 2006. https://doi.org/10.1021/bi061058e.

(9) Lin, S.; Yang, X.; Jia, S.; Weeks, A. M.; Hornsby, M.; Lee, P. S.; Nichiporuk, R. V.; Iavarone, A. T.; Wells, J. A.; Toste, F. D.; Chang, C. J. Redox-Based Reagents for Chemoselective Methionine Bioconjugation. *Science (80-.).* **2017**. https://doi.org/10.1126/science.aal3316.

(10) Christian, A. H.; Jia, S.; Cao, W.; Zhang, P.; Meza, A. T.; Sigman, M. S.; Chang, C. J.; Toste, F. D. A Physical Organic Approach to Tuning Reagents for Selective and Stable Methionine Bioconjugation. *J. Am. Chem. Soc.* **2019**. https://doi.org/10.1021/jacs.9b04744.

(11) Bagchi, S.; Fredriksson, R.; Wallén-Mackenzie, Å. In Situ Proximity Ligation Assay (PLA). *Methods Mol. Biol.* **2015**. https://doi.org/10.1007/978-1-4939-2742-5_15.

(12) Li, G.; Montgomery, J. E.; Eckert, M. A.; Chang, J. W.; Tienda, S. M.; Lengyel, E.; Moellering, R. E. An Activity-Dependent Proximity Ligation Platform for Spatially Resolved Quantification of Active Enzymes in Single Cells. *Nat. Commun.* **2017**. https://doi.org/10.1038/s41467-017-01854-0.

(13) Gao, X.; Hannoush, R. N. Method for Cellular Imaging of Palmitoylated Proteins with Clickable Probes and Proximity Ligation Applied to Hedgehog, Tubulin, and Ras. *J. Am. Chem. Soc.* **2014**. https://doi.org/10.1021/ja410068g.

(14) Huang, Y. L.; Walker, A. S.; Miller, E. W. A Photostable Silicon Rhodamine Platform for Optical Voltage Sensing. *J. Am. Chem. Soc.* **2015**. https://doi.org/10.1021/jacs.5b06644.

(15) Xie, J.; Black, D. L. A CaMK IV Responsive RNA Element Mediates Depolarization-Induced Alternative Splicing of Ion Channels. *Nature* **2001**. https://doi.org/10.1038/35073593.

(16) Farmer, C. E.; Smith, K. J.; Docherty, R. J. Low Concentrations of Tetrodotoxin Interact with Tetrodotoxin-Resistant Voltage-Gated Sodium Channels. *Br. J. Pharmacol.* **2008**. https://doi.org/10.1038/bjp.2008.235.

Appendix 5

Automated Region of Interest Selection of Retina poRhoVR and MEA Imaging

This work was done in collaboration with Jeremey Dworkin, who simplified the workflow of this script.

A5.1 Automated ROI selection with Rings_Quads_Rectangles

Circular regions of interest and rectangular regions of interest (ROIs) were automatically delineated using a MATLAB R2020a script. This script was used to extract poRhoVR **14** and GCaMP6f traces from tiff stacks collected during simultaneous optical recording of calcium (GCaMP 6f) and transmembrane potential (poRhoVR **14**) fluctuations as well as electrical recordings of extracellular potential fluctuations (multi-electrode array) in mouse retina (see **Figures 4.4.1-2**). Ring_Quads_Rectangles works by identifying the black electrodes in an image and drawing the various ROIs based off the coordinates of the center of the black electrodes. This program will not work without these distinct black markers. The ROIs drawn by the program will be rings around the electrodes (16 pixels wide) (**Figure 4.4.1**), rectangles between the two electrodes (height= 32 pixels, width is dependent on number of rectangles draw) (**Figure 4.4.2**). The program will also divide the ring ROIs into 4 quadrants.

To use Rings_Quads_Rectangles follow the instructions below:

1. Set path to a folder that contains Rings_Quads_Rectangles_MAC.m, tiffStackReader, and your sample data
2. In the "Rings Specifications" section
    a. Change the value of Rmin to be the values of the radius you wish the program to detect for the inner ring
    b. Change the value of Rmax to be the values of the radius you wish the program to detect for the outer ring
3. In the "Rectangles Specification" section
    a. Change the value of n to be the number of rectangles you wish to create
    b. Change the value of d to be how close you want the rectangles to be to either electrode head
4. Type into the command window "Rings_Quads_Rectangles_MAC('fImage,' 'movie', 'filename')
    a. Replace fImage with the .tiff image file for the first frame of the movie
    b. Replace movie with the .tiff file for the movie
    c. Replace filename with the title of the folder you wish to generate your data into
5. Hit enter
6. To use this script with a PC change "/" to "\" so that the variables will save properly.

A5.2 Rings_Quads_Rectangles for MAC

```
function Rings_Quads_Rectangles_MAC(movie, filename)
%% RINGS specifications

Inside_radius_prompt = {'Input deired inner radius length in
pixels (12)'};
inner_Radius = inputdlg(Inside_radius_prompt);
Interior_Radius = str2double(inner_Radius);
outside_radius_prompt = {'Input desired outer radius length in
pixels (16)'};
outer_Radius = inputdlg(outside_radius_prompt);
Exterior_Radius = str2double(outer_Radius);

%% QUADS specifications

%% RECTANGLES specifications

rectangels_prompt = {'Input desired number of rectangles to be
drawn'};
number_rectangles = inputdlg(rectangels_prompt); %number of
rectangles
number_of_rectangles = str2double(number_rectangles);
distance_rectangles_are_from_electrode = 7; %d = the distance
the rectangle is from the electrode (in map units)

%%

mkdir(filename, 'Rings');
mkdir(filename, 'Quads');
mkdir(filename, 'Rectangles');

%load tif stack as a 3d matrix
tempStack = tiffStackReader(movie);
tempStack = uint16(tempStack);
info=imfinfo(movie);
number_of_images=numel(info);

%% RINGS - finds electrodes and measures centers and radii
figure('Name', 'Rings');
Info=imread(movie);
imshow(imadjust(Info))

% sensitivity can range from 0-1, 0 being most sensitive,
edgethreshhold
```

```
% can range from 0-1, 0 being most sensitive, method can be
phasecode or
% twostage
[centers_Dark, radii_Dark] = imfindcircles(Info,[Interior_Radius
Exterior_Radius],'ObjectPolarity','dark',
'Sensitivity',0.75,'EdgeThreshold',1e-1000,'Method','twostage');
viscircles(centers_Dark, radii_Dark,'LineStyle','--');

%identifying Left and Right center coordinates
[x_center_LeftRing, row_value_Left] = min(centers_Dark(:,1));
%finds min x value in first column of centersDark, irL is the
row value is in
y_center_LeftRing = centers_Dark(row_value_Left,2); %using irL
identify y value corresponding to min x value using the row
index
[x_center_RightRing, row_value_Right] = max(centers_Dark(:,1));
%same idea as before but now find max x value in the first
column of centersDark which is the right
y_center_RightRing = centers_Dark(row_value_Right,2);

%makes a circle around the left electrode
diameter_Left = 2* radii_Dark(row_value_Left);
electrode_radius_Left = radii_Dark(row_value_Left);
x_Min_Left= x_center_LeftRing - electrode_radius_Left;
y_Min_Left = y_center_LeftRing - electrode_radius_Left;
ellipse_Left = imellipse(gca,[x_Min_Left, y_Min_Left,
diameter_Left, diameter_Left]);

%makes a circle around the right electrode
diameter_Right = 2* radii_Dark(row_value_Right);
electrode_radius_Right = radii_Dark(row_value_Right);
x_Min_Right= x_center_RightRing - electrode_radius_Right;
y_Min_Right = y_center_RightRing - electrode_radius_Right;
ellipse_Right = imellipse(gca,[x_Min_Right, y_Min_Right,
diameter_Right, diameter_Right]); %#ok<*IMELLPS>

%makes a second larger elipse around electrodes
diameter_Left_Ring = 2* (radii_Dark(row_value_Left)+ 16);
radius_Left_Ring = radii_Dark(row_value_Left)+16;
x_Min_Left_Ring = x_center_LeftRing - radius_Left_Ring;
y_Min_Left_Ring = y_center_LeftRing - radius_Left_Ring;
ellipse_Left_Ring = imellipse(gca,[x_Min_Left_Ring,
y_Min_Left_Ring, diameter_Left_Ring, diameter_Left_Ring]);

diameter_Right_Ring = 2* (radii_Dark(row_value_Right)+ 16);
radius_Right_Ring= radii_Dark(row_value_Right)+16;
```

```
x_Min_Right_Ring= x_center_RightRing - radius_Right_Ring;
y_Min_Right_Ring = y_center_RightRing - radius_Right_Ring;
ellipse_Right_Ring = imellipse(gca,[x_Min_Right_Ring,
y_Min_Right_Ring, diameter_Right_Ring, diameter_Right_Ring]);

%Saves the Rings Figure
folder = strcat(filename, '/Rings');
figure1 = [folder, '/Rings - shown on image'];
savefig(figure1);

%Uses ellipse to create masks on electrodes
Left_Electrode = ellipse_Left.createMask();
Left_Electrode = uint16(Left_Electrode);

Right_Electrode = ellipse_Right.createMask();
Right_Electrode=uint16(Right_Electrode);

%Uses second ellipse to create mask
Left_Ring_Electrode = ellipse_Left_Ring.createMask();
Left_Ring_Electrode=uint16(Left_Ring_Electrode);

Right_Ring_Electrode = ellipse_Right_Ring.createMask();
Right_Ring_Electrode=uint16(Right_Ring_Electrode);

%subtracts two previous elliptical masks to make a mask shaped
as a ring
%around the electrodes
ellipse_Left_Ring = Left_Ring_Electrode - Left_Electrode;
ellipse_Right_Ring = Right_Ring_Electrode - Right_Electrode;


%Display masks and masks applied to image
%to display masks use
figure('Name', 'Left Ring Mask');
imshow(imadjust(ellipse_Left_Ring));
figure2 = [folder, '/Left Ring Mask'];
savefig(figure2);
figure('Name', 'Right Ring Mask');
imshow(imadjust(ellipse_Right_Ring));
figure3 = [folder, '/Right Ring Mask'];
savefig(figure3);

%Applies mask to left electrode in each image in stack and avgs
fluorescence from ROI to make
%trace y axis is counts x axis is frames
Voltage_Trace_Left = zeros(length(tempStack), 1);
```

```
for j=1:number_of_images
    Left_Ring_Mask = int16(ellipse_Left_Ring);

Voltage_Movie_Left=(int16((tempStack(:,:,j))).*Left_Ring_Mask);%
int16 so that can register negative numbers
    Voltage_Movie_Left(Voltage_Movie_Left<0)=0;
    Voltage_Trace_Left(j)=
(mean(nonzeros(Voltage_Movie_Left)))';
    Voltage_Trace_Left_Ring = Voltage_Trace_Left';
end

%Applies mask to right electrode in each image in stack and avgs
fluorescence from ROI to make
%trace y axis is counts x axis is frames
Voltage_Trace_Right = zeros(length(tempStack), 1);
for j=1:number_of_images
    Right_Ring_Mask = int16(ellipse_Right_Ring);

Voltage_Movie_Right=(int16((tempStack(:,:,j))).*Right_Ring_Mask)
;%int16 so that can register negative numbers
    Voltage_Movie_Right(Voltage_Movie_Right<0)=0;
    Voltage_Trace_Right(j)=mean(nonzeros(Voltage_Movie_Right));
    Voltage_Trace_Right_Ring = Voltage_Trace_Right';
end

s1 = strcat(folder, '/Variables');
s2 = strcat(folder, '/VoltTraces');
save(s1, 'movie', 'centers_Dark', 'radii_Dark',
'Left_Electrode', 'Right_Electrode', 'Left_Ring_Electrode',
'Right_Ring_Electrode', 'ellipse_Left_Ring',
'ellipse_Right_Ring',
'x_center_LeftRing','y_center_LeftRing','x_center_RightRing','y_
center_RightRing','row_value_Left','row_value_Right')
save(s2, 'Voltage_Trace_Left_Ring', 'Voltage_Trace_Right_Ring')

%% QUADS - Splits up ring around the left electrode into
quadrants

Left_Ring_Mask_NorthEast = ellipse_Left_Ring;
for f = 1:size(ellipse_Left_Ring, 1)
    for g = 1:size(ellipse_Left_Ring, 2)
        if (f >= round(y_center_LeftRing))
            Left_Ring_Mask_NorthEast(f, g) = 0;
        elseif (g < round(x_center_LeftRing))
            Left_Ring_Mask_NorthEast(f, g) = 0;
```

```
        end
    end
end

folder = strcat(filename, '/Quads');
figure('Name', 'Left Ring NE Mask');
imshow(imadjust(Left_Ring_Mask_NorthEast));
figure2 = [folder, '/Left Ring NE Mask'];
savefig(figure2);


Left_Ring_Mask_SouthEast = ellipse_Left_Ring;
for f = 1:size(ellipse_Left_Ring, 1)
    for g =1:size(ellipse_Left_Ring, 2)
        if (f < round(y_center_LeftRing))
            Left_Ring_Mask_SouthEast(f, g) = 0;
        elseif (g <= round(x_center_LeftRing))
            Left_Ring_Mask_SouthEast(f, g) = 0;

        end
    end
end

figure('Name', 'Left Ring SE Mask');
imshow(imadjust(Left_Ring_Mask_SouthEast));
figure3 = [folder, '/Left Ring SE Mask'];
savefig(figure3);


Left_Ring_Mask_SouthWest = ellipse_Left_Ring;
for f = 1:size(ellipse_Left_Ring, 1)
    for g =1:size(ellipse_Left_Ring, 2)
        if (f <= round(y_center_LeftRing))
            Left_Ring_Mask_SouthWest(f, g) = 0;
        elseif (g > round(x_center_LeftRing))
            Left_Ring_Mask_SouthWest(f, g) = 0;

        end
    end
end

figure('Name', 'Left Ring SW Mask');
imshow(imadjust(Left_Ring_Mask_SouthWest));
figure4 = [folder, '/Left Ring SW Mask'];
savefig(figure4);
```

```
Left_Ring_Mask_NorthWest = ellipse_Left_Ring;
for f = 1:size(ellipse_Left_Ring, 1)
    for g =1:size(ellipse_Left_Ring, 2)
        if (f > round(y_center_LeftRing))
            Left_Ring_Mask_NorthWest(f, g) = 0;
        elseif (g >= round(x_center_LeftRing))
            Left_Ring_Mask_NorthWest(f, g) = 0;

        end
    end
end

figure('Name', 'Left Ring NW Mask');
imshow(imadjust(Left_Ring_Mask_NorthWest));
figure5 = [folder, '/Left Ring NW Mask'];
savefig(figure5);

%Splits up ring around the right electrode into quadrants
Right_Ring_Mask_NorthEast = ellipse_Right_Ring;
for f = 1:size(ellipse_Right_Ring, 1)
    for g =1:size(ellipse_Right_Ring, 2)
        if (f >= round(y_center_RightRing))
            Right_Ring_Mask_NorthEast(f, g) = 0;
        elseif (g < round(x_center_RightRing))
            Right_Ring_Mask_NorthEast(f, g) = 0;

        end
    end
end

figure('Name', 'Right Ring NE Mask');
imshow(imadjust(Right_Ring_Mask_NorthEast));
figure7 = [folder, '/Right Ring NE Mask'];
savefig(figure7);


Right_Ring_Mask_SouthEast = ellipse_Right_Ring;
for f = 1:size(ellipse_Right_Ring, 1)
    for g =1:size(ellipse_Right_Ring, 2)
        if (f < round(y_center_RightRing))
            Right_Ring_Mask_SouthEast(f, g) = 0;
        elseif (g <= round(x_center_RightRing))
            Right_Ring_Mask_SouthEast(f, g) = 0;

        end
    end
```

```
end

figure('Name', 'Right Ring SE Mask');
imshow(imadjust(Right_Ring_Mask_SouthEast));
figure8 = [folder, '/Right Ring SE Mask'];
savefig(figure8);


Right_Ring_Mask_SouthWest = ellipse_Right_Ring;
for f = 1:size(ellipse_Right_Ring, 1)
    for g =1:size(ellipse_Right_Ring, 2)
        if (f <= round(y_center_RightRing))
            Right_Ring_Mask_SouthWest(f, g) = 0;
        elseif (g > round(x_center_RightRing))
            Right_Ring_Mask_SouthWest(f, g) = 0;

        end
    end
end

figure('Name', 'Right Ring SW Mask');
imshow(imadjust(Right_Ring_Mask_SouthWest));
figure9 = [folder, '/Right Ring SW Mask'];
savefig(figure9);

Right_Ring_Mask_NorthWest = ellipse_Right_Ring;
for f = 1:size(ellipse_Right_Ring, 1)
    for g =1:size(ellipse_Right_Ring, 2)
        if (f > round(y_center_RightRing))
            Right_Ring_Mask_NorthWest(f, g) = 0;
        elseif (g >= round(x_center_RightRing))
            Right_Ring_Mask_NorthWest(f, g) = 0;

        end
    end
end

figure('Name', 'Right Ring NW Mask');
imshow(imadjust(Right_Ring_Mask_NorthWest));
figure10 = [folder, '/Right Ring NW Mask'];
savefig(figure10);

%Applies masks to  each image in stack and avgs fluorescence
from ROI to make trace y axis is counts x axis is frames
Voltage_Trace_Left_NorthEast = zeros(length(tempStack), 1);
for j=1:number_of_images
```

```
    Left_Ring_Mask_NorthEast_int16 =
int16(Left_Ring_Mask_NorthEast);

Voltage_Movie_Left_NorthEast=(int16((tempStack(:,:,j))).*Left_Ri
ng_Mask_NorthEast_int16);%int16 so that can register negative
numbers

Voltage_Movie_Left_NorthEast(Voltage_Movie_Left_NorthEast<0)=0;

Voltage_Trace_Left_NorthEast(j)=mean(nonzeros(Voltage_Movie_Left
_NorthEast));
    Voltage_Trace_Left_NorthEast =
Voltage_Trace_Left_NorthEast';
end

Voltage_Trace_Left_SouthEast = zeros(length(tempStack), 1);
for j=1:number_of_images
    Left_Ring_Mask_SouthEast_int16 =
int16(Left_Ring_Mask_SouthEast);
    Voltage_Movie_Left_SouthEast =
(int16((tempStack(:,:,j))).*Left_Ring_Mask_SouthEast_int16);%int
16 so that can register negative numbers

Voltage_Movie_Left_SouthEast(Voltage_Movie_Left_SouthEast<0)=0;
    Voltage_Trace_Left_SouthEast(j) =
mean(nonzeros(Voltage_Movie_Left_SouthEast));
    Voltage_Trace_Left_SouthEast =
Voltage_Trace_Left_SouthEast';
end

Voltage_Trace_Left_SouthWest = zeros(length(tempStack), 1);
for j=1:number_of_images
    Left_Ring_Mask_SouthWest_int16 =
int16(Left_Ring_Mask_SouthWest);

Voltage_Movie_Left_SouthWest=(int16((tempStack(:,:,j))).*Left_Ri
ng_Mask_SouthWest_int16);%int16 so that can register negative
numbers

Voltage_Movie_Left_SouthWest(Voltage_Movie_Left_SouthWest<0)=0;

Voltage_Trace_Left_SouthWest(j)=mean(nonzeros(Voltage_Movie_Left
_SouthWest));
    Voltage_Trace_Left_SouthWest =
Voltage_Trace_Left_SouthWest';
end
```

```
Voltage_Trace_Left_NorthWest = zeros(length(tempStack), 1);
for j=1:number_of_images
    Left_Ring_Mask_NorthWest_int16 =
int16(Left_Ring_Mask_NorthWest);

Voltage_Movie_Left_NorthWest=(int16((tempStack(:,:,j))).*Left_Ri
ng_Mask_NorthWest_int16);%int16 so that can register negative
numbers

Voltage_Movie_Left_NorthWest(Voltage_Movie_Left_NorthWest<0)=0;

Voltage_Trace_Left_NorthWest(j)=mean(nonzeros(Voltage_Movie_Left
_NorthWest));
    Voltage_Trace_Left_NorthWest =
Voltage_Trace_Left_NorthWest';
end

Voltage_Trace_Right_NorthEast = zeros(length(tempStack), 1);
for j=1:number_of_images
    Right_Ring_Mask_NorthEast_int16 =
int16(Right_Ring_Mask_NorthEast);

Voltage_Movie_Right_NorthEast=(int16((tempStack(:,:,j))).*Right_
Ring_Mask_NorthEast_int16);%int16 so that can register negative
numbers

Voltage_Movie_Right_NorthEast(Voltage_Movie_Right_NorthEast<0)=0
;

Voltage_Trace_Right_NorthEast(j)=mean(nonzeros(Voltage_Movie_Rig
ht_NorthEast));
    Voltage_Trace_Right_NorthEast =
Voltage_Trace_Right_NorthEast';
end

Voltage_Trace_Right_SouthEast = zeros(length(tempStack), 1);
for j=1:number_of_images
    Right_Ring_Mask_SouthEast_int16 =
int16(Right_Ring_Mask_SouthEast);

Voltage_Movie_Right_SouthEast=(int16((tempStack(:,:,j))).*Right_
Ring_Mask_SouthEast_int16);%int16 so that can register negative
numbers
```

```
Voltage_Movie_Right_SouthEast(Voltage_Movie_Right_SouthEast<0)=0
;

Voltage_Trace_Right_SouthEast(j)=mean(nonzeros(Voltage_Movie_Rig
ht_SouthEast));
    Voltage_Trace_Right_SouthEast =
Voltage_Trace_Right_SouthEast';
end

Voltage_Trace_Right_SouthWest = zeros(length(tempStack), 1);
for j=1:number_of_images
    Right_Ring_Mask_SouthWest_int16 =
int16(Right_Ring_Mask_SouthWest);

Voltage_Movie_Right_SouthWest=(int16((tempStack(:,:,j))).*Right_
Ring_Mask_SouthWest_int16);%int16 so that can register negative
numbers

Voltage_Movie_Right_SouthWest(Voltage_Movie_Right_SouthWest<0)=0
;

Voltage_Trace_Right_SouthWest(j)=mean(nonzeros(Voltage_Movie_Rig
ht_SouthWest));
    Voltage_Trace_Right_SouthWest =
Voltage_Trace_Right_SouthWest';
end

Voltage_Trace_Right_NorthWest = zeros(length(tempStack), 1);
for j=1:number_of_images
    Right_Ring_Mask_NorthWest_int16 =
int16(Right_Ring_Mask_NorthWest);

Voltage_Movie_Right_NorthWest=(int16((tempStack(:,:,j))).*Right_
Ring_Mask_NorthWest_int16);%int16 so that can register negative
numbers

Voltage_Movie_Right_NorthWest(Voltage_Movie_Right_NorthWest<0)=0
;

Voltage_Trace_Right_NorthWest(j)=mean(nonzeros(Voltage_Movie_Rig
ht_NorthWest));
    Voltage_Trace_Right_NorthWest =
Voltage_Trace_Right_NorthWest';
end
```

```
Save1 = strcat(folder, '/Quad Masks');
Save2 = strcat(folder, '/VoltTraces - Quads');

save(Save1, 'Left_Ring_Mask_NorthEast',
'Left_Ring_Mask_SouthEast','Left_Ring_Mask_SouthWest','Left_Ring
_Mask_NorthWest','Right_Ring_Mask_NorthEast','Right_Ring_Mask_So
uthEast', 'Right_Ring_Mask_SouthWest');
save(Save2, 'Voltage_Trace_Left_NorthEast',
'Voltage_Trace_Left_NorthWest', 'Voltage_Trace_Left_SouthEast',
'Voltage_Trace_Left_SouthWest', 'Voltage_Trace_Right_NorthEast',
'Voltage_Trace_Right_NorthWest',
'Voltage_Trace_Right_SouthEast',
'Voltage_Trace_Right_SouthWest');

%% Calculated Rectangles - Analysis of area directly between
electrodes

%load image of first slice as a tiff
figure('Name', 'All Rectangles');
Info=imread(movie);
imshow(imadjust(Info))

%radL is the radius of the left electrode
electrode_radius_Left = radii_Dark(row_value_Left);
electrode_radius_Right = radii_Dark(row_value_Right);

%h = the height of the rectangles to be drawn in pixels, w = the
width of
%the rectangles to be drawn
height = 32;
width = (x_center_RightRing-x_center_LeftRing-
(2*distance_rectangles_are_from_electrode)-
electrode_radius_Left-
electrode_radius_Right)/number_of_rectangles;

%Create rectangles and add them to a list. Start at left
electrode and
%build to the right
upperbound = y_center_LeftRing + (height/2);
lowerbound = y_center_LeftRing - (height/2);
Rectangle_List = cell(1,number_of_rectangles);
Voltage_Trace_List = zeros(number_of_images,
number_of_rectangles);
for i = 0:number_of_rectangles-1
```

```
    leftbound = x_center_LeftRing +
distance_rectangles_are_from_electrode + electrode_radius_Left +
i*width;
    rightbound = leftbound+width;
    rect = images.roi.Polygon(gca, 'Position', [leftbound,
upperbound; leftbound, lowerbound; rightbound, lowerbound;
rightbound, upperbound]);
    Rectangle = polyshape([leftbound leftbound rightbound
rightbound], [upperbound lowerbound lowerbound upperbound]);
    Rectangle_List{:, i+1} = Rectangle(1);

    %create each rectangle mask
    rectangle_Mask = createMask(rect);
    Rectangle_Mask = uint16(rectangle_Mask);
    if i == 0
        Size_Array = size(Rectangle_Mask);
        x = Size_Array(1);
        y = Size_Array(2);
        Rectangle_Mask_List = ones(x, y, number_of_rectangles);
        Rectangle_Mask_List(:, :, i+1) = Rectangle_Mask;
    else
        Rectangle_Mask_List(:, :, i+1) = Rectangle_Mask;
    end


    %Apply each rectangle mask to the tiff stack
    Voltage_Trace = zeros(number_of_images, 1);
    for j=1:number_of_images
        Applied_Rectangle_Mask = int16(Rectangle_Mask);

Voltage_Movie=(int16((tempStack(:,:,j))).*Applied_Rectangle_Mask
);%int16 so that can register negative numbers
        Voltage_Movie(Voltage_Movie<0)=0;
        Voltage_Trace(j, 1) = mean(nonzeros(Voltage_Movie));
    end
    Voltage_Trace_List(:, i+1)= Voltage_Trace;
end

%Save the frame 1 image with all rectangles shown
folder = strcat(filename, '/Rectangles');
figure1 = [folder, '/All Rectangles'];
savefig(figure1);

%Generate and save images of the rectangles masks
for m = 1:number_of_rectangles
    title = strcat('Rectangle', num2str(m));
```

```
    figure('Name', title);
    imshow(imadjust(Rectangle_Mask_List(:,:,m)));
    figuretitle = [folder, (strcat('/', title))];
    savefig(figuretitle);
end

%Save all of the voltage and rectangle data
saveA = strcat(folder, '/VoltTraceList');
saveB = strcat(folder, '/RectangleData');
save(saveA, 'Voltage_Trace_List');
save(saveB, 'Rectangle_List', 'Rectangle_Mask_List');
end
```